THE UNIVERSITY *of* EDINBURGH

Rock Physics in Four Dimensions

Jonathan Rajan Singh

Doctor of Philosophy

University of Edinburgh

2019

To my parents

You mustn't be afraid to dream a little bigger, darling.

Eames, *Inception (2010)*

Declaration

I declare that this thesis was composed by myself, that the work contained herein is my own except where explicitly stated otherwise in the text, and that this work has not been submitted for any other degree or professional qualification except as specified.

Jonathan Rajan Singh

September 2019

Abstract

The measurement of the seismic velocity of a medium is fundamental to many applications in geoscience and engineering. Examples include the monitoring of: ice sheet melting, the health of concrete structures, temperature in volcanic regions, and sub-surface fluid pressure due to hydrocarbon extraction or the injection of CO_2 to mitigate climate change. Velocities are also used to infer elastic properties, such as bulk and shear moduli and density, which can then be used to develop a wide range of rock physics models. This thesis addresses two key areas of research related to the seismic velocity: first, the improvement in the methodology of measuring changes in velocity in the time-lapse or four dimensional mode; and second, the interpretation of changing velocity measurements in terms of underlying processes, using various rock physics models.

First, I investigate the use of *coda wave interferometry* (CWI) for measuring temporal changes in bulk velocity, particularly in an experimental rock physics setting. CWI uses the diffuse, multiply-scattered waves that arrive in the tail of the seismogram, sampling the entire medium and sampling the same sub-volumes many times, thus coda waves are far more sensitive to changes in a medium compared to the first arriving ballistic waves. Compared to conventional methods of phase picking of first arriving waves, CWI provides significant improvements in the accuracy and precision of estimates of velocity changes and is far more robust in the presence of background noise. CWI is also capable of jointly estimating changing source locations, allowing the estimation of the relative locations of a cluster of acoustic emissions with simultaneous velocity

perturbations, all with a single receiver. Previously, the estimate of velocity change made by CWI has been an average of changes in compressional (P) and shear (S) wave velocities, which has previously been a major limitation to the application of the CWI method. I present a new method to use CWI for estimating changes in both P and S wave velocities individually. I then validate this method using numerical simulations on a range of media and the results of triaxial rock deformation experiments.

The second part of this thesis is based on understanding the relationship between seismic velocity and time-dependent variables, including the evolving differential stress during deformation and changes in porosity during cementation. I investigate the seismic velocity-differential stress relationship during the experimental deformation of two finely laminated carbonate samples, using CWI to measure the temporal changes in both P and S wave velocity, allowing the inversion of crack density to interpret the mechanical behaviour of these carbonate samples. I then investigate the velocity-porosity relationship with an entirely digital method, using digital rocks where deposition and cementation are computationally simulated. I then simulate wavefield propagation through the digital rocks using a 3D finite-difference method to estimate the velocity of the medium. I statistically test two competing inclusion models for modelling elastic moduli-porosity data and find one that allows variable inclusion aspect ratio to be the most appropriate for fitting the data.

I find CWI to be an effective method characterising changes in a medium in a rock physics environment. By providing a method for estimating separate changes in P and S wave velocity, I greatly improve the relevance and applicability of CWI for experimental rock physics. The method can be extended for the characterisation of media for a variety of applications in geoscience and engineering.

Lay Summary

Imagine standing in a large empty room and clapping your hands together as hard as you can.

What would you hear?

As your hands make contact, they create a pressure wave that travels in all directions. As the wave reaches the air within your ears, the air vibrates, which is what you would perceive as sound.

You may then hear an echo, which occurs when the pressure wave reaches a wall in the room, reflects off the wall, and travels back to you. You may then hear an even later echo, which is where the wave bounces in-between multiple walls before reaching your ears. This process can continue, where waves bounce between more walls and arriving at your ears later for each echo. The later you hear the sound, the larger distance the wave has travelled. The pressure waves here travel at a constant velocity (approximately 330 meters in a second).

In the same way, an acoustic wave can travel through solid materials, such as rocks. Measuring the velocity at which a wave travels through different materials is particularly important for time-lapse (or four dimensional) monitoring purposes, for example, the velocity of the subsurface changes as the fluid properties change during the injection of CO2 or the extraction of hydrocarbons.

In this thesis, I use a method called *coda wave interferometry* (CWI), which estimates a change in a medium with greater accuracy (closer to the true velocity change) and precision (less variability in repeated estimates) compared to conventional methods. This method uses the echoes (multiply-reflected waves) as opposed to the first arriving waves. The echoes travel through the same regions multiple times so are more sensitive to any changes in the medium. I demonstrate how this method can be used to characterise a change in velocity in laboratory rock physics experiments. In addition, the echoes can also be used to estimate any changes in the location of the acoustic sources - imagine clapping your hands in different locations in the room, CWI is able to estimate the distance between these locations by comparing the arrival times of the echoes.

I also seek to improve the understanding of the relationship between the velocity of a medium and time-dependent variables, such as the amount of cracks in a rock during experimental deformation, or the amount of pore space in a rock during cementation (precipitation of minerals into the pore space). I investigate the velocity-crack density relationship with a laboratory experiment using two cores of finely laminated carbonate rock, and I investigate the velocity-porosity relationship using digital rock physics, where synthetic rocks are constructed with computer simulations of deposition and cementation.

Throughout this thesis I make some major improvements to the methods used for measuring a change in velocity, making CWI much more applicable for conventional rock physics models and experiments. The method can in principle be applied to larger field-scale seismic problems.

Acknowledgements

There are many people who have offered an abundance of help and support during my time completing the work within this thesis. Firstly I would like to thank Ian Main and Andrew Curtis, who have always had open doors and helped me in so many aspects of scientific research. Ian has provided endless support and guidance, particularly helping improve my writing style allowing me to publish my work and finish this thesis. Andrew's enthusiasm and guidance has been invaluable, sparking my interest in the field of research.

I would also like to thank the rest of the 4DRP team: Alexis Cartwright-Taylor, Michael Flynn, Mark Chapman, Ian Butler and Florian Fusseis - my work would not have been possible without their help and support in the lab and in data processing. I also extend gratitude to Satyan Singh, who has always gone the extra mile in helping me out with any problems I had. I extend my thanks to my thesis examiners: Katriona Edlmann and Celine Hadziioannou, for the time they spent reading through the thesis, their interesting a helpful discussion, and the useful suggestions they gave for improving this thesis.

I would like to thank my friends at the University of Edinburgh, for keeping the spirits high and supplying plenty of coffee. Special thanks to Ali, Allen, Amjad, Angus, Berit, Dom, Felix, Flo, Megan, Phil and Roseanne. Thank you to Kirsten for your unwavering support and many meals during my write-up. Finally, thank you to my Mum, Dad and Esther for their constant love, support and prayers throughout my PhD.

Contents

List of Tables

List of Figures

Chapter 1

Introduction

1.1 The Review

The complex nature of seismic wave propagation in rocks is studied in great detail across many different applications in geoscience. These studies are often performed to deduce relationships between changes in external conditions and seismic properties such as velocity (Wang, 2001), anisotropy (Christensen, 1966; Sayers and Kachanov, 1995) and attenuation (Toksöz *et al.*, 1979; Sams *et al.*, 1997), and to examine the process of rock fracturing (Pyrak-Nolte *et al.*, 1990) including the distribution of acoustic emissions accompanying microfracturing (Lockner *et al.*, 1992; Lockner, 1993). The measurement and application of the seismic velocity is particularly broad. For example, velocity maps of the subsurface are used in seismic imaging (Robein, 2003), which are particularly important for the migration of seismic data (Versteeg, 1993), estimating fluid pressure change due to fluid extraction or deformation due to stress from velocity changes measured in time lapse 4D seismic data (Guilbot and Smith, 2002; Arts *et al.*, 2004; Stork *et al.*, 2018), deformation during laboratory rock physics experiments (Wang, 2001; King, 1966), using changes in velocity to quantify precursory damage accumulation before earthquakes (Volti and Crampin, 2003; Gao and Crampin, 2004), and using compressional (V_P) and shear (V_S) wave velocities as input to a wide

range of rock physics models (Mavko *et al.*, 2009).

Standard methods for measuring either the velocity, or changes in the velocity (in the 'four dimensional' mode) of a medium involve the picking of first-break arrival times of seismic waves traveling between a fixed source and receiver pair. Though the term 'first-break' is ambiguous, and can be taken to mean the signal onset which is the time of first-arriving energy (Brillouin, 1960), the arrival time of the first peak or the time of first zero-crossing (Hornby, 1998). The velocity of the medium is then estimated using the known straight-line distance between the source and receiver. Problems with the first-break method can occur in wave propagation experiments, particularly when wavelengths are smaller or approximately the same size as the scattering heterogeneities in the medium. One concern is that the first-break method is only sensitive to a specific path between the source and receiver, therefore any estimates of velocity are unrepresentative of the bulk medium. In addition to this, any perturbations that are not located on the fastest ray path can not be detected. Such errors in velocity estimation are carried forward to any subsequent calculations, notably in locating seismic source positions.

Monitoring the relative locations of seismic sources is important for a variety of applications in field and global scale seismology, such as the monitoring of induced seismicity (Ake *et al.*, 2005; Ellsworth, 2013), studying earthquake triggering and interaction (Chen *et al.*, 2013), and imaging of fault planes (Dodge *et al.*, 1995; Waldhauser and Ellsworth, 2002). Absolute source locations are commonly estimated using multilateration, which takes the measured arrival time at each receiver to estimate the source position and origin time (Lee, 1975). These estimates are strongly dependent on the quality of the velocity model, the station coverage, and source-to-receiver distance. Therefore, the uncertainty of earthquake locations can be on the order of kilometers (Shearer, 1999). The accuracy of estimates for relative source locations significantly improves when the distance between two sources is directly estimated rather than their absolute locations (Douglas, 1967; Waldhauser and Ellsworth, 2000).

However, these methods fail in areas with poor seismic station coverage, such as intra-plate regions (Robinson *et al.*, 2013).

Snieder *et al.* (2002) uses the seismic coda (as opposed to the first arriving ballistic waves) to accurately and precisely estimate changes in velocity and in source location. Coda waves are the diffuse multiply-scattered waves that are recorded at the tail of the seismogram. Recordings of coda waves are far more sensitive than first arriving waves to changes in external properties, such as pore-pressure or temperature (Snieder *et al.*, 2002; Vlastos *et al.*, 2006), due to the fact that coda waves follow much longer and more complex paths, eventually sampling the entire medium, and sampling any sub-volume of the medium multiple times. There are now established methods grouped under the name *coda wave interferometry* (CWI) that estimate changes in the velocity of the medium, changes in the locations of sources or receivers, or changes in the location of scatterers using the coda (Snieder, 2006). There have been several field and laboratory applications of CWI, including the monitoring of velocity changes in ice sheets (Mordret *et al.*, 2016; James *et al.*, 2017), concrete (Larose and Hall, 2009; Planès and Larose, 2013), mining environments (Grêt *et al.*, 2006), engineering structures such as bridges (Salvermoser *et al.*, 2015) and volcanic regions (Sens-Schönfelder and Wegler, 2006). CWI has also been used to study velocity changes associated with earthquakes (Hadziioannou *et al.*, 2011), earthquake focal mechanisms (Robinson *et al.*, 2007), earthquake separation distances (Snieder and Vrijlandt, 2005; Robinson *et al.*, 2011), and relative source network locations of induced micro-seismic events (Zhao *et al.*, 2017; Zhao and Curtis, 2019).

One of the major limitations to the application of CWI for experimental rock physics is that the resulting estimate of velocity change ($\Delta V/V$) represents an unknown weighted combination of the change in compressional and shear wave velocities (V_P and V_S). These velocities are required as input to a wide range of rock physics models (Mavko *et al.*, 2009). Aki and Chouet (1975) first describe coda waves as being predominately comprised of shear waves. Snieder (2002) later uses a simple analytical model for wave scattering and conversions between P and S waves in a

constant velocity medium with uniformly distributed point scatterers, and derives the relationship between V_P/V_S ratios and the proportion of changes in V_P and V_S that contribute to the change in velocity measured by CWI at equilibrium. In a Poisson medium where $V_P = \sqrt{3}V_S$ (Poisson's ratio $\nu = 0.25$), this relationship becomes: $\Delta V/V = 0.09[\Delta V_P/V_P]+0.91[\Delta V_S/V_S]$. The change in P and S wave velocity ($\Delta V_P/V_P$ and $\Delta V_S/V_S$), which are the desired measurements for rock physics modelling, still remain unknown.

In order to interpret a change in the measured seismic velocity, a suitable rock physics model is required. There is an abundance of methods used in rock physics for the modelling of elastic moduli-porosity or velocity-porosity data. There are many flavours of rock physics models including empirical models based on trends on observed data (Eberhart-Phillips *et al.*, 1989; Gardner *et al.*, 1974), bounding models which give a physics-based range of expected moduli (Voigt, 1928; Reuss, 1929), or inclusion-based models which assume an unrealistic, ellipsoidal inclusion shape embedded into a background material (Eshelby, 1957; Mori and Tanaka, 1973; Berryman, 1992). The assumptions of these models often over-simplify the physical interactions occurring within the rock geometry. This limitation is the motivation of using digital rock physics to effectively charecterise the micro-structure of a rock. A digital rock is a three-dimensional representation of a rock fabric, where individual phases within a rock (e.g., each mineral component and pore space/fluid) are known for each voxel in three dimensions (Andrä *et al.*, 2013a,b), from which the physical properties can then be estimated, such as permeability (Martys *et al.*, 1999; Keehm, 2003), seismic velocity (Saenger *et al.*, 2000; Arns *et al.*, 2002), thermal conductivity (Wiegmann and Zemitis, 2006) or electrical resistivity (Liu *et al.*, 2009; Zhan *et al.*, 2010). Digital rock physics allows for fast and flexible experimentation, and can be used to test hypotheses and establish trends of evolving geophysical properties responding to specific geological processes, as well as the ability to test the accuracy of methods such as CWI compared to conventional first-break methods.

1.2 The Claim

In this thesis, I test the hypothesis that coda wave interferometry can provide an improvement in accuracy and precision when inferring and quantifying the changes in bulk velocity and relative source locations in rock samples, in comparison with commonly used methods for numerical and laboratory experiments at the core-scale. I show how separate perturbations in both velocity and source location can be independently estimated when both perturbations occur simultaneously. This is a significant step forward in passive seismology, as a changes in bulk velocity in a medium can now be determined using passive sources at different locations, using a single receiver.

I make some fundamental improvements to the CWI method, by providing a new method for estimating the changes in P-wave and S-wave velocity independently. The method uses CWI measurements for velocity change at multiple times along the signal, and an extension to the model of Snieder (2002) to incorporate a fluid phase (where shear waves are not supported). I also describe a method to separate the change in fluid velocity from the change in the solid matrix of a medium, provided an estimate of the fluid fraction/saturated porosity. I use results from the triaxial deformation of two oriented finely laminated carbonates as a demonstration of this method, and use the resulting estimates for P and S wave velocity change to monitor the compressional-to-shear wave velocity ratio and invert for changes in crack density. I test the hypothesis that measurements made from the coda can be used in conjunction with axial first-break measurements to understand any anisotropy present in the samples, utilising the directional information for the first-break, and the isotropic average that is inherent to CWI.

Finally, I combine a process-based model for deposition and cementation of digital rocks with the finite-difference simulation of wave propagation to determine the relationship between elastic properties and cementation. I statistically test two competing inclusion-based rock physics models for their ability to capture the effects of varying cementation,

cement type, and initial rock fabric. I also investigate the effect of underlying structural anisotropy on the relationship between porosity and elastic properties.

1.3 Thesis Overview

- Chapter 2 is a literature review of the main research areas in this thesis, first looking at methods for monitoring seismic velocity and measuring inter-source earthquake distances. I then review monitoring methods that utilise the seismic coda. As there is a strong focus on the application to experimental rock physics in this thesis, I also review rock physics and digital rock physics methodologies and models. After identifying some of the gaps in the current literature, I form a series of research questions that provide the motivation for the work included in this thesis.

- In Chapter 3, I compare coda wave interferomety with the conventional first-break method for measuring changes in velocity and source locations. I perform a variety of numerical and laboratory experiments at the rock core scale. Experiments include the performance of the methods with increasing levels of background noise and investigating the performance of CWI when separate perturbations of velocity and source location occur simultaneously. I also present a new method for unravelling the CWI estimate for velocity change to separate estimates of changes in P and S wave velocity.

- Chapter 4 is an extension of the previous chapter, where I describe in full the method for estimating separate changes in P and S wave velocity. I test this method for a range of numerical models with varying size and complexity.

- Chapter 5 is an application of the CWI method for estimating changes in P and S wave velocity. I use laboratory data for the triaxial deformation of two oriented laminated carbonates, and use the CWI results as input to a rock physics model for crack density.

- Chapter 6 is a study of how seismic velocity varies with cementation in carbonate digital rocks. I use models generated from the process based simulation of

deposition and cementation for a grainstone (spherical grains) and coquina (shelly fragment grains). Using the estimated elastic properties, I statistically test two competing rock physics models.

- In Chapter 7, I discuss some of the remaining questions and limitations to coda wave interferometry and digital rock physics. I also present some areas of possible future research.

- Chapter 8 concludes this thesis, where I present my main findings and provide answers to the research questions posed at the end of Chapter 2.

Chapters 3, 4, 5 and 6, are written in the form of journal articles, which have either been accepted, submitted or are in preparation for submission at the time of writing. At the beginning of each of these chapters I write a short preface indicating the current status each manuscript, highlighting my contributions to each of the articles and linking the chapter to the broader context of the thesis as a whole.

Chapter 2

Literature Review

This chapter presents an overview of the current literature within each of the main research areas covered in this thesis. First I review some basic seismology and methods for measuring the seismic velocity. The work in this thesis has a strong link to the applications in rock physics, therefore I also review some rock physics and digital rock physics methods. After identifying some of the gaps in the current understanding in these fields, I outline the key research questions that form the motivation for this thesis.

2.1 Seismic Waves

The way in which a seismic wave travels through a medium is studied across many disciplines within geosciences: to examine the process of rock fracturing (Pyrak-Nolte *et al.*, 1990) and acoustic emissions (Lockner *et al.*, 1992; Lockner, 1993), to develop relationships between changes in external conditions and seismic properties such as seismic velocity (Wang, 2001), anisotropy (Christensen, 1966; Sayers and Kachanov, 1995) and attenuation (Toksöz *et al.*, 1979; Sams *et al.*, 1997). The recording of a seismic wave at a receiver, known as a seismogram, includes some main features (labelled in the example seismogram in Figure 2.1a). These are the first arrivals of the compressional wave (P wave) and shear waves (S wave), and the coda waves, which

are found in the tail of the seismogram. In a homogenous, isotropic and elastic case, the motion of a wave through a medium can be described mathematically for the displacement $\mathbf{u}$ at a given point in space $\mathbf{x}$:

$$\rho \frac{\partial^2 \mathbf{u}(\mathbf{x}, t)}{\partial t^2} = (\lambda + \mu)\nabla(\nabla \cdot \mathbf{u}(\mathbf{x}, t)) + \mu \nabla^2 \mathbf{u}(\mathbf{x}, t), \tag{2.1}$$

where ρ is the density, λ and μ are the Lamé parameters, and t is time (Stein and Wysession, 2009). The velocity at which compressional (P) waves and shear (S) waves travels (V_P and V_S) can be derived from applying the divergence and curl operators to Equation 2.1, respectively. The velocities are given by

$$V_P = \sqrt{\frac{\lambda + 2\mu}{\rho}} = \sqrt{\frac{K - \frac{4}{3}\mu}{\rho}}, \tag{2.2}$$

where K is the bulk modulus, and

$$V_S = \sqrt{\frac{\mu}{\rho}}. \tag{2.3}$$

The measurement and application of seismic velocity (or the associated elastic moduli) is broad, and is the main focus of this thesis. For example, velocities are used to build maps of the subsurface (or velocity models) which are used in seismic imaging (Robein, 2003), notably important for the migration of seismic data (Versteeg, 1993). Other applications include estimating fluid pressure change due to fluid extraction or deformation due to stress from time lapse 4D seismic data (Guilbot and Smith, 2002; Arts *et al.*, 2004; Stork *et al.*, 2018), deformation during laboratory rock physics experiments (Wang, 2001; King, 1966), using changes in velocity to quantify precursory damage accumulation before earthquakes (Volti and Crampin, 2003; Gao and Crampin, 2004), and using V_P and V_S as input to a wide range of rock physics models (see Section 2.3.2), for example allowing for the inversion of effective pore geometries or crack densities. The seismic velocity is a vital property in geoscience, therefore the accurate and precise measurement of velocity is of the utmost importance.

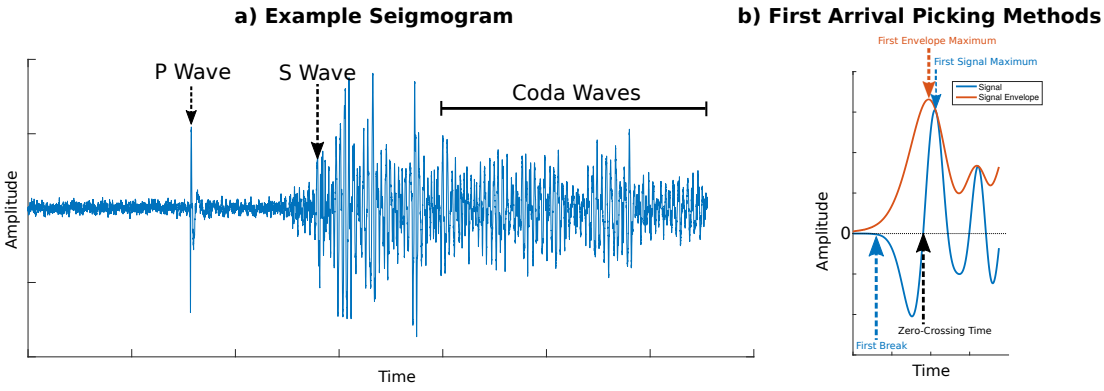

Figure 2.1: a) Example seismogram with the arrival times of the compressional (P), shear (S) and coda waves labelled. b) Illustration of the range of methods that can be used for picking the travel time of the first arriving wave.

2.1.1 Estimating Seismic Velocity

Standard methods for measuring the velocity - as well as *changes* in the velocity of a medium - involve picking of first-break arrival times of seismic waves traveling between a fixed source and receiver pair. The term 'first-break' can be quite ambiguous, and can be picked as the signal onset (Brillouin, 1960), the arrival time of the first peak or envelope peak (Nichols, 1996), or the time of first zero-crossing (Hornby, 1998). These different methods are illustrated in Figure 2.1b. If the propagating wavelet shape does not evolve with time, the determination of velocity (or changes in velocity) using any of these methods should yield identical results. However, in reality intrinsic absorption and scattering contribute to signal attenuation, and estimates with the different methods diverge in practice (Molyneux and Schmitt, 1999). The unaffected signal onset may then be the most appropriate, though is the lowest amplitude and therefore most difficult to identify, especially in the presence of background noise.

In laboratory experiments, where wavelengths are often on the same order of magnitude as the scale of the heterogeneities within the samples, there are various problems that occur in the determination of velocity: 1) the measured velocity is not sensitive to the bulk properties of a medium, but rather to properties along a very specific (fastest) ray path between the source and receiver, resulting in a bias towards higher velocities.

2) The path followed by the first-arriving energy is unlikely to be straight, so that velocity estimates made by assuming a straight-line path are biased towards lower values. 3) Biases in points 1 and 2 are generally unrelated so are not expected to cancel. 4) The effects of small perturbations in the medium that are not located along the specific source-receiver path cannot be detected. 5) Such systematic and random errors in velocity estimation are carried forward to any subsequent calculations, notably in locating acoustic source positions.

2.1.2 Estimating Relative Source Locations

Another topic of importance to this thesis is the estimation of the location of seismic source, and specifically the 3D relative locations of a cluster of sources, rather than their location in an absolute framework. Monitoring the relative locations of seismic sources is essential for a variety of applications in field and global scale seismology, such as the monitoring of induced seismicity (Ake *et al.*, 2005; Frohlich and Brunt, 2013; Ellsworth, 2013), studying earthquake triggering and interaction (Chen *et al.*, 2013), and imaging of fault planes (Got *et al.*, 1994; Dodge *et al.*, 1995; Waldhauser and Ellsworth, 2002). Absolute locations are commonly estimated using multilateration, which takes the arrival times measured at multiple receivers and an estimated velocity model of the medium, and solves for the source locations and origin time (Lee, 1975). Relative locations can be obtained from estimated absolute locations, but these estimates are strongly dependent on the quality of the velocity model, the station coverage, and source to receiver distance. Therefore, the uncertainty of earthquake locations can be on the order of kilometers (Shearer, 1999).

The accuracy of estimates for distances between source locations is greatly improved when directly calculating the relative locations. There are several suitable algorithms with differing degrees of accuracy. Douglas (1967) first developed the *Joint Epicenter Determination* method, which simultaneously estimates the relative location of a cluster of events by accounting for azimuth dependent travel-time variations. Dodge *et al.* (1995) later built on this method and proposes the *Joint Hypocenter Determination* method, which uses cross-correlation to measure travel-time variations. These methods

are somewhat limited, requiring inter-event separations to be small compared to the dominant wavelength. Waldhauser and Ellsworth (2000) partly overcome this limitation with the *Double-Difference* method, which constructs links between multiple event clusters, thus the method is able to relocate earthquakes distributed over larger distances. However, the Double-Difference method fails in areas with poor seismic station coverage, such as intra-plate regions (Robinson *et al.*, 2013). All these methods estimate locations solely from the P and/or S wave arrivals.

2.2 Coda Waves

The coda, or *tail*, of a seismogram is comprised of the late arriving, multiply scattered waves. Aki and Chouet (1975) first described the characteristics of the seismic coda for local earthquakes. Their observations are summarized in Sato *et al.* (2012) as:

1. the spectral contents of the later portions of coda waves are the same at different stations,
2. the duration of a seismogram can be reliably calculated as the length of time between the P wave onset time and the time where the coda amplitudes decrease to that of the background microseisms,
3. the temporal decay of coda amplitude are independent of earthquake magnitude,
4. the coda amplitude depends on the local geology of the recording site,
5. coda waves are not regular plane waves travelling directly from the source location.

It is therefore clear that recordings of coda waves are more that mere 'noise' but rather carry some useful and extractable information regarding the properties of the medium.

2.2.1 Monitoring with Coda Waves

Coda waves sample a large volume and with long transit times, often sampling the same volumes multiple times. Therefore, measurements of characteristics or properties

of the coda can be much more sensitive to temporal changes in the medium when compared against conventional measurements of velocity or attenuation using direct waves (Sato *et al.*, 2012). There is therefore strong potential for the use of coda waves for monitoring purposes. There are early reports of temporal changes in the coda attenuation Q_c^{-1} associated with the occurrence of earthquakes (Gusev and Lemzikov, 1985; Jin and Aki, 1986) and volcanic eruptions (Fehler *et al.*, 1988). Jin and Aki (1991) cite 12 cases where precursor-like changes in Q_c^{-1} have been reported associated with earthquakes, however there have been several studies criticising the use of a change in Q_c^{-1} as an earthquake pre-cursor as there are other possible influences such as different earthquake focal regions and mechanisms (Frankel, 1991; Sato, 1988). Poupinet *et al.* (1984) first noted the phase difference between coda waves of earthquake doublets where the average bulk velocity of the medium is different between the occurrence of the two earthquakes. They find a decrease in velocity of 0.2% associated with the occurrence of the Coyote Lake earthquake in California. Following this, Ratdomopurbo and Poupinet (1995) apply the same method to coda recorded at Merapi volcano, Indonesia, and find a 1% increase in seismic velocity at shallow depths several months before an eruption in 1992. Snieder *et al.* (2002) later formalises the mathematical background for using coda waves to measure changes in a medium, naming the method *Coda Wave Interferometry*, which forms the basis for much of the work carried out as part of this thesis.

2.2.2 Coda Wave Interferometry (CWI)

Interferometry is a broad family of methods in which waves, e.g., electromagnetic, seismic or acoustic waves are superimposed, causing interference, in order to extract some information. There are now also established methods called coda wave interferometry (CWI) that estimate changes in the velocity of the medium, changes in the locations of sources or receivers, or changes in the scatterer locations (Snieder *et al.*, 2002; Snieder, 2006). These three perturbation types, and their effect on the seismic coda are shown in Figure 2.2.

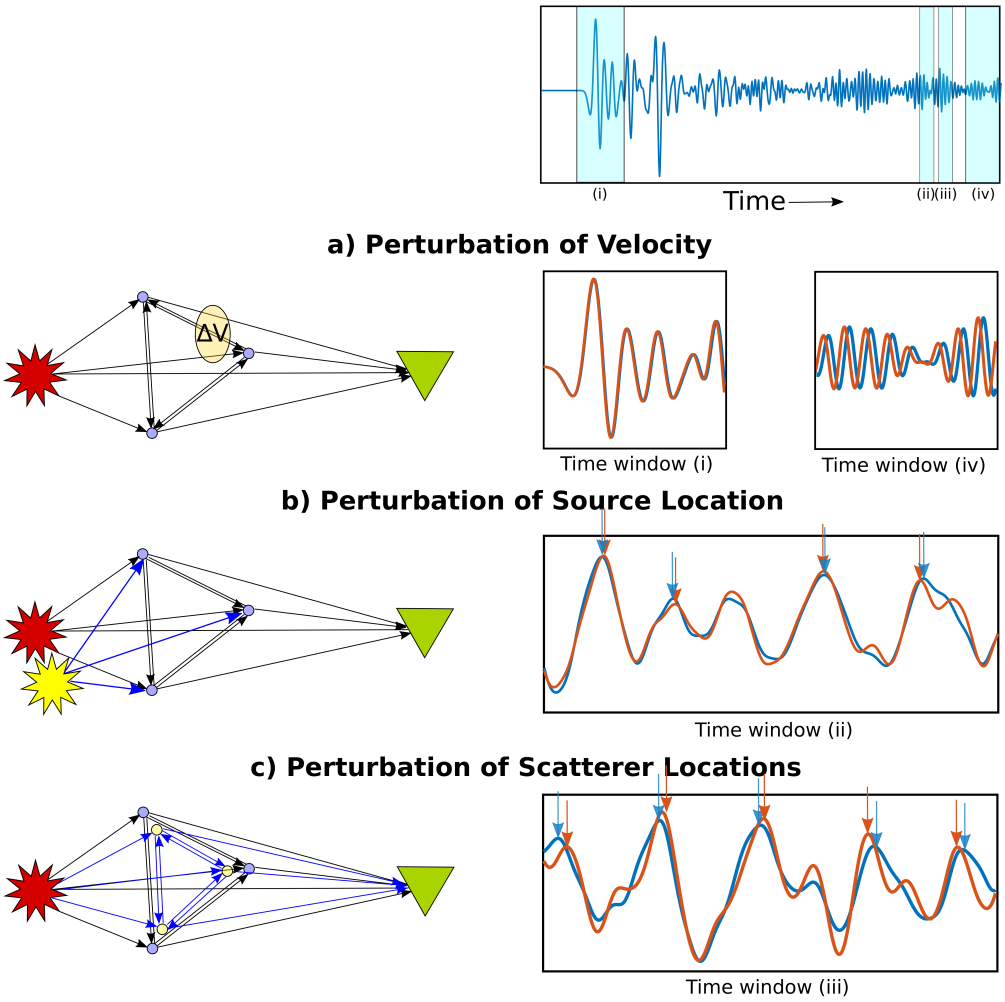

Figure 2.2: Illustrations of different perturbation types and their effects on coda waves. The cartoons (left) represent a scattering medium, with a source (star), receiver (triangle), and point scatterers (circles). Ray paths between the source and receiver, including multiple reverberations, are represented as black arrows. A velocity perturbation (a) is represented as a yellow ellipse, which has a velocity different to the background medium. New ray paths that are introduced due to changes in source location (b) and scatterer locations (c) are represented as blue arrows. Example recorded signals (right) at a range of time windows (i-iv) are shown before and after each perturbation takes place (blue and red, respectively). Differences in travel times of arriving energy for b) and c) are highlighted by vertical arrows.

Velocity Change

First, consider the effect of a velocity perturbation (ΔV in Figure 2.2a). The direct arriving wave between a source and receiver would only sample the perturbed area once (or not at all), whereas multiply scattered waves are free to pass through the perturbed region many times. Therefore the effect of the velocity perturbation on the arrival times for multiply scattered waves are amplified. Thus the change in arrival times for later arriving waves (time window *iv* in Fig. 2.2a) is larger than for the first arrival (time window *i*). There are several methods to estimate a change in velocity using interferomtery: the double wavelet (Snieder *et al.*, 2002), trace stretching (Lobkis and Weaver, 2003; Sens-Schönfelder and Wegler, 2006) and dynamic time warping methods Mikesell *et al.* (2015), each with their own advantages (see Hadziioannou *et al.* (2009) and Mikesell *et al.* (2015) for comparisons). All these methods provide an estimate of $\Delta V/V$, which is the ratio of the change in velocity ΔV to the original velocity V. A major difference between the estimate of velocity change given by CWI and by the conventional first break method is the directionality implicit to the measurements. Coda waves eventually travel in all directions and throughout the entire medium, so that $\Delta V/V$ is an isotropic average of the medium, whereas the conventional measurements of V_P or V_S are only sensitive to the direction along the fastest wave path, assumed straight. Comparing these two methods may therefore give insight to any structural anisotropy present in a medium.

There have been several field and laboratory applications of CWI for estimating changes in velocity to date, including the monitoring of velocity changes in ice sheets (Mordret *et al.*, 2016; James *et al.*, 2017), concrete (Larose and Hall, 2009; Planès and Larose, 2013), large scale structures such as bridges (Salvermoser *et al.*, 2015), mining environments (Grêt *et al.*, 2006), volcanic regions (Sens-Schönfelder and Wegler, 2006), as well as changes associated with earthquakes (Hadziioannou *et al.*, 2011). The application of CWI for laboratory rock physics experiments has been comparatively limited to date.

One major limitation to the application of CWI, especially for rock physics experiments, is the complicated nature of the resulting estimate of velocity change $\Delta V/V$, which reflects a unknown combination of both changes in P and S wave velocities. This severely limits the applicability and interpretation of velocity changes as estimates of V_P and V_S are required for bulk and shear moduli to be estimated (given an estimate of density), which are parameters that appear in the majority of rock physics models. Aki and Chouet (1975) first note that coda waves are comprised mainly of shear waves, later Snieder (2002) derives a relationship between the proportions of P and S waves in the coda, to the P and S wave velocities:

$$\frac{\Delta V}{V} = \frac{V_S^3}{2V_P^3 + V_S^3}\frac{\Delta V_P}{V_P} + \frac{2V_P^3}{2V_P^3 + V_S^3}\frac{\Delta V_S}{V_S}. \tag{2.4}$$

In a Poisson medium, where $V_P = \sqrt{3}V_S$ (Poisson ratio $\nu = 0.25$), this relationship becomes:

$$\frac{\Delta V}{V} = 0.09\frac{\Delta V_P}{V_P} + 0.91\frac{\Delta V_S}{V_S}. \tag{2.5}$$

Knowing the relative contributions of $\Delta V_P/V_P$ and $\Delta V_S/V_S$ to the CWI estimate of $\Delta V/V$, while somewhat useful, does not give the actual velocity changes $\Delta V_P/V_P$ and $\Delta V_S/V_S$. It is therefore desirable find a suitable method for unravelling the CWI estimate of $\Delta V/V$ into independent changes in V_P and V_S.

Source Location Change

A second perturbation type that CWI is able to monitor is the displacement of the source or receiver location (Figure 2.2b shows an example source displacement). In this case, the difference in the ray paths before and after the perturbation is only the difference between the source and the first scattering point (blue arrows in Figure 2.2b), following the first scattering point, the waves follow the exact same paths. The different paths are shortened or lengthened depending on the location of the first scatterer, which manifests as the advancement and retardation of signal peaks highlighted by red and blue arrows in Figure 2.2b. Providing the source displacement is small compared to the seismic wavelength, the extent to which these travel times

are perturbed (specifically, the variance of the travel time perturbations) is directly proportional to the displacement.

There are various applications of CWI for estimating inter-source separation for earthquakes (Snieder and Vrijlandt, 2005; Robinson *et al.*, 2011; Hayward and Bostock, 2017) and in ice (Allstadt and Malone, 2014). CWI has also been used to study changes in earthquake focal mechanisms (Robinson *et al.*, 2007). If the separation between a pair of sources can be estimated, the 3D relative locations for a network of sources can also be estimated (Robinson *et al.*, 2013). This method has been applied for mining induced micro-seismic events (Zhao *et al.*, 2017) using the now publicly available source package of Zhao and Curtis (2019).

Change in Scattering

A third perturbation type that CWI can monitor is the average displacement of all scattering points (yellow circles in Figure 2.2c): in this case, all paths between scattering points are perturbed (both shortened and lengthened), and similarly to the previous case the variance of travel time perturbations is proportional to the displacement of scattering points. This method has relevance for studying the motion of particles in suspensions (Heckmeier and Maret, 1997; Cowan *et al.*, 2000), though application of this method is comparatively limited (Snieder and Page, 2007).

2.2.3 Locating a perturbation

The late arriving, multiply scattered coda waves sample the entire medium, therefore CWI monitors the *bulk* properties of a medium. Many real-world situations involve a localized perturbation, and not simply an average perturbation occurring throughout the entire medium. Rossetto *et al.* (2011) describe a method for locating changes in the diffuse waves known as LOCADIFF, which uses a maximum likelihood approach combined with a diffusive propagation model. These methods assume statistical homogeneity of the scattering properties therefore may not be appropriate for realistic media with correlated structures. Obermann *et al.* (2016) use the time-dependent

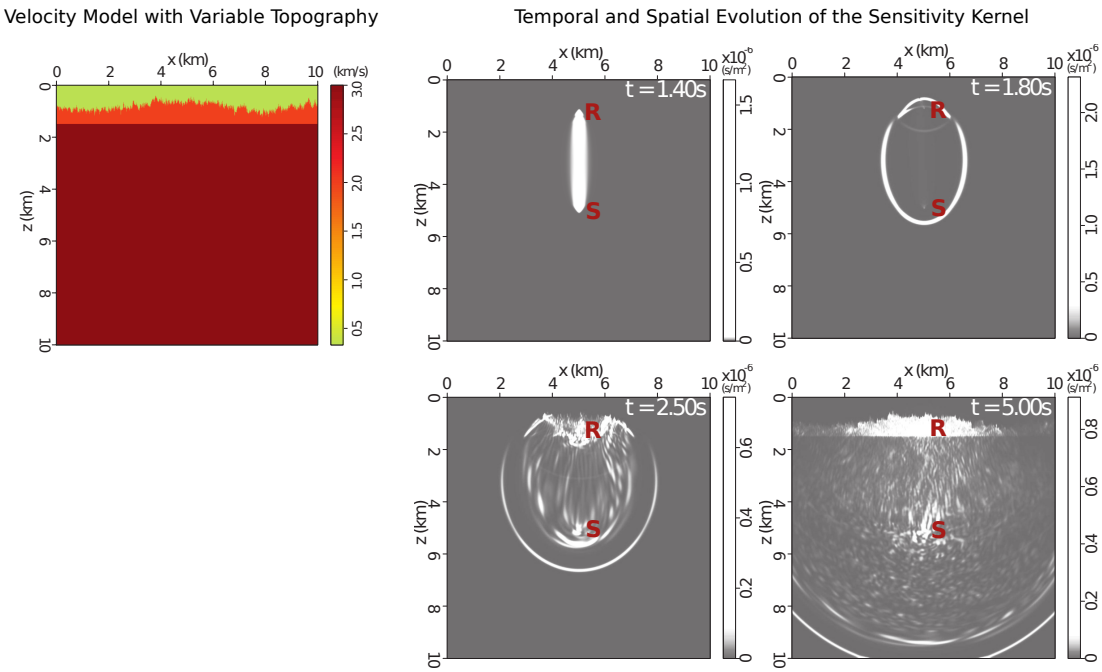

Figure 2.3: Figure adapted from Kanu and Snieder (2015) illustrating the localisation of wave energy as a function of time. The far left panel is a velocity model containing a low-velocity near surface. The four grey panels are the numerically computed sensitivity kernels at different times corresponding to different wave scattering regimes: ballistic wave propagating (top left), single scattering (top right), multiple scattering (bottom left), and a surface saturated regime (bottom right).

sensitivity of the coda to different depths allowing the localisation of perturbations. Kanu and Snieder (2015) propose the use of numerical-based sensitivity kernels for locating perturbations in structurally correlated media (see also Margerin *et al.* (2015)). This method uses simulated wavefields to compute the sensitivity kernels as a function of time along a recorded signal, showing where the wave energy is distributed thus showing the locations contributing to the travel time perturbations measured at a given time. An example of this method from Kanu and Snieder (2015) is shown in Figure 2.3, showing the dominance of the low velocity near surface contributing to the recorded signal at late times. This method requires detailed knowledge of the medium and the accurate locations of any reflectors, which in practice are rarely known.

2.3 Rock Physics

One major objective of this thesis is to determine how coda wave interferometry can be applied in experimental rock physics. It is therefore appropriate to review the methods and models involved for both experimental and digital rock physics, the latter is reviewed in Section 2.4.

2.3.1 Principles of Experimental Rock Physics

Variations in the stress field of the Earth's crust control a range of geological processes such as plate tectonics, regional deformation and earthquakes. These variations in stress control the extent and type of deformation that occur in the Earth (Ruff, 2002). *In-situ* stresses can be measured directly but this process often involves the expensive processes of drilling and pumping fluid into the subsurface (Zoback and Zoback, 1980). Alternatively, the stress field can be simulated in experimental rock physics. These experiments allow for the monitoring of stress, strain and physical properties such as elastic wave velocity (Wang, 2001), electrical properties (Olhoeft, 1981), permeability (Sahimi, 2011), acoustic emissions (Lockner *et al.*, 1992; Lockner, 1993), and pore fluid volume (Sammonds *et al.*, 1992). These experiments also allow the understanding of deformation mechanisms and the ability to isolate processes that occur simultaneously in the field.

Stress and Strain

Nye *et al.* (1985) states that a body being acted upon by an external force is in a state of stress. The orientation and strength of these stresses can be described by the stress tensor $\sigma_{ij}(i, j = 1, 2, 3)$, where nine stress components in the three principal directions, x_1, x_2 and x_3, fully describe the stress at any point in the body (Fung, 1965):

$$\sigma_{ij} = \begin{pmatrix} \sigma_{11} & \sigma_{12} & \sigma_{13} \\ \sigma_{21} & \sigma_{22} & \sigma_{23} \\ \sigma_{31} & \sigma_{32} & \sigma_{33} \end{pmatrix} \tag{2.6}$$

Within the tensor, normal stresses are the diagonal σ_{ii} components and shear stresses are the off-diagonal $\sigma_{ij}(i \neq j)$ components. The hydrostatic (or isotropic) pressure P is defined as the mean value of the normal stresses (Poirier, 1985):

$$P = \frac{1}{3}\sum_{i-1}^{3}\sigma_{ii} = \frac{1}{3}(\sigma_{11} + \sigma_{22} + \sigma_{33}) \tag{2.7}$$

and when shear stresses are not present, the differential stress (or non-isotropic stress) σ is defined as:

$$\sigma = \sigma_{max} - \sigma_{min} \tag{2.8}$$

where σ_{max} and σ_{min} are the maximum and minimum normal stresses, respectively.

The strain of the body describes the change in size or shape when an external stress is applied (Twiss and Moores, 1992). The displacement tensor D_{ij} describes a body's deformation for the position x_j with it's displaced location (u_i):

$$D_{ij} = \frac{\partial u_i}{\partial x_j}, \tag{2.9}$$

which can be split into two components: the rotation tensor ω_{ij}, which is the asymmetric part of D_{ij}, and the strain tensor ϵ_{ij} which is the symmetric part. The strain tensor is formulated in the same way as the stress tensor (Equation 2.6), where there is normal strain (diagonal components, ϵ_{ii}) and shear strain (off diagonal components, $\epsilon_{ij}(i \neq j)$). Normal strain describes the linear or volumetric stretching or compression whereas shear strain describes the angular distortion of a material. A common measurement in experimental rock physics is linear strain ϵ_l and the volumetric strain ϵ_v, which are the relative change in length measured along it's respective dimension:

$$\epsilon_l = \frac{l_0 - l}{l} = \frac{\partial u_1}{\partial x_1} \tag{2.10}$$

and the ratio of the change in volume Δv of a body to it's original volume v:

$$\epsilon_v = \frac{\Delta v}{v} \approx \frac{\partial u_1}{\partial x_1} + \frac{\partial u_2}{\partial x_2} + \frac{\partial u_3}{\partial x_3}. \tag{2.11}$$

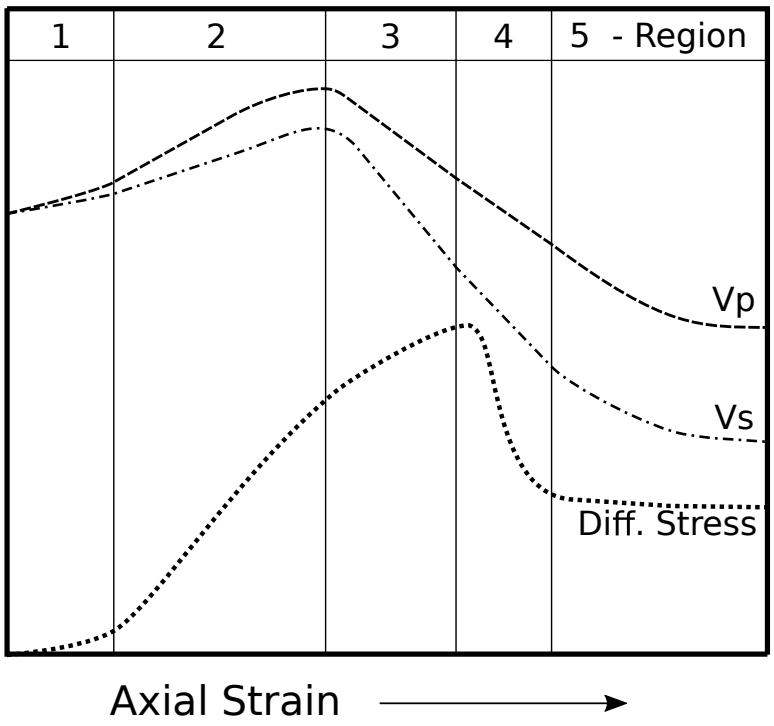

Figure 2.4: The stages of deformation typical of a triaxial compression experiment outlined in section 2.3.1, showing differential stress, P wave velocity (V_P) and S wave velocity (V_S) as a function of axial strain. Figure adapted after Sammonds *et al.* (1989).

Properties such as linear strain and seismic velocities are often evaluated with varying differential stress in rock physics experiments.

Evolution of Physical Properties during Deformation

Typically deformation during 'triaxial' compression occurs in a load cell where the axial stress is the maximum and the two radial stresses are equal ($\sigma_1 > \sigma_2 = \sigma_3$). The stress-strain curve typically plots axial stress, which is gradually increased at a constant strain rate. The stress-strain curve can be divided into five regions based on the mechanical processes that occur (Brace *et al.*, 1966; Scholz *et al.*, 1973; Sammonds *et al.*, 1989). These regions are shown on Figure 2.4 for stress, V_P and V_S as a function of axial strain. These stages are described below:

1. The first stage represents crack and pore closure. Initially, strain requires

increasing stress resulting in a concave upward trend in the stress-strain curve. Closure of cracks and pores, particularly those at high angles to the loading axis, reduces void space and causes an increase in both V_P and V_S.

2. The second stage is where the sample exhibits linear elasticity, where stress and strain are almost directly proportional and deformation is elastic. Velocities continue to increase indicative of crack and pore closure. Loading and unloading in this region will not produce irreversible changes in the properties or structure of the rock (Jaeger *et al.*, 2009).

3. The next stage, which occurs at approximately two thirds of the peak stress (Hallbauer *et al.*, 1973), represents the onset of irreversible change occurring in the rock. The stress-strain curve begins to curve downwards, marking the onset of microcrack formation. Velocities begin to decrease, where V_S commonly decreases at a faster rate than V_P, especially when measured parallel to the loading axis, sensitive to cracks forming parallel or oblique to loading. At this stage irreversible changes occur in the rock that lead to unrecoverable strain once the load is removed (Jaeger *et al.*, 2009).

4. The fourth regions represents the coalesence of microcracks and the formation of the main macroscopic fractures. At peak stress, the rocks ability to support load rapidly decreases, thus the gradient of the stress-strain curve becomes negative. Velocities in all directions continue to decrease.

5. Finally is the occurrence of frictional sliding alone the failure planes. The stress-strain curve as well as the measured velocities become constant as stress becomes independent of strain, and stable sliding occurs along the fracture plane(s).

2.3.2 Rock Physics Models

There is a vast abundance of tools and models used in rock physics, far too many to be fully described here. Therefore I review a non-exhaustive list comprised of models pertinent to the contents of this thesis. There are many comprehensive reviews on rock physics models that provide full details on the derivations, applications and limitations

of such models (Cleary *et al.*, 1980; Wang, 2001; Jaeger *et al.*, 2009; Mavko *et al.*, 2009; Christensen, 2012; Price *et al.*, 2017).

Statistical models

Statistical methods are entirely based on empirical matches to trends in observed data. Such models determine the relationships between a wide range of physical properties. For example, velocity-porosity models (Raymer *et al.*, 1980), velocity-density models (Gardner *et al.*, 1974; Christensen and Mooney, 1995), velocity-porosity-clay models (Tosaya and Nur, 1982; Han *et al.*, 1986), velocity-pressure-porosity-clay models (Eberhart-Phillips *et al.*, 1989), and V_P-V_S models (Pickett, 1963; Castagna *et al.*, 1985). The assumptions and limitations for these methods are generally consistent; strictly speaking, empirical relations only apply to the set of rocks studied (Mavko *et al.*, 2009), thus the extrapolation of empirically determined models can be unreliable. Another limitation to these methods are that the statistical fitting of trends do not provide any physical meaning, therefore no unique interpretation of the underlying processes can be achieved, though the trends can provide significant constraints.

Bounding models

Bounding models recognize the uncertainty of elastic moduli for a given porosity and therefore give a range of moduli, where the exact value depends on geometric factors of the medium. The geometric interpretation of these models are shown in Figure 2.5. An example would be the Voigt upper bound M_V (Voigt, 1928) and the Reuss lower bound M_R (Reuss, 1929):

$$M_V = \sum_{i=1}^{N} f_i M_i, \tag{2.12}$$

$$\frac{1}{M_R} = \sum_{i=1}^{N} \frac{f_i}{M_i}, \tag{2.13}$$

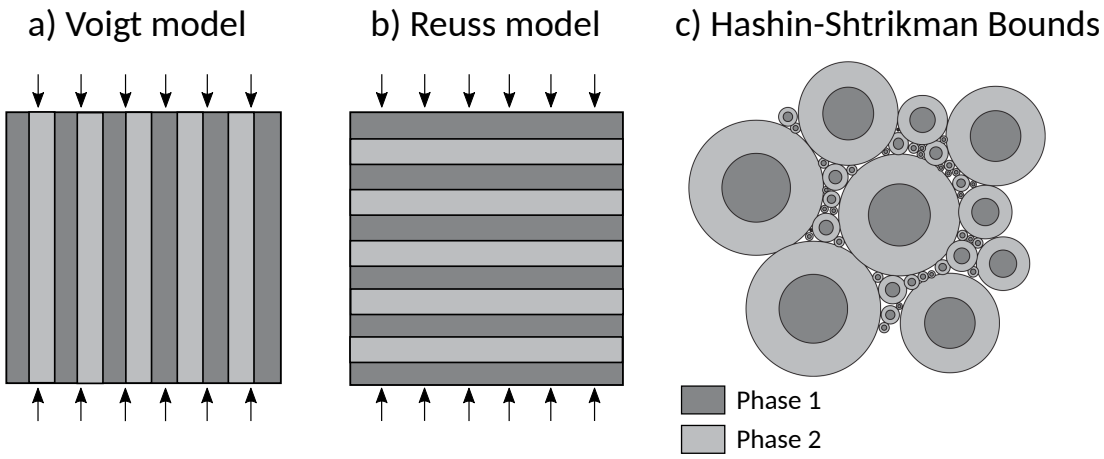

Figure 2.5: Geometric interpretations of the Voigt upper bound model (a), the Reuss lower bound model (b), and the Hashin-Shtrikman bound (c). The upper and lower Hashin-Shtrikman bounds are calculated by interchanging phase 1 and phase 2. Figure adapted from Mavko *et al.* (2009).

where f_i is the volume fraction of the ith phase and M_i is the elastic modulus of the ith phase, M can represent the bulk modulus K or the shear modulus μ. Another example are the Hashin-Shtrikman bounds (Hashin and Shtrikman, 1963):

$$K^{HS\pm} = K_1 + \frac{f_2}{(K_2 - K_1)^{-1} + f_1(K_1 + \frac{4}{3}\mu_1)^{-1}} \tag{2.14}$$

$$\mu^{HS\pm} = \mu_1 + \frac{f_2}{(\mu_2 - \mu_1)^{-1} + 2f_1(K_1 + 2\mu_1)/[5\mu_1(K_1 + \frac{4}{3}\mu_1)]} \tag{2.15}$$

where the subscripts 1 and 2 refer to the two phases in the medium and the upper and lower bounds are computed by interchanging which phase is termed 1 and 2 (Mavko *et al.*, 2009). The limitations of these methods are that the bounds are often far too broad for many practical applications, and that the models assume each constituent phase is isotropic, linear, and elastic.

Contact models

These models use spheres as idealized representations of grains in unconsolidated or poorly consolidated granular media. This allows for the analytic treatment of mechanical grain interactions under varying stress (Mavko *et al.*, 2009). Effective elastic properties depend on the normal and tangential contact stiffness, which are a

function of the grain elastic properties and coordination number (e.g., Mindlin (1949) and Walton (1987)). These models assume that strains are small, grains are identical, homogeneous, isotropic and elastic spheres, and wavelengths are much larger than the size of the grains.

Inclusion models

Inclusion-based models such as Eshelby (1957); Mori and Tanaka (1973); Berryman (1992) assume a specific inclusion shape embedded into a background material. This physics-based approach generally leads to more intuitive interpretation and closer resemble real-rock scenarios. Further information such as crack density and mean crack aspect ratio can be inferred from changes in velocity due to a change in stress distribution modified by the presence of damage (Walsh, 1965; Ayling *et al.*, 1995; Stanchits *et al.*, 2006). A common approach is the self-consistent effective medium model of O'Connell and Budiansky (1974).

However, the assumption of idealized ellipsoidal (or spheroidal) inclusion may be unrealistic, particularly in granular media (Makse *et al.*, 1999).

2.4 Digital Rock Physics

The rock physics models described above are either based on empirical relationships from laboratory data or theoretical models based on idealized rock micro-structures. These models are undoubtedly important for many aspects of geoscience, but their assumptions often over-simplify the physical interactions occurring within the rock geometry. This limitation is the motivation for using digital rock physics. A digital rock is a three-dimensional representation of a rock fabric, where individual phases within a rock (e.g., each mineral component and pore space/fluid) is known for each voxel in three dimensions. Digital rock physics uses these models to compute effective properties such as elastic moduli, electrical resistivity, and permeability (Andrä *et al.*, 2013a,b). Digital rock models are far more flexible and far less expensive to run compared to laboratory experiments, and can be used to test hypotheses and establish trends of

evolving geophysical properties responding to different processes, including the response to stress or to specific diagentic events. Digital rocks also allow rapid sensitivity analyses to the variability of bulk properties due to changes in model parameters. The applications for digital rock physics are broad, including the estimation of permeability (Martys *et al.*, 1999; Keehm, 2003), seismic velocity (Saenger *et al.*, 2000; Saenger, 2008; Arns *et al.*, 2002), thermal conductivity (Wiegmann and Zemitis, 2006) and electrical resistivity (Liu *et al.*, 2009; Zhan *et al.*, 2010).

2.4.1 Generating Digital Rocks

There are two approaches to the generation of digital rocks: either by taking a 'real rock' (via x-ray imaging) and segmenting intensity values into individual material phases, or by constructing a rock entirely computationally (e.g., simulating mineral deposition).

X-ray Microtomography (μCT)

In the majority of cases in digital rock physics, images are acquired using high resolution x-ray micro-tomography to capture complex grain, crystal, and pore size and shape distributions. There are several reviews summarising the underlying methodology, the applications, and issues with the method (Betz *et al.*, 2007; Stock, 2008; Baker *et al.*, 2012; Cnudde and Boone, 2013; Wildenschild and Sheppard, 2013; Fusseis *et al.*, 2014), all of which inform the review presented here.

μCT utilizes material-specific absorption of x-rays (absorption contrast tomography) or variations in refractive index (phase contrast tomography). Absorption tomography is based on the Beer-Lambert law, describing the exponential decrease of X-ray intensity as a function of the line integral of the linear attenuation coefficients along the path:

$$I = I_0 \cdot exp\Big[- \int_{-\infty}^{\infty} \mu(x) dx \Big] \tag{2.16}$$

where $\mu(x)$ is the linear absorption coefficient at position x along a particular ray (Fusseis *et al.*, 2014). Figure 2.6 demonstrates how with a large number of ray

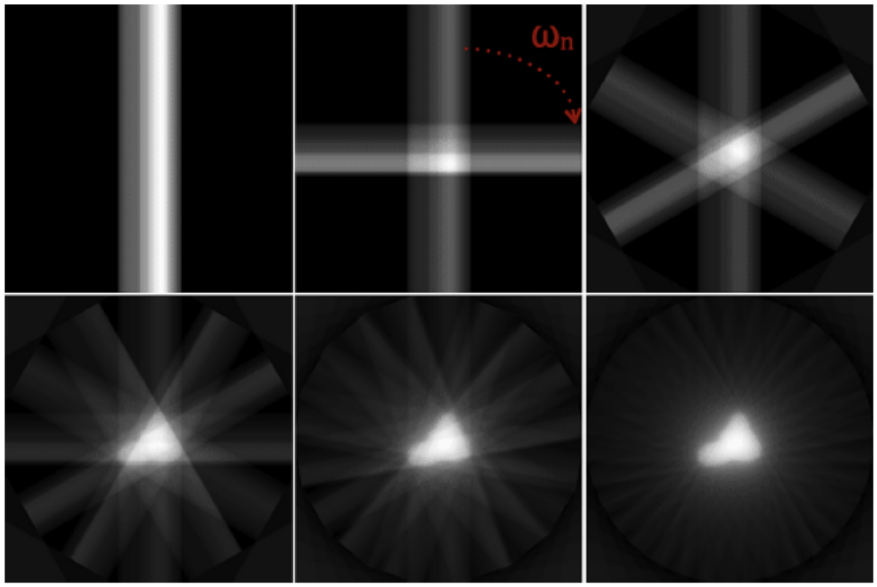

Figure 2.6: Reconstruction of the physical horizontal image slice from back-projection of absorption intensity signals at different rotation angles around the sample. Image from taken Fusseis *et al.* (2014).

paths passing through a sample at different angles, a 2D image representing spatial variation in absorption coefficients can be reconstructed. This process is completed over a large number of slices to build up a high resolution three dimensional image of a sample. Other methods such as phase contrast tomography, which uses material-specific temporal phase shifts as an X-ray passes through a sample (Cloetens *et al.*, 2002), or Neutron tomography, which uses a neutron source, are also popular methods in microtomography imaging. Tomographic output data is comprised of voxels, each with a unique spatial coordinate and an intensity or temporal phase shift value ascribed to it. Isolating intensity values from voxels and assigning a particular target material phase, such as pore space, or a particular mineral phase, is called image segmentation. There are several reviews on image segmentation methods (Kaestner *et al.*, 2008; Iassonov *et al.*, 2009; Wang *et al.*, 2011) covering a vast range of segmentation algorithms, each with specialized applications. Fusseis *et al.* (2014) states that the choice of the most suitable segmentation algorithm depends on the number of phases, their separability, the size of individual object, their spatial arrangements and shapes. Segmentation is a key step towards any following data analysis, where size, shapes and orientations of can be quantified, and effective physical properties can be estimated.

Process Based Simulation of Digital Rocks

There are several examples of the process-based simulation of digital rocks, where geological processes, such as deposition, cementation or dissolution, are simulated to generate digital rocks. These simulations allow the investigation of the influence of such geological processes on petrophysical and hydraulic properties. These digital rocks are generated entirely computationally, thus do not require the additional step of segmentation. Examples include cementation in both sandstones (Mousavi and Bryant, 2012; Latief *et al.*, 2010) and carbonates (Biswal *et al.*, 2007; Mousavi *et al.*, 2012) as well as dissolution in simple porous media (Kang *et al.*, 2003) and carbonates (Hosa and Wood, 2017). However, the physical properties investigated during cementation are most commonly transport properties such as permeability and electrical conductivity, e.g., Keehm *et al.* (2001). To date there have been no applications of process-based cementation modelling for the estimation of elastic properties using digital rocks.

2.4.2 Computing Effective Properties

Following the imaging of a rock sample and the digital processing and segmentation of material phases, or the process-based simulation of a digital rock, one can simulate physical processes within the microstructural image to determine effective properties (provided knowledge of the physical properties of the material phases). Two common methods for computing effective properties are the finite-difference (FDM) and finite-element methods (FEM), both involve the discretization of the underlying partial differential equations (e.g., Equation 2.1 for elastic property estimators) on a regular Cartesean grid (Andrä *et al.*, 2013b). The FDM is comparatively more straightforward than the FEM as coordinates of image voxels directly transfer to the grid required for the FDM, whereas the FEM requires an additional step of meshing, where the medium is subdivided into smaller and simpler shapes, most commonly using triangles. The majority of digital rock physics applications take high-resolution three-dimensional images, which are not always widely available. Therefore, several authors

use reconstruction of two-dimensional images and empirical two-dimensional to three-dimensional relations (Karimpouli and Tahmasebi, 2016; Karimpouli *et al.*, 2018; Saxena and Mavko, 2016), which allows the use of more readily available thin-sections as the input images.

Elastic property estimators

There have been many applications of digital rock physics for the estimation of elastic properties in a range of media, including siliciclastics (Saenger *et al.*, 2011; Saxena and Mavko, 2016), carbonates (Kalam, 2012; Saenger *et al.*, 2014; Jouini *et al.*, 2015), gas hydrate-bearing sediments (Sell *et al.*, 2016), and also the estimation of changing elastic properties as a function of effective stress (Madonna *et al.*, 2012). Dvorkin *et al.* (2011) compares estimated seismic velocity from digital rocks with the experimental estimation of the equivalent 'real rocks', finding that generally the estimated velocities from digital rocks are higher than for those estimated for real rocks. This highlights the limitation of image resolution on digital rock physics estimates. Compliant cracks and grain contacts are often too small to be imaged with conventional imaging techniques, but have a significant contribution to the elastic properties of a rock. If these softer elements are missing in the digital rock, the computed elastic moduli are unrealistically high. There are various approached to mitigate the overestimation of elastic moduli: Knackstedt *et al.* (2009) replace the mineral material at grain contacts with a hypothetical softer material and other authors combine images taken at a range of resolutions to more accurately charecterise the porosity (Saenger *et al.*, 2014; Jouini *et al.*, 2015).

Transport property estimators

Properties such as permeability can be estimated by attempting to numerically solve the Navier-Stokes equation for low-Reynolds-number fluid flow in porous media (Martys *et al.*, 1999; Keehm *et al.*, 2001). Keehm (2003) provides a comprehensive review of finite-difference, finite-element, lattice-gas automata and Lattice-Boltzmann methods for fluid flow in porous media. Similarly, the electrical resistivity (and conductivity) can be numerically estimated (Liu *et al.*, 2009; Zhan *et al.*, 2010). In the majority

of rocks, the resitivity of solid grain materials are orders of magnitude higher than the the pore fluids, therefore the estimated electrical properties depend mostly on the fluid properties, the porosity and the connectivity of pore space. Andrä *et al.* (2013b) compares a range of algorithms for estimating permeability and and electrical resistivity and find that there is generally good agreement with digital rock estimates and laboratory 'real rock' estimate, with a much greater accuracy compared to estimates for elastic moduli. The difference in accuracy highlights the dependence on larger scale macro-porosity for transport properties, whereas elastic properties are strongly controlled by sub-resolution features such as grain contacts and microcracks (Jouini *et al.*, 2015).

2.5 Research Questions

From the literature summarised above, I have identified current gaps and areas for research that set the foundation for what follows in this thesis. These are formulated as a series of research questions below:

1. For experimental rock physics, how do estimates for velocity change and source separation vary between coda wave interferometry (CWI) and conventional first arrival methods?

2. Can CWI estimates of velocity change and source separation be jointly estimated when both perturbations occur simultaneously?

3. Can the estimate of velocity change provided by CWI be unravelled further into estimates of changes in V_P and V_S or changes in fluid velocity and solid matrix velocity?

4. Can CWI be used in conventional rock physics models, e.g., for the inversion of crack density?

5. What are the implications of the implicit isotropic averaging of CWI compared to the directionality of the first-break method?

6. Using process-based simulation of digital rocks, what is the effect of cementation on seismic velocity?

7. What is the most appropriate rock physics model for digital carbonate rocks?

This thesis contains chapters which include submitted or draft research papers which address these questions. For these chapters I include a short preface where I identify which of these key research questions the chapter seeks to answer.

Chapter 3

Coda Wave Interferometry for Accurate Simultaneous Monitoring of Velocity and Acoustic Source Locations in Experimental Rock Physics

This chapter describes some of the most important components of my thesis, seeking to improve the way in which a change in the velocity of a medium is measured. In the paper that follows, I introduce coda wave interferometry as a method for estimating a changes in the bulk velocity of a medium and acoustic source locations. I compare the method with conventional first-break methods in an experimental rock physics environment. I also show that CWI can jointly estimate separate bulk velocity and source location perturbations when both perturbations occur simultaneously. Finally I present a method for the estimation of changes in P and S wave velocity using CWI. From the series of research question that I identified in Section 2.5, the themes of this chapter cover questions 1, 2 and 3.

This manuscript has been published in the Journal of Geophysical Research: Solid Earth. The co-authors of the paper include Andrew Curtis, Youqian Zhao, Alexis Cartwright-Taylor and Ian Main. I acted as the lead author for this paper. I performed

all the experiments and analysis described herein with the exception of the inversion of relative source locations described in Section 3.4.5, which was performed by Youqian Zhao. Accompanying the paper is a MATLAB code package for the estimation of changes in velocity and source location using coda wave interferometry. The user guide for this code package can be found in Appendix A.

3.1 Abstract

In many geoscientific, material science and engineering applications it is of importance to estimate a representative bulk seismic velocity of materials, or to locate the source of recorded seismic or acoustic waves. Such estimates are necessary in order to interpret industrial seismic and earthquake seismological data, for example in non-destructive evaluation and monitoring of structural materials, and as an input to rock physics models that predict other parameters of interest. Bulk velocity is commonly estimated in laboratories from the time-of-flight of the first-arriving wave between a source and a receiver, assuming a linear raypath. In heterogeneous media, that method provides biased estimates of the bulk velocity, and of derived parameters such as temporal velocity changes or the locations of acoustic emissions. We show that Coda Wave Interferometry (CWI) characterizes changes in the bulk properties of scattering media far more effectively on the scale of laboratory rock samples. Compared to conventional methods, CWI provides significant improvements in both accuracy and precision of estimates of velocity changes, and distances between pairs of acoustic sources, remaining accurate in the presence of background noise, and when source location and velocity perturbations occur simultaneously. CWI also allows 3D relative locations of clusters of acoustic emissions to be estimated using only a single sensor. We present a method to use CWI to infer changes in both P and S wave velocities individually. These innovations represent significant improvements in our ability to characterize the evolution of properties of media for a variety of applications.

3.2 Introduction

Experimental studies of wave propagation in rock cores are often performed to deduce relationships between changes in external conditions and seismic properties such as seismic velocity (Wang, 2001), anisotropy (Christensen, 1966; Sayers and Kachanov, 1995) and attenuation (Toksöz *et al.*, 1979; Sams *et al.*, 1997), and to examine the process of rock fracturing (Pyrak-Nolte *et al.*, 1990) or the distribution of acoustic emissions (Lockner *et al.*, 1992; Lockner, 1993). Established relationships between seismic attributes and underlying rock physical properties are particularly important for monitoring purposes in the hydrocarbon industry and in subsurface CO_2 storage projects, notably for relating effective stress changes during subsurface injection or production to changes that may be observed in the seismic velocity (Arts *et al.*, 2004; Brown, 2002; Guilbot and Smith, 2002; Herwanger and Horne, 2009; Stork *et al.*, 2018). It is therefore of great importance that models developed from laboratory experiments accurately represent the response of in-situ rocks.

Standard methods for measuring either the velocity, or changes in the velocity of a medium involve picking of first-break arrival times of seismic waves traveling between a fixed source and receiver pair. The term 'first-break' is ambiguous, and can be taken to mean the signal onset which is the time of first-arriving energy (Brillouin, 1960), the arrival time of the first peak or the time of first zero-crossing (Hornby, 1998). Manual picking of first-breaks is slow and may incur inconsistent user bias and error, therefore there are many methods available for automatic picking of first-breaks (Earle and Shearer, 1994; Boschetti *et al.*, 1996; Hatherly, 1982; Peraldi and Clement, 1972; Ervin *et al.*, 1983; Molyneux and Schmitt, 1999). Here, unless otherwise stated, we use the term first-break method to mean picking the first maximum (or extremum). This represents the point with the highest signal to noise ratio. The velocity of the medium is then estimated using the known straight-line distance between the source and receiver. For many laboratory experiments measuring such velocities, the wavelengths used are on the same order as heterogeneities in the medium (e.g., pore and grain sizes). Obvious problems then occur: 1) the measured velocity is not sensitive to the bulk properties of

a medium, but rather to properties along a very specific (fastest) ray path between the source and receiver, resulting in a bias towards higher velocities. 2) The path followed by the first-arriving energy is unlikely to be straight, so that velocity estimates made using the straight-line path are biased towards lower values. 3) Biases in points 1 and 2 are generally unrelated so are not expected to cancel. 4) The effects of small perturbations in the medium that are not located along the specific source-receiver path cannot be detected. 5) Such systematic and random errors in velocity estimation are carried forward to any subsequent calculations, notably for example to the location of acoustic source positions. Also, the presence of attenuation and dispersion changes the shape of a propagating wave (Molyneux and Schmitt, 2000), thus the determination of meaningful velocity measurements can be problematic.

Weaver and Lobkis (2001) and Lobkis and Weaver (2001) showed that information about a medium can be extracted from recordings of coda waves and background ambient noise. Coda waves are the multiply-scattered waves that are recorded after the arrival of the main ballistic waves. Recordings of coda waves are far more sensitive than first arrivals to changes in pore-pressure, fracture density and temperature (Snieder *et al.*, 2002; Vlastos *et al.*, 2006, 2007), due to the fact that coda waves follow much longer and more complex paths, eventually sampling the entire medium, and sampling any sub-volume of the medium multiple times. There are now established methods grouped under the name *coda wave interferometry* (CWI) that estimate *changes* in the velocity of the medium (rather than the absolute velocity), or changes in the locations of sources or receivers using the coda (Snieder, 2006). There have been several field and laboratory applications of CWI to date, including the monitoring of velocity changes in ice sheets (Mordret *et al.*, 2016; James *et al.*, 2017), concrete (Larose and Hall, 2009; Planès and Larose, 2013), mining environments (Grêt *et al.*, 2006), and volcanic regions (Sens-Schönfelder and Wegler, 2006). CWI has also been used to study earthquake focal mechanisms (Robinson *et al.*, 2007), earthquake separation distances (Snieder and Vrijlandt, 2005; Robinson *et al.*, 2011), and source network locations of induced micro-seismic events (Zhao *et al.*, 2017; Zhao and Curtis, 2019). So far its implications for the interpretation of laboratory rock physics experiments has been comparatively

limited.

In this paper we test the hypothesis that Coda Wave Interferometry (CWI) can provide an improvement in accuracy and precision when inferring and quantifying the changes in bulk velocity and relative source locations in rock samples in laboratory settings. We test the hypotheses that CWI provides more representative measures of bulk properties, in comparison with commonly used methods in numerical and laboratory experiments at the core-scale, and at high frequencies commonly used in a laboratory setting.

First we outline the theory of Coda Wave Interferometry and how it can be used in an experimental setting. Then we examine multiple samples of varying rock type and heterogeneity using both numerical simulations and laboratory experiments, where changes in source location and velocity are estimated using both CWI and standard methods (manually-picked first breaks for velocities and multilateration for source locations). We show how changes in source position and velocity can be jointly estimated by CWI when both perturbations occur simultaneously. We then demonstrate an optimization algorithm for estimating the relative locations of sources within a cluster, given the source separations estimated from CWI, and show that it can be applied even in the case of having only a single transducer. Following this, we test the sensitivity of CWI as well as conventional methods to increasing contamination of noise. In all cases CWI is shown to out-perform conventional methods.

Accompanying this manuscript, we provide a well-commented set of MATLAB functions for implementing the CWI method to estimate velocity changes, and for the joint estimation of velocity change and source separation. These codes use a form of CWI that estimates changes relative to a moving reference seismogram, which is particularly important for longer deformation experiments in which scattering paths may change significantly, a situation which contravenes the assumptions of standard CWI theory, and requires the reference seismogram to be updated periodically. Together with the suite of CWI codes made publicly available by Zhao and Curtis (2019) this allows all techniques used in this paper to be implemented and reproduced.

3.3 Coda Wave Interferometry (CWI)

CWI is a method that allows small changes in velocity, the displacement of source or receiver locations, or movement of scatterers to be monitored (Snieder *et al.*, 2002; Sens-Schönfelder and Wegler, 2006; Snieder, 2006). These different perturbations and their effect on recorded signals are illustrated in Figure 3.1. First consider the effect of a velocity perturbation (ΔV in Figure 3.1a). The direct arriving wave between a source and receiver would only sample the perturbation once (or not at all), whereas the multiply reflected wavefield samples the perturbation many times. Therefore the change in arrival times for later arriving waves (time window iv) is larger than for the first arrival (time window i). The second perturbation type is a displacement of the source or receiver location (Figure 3.1b shows a source displacement). In this case, the difference in ray paths before and after the perturbation is the path between the source and the first scattering point (blue arrows in Figure 3.1b). Different paths are shortened or lengthened depending on the location of the first scatterer; this is reflected by the advancement and retardation of peaks highlighted by red and blue arrows. Providing the source displacement is small, the extent to which these travel times are perturbed (specifically, the variance of the perturbation) is directly proportional to the displacement. The third perturbation type is the displacement of all scattering points (yellow circles in Figure 3.1c): in this case, all paths between scattering points are perturbed (both shortened and lengthened), and similarly to the previous case the variance of travel time perturbations is proportional to the displacement of scattering points. All three perturbation types can be monitored by using a cross correlation of the unperturbed (u_{unp}) and perturbed (u_{per}) waveforms - the waveforms from the source recorded by the receiver before and after the change or displacement takes place.

One method to estimate the change in velocity is known as trace stretching (Sens-Schönfelder and Wegler, 2006), where the perturbed waveform is assumed to be a time-stretched version of a reference waveform; this follows if one assumes that a velocity perturbation is uniform across the entire medium, so all arriving energy is perturbed at the same temporal rate. This method also assumes no changes in the intrinsic

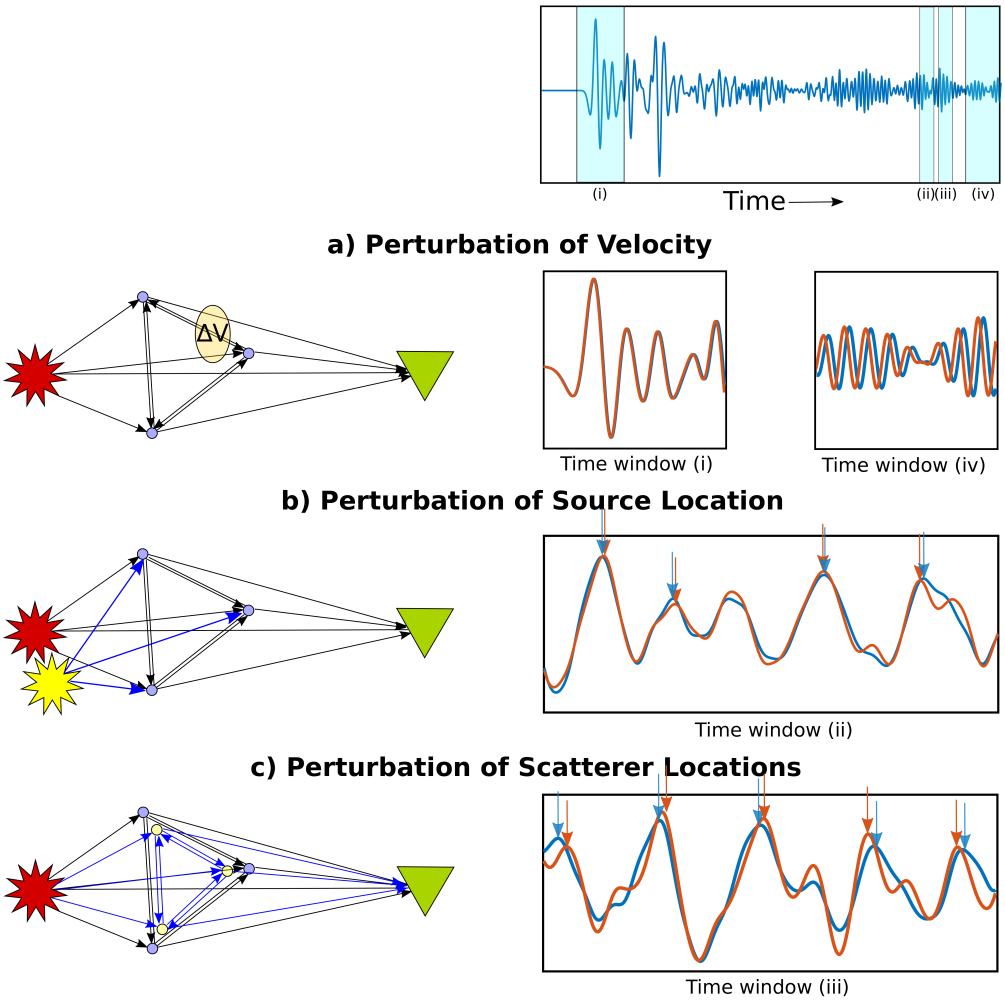

Figure 3.1: Illustrations of different perturbation types and their effects on coda waves. The cartoons (left) represent a scattering medium, with a source (star), receiver (triangle), and point scatterers (circles). Ray paths between the source and receiver, including multiple reverberations, are represented as black arrows. A velocity perturbation (a) is represented as a yellow ellipse, which has a velocity different to the background medium. New ray paths that are introduced due to changes in source location (b) and scatterer locations (c) are represented as blue arrows. Example recorded signals (right) at a range of time windows (i-iv) are shown before and after each perturbation takes place (blue and red, respectively). Differences in travel times of arriving energy for b) and c) are highlighted by vertical arrows.

attenuation of the medium. We stretch the time axis of the perturbed signal by a range of stretching factors (ϵ) and compute the correlation coefficient R between $u_{unp}(t)$ and the stretched version of the perturbed waveform $u_{per}(t[1+\epsilon])$ over a given time window (t_1, t_2):

$$R^{(t_1,t_2)}(\epsilon) = \frac{\int_{t_1}^{t_2} u_{unp}(t)u_{per}(t[1+\epsilon])dt}{\sqrt{\int_{t_1}^{t_2} u_{unp}^2(t)dt \int_{t_1}^{t_2} u_{per}^2(t[1+\epsilon])dt'}}. \tag{3.1}$$

The optimum stretching factor ϵ_{max} that maximizes the correlation coefficient (for which $R = R_{max}$), is related to the ratio of the change in velocity ΔV to the original velocity V by

$$\epsilon_{max} = -\frac{\Delta V}{V}, \tag{3.2}$$

(Sens-Schönfelder and Wegler, 2006). This method requires that velocity changes are small to avoid cycle skipping in the calculation of R in Equation 3.1. In cases where the medium changes significantly, such as during material deformation where new scattering paths are introduced due to fracturing, it may not be appropriate to use a constant reference trace (u_{unp}) for all recorded waveforms during deformation. We therefore propose the use of a moving reference trace, where the optimum stretching factor from the initial reference trace (u_0) to any other recorded waveform during deformation (u_n) can be calculated as

$$\epsilon_{u_0 u_n} = \epsilon_{u_0 u_s} + \epsilon_{u_s u_n}, \tag{3.3}$$

where $\epsilon_{u_i u_j}$ is the stretching factor of trace u_j relative to u_i, $s = k\lfloor n/k \rfloor$, n is the trace number, k is the user-selected step size of the moving reference trace, and $\lfloor \ldots \rfloor$ denotes a floor function, which outputs the greatest integer less than or equal to the argument.

Accompanying this manuscript are a suite of MATLAB functions for implementing the moving-reference stretching CWI method. Snieder (2002) derived the relationship between the inferred medium velocity change from CWI, and changes in P-wave and S-wave velocities in an isotropic case:

$$\frac{\Delta V}{V} = \frac{\beta^3}{2\alpha^3 + \beta^3}\frac{\Delta\alpha}{\alpha} + \frac{2\alpha^3}{2\alpha^3 + \beta^3}\frac{\Delta\beta}{\beta}, \tag{3.4}$$

where α and β are the velocities of P and S waves, respectively. In an initial Poisson medium where $\alpha = \sqrt{3}\beta$, if either or both of the P or S wave velocity changes then the relation simplifies to

$$\frac{\Delta V}{V} = 0.09\frac{\Delta\alpha}{\alpha} + 0.91\frac{\Delta\beta}{\beta}, \tag{3.5}$$

and if α and β change such that the Poisson medium is preserved then

$$\frac{\Delta V}{V} = \frac{\Delta\alpha}{\alpha} = \frac{\Delta\beta}{\beta}. \tag{3.6}$$

The strengths of the CWI technique lie in the ability to resolve very small changes in velocity compared to standard methods. If we take the sampling interval of a recorded signal to be dt, the duration of the signal to be t_{max}, and make the conservative assumption that one sample interval is the smallest resolvable time difference between waveforms in the two recordings, then the maximum resolution of CWI (the smallest resolvable change in velocity that can be measured) is

$$\left[\frac{\Delta V}{V}\right]_{min}^{CWI} = \frac{dt}{t_{max}}. \tag{3.7}$$

The maximum resolution for measuring $\Delta V/V$ from the standard first-break method would be

$$\left[\frac{\Delta V}{V}\right]_{min}^{FB} = \frac{dt}{(t_0 + dt)}, \tag{3.8}$$

where t_0 is the first-break arrival time. Both equations 3.7 and 3.8 assume no background noise and hence no uncertainty in the recorded waveforms, nor ambiguity in defining a first break which can be highly uncertain in many cases. Inserting typical values for laboratory core scale measurements, such as those used in the experiments in the following section (sampling interval $dt = 0.04\mu$s, signal duration $t_{max} = 640\mu s$, and arrival time $t_0 = 65\mu s$), the smallest perturbations that theoretically can be detected are 0.00625% for CWI and 0.062% for the standard first break method. Hence, CWI offers an order of magnitude improvement in precision in the absence of noise. The CWI method also computes the cross-correlation function using many more data points, which should make it less susceptible to the effects of noise than a single point measure of say the first peak for the first break estimate. We test the hypothesis that CWI provides a more accurate measure of relative velocity changes in the experiments outlined in Section 3.4.3.

Another advantage of using CWI is that it allows a joint estimate of both a velocity perturbation and the separation r between two source/receiver locations to be made from a single receiver. This is because velocity perturbation information is retrieved from the consistent phase information along the waveforms, whereas the source or receiver separation is related to the variance of inconsistent phase perturbations and hence to the maximum value of the cross correlation value (R_{max}) in Equation 3.1, and these two attributes may be observed independently. Figure 3.1b illustrates how the perturbations of travel times (advancement and retardation of individual peaks) relates to the displacement of the source or receiver. Snieder (2006) derives the relationship between the maximum cross-correlation and the variance of the travel time perturbations (σ_τ^2) as

$$R_{max} = 1 - \frac{1}{2}\bar{\omega}^2\sigma_\tau^2, \tag{3.9}$$

where $\bar{\omega}^2$ is the dominant mean-squared angular frequency in the recorded waveform which can be computed as:

$$\bar{\omega}^2 = \frac{\int_{t_1}^{t_2} \dot{u}^2(t')dt'}{\int_{t_1}^{t_2} u^2(t')dt'}, \tag{3.10}$$

where $\dot{u}$ is the temporal derivative of the waveform u. When a source/receiver is displaced relative to another source/receiver by distance r, one can estimate separation r from the variance of the travel time perturbations in a range of scenarios. For isotropic sources in a two-dimensional acoustic medium:

$$\sigma_\tau^2 = \frac{1}{2\alpha^2}r^2. \tag{3.11}$$

For isotropic sources in a three-dimensional acoustic medium:

$$\sigma_\tau^2 = \frac{1}{3\alpha^2}r^2. \tag{3.12}$$

For double couple sources on the same fault plane, with the same source mechanism and in elastic media:

$$\sigma_\tau^2 = \frac{(\frac{6}{\alpha^8} + \frac{7}{\beta^8})}{7(\frac{2}{\alpha^6} + \frac{3}{\beta^6})}r^2, \tag{3.13}$$

where α and β are estimates of the P- and S-wave velocities of the medium (Snieder and Vrijlandt, 2005). These estimates of velocity represent an average for all scattering

paths, assuming coda waves are evenly distributed in an isotropic medium. The type of spatial averaging that is implicit in the CWI estimate is analyzed in Section 3.6.

To summarize, the main advantages of using CWI over conventional first-break method in an experimental setting (at least in theory) are that: 1) CWI is more representative of changes in the bulk properties of a medium because coda waves sample the entire medium. 2) Coda waves sample the same area multiple times, so CWI is capable of resolving smaller changes in the medium giving a theoretical order of magnitude increase in precision for typical laboratory experiments. 3) CWI is generally less susceptible to the presence of noise as it uses many more data points, providing more robust estimates. 4) CWI allows for the separation between nearby sources to be estimated from a single receiver, even in cases where medium velocity changes occur simultaneously, as the two estimates utilize different measurements made from the correlation function in Equation 3.1. The source-separation data are then sufficient to estimate the 3D relative locations of clusters of sources using CWI with a single receiver. We now test how CWI works in practice, using numerical simulations and laboratory experiments.

3.4 Results

3.4.1 Estimating Velocity and Source Locations: Synthetic Examples

Rock cores typically used for geomechanics and rock physics experiments are on the scale of 3 mm to 100 mm in diameter, and seismic wave frequencies studied are on the order of kHz - MHz. At these frequencies, wavelengths are similar to the scale of the key heterogeneities such as pores and grains, therefore many rock samples act as strongly scattering media. Most recorded waves take very complex, long paths and experience multiple reflections, diffractions and reflections (Sato *et al.*, 2012). Therefore there are strong frequency dependent effects on properties derived from ultrasonic recordings at these scales (Mason and McSkimin, 1947). The complex nature of wave propagation through highly scattering media, such as the samples shown in Figure 3.2, can be studied using methods of digital rock physics (Madonna *et al.*, 2012). First

Table 3.1: Parameters used for finite difference wavefield simulation through the samples shown in Figure 3.2. Values are Voigt-Reuss-Hill averages taken from Bass (1995) and Mavko *et al.* (2009).

Phase	**Density (kg/m^3)**	**Velocity (m/s)**
Pore Fluid	1000	1500
Calcite	2710	6500
Plagioclase	2620	6500
Quartz	2650	5800
Potassium Feldspar	2560	6300
Biotite	3090	5260
Muscovite	2790	6460

a reconstructed micro-tomography (μCT) cross-section is segmented into appropriate mineral and pore phases, and converted into velocity and density models (wave physics parameters used for different phases are shown in Table 3.1). Using finite difference methods (Moczo *et al.*, 2007), wave propagation through the medium can be simulated so that full waveforms can be generated, as though they have been recorded at any point within the medium. These methods are increasingly used for estimating the acoustic or elastic properties of rocks based on μCT images (Saenger *et al.*, 2014; Saxena and Mavko, 2016). These methods are limited by the resolution of μCT images, which fail to resolve sub-micron scale structures such as any microcracks that may exist.

Our aim is to understand and address problems facing core-scale experimental rock physics, especially where strong scattering occurs. To emulate these physical experiments, we simulate wave propagation using a two-dimensional, acoustic, rotated staggered-grid finite-difference solver, through three different digital rock samples: Tivoli Travertine (TT), Westerly Granite (WG) and Copp-Crag Sandstone (CS). These rock types have been selected to represent a range of types of heterogeneity, where Tivoli Travertine has high porosity with complex pore shapes and pore size distribution, Copp-Crag is a relatively homogeneous sandstone with more uniform pore shapes and pore size distribution, and Westerly Granite is the most homogeneous and exhibits little porosity. The μCT slices and corresponding models of segmented phases for each

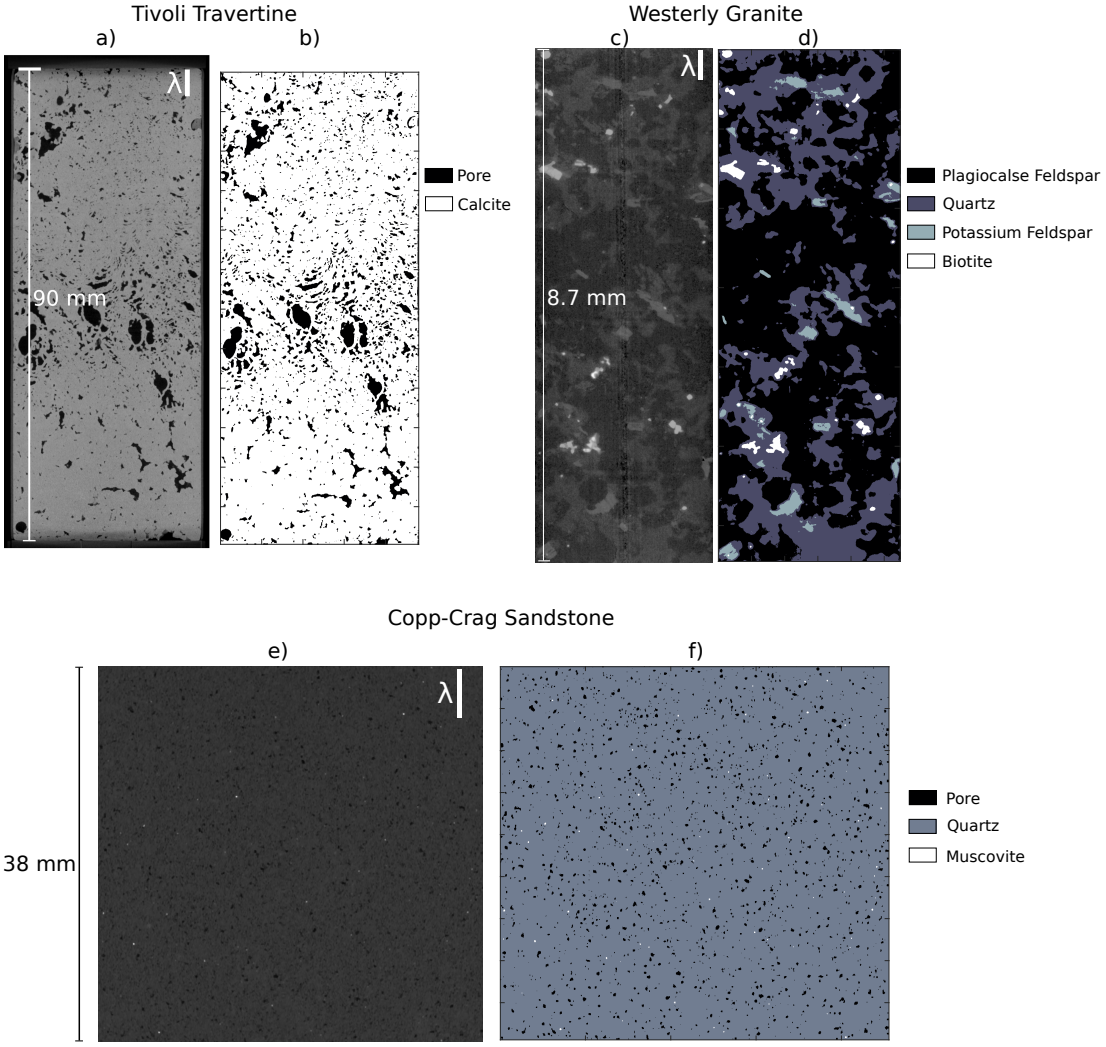

Figure 3.2: Set of X-ray μCT slices (left images) and equivalent models of segmented phases (right images) for three rock cores with varying heterogeneity and rock type: a) and b) Tivoli Travertine, c) and d) Westerly Granite, e) and f) Copp-Crag Sandstone. Model sizes are: 900x2400, 1000x3000 and 900x900 pixels for Tivoli Travertine, Westerly Granite and Copp-Crag, respectively. Approximate wavelength λ for each sample is labeled with a white bar, where the source signals contain a peak frequency of 30 MHz for Tivoli Travertine and Copp-Crag Sandstone, and 200 MHz for the smaller Westerly Granite model. The properties assigned to each material phase for wavefield simulation can be found in Table 3.1.

rock type are shown in Figure 3.2 and are converted to wave physics models using the parameters stated in Table 3.1 (assuming isotropic mineralogy). The simulations do not include any effects caused by attenuation or dispersion. Each pixel is mapped to a regular grid of cells used for the finite difference method, with cell sizes of 37.5 μm, 42 μm and 2.9 μm for the TT, CS and WG, respectively. The model includes reflecting boundaries to account for side wall reflections.

The source input pulses used are Ricker wavelets with peak frequencies of 30 MHz for the TT and CS models, and 200 MHz for the smaller WG model. These frequencies are significantly higher than those conventionally used in laboratory experiments, which typically use peak frequencies around 1 MHz for 38 mm core diameter experiments. For comparison with conventional methods, we also use a Ricker wavelet with peak frequency of 1 MHz for the TT model. The simulations here are well within the high-frequency regime (approximate wavelengths for each sample are labeled as λ in Figure 3.2). We assume a point source and point receivers, much smaller than the apertures of conventional transducers used in laboratory experiments. We also assume perfect transducer coupling, which in a laboratory setting is unknown and may be sensitive to external conditions. Accordingly our results explore a best-case scenario at this stage of the modelling. High-contrast discontinuities such as those between pores and mineral phases may cause instability problems on a staggered grid. To avoid these difficulties, we implement the rotated staggered grid technique (Saenger and Bohlen, 2004).

First, we simulate a single point source located at the top of each sample and a row of point receivers along the bottom (e.g., Figure 3.3e). Velocity is estimated at each receiver by manually picking the arrival time of the first peak (as well as the signal onset for the TT model) and assuming straight ray paths between the known source and receiver locations (shown in Figure 3.3a, b, c and d). For the three samples, the estimated velocities at each receiver show considerable variation depending on where the receiver is located. For the TT model, we compare varying the source frequency (1 MHz and 30 MHz) as well as the method used for picking the first arrival (picking the first maximum in panel a in Figure 3.3, and the signal onset in panel b). The strong

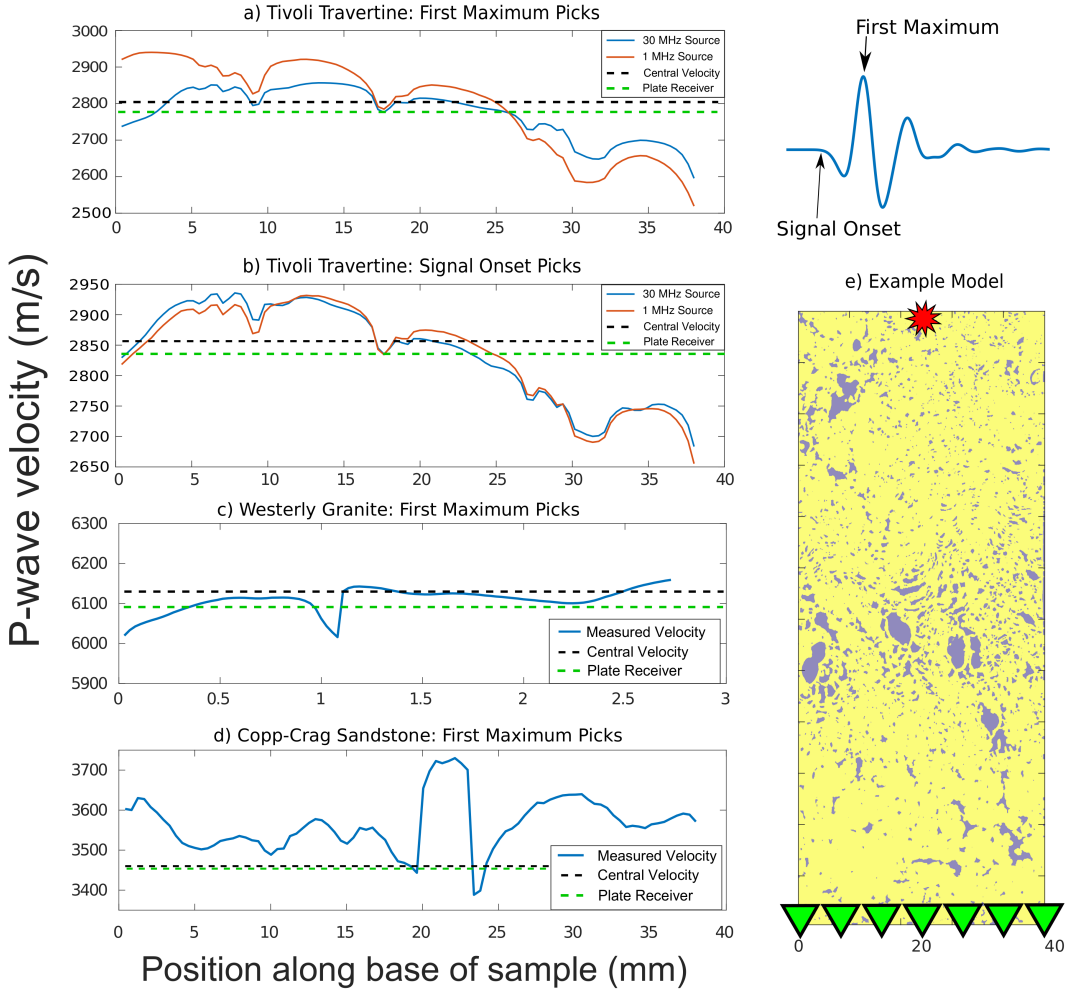

Figure 3.3: (a-d) Estimated seismic velocity as a function of receiver position, obtained from simulated waveforms through a μCT digital rock sample in a model shown (e) for the Tivoli Travertine. The source (star) is fixed at the top and receivers (triangles) are distributed along the bottom. The blue curve shows velocity estimates made using first-break arrival times and straight-line source-to-receiver distances. The dashed green line represents the conventional estimate of velocity using a single receiver at the center of the core. The dashed black line represent the fastest measured velocity. Results are for a) Tivoli Travertine picking the travel time of the first maximum and using a 30 MHz (blue) and 1 MHz (red) sources, b) Tivoli Travertine picking the travel time of the signal onset and using a 30 MHz (blue) and 1 MHz (red) sources c) Westerly Granite (200 MHz source), and d) Copp-Crag Sandstone (30 MHz source). The results in panels c and d are from picking the first maximum.

variation in velocity depending on receiver position is present for both frequencies and both picking methods. This response is concerning as in many cases a single receiver and hence a simple, non-representative velocity may be used to characterize an entire sample - from a receiver at the center of the core in conventional experimental configurations (shown as dashed black lines in Figure 3.3). Sometimes a plate-like receiver is used which spans the entire base of the sample; in that case the signal recorded would be approximately equal to the superposition of all the distributed transducers (Li *et al.*, 2018), and the velocity estimated using this method is shown as a dashed green line.

To further explore the variation of measured velocity, a similar numerical experiment was carried out on the three velocity models in which eikonal ray tracing was implemented using the methods outlined by Margrave (2007). This gives an estimated arrival time ($t[\boldsymbol{x}]$) for every point $\boldsymbol{x}$ in the model for a fixed source location (in this case the source is located at the center-top of each sample). Using these arrival times, we can imagine a receiver placed at every point within and on the boundary of a model, and an estimate of the velocity for that source-to-receiver path can be calculated using the standard travel time method assuming straight rays. Figure 3.4 shows the calculated velocity $v[\boldsymbol{x}]$ for all model points $\boldsymbol{x}$ in each sample, again showing that measured velocity may be strongly dependent on source and/or receiver locations. For Tivoli Travetine (Figure 3.4a) the variation in velocity estimates are greater than for Copp-Crag Sandstone (Figure 3.4c), and Westerly Granite (Figure 3.4b) has the smoothest image, reflecting the smallest variation in estimated velocity $v[\boldsymbol{x}]$. In all cases the longer the source-to-receiver distance, the more stable is the result.

There are therefore several concerning implications of characterizing a medium with velocities calculated from standard methods: 1) a measured cross-core velocity is not sensitive to the bulk properties of a medium, but rather to the velocities along a specific ray path between the point source and point receiver, as demonstrated by the variation of estimated velocity with receiver position in Figures 3.3 and 3.4. Therefore, 2) the effects of small perturbations in a medium that are not located on the specific source-to-receiver path will not be detectable using these methods. In addition, although the

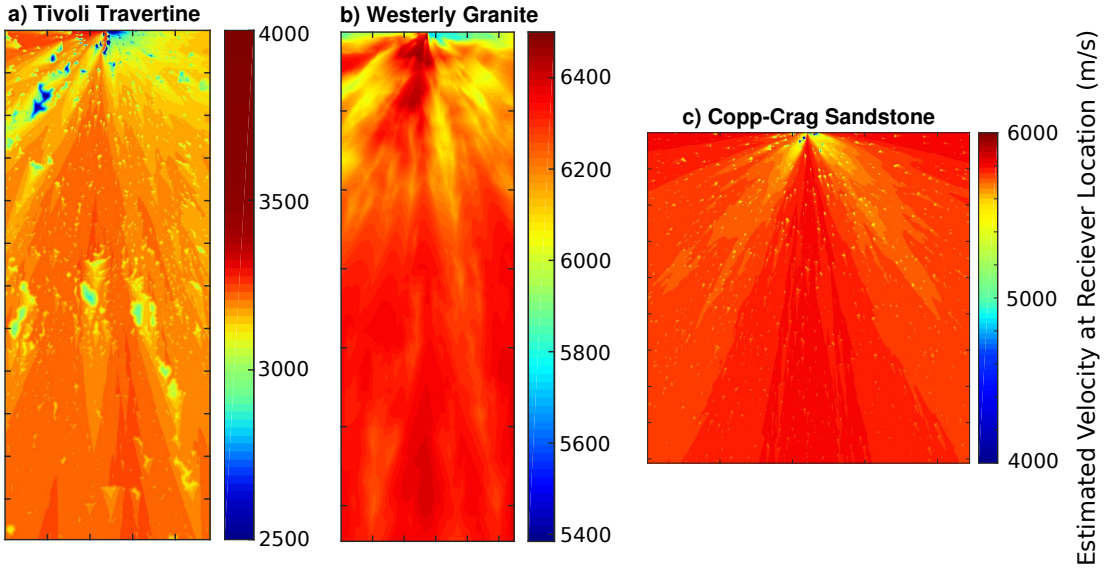

Figure 3.4: The estimated velocity as if a receiver was placed at every position in the model $\boldsymbol{x}$, using a fixed source location (centre of the top of the sample). To emulate estimates from the first break method, an eikonal ray tracing method (Margrave, 2007) was used to calculate travel times $t[\boldsymbol{x}]$, while a straight source-to-receiver ray path was used to calculate velocity $v[\boldsymbol{x}]$. Results are for a) Tivoli Travertine, b) Westerly Granite, and c) Copp-Crag Sandstone.

results stabilize for a more distant source and receiver pair, they are still expected to stabilize at a velocity that is biased relative to the average across the sample since first-arrival travel times are measured along shortest travel time ray paths.

The assumption that a medium is represented by a single constant 'bulk' velocity also introduces errors into subsequent calculations, such as in the estimation of source locations. This effect can be examined using a further numerical experiment. We simulate a series of regularly spaced sources placed on a rectilinear grid throughout each of the three media, representing acoustic emissions occurring throughout the sample. We measure the arrival times for each source (S) at a set of receivers (i) as t_S^i using the first-break method, and use a single measured velocity through each sample (V_{med}), which is assumed to be representative of the entire medium. In our implementation the exact value of this velocity does not affect source locations - it only affects the estimates of the source origin time (t_0). In this case it is therefore not inaccuracy in the velocity estimate that will effect locations, but rather the assumption that there

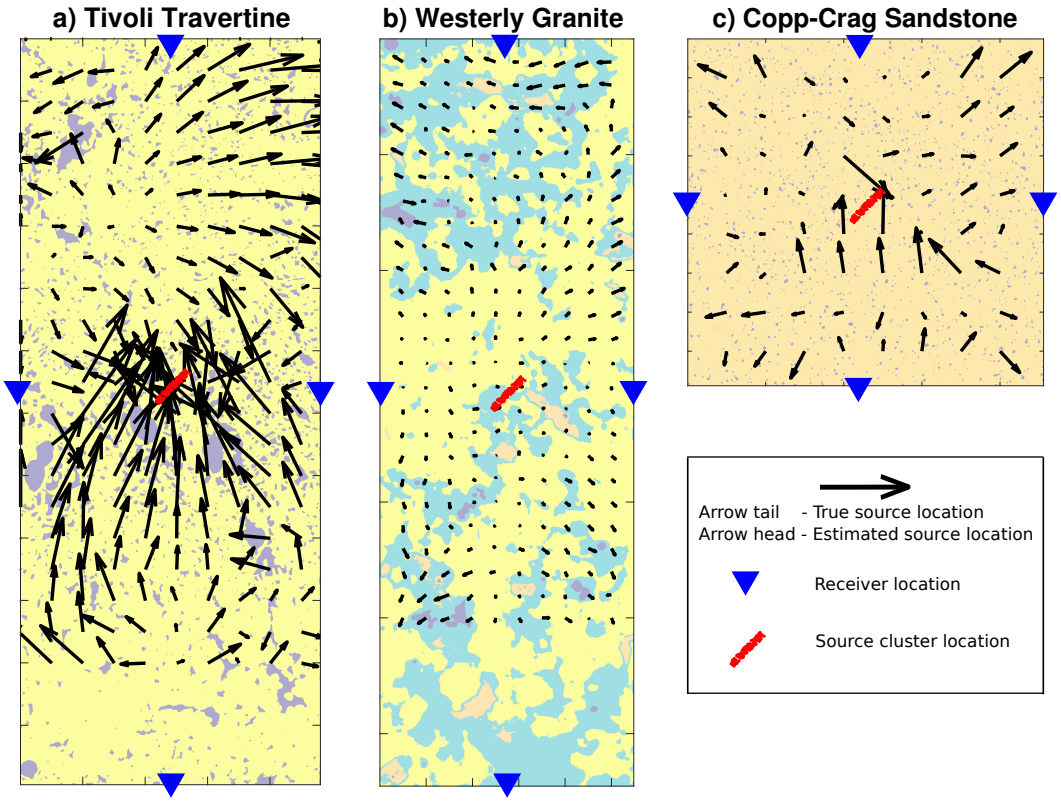

Figure 3.5: The resulting systematic errors in source location, represented as black arrows, using standard phase picking methods that assume a single representative velocity for each sample, for a) Tivoli Travertine, b) Westerly Granite, and c) Copp-Crag Sandstone. The base of each arrow is located at the true source positions (S_j), and estimated locations (S_{est}) are displayed at arrow tips. The red points represent the source cluster used for the source location experiment with results shown in Figure 3.7.

is a single representative medium velocity. We estimate source locations (S_{est}) using multilateration, by implementing a grid-search through all model positions ($\boldsymbol{x}$) for each receiver location ($\boldsymbol{x}_i$) and through a range of source origin times (t_0), to find values of $\boldsymbol{x}$, and t_0 that minimize the objective function

$$\varphi(\boldsymbol{x}, t_0) = \sum_{i=1}^{N^i} [V_{med} \times (t_S^i - t_0) - |\boldsymbol{x}_i - \boldsymbol{x}|]. \tag{3.14}$$

The estimated source location S_{est} is the location $\boldsymbol{x}$ that minimizes φ. Figure 3.5

displays the systematic error in estimated source locations S_{est} (arrowheads) compared to true locations (arrow tails) for each of the three samples. For the majority of sources in Tivoli Travertine (3.5a) and Copp-Crag Sandstone (3.5c), the resulting systematic error in source location is significant in both amplitude and direction. In Westerly Granite (3.5b), such errors have much smaller amplitudes. It is therefore clear that in more heterogeneous media, a single velocity is not appropriate and estimated source locations in many areas are highly inaccurate when estimated using conventional methods of multilateration assuming a single bulk velocity.

3.4.2 CWI and Conventional Estimates of Changes in Velocity and Source Location: Synthetic Tests

We now test CWI against conventional methods for measuring a *change* in the velocity of a medium, using finite difference numerical wavefield simulations through the three μCT slices in Figure 3.2. Two slightly different velocity models for each sample are generated: one is the unperturbed medium and the other has perturbed velocities of both mineral and fluid phases equal to a -1% ($\Delta V/V = -0.01$). The simulated signals are obtained from an array of receiver positions along the bottom of the sample as used in Figure 3.3. The change in velocity ($\Delta V/V$) between each pair of models is estimated from these signals by CWI (using Equations 3.1 and 3.2), and using the conventional method of manual phase-picking of first-break arrivals (time of first peak) assuming straight rays. Figure 3.6 compares these estimates for each sample. For all samples, CWI gives more accurate (closer to the true perturbation of the model) and more precise (lower standard deviation) estimates of $\Delta V/V$, and is more robust (shows significantly less variation between different receiver locations) when compared to the first-break method. This effect is clearly dependent on the complexity of the medium: the first-break estimates for Tivoli Travertine (Figure 3.6a) show much stronger variation than those for Westerly Granite (Figure 3.6b). The CWI estimates for $\Delta V/V$, however, do not vary between samples of differing complexity. Coda waves sample the entire medium rather than a specific (fastest) ray path, therefore CWI is more robust to changes in receiver location. This consistency of estimates shows that CWI is less dependent

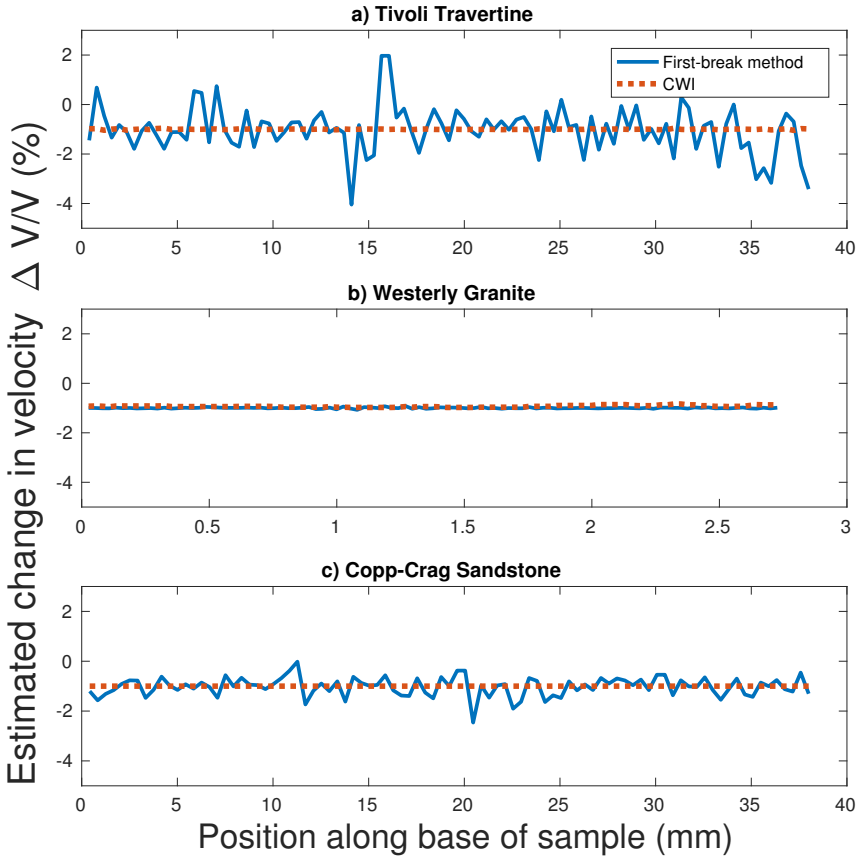

Figure 3.6: The estimation of a relative velocity change $\Delta V/V$ for a true change in velocity of -1%, i.e., $\Delta V/V$ = -0.01. Results for a) Tivoli Travertine, b) Westerly Granite, and c) Copp-Crag Sandstone. $\Delta V/V$ is estimated using the standard phase-picking method and Coda Wave Interferometry using each of 100 receiver locations along the base of each sample and a single source location at the center-top of each sample.

on sample complexity, and on receiver location, and confirms the hypothesis that the multiply reflected waves used in CWI effectively sample the entire medium, providing more representative measures of velocity changes from any source and receiver pair.

We also test CWI and conventional methods for estimating *changes* in source locations. For this test, waveforms were simulated for a cluster of sources along a fracture plane in the middle of each of the three samples, and with receivers located at the bottom and at either side of the model (experimental configuration and source cluster locations shown in Figure 3.5). The standard method of multilateration (minimizing Equation 3.14)

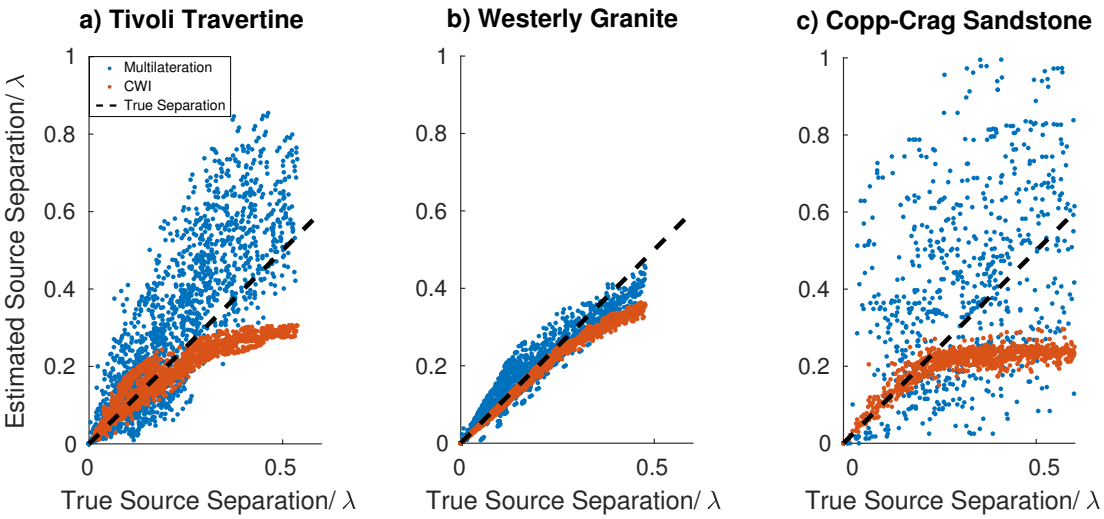

Figure 3.7: A comparison of estimated inter-source separation as a function of true inter-source separation (scaled by the wavelength λ at peak frequency) for the conventional multilateration method (using arrival times obtained from phase picking of first arrivals) and Coda Wave Interferometry. The true source cluster locations are represented as red dots in Figures 3.5a, b and c. a) Tivoli Travertine, b) Westerly Granite, and c) Copp-Crag Sandstone. The dashed line indicates the graph locations corresponding to perfect estimates.

is used to locate source positions for each source in the cluster, assuming a constant bulk velocity which is measured with a single source and receiver placed at the top-center and bottom-center of the sample respectively. CWI provides the separation between pairs of sources (it does not provide source locations in an absolute frame of reference), so Figure 3.7 compares separations between the estimated source locations from multilateration with source separations estimated from CWI. The latter estimates are from Equations 3.9 and 3.13, and an estimate of the bulk velocity of the medium (the same measured velocity used in multilateration) for each sample, and separations were obtained using only the top receiver (multilateration estimates require the use of all four receivers). For all three media, the multilateration-method estimates are relatively scattered, particularly for Tivoli Travertine and Copp-Crag Sandstone. CWI estimates of the relative source locations are more precise, and are more accurate up to approximately 0.2-0.4λ, where λ is the dominant wavelength. At larger separations cycle-skipping in the cross-correlation is likely to interfere with the signals that we seek in the maximum of the correlation function, causing estimates to tend to a constant

value at larger source separations. We demonstrate in Section 3.4.5 below how relative locations of sources can be obtained using separation data from even only a single receiver, and how the working-range of source separations can be increased beyond 0.4λ.

3.4.3 Experimental Examples

In experimental rock physics, trends in velocity are often measured to model the response of seismic velocity to changes in external conditions (e.g., temperature, effective and differential stresses, fluid properties, etc.), conferring particular importance to the interpretation of dynamic changes. This is important for a range of geophysical scenarios on a larger scale, such as monitoring subsurface fluid reservoirs or changes in rock properties using time-lapse (4D) seismic methods. Here we show results of two laboratory experiments that impose changes in the external conditions of temperature and stress. In the first experiment illustrated in Figure 3.8a, a 10 cm^3 block of Halldale Sandstone was heated from room temperature to an external temperature of 54°C over one hour, and then left to relax to room temperature. In this experiment we do not aim for thermal equilibrium, because the CWI method does not require a constant medium velocity. The experiment varies temperature simply to induce a non-uniform change in velocity within the medium for comparison of CWI and conventional methods. A thermocouple was attached to an external face for continuous temperature monitoring, and two piezoelectric transducers (PZT) were attached on opposite faces of the sample for continuous ultrasonic surveys, which were undertaken during the cooling phase back down to room temperature. As the maximum temperature variation is relatively small ($\Delta 8$°C), we assume that the PZT response to temperature variation is negligible.

To measure P-wave velocity we use Glaser-type conical piezoelectric sensors sensitive to displacement normal to the sensor face (McLaskey and Glaser, 2012). These laboratory-standard, wide-band sensors are calibrated against theoretical displacement time history and have an almost flat displacement response spectrum in the 20 kHz to 1 MHz frequency band. This means that, in this frequency band, they are essentially displacement sensors and their voltage output is linearly proportional to the surface

a) Experiment I: Temperature

Sample Details:
Fine grained
Quartz rich
ϕ = 15.1%
ρ = 2248 kg/m^3
Size: 10x10x10 cm
Saturation: Dry

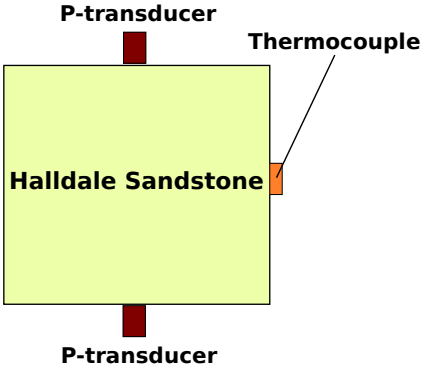

b) Experiment II: Differential Stress

Sample Details:
Core parrallel with laminations
Finely laminated carbonate
ϕ = 10.3%
ρ = 2374 kg/m^3
Length = 75 mm
Diameter = 38 mm
Saturated with deionized water

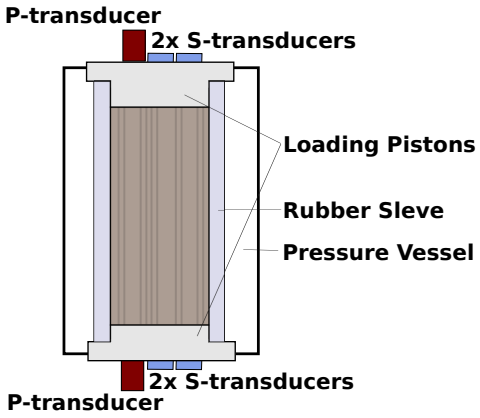

Figure 3.8: Schematic diagrams for the two experimental examples used for inducing a velocity change in the medium. a) Experiment I uses a variation in temperature of a cubic block of Halldale Sandstone. b) Experiment II uses varying differential stress on a finely laminated carbonate within a triaxial Hoek cell. Values for porosity (ϕ), density (ρ) and other properties of each sample are shown for each case.

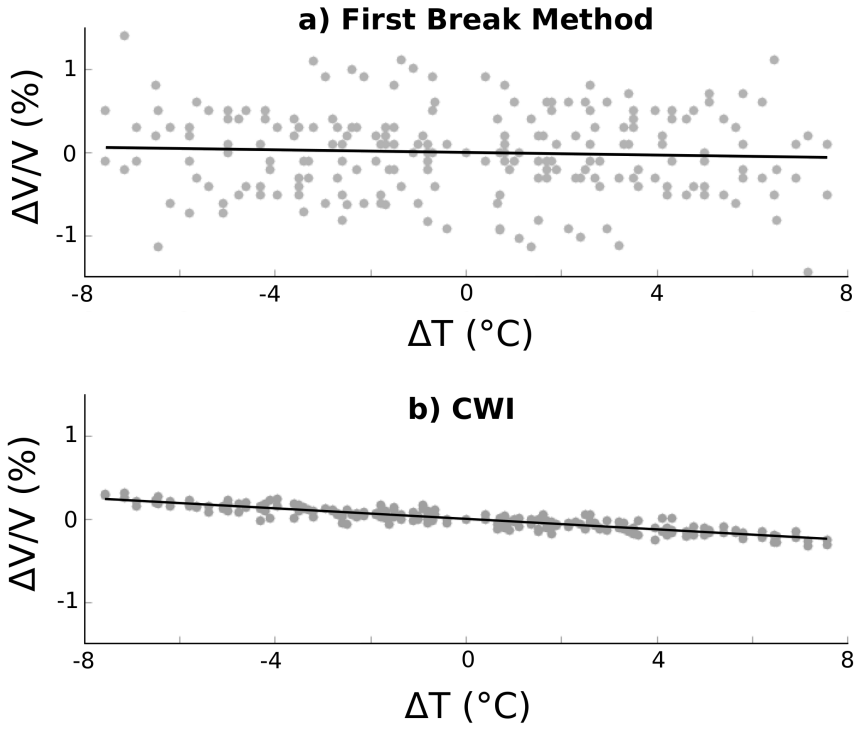

Figure 3.9: Estimated values of percentage velocity change ($\Delta V/V$) as a function of the change in temperature (ΔT) in a 10 cm^3 sample of Halldale Sandstone, a) for the standard method of picking arrival times, and b) for Coda Wave Interferometry. Solid lines are best-fit linear regressions. The zero point on the x axis ($\Delta T = 0$) is arbitrary.

normal displacement. Aperture effects are reduced due to the relatively small 0.5 mm sensor contact area (which is even higher than the resolution used in Figure 3.3). We used an Itasca Image pulser-amplifier system with operating frequency range of 100 kHz to 1 MHz and pre-amp gain of 40 dB, which switches between all transducers in an ultrasonic array, allowing each to act as both a transmitter and a receiver. The amplitude of the pulse spike is 500 V with approximate signal rise time of 0.3 μs and total duration of 2.8 μs, the sampling period is 40 ns. The output recorded waveform at each receiver is a stack of received waveforms from 25 source pulses with a pulse repetition frequency of 20 kHz (as the pulse repetition is high, we assume no loss in phase resolution).

The change in velocity ($\Delta V/V$) for each temperature change (ΔT) were estimated

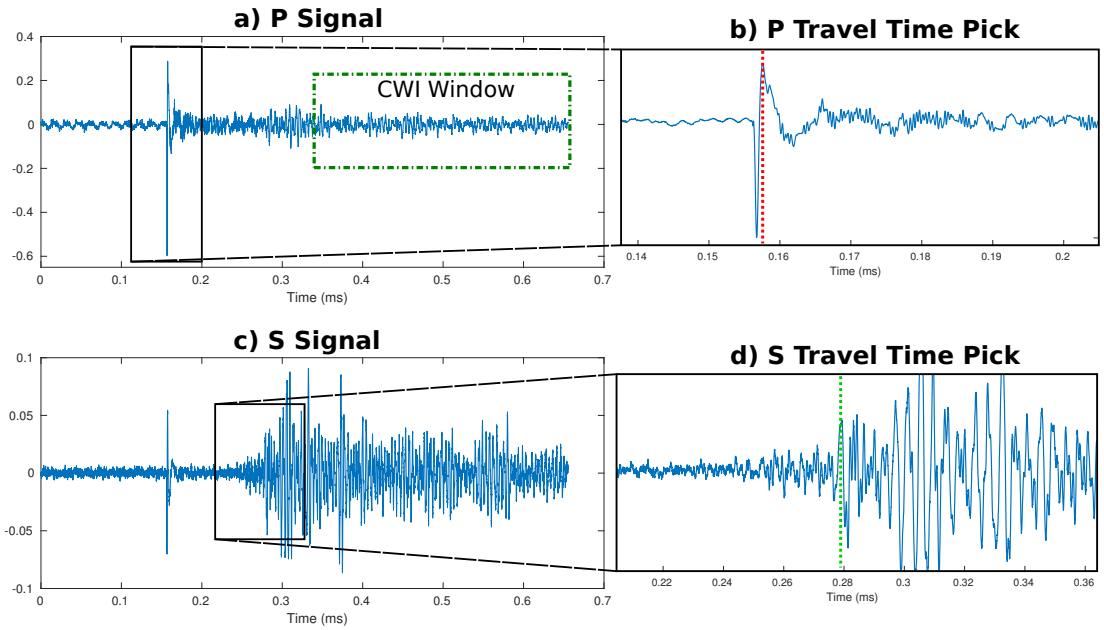

Figure 3.10: Example waveforms to illustrate the picking procedure for the first break method. a) Full recorded signal using Glaser-type sensors sensitive to displacement normal to the sensor face. b) First arriving waves: the first maximum is manually picked as the arrival time. c) Full recorded signal using S wave transducers for the source and receiver, sensitive to displacement tangential to the sensor face. d) Manually picked first arriving S wave maximum. The time window used for CWI is labeled in panel a.

using both the first-break method (manually picking the first extremum) and the CWI stretching technique (plotted in Figure 3.9). There is a large amount of scatter in the $\Delta V/V$ estimates for the first break method, where there is no clear trend that can be resolved above the noise. In contrast, the $\Delta V/V$ estimates using CWI form a clear and coherent response to changes in temperature - a linear, negative correlation due to thermal contraction. This highlights the sensitivity of standard methods to noise, and CWI's ability to resolve small changes in spite of the presence of noise.

A second experiment was carried out, illustrated in Figure 3.8b, where a 38 mm diameter, 75 mm length core of a fine grained laminated carbonate was held at 45 MPa effective pressure, and a differential stress was applied with a strain rate of 10^{-5}s^{-1}, until a peak stress of 235 MPa. The stress loading history is plotted in Figure 3.11a, where pauses in loading are periods during which the permeability of the sample was

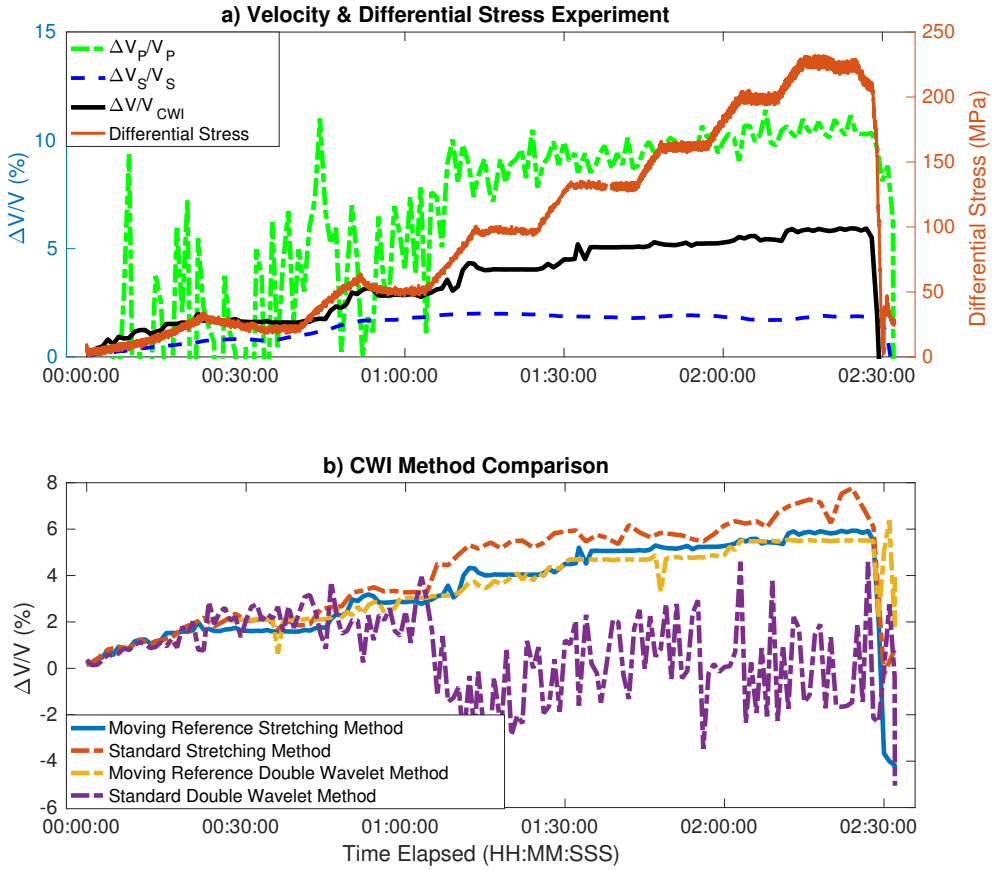

Figure 3.11: a) Velocity change of a finely laminated carbonate rock during experimental deformation by increasing differential stress (red), with corresponding stress values labeled on the right axis. The response of velocity ($\Delta V/V$), labeled on the left axis, is estimated by the first-break method for P and S wave velocities (dashed lines) and by a CWI moving-reference trace method (black). b) A comparison of CWI algorithms, showing the effect of implementing a moving reference trace (Equation 3.3) for both the stretching and double wavelet methods.

measured. P wave velocity is estimated using the Glaser-type sensors described above. We measure S wave velocity using sensors with PZT sensitive to displacement tangential to the sensor face, with a central frequency of 700 kHz and a contact area of 20 mm^2. Example waveforms for this experiment are shown in Figure 3.10. The variation of velocity during the experiment is estimated using the standard first break method for estimating P and S wave velocities, and the CWI moving reference trace method (from Equations 3.1, 3.2 and 3.3) using the time window labeled in Figure 3.10a ($t1 = 0.35ms$, $t2 = 0.65ms$). In Figure 3.11a we see CWI provides a far clearer and more consistent response to external stress changes compared against the change in P wave velocity estimated using first-breaks, accurately mirroring the stepped stress program with far less scatter in the estimated $\Delta V/V$ values, most strikingly for the earlier stress steps. First-break S wave velocities exhibit a smoother response (less scatter), but also fail to mirror the stepped stress program. $\Delta V/V$ estimates from CWI approximately mark the average between changes in P and S wave velocities - we discuss the way in which CWI averages changes in P and S wave velocities in Section 3.5. The higher $\Delta V_P/V_P$ in estimates from the conventional method may also reflect the bias towards higher velocities, as the first arriving waves follow only the fastest ray path. As deformation occurs, compaction is localized to specific regions of the sample; if the fastest travel path samples such regions, the estimated change in velocity ($\Delta V_P/V_P$) would be larger using first-breaks than estimates using CWI which is more representative of the changing bulk properties of the sample.

As CWI uses a cross-correlation function, the method breaks down if there are very large changes in the medium due to wave paths being significantly altered and (if the medium fractures) new scattering points being introduced. This means that a single reference trace is not appropriate for CWI in such deformation experiments where the rock structure is significantly deformed. This effect can be seen in Figure 3.11b, where different CWI algorithms are compared. The "double wavelet" method (Snieder *et al.*, 2002) measures delay times ($\delta\tau$) for multiple time windows down the coda: these relate to the velocity perturbation by $\Delta V/V = -\delta\tau/t$. It is clear that at later stages in the experiment (after 1 hour), the estimates of $\Delta V/V$ using the

double wavelet method with a fixed reference trace (dashed purple line) are heavily distorted due to the deformation occurring within the sample. The large amount of scatter exhibited by this method highlights the problem of large changes occurring in the medium. The stretching method, without implementing a moving reference trace (dashed red line), provides more consistent estimates of $\Delta V/V$ than the double wavelet method, estimating a consistent increase in velocity. At later stages in the experiment, these estimates of $\Delta V/V$ become more scattered and the mirroring of the stepped stress program becomes less clear. For both methods, implementing the moving reference trace method (Equation 3.3) limits estimates to small changes in velocity, for which CWI remains accurate, to obtain an overall estimate in $\Delta V/V$ that shows a much clearer stepped response. This suggests that the moving (or periodically updated) reference trace method can account for the more extreme changes that occur in the medium. There is no prescribed value for how frequently the reference trace should be updated (k in Equation 3.3) as it depends on the rate of deformation and the surveying frequency, except that it should be introduced before any changes produce a half-wavelength change in the waveform in the latest time window. However, the strengths of CWI lie in the ability to resolve small changes in velocity, therefore the step size k should remain small ($k = 5$ for results shown in Figure 3.11b, where surveys are taken every minute).

3.4.4 Joint Estimation of Source Separation and Velocity Change

Since CWI estimates of the bulk velocity change ($\Delta V/V$) and source separation (r) are derived from different information (the phase and the maximum value of correlation as shown in equations 3.2 and 3.9, respectively), estimates of each can be made independently when both effects occur simultaneously. This has significant experimental advantages, as fixed source and receiver locations might no longer be necessary for continuous velocity measurements, and in deformation experiments when acoustic emissions might accompany bulk velocity changes these two effects could be analyzed independently - all using a single receiver.

We test the accuracy of these estimates using a series of finite-difference simulations

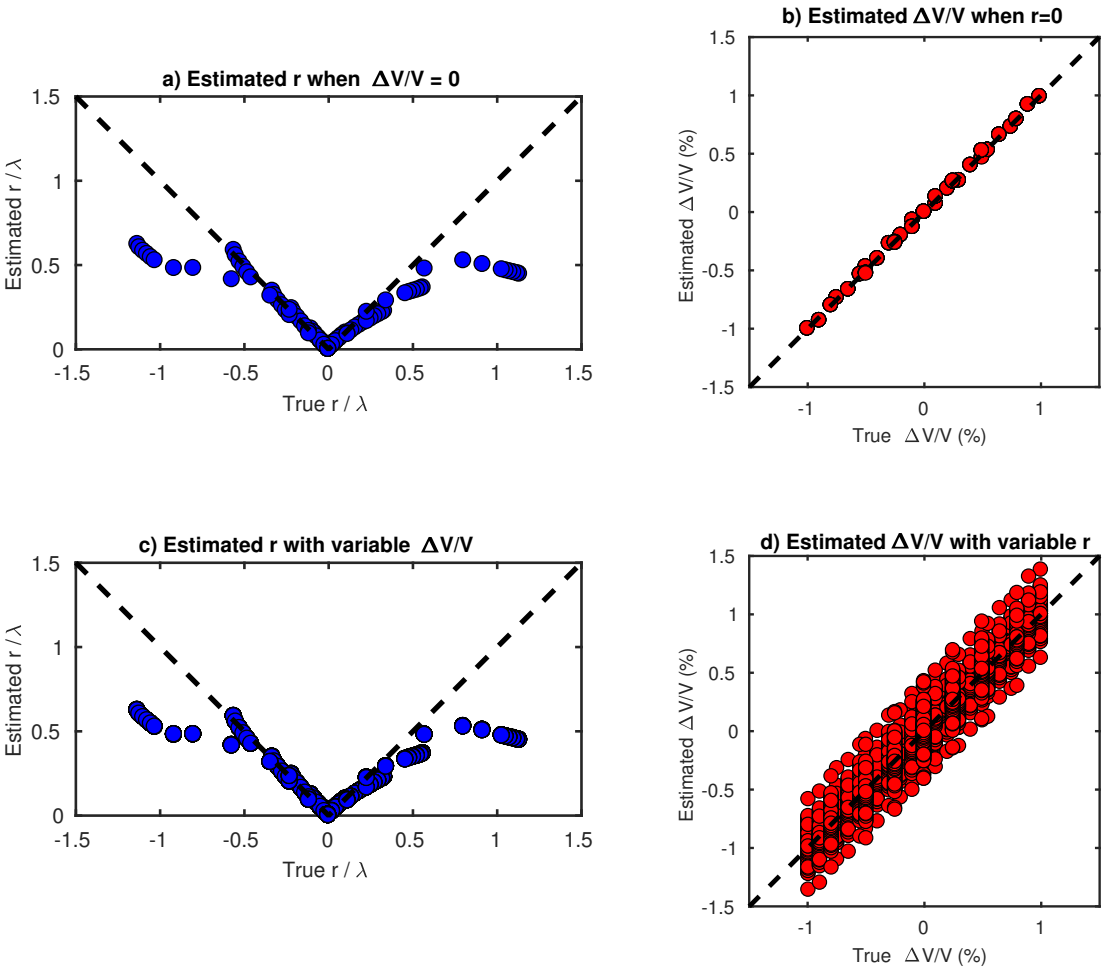

Figure 3.12: Assessing the ability of CWI to estimate velocity changes $\Delta V/V$ and inter-source separation r simultaneously in the presence of both velocity and source location perturbations. a) Estimated r when velocity is not perturbed. b) Estimated $\Delta V/V$ when the source location is not perturbed. c) Estimates of r with simultaneous velocity perturbations. d) Estimates of $\Delta V/V$ with simultaneous perturbations of source location.

taking a central source location and changing the location by up to 1.2λ and simultaneous velocity perturbations of up to 1%. Figures 3.12a and b show estimates of source separation (r) where no velocity perturbation occurs, and the reverse - changes in velocity when the source remains stationary. These represent the best possible estimates from CWI, as only one perturbation type occurs at a time. The additional errors associated with simultaneous perturbations of r and V are shown in Figures 3.12c and d. We see that estimates of source perturbation are barely affected by the presence of a velocity perturbation: the stretching method of CWI removes the effect of any velocity perturbation. However, estimates of velocity perturbation are far more sensitive to source location perturbations, giving errors of 0.5% for a source displacement of around one wavelength (a relatively large error given the accuracy otherwise expected from CWI). The additional error appears to stem from the effect of cycle skipping in the cross-correlation function when changes result in the alteration of travel times to on the order of half a wavelength.

These results also show that in the case of simultaneous perturbations of source location and velocity, source separation can be estimated much more accurately than estimates of the change in velocity. Therefore, we would expect that the 3D network of relative locations of acoustic emissions that occur during deformation can be estimated robustly using laboratory datasets even if velocity changes occur in the medium (Zhao *et al.*, 2017; Zhao and Curtis, 2019). This is demonstrated in the following section.

3.4.5 Relocating relative source locations from inter-source distance

Using the inter-source distances or separations between many pairs of sources, it is possible to find the relative locations of a cluster of sources, provided that inter-source distances are within the working range of CWI . However as we see in Figure 3.7, CWI provides a slightly biased estimate of these separations. The relocation method solves for the relative location of a cluster of sources in a probabilistic framework within which it is possible to correct this bias to a significant extent (Robinson *et al.*, 2013; Zhao *et al.*, 2017; Zhao and Curtis, 2019). For one pair of events, according to Bayes' theorem

$$P(\tilde{\delta}_t|\tilde{\delta}_{CWI}) \propto P(\tilde{\delta}_{CWI}|\tilde{\delta}_t) \times P(\tilde{\delta}_t), \tag{3.15}$$

where the posterior probability $P(\tilde{\delta}_t|\tilde{\delta}_{CWI})$ is the probability of the true separation having value $\tilde{\delta}_t$ given that the estimated separation from CWI is $\tilde{\delta}_{CWI}$. This is proportional to the likelihood $P(\tilde{\delta}_{CWI}|\tilde{\delta}_t)$ of having observed $\tilde{\delta}_{CWI}$ in the case that the true separation is $\tilde{\delta}_t$, multiplied by the prior probability $P(\tilde{\delta}_t)$ which describes any available information about event locations known prior to the location process. The likelihood function $P(\tilde{\delta}_{CWI}|\tilde{\delta}_t)$ describes the bias in separations estimated by CWI, and can be approximated by a Gaussian probability density function whose mean and standard deviation are described by empirical functions proposed by Robinson *et al.* (2011). The tilde over parameters indicates that the separation quantities are used in normalized form - they are the true values divided by the wavelength of the dominant frequency recorded in the seismogram coda.

For multiple events, Equation 3.15 holds for each event pair. The separation estimated from CWI for a cluster of events can be incorporated into a joint posterior function by multiplying the formulae for all available event pairs, assuming that they are independent of one another (Robinson *et al.*, 2013):

$$P(\boldsymbol{e}_1, \ldots, \boldsymbol{e}_n|\tilde{\delta}_{CWI}) = c\prod_{i=1}^{n} P(\boldsymbol{e}_i) \times \prod_{i=1}^{n-1}\prod_{j=i+1}^{n} P(\tilde{\delta}_{CWI,ij}|\boldsymbol{e}_i, \boldsymbol{e}_j), \tag{3.16}$$

where c is a constant, n is the number of events, $\boldsymbol{e}_i = (x_i, y_i, z_i)$ is the location of event i. Within the last term we use the locations of the ith and jth events ($\boldsymbol{e}_i$ and $\boldsymbol{e}_j$) from which we can calculate their separation $\delta_{t,ij} = ||\boldsymbol{e}_i - \boldsymbol{e}_j||_2$ (subscript 2 denotes the L-2 norm), and thus we implicitly include Equation 3.15. The most probable set of the event locations can be found where the joint posterior function attains its maximum. Therefore, the event locations can be estimated by solving an optimization problem. The optimization problem is converted to a minimization problem by taking the negative logarithm of Equation 3.16:

$$-ln[P(\boldsymbol{e}_1,\ldots,\boldsymbol{e}_n|\tilde{\delta}_{CWI})] = -ln[c] - \sum_{i=1}^{n} ln[P(\boldsymbol{e}_i)] - \sum_{i=1}^{n-1}\sum_{j=i+1}^{n} ln[P(\tilde{\delta}_{CWI,ij}|\boldsymbol{e}_i,\boldsymbol{e}_j)]. \tag{3.17}$$

A uniform prior $P(\boldsymbol{e}_i)$ is considered in this work, so the terms containing $ln[P(\boldsymbol{e}_i)]$ are constant, and the term $ln[c]$ can be ignored in the minimization problem. Thus, the objective function becomes:

$$L(\boldsymbol{e}_1,\ldots,\boldsymbol{e}_n) = -\sum_{i=1}^{n-1}\sum_{j=i+1}^{n} ln[P(\tilde{\delta})_{CWI,ij}|\boldsymbol{e}_i,\boldsymbol{e}_j)]. \tag{3.18}$$

This function can be minimized using a conjugate gradient algorithm (Press *et al.*, 1986).

We test this location method using the Tivoli Travertine model shown in Figure 3.2b, and source locations shown in Figure 3.13a, simulating a cluster of 80 acoustic emissions around a fracture plane. We divided the events into multiple sub-clusters with 20 overlapping event locations, where the maximum separations in each sub-cluster remained roughly within or just outside of the working range of CWI (approximately 0.5λ). The separation into sub-clusters can be achieved using only the pairwise separation estimates from CWI, by sorting pairs of events by estimated proximity, an optimal configuration of sub-clusters can be found so that all separation values are within 0.5λ. We therefore do not require knowledge of the true source locations for this step in the method.

For each sub-cluster, we solved for the relative event locations by minimizing Equation 3.18 using the publicly available CWI-relocation code package of Zhao and Curtis (2019), taking the CWI separation estimates as inputs. We conducted the location process five times with different randomly distributed initial event locations to ensure

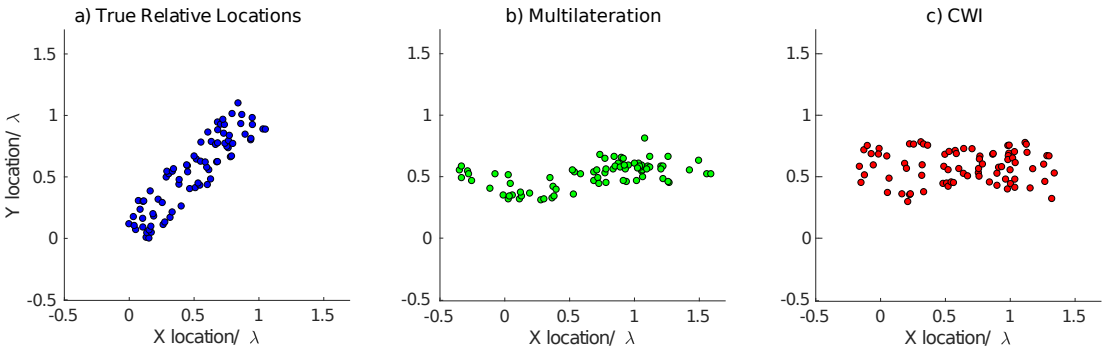

Figure 3.13: a) True locations of a cluster of acoustic emissions simulated in the Tivoli Travertine μCT slice in Figure 3.2b. b) Estimated cluster locations using the conventional method of first-break arrival times and multilateration using the receiver geometry in Figure 3.5a. c) Estimated relative locations found by implementing the CWI-based optimization algorithm described in Zhao *et al.* (2017), using the inter-source separations estimated from CWI using the same receiver geometry (note these locations have been rotated in plane to best fit the locations in panel b for fair for comparison, as the optimization provides only relative locations).

convergence to the global minimum of the objective function (Equation 3.17). The optimizations all converge to the same minimum to within trivial numerical differences. Receiver locations follow the same configuration as shown in Figure 3.5a. Since absolute event locations remain unknown in this method, we then rotate and translate the resulting sub-clusters to match locations of the overlapping sources. For comparison, we also performed the conventional method for locating sources, using manual phase-picking of first-break (first extremum) arrivals for multiple receivers, and multilateration (Equation 3.14) to estimate locations of sources. The results of multilateration and CWI relocations are shown in Figure 3.13b and c, respectively in order to cluster events.

We note immediately that the cluster of events from multilateration in Figure 3.13b is rotated by 45° relative to the true locations due to velocity heterogeneity in the sample. Since CWI only provides *relative* locations, the cluster of CWI location in panel c has been rotated to best match the results in panel b for fair comparison. The spatial area of events in panel c appears to be more rectangular (like the true shape of the area in panel a) than the area in panel b. Nevertheless, it is difficult to decide which of Figure 3.13b and c is better from these plots alone so Figure 3.14 shows the source

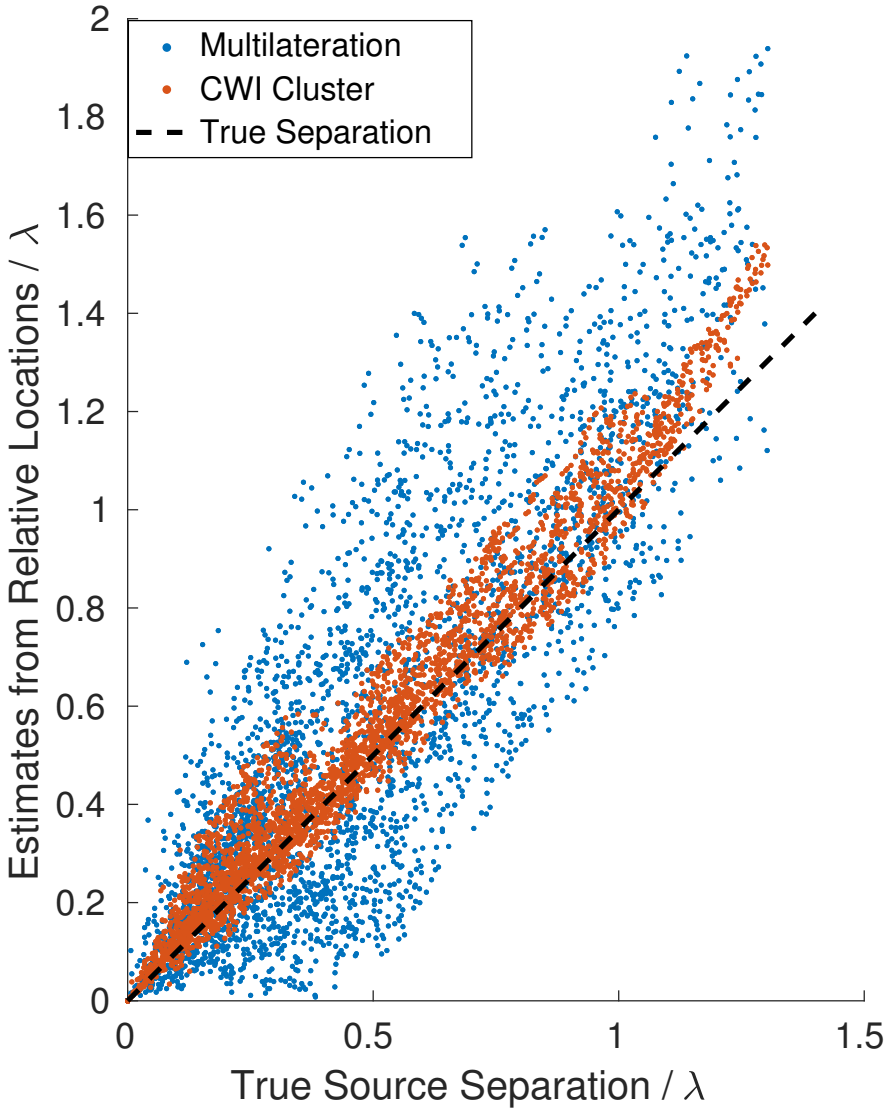

Figure 3.14: Source separation values from the estimated location clusters shown in Figures 3.13b and c, as a function of true source separation. The dashed line shows where true separation estimates would lie.

separation values of these two clusters as a function of true source separation normalized by wavelength λ. This highlights the improvement of accuracy and precision offered by the CWI source relocation procedure. It is also important to note from Figure 3.14 that using the sub-cluster matching methods, the overall source network size can extend well beyond the usual working range of CWI and the source-separation bias can be largely corrected, providing there are overlapping sources between sub-clusters.

3.4.6 Sensitivity to Noise

In order to test the ability of CWI to estimate changes in velocity and in source or receiver location when using noise-contaminated data, we generate a synthetic record of noise which is superimposed onto the numerically simulated signals used above. We generate realistic noise as follows: 1) measure a long noise record in the Edinburgh rock physics laboratory, and process it to create a record of de-meaned and de-trended seismic noise. 2) Take the Fourier Transform of the noise recording, and smooth the record in the Fourier domain to ensure there are no spectral gaps (frequency bands without noise). 3) Convolve the resulting spectrum with a sample of random Gaussian white noise so that generated noise is uncorrelated and transform back into the time domain. The resulting signal is therefore a randomly generated recording of realistic noise, which can be superimposed on the effectively noiseless waveforms generated from synthetic finite difference simulations. The signal-to-noise ratio (SNR) is calculated as $SNR = P_{signal}/P_{noise}$, where P is the average power. We add the noise at different SNR values to a range of numerically simulated signals where the velocity has been perturbed from 0 - 10% and where the source location is perturbed by 0.01λ. Estimates of the range of velocity perturbations are calculated using CWI, as well as by using conventional phase-picking methods for each level of noise contamination. For the phase-picking of first arrivals, we use automatic methods (STA/LTA method described by Earle and Shearer (1994)) as well as manually picking the time of the first extremum. These estimates are shown for low noise contamination (SNR=8) and high noise contamination (SNR=0.43) in Figure 3.15. The total error at each SNR value, calculated as the sum of residuals of each estimate to the true $\Delta V/V$ value is shown in

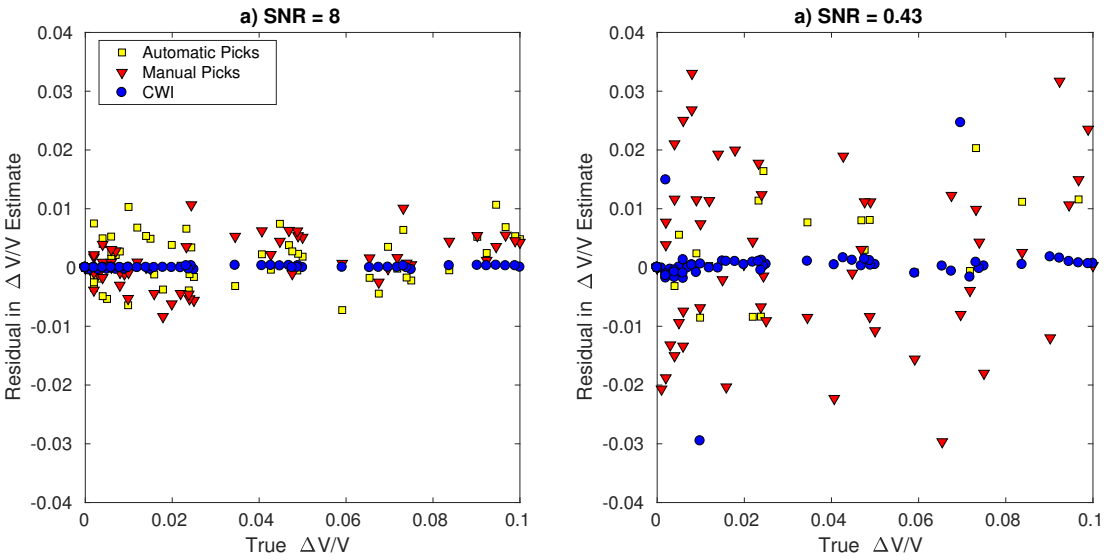

Figure 3.15: Residuals of estimated $\Delta V/V$ from Coda Wave Interferometry, and from travel times obtained by auto-picking and manual picks, estimated at a) SNR = 8 and b) SNR = 0.43 and plotted as a function of the true velocity change.

Figure 3.16a. We find that at high SNR values, all estimates for $\Delta V/V$ show a clear response to the increasing velocity perturbation, though CWI estimates are over an order of magnitude more accurate. At low SNR values, conventional methods based on phase-picking show much more scatter in the estimates of $\Delta V/V$, whereas CWI is much more precise, and is mostly unaffected by the increased contamination of noise. The first-break arrivals are of lower amplitude and are therefore more susceptible to contamination by noise, whereas CWI uses the entire signal, including many more data points, and is therefore more robust in the presence of noise.

For estimation of source separation in the presence of noise (see Figure 3.16b), the absolute locations of sources within a small cluster were estimated by multilateration by assuming a constant, isotropic P-wave velocity. However, because CWI does not provide absolute source locations but instead gives the separation between two sources, r, we estimate the separation r between pairs of absolute locations from multilateration for comparison. We compare this to the r estimate from CWI for each pair of sources, and plot the sum of individual residuals for all source pairs and for each method in Figure 3.16. We find that at all SNR values CWI outperforms multilateration,

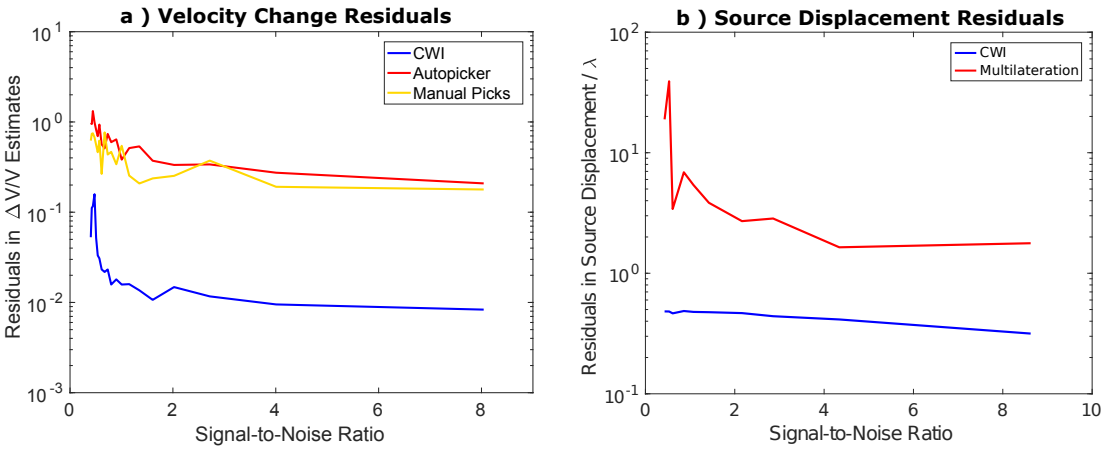

Figure 3.16: a) Residuals between true and estimated velocity change ($\Delta V/V$) as a function of signal-to-noise ratio. b) Residuals between true and estimated source displacement r/λ as a function of signal-to-noise ratio.

particularly at high levels of noise. These results show that CWI is a more robust way to characterize changes in a medium's velocity or in relative source locations in the presence of noise. Since no phase picking is necessary for CWI, this also means that less pre-processing of data is required before analysis. CWI requires the computation of many cross-correlation functions, therefore can be computationally expensive compared to conventional methods, however we have demonstrated this method to offer significant improvements in both accuracy and precision.

3.5 Individual P and S Wave Contributions to CWI Observations

The results from CWI only provide a measure of the change in velocity and not the absolute velocity itself. In itself this is not of particular concern since in many real-world problems, such as those relating to the interpretation of 4D seismic data, we seek to characterize the dynamic dependence of velocity on changes in external properties (Landrø and Stammeijer, 2004). However, ΔV/V estimates from CWI are more difficult to interpret than separate estimates of V_P and V_S that are obtainable from conventional methods. Given an estimate of density, estimates of V_P and V_S allow bulk and shear

moduli to be estimated, and these are parameters that appear in the majority of rock physics models. CWI estimates of $\Delta V/V$ reflect a combination of P-wave and S-wave velocity information due to the multiple phase conversions that occur during wave propagation.

To aid the interpretation of CWI $\Delta V/V$ estimates, consider the scattering model presented by Snieder (2002) which assumes isotropic point scatterers inside a constant velocity medium. This model represents P and S wave states as many packets of energy traveling with velocities V_P and V_S. A packet can only be in one state at a given time. When a packet of P energy travels distance a (the average distance between scatterers), it has a probability p_{PS} of converting to an S state; likewise a packet of S energy has a probability p_{SP} of converting to the P state. Over a time interval dt, a packet in the P state encounters $V_P dt/a$ scatterers, meaning that in a system with N_P and N_S packets in the P and S states, the reduction in P packets due to $P-to-S$ conversions is given by $-2p_{PS}N_P V_P dt/a$ and the increase due to $S-to-P$ conversions is given by $p_{SP}N_S V_S dt/a$. Following from this, Snieder (2002) derives the following system of differential equations:

$$\dot{N_P} = \frac{1}{a}(p_{SP}V_S N_S - 2p_{PS}V_P N_P), \tag{3.19}$$

$$\dot{N_S} = \frac{1}{a}(2p_{PS}V_P N_P - p_{SP}V_S N_S), \tag{3.20}$$

where the dot over N_P and N_S on the left side indicates a rate of change over time. Now consider a receiver not co-located with the source, at which the time of first arriving energy in the signal is comprised of only P state energy. After this time the proportions of P and S wave energy can be calculated using equations 3.19 and 3.20, and therefore so can the proportions of *changes* in P-wave velocity ($\Delta V_P/V_P$) and S-wave velocity ($\Delta V_S/V_S$). The way in which these proportions of $\Delta V/V$ vary as a function of time is shown in Figure 3.17. For time values to be independent of the scattering properties of the medium, time is normalized by the travel time of one mean free path ($\tau_P = l_P/V_P$), where the mean free path l_P is defined as $l_P = a/(2P_{PS})$. In practice, the mean free

path of a scattering medium can be estimated from the apparent attenuation of energy in recorded signals (Anugonda *et al.*, 2001; Obermann *et al.*, 2013). Figure 3.17 shows how the proportions of $\Delta V_P/V_P$ and $\Delta V_S/V_S$ change depend on the V_P/V_S ratio. At equilibrium, the proportion of $\Delta V_S/V_S$ is higher than $\Delta V_P/V_P$, even at very low V_P/V_S ratios (Figure 3.17a), explained by S having two states (S_1 and S_2, which represent the two polarizations of S waves) where P only has one state. As V_P/V_S increases, so does the proportion of $\Delta V_S/V_S$ at equilibrium, as energy in S waves are traveling more slowly than P waves and so spend more time in that state before encountering scatterers.

We can use this model to estimate the independent changes of P and S wave velocity. Define $q(t,\gamma)$ to be the relative contribution of $\Delta V_S/V_S$ (the red curves in Figure 3.17), where $\gamma = V_P/V_S$. The function q depends on time t and on the V_P/V_S ratio γ, and the relative contribution of $\Delta V_P/V_P$ (blue curves in Figure 3.17) is $1-q(t,\gamma)$. If P and S wave velocities change by different amounts, the measured change in velocity from CWI $[\Delta V/V]_{CWI}$ therefore varies as a function of time along the coda by

$$\left[\frac{\Delta V}{V}\right]_{CWI}(t) = [1-q(t,\gamma)]\left[\frac{\Delta V_P}{V_P}\right] + q(t,\gamma)\left[\frac{\Delta V_S}{V_S}\right]. \tag{3.21}$$

For a single time window, this equation has two unknown parameters, $\Delta V_P/V_P$ and $\Delta V_S/V_S$; the value of $[\Delta V/V]_{CWI}$ can be measured and $q(t,\gamma)$ is known (from Figure 3.17). Measuring $[\Delta V/V]_{CWI}$ in multiple time windows along the coda therefore gives multiple equations, the same number as there are time windows. Quantities $\Delta V_P/V_P$ and $\Delta V_S/V_S$ can be estimated using an ordinary least squares inversion approach to solve the system: $d = Am$, where d is a matrix of measured values of $[\Delta V/V]_{CWI}$ for each time window, and A is matrix of $(1-q)$ and q values expected at each time window for a given V_P/V_S ratio γ. The resulting vector m contains estimates of $\Delta V_P/V_P$ and $\Delta V_S/V_S$ for a given V_P/V_S ratio, and we denote these estimates by $[\widehat{\Delta V_P/V_P}]_\gamma$ and $[\widehat{\Delta V_S/V_S}]_\gamma$, respectively. Clearly, in order to estimate the changes of V_P and V_S independently we need to be able to estimate $\gamma = V_P/V_S$.

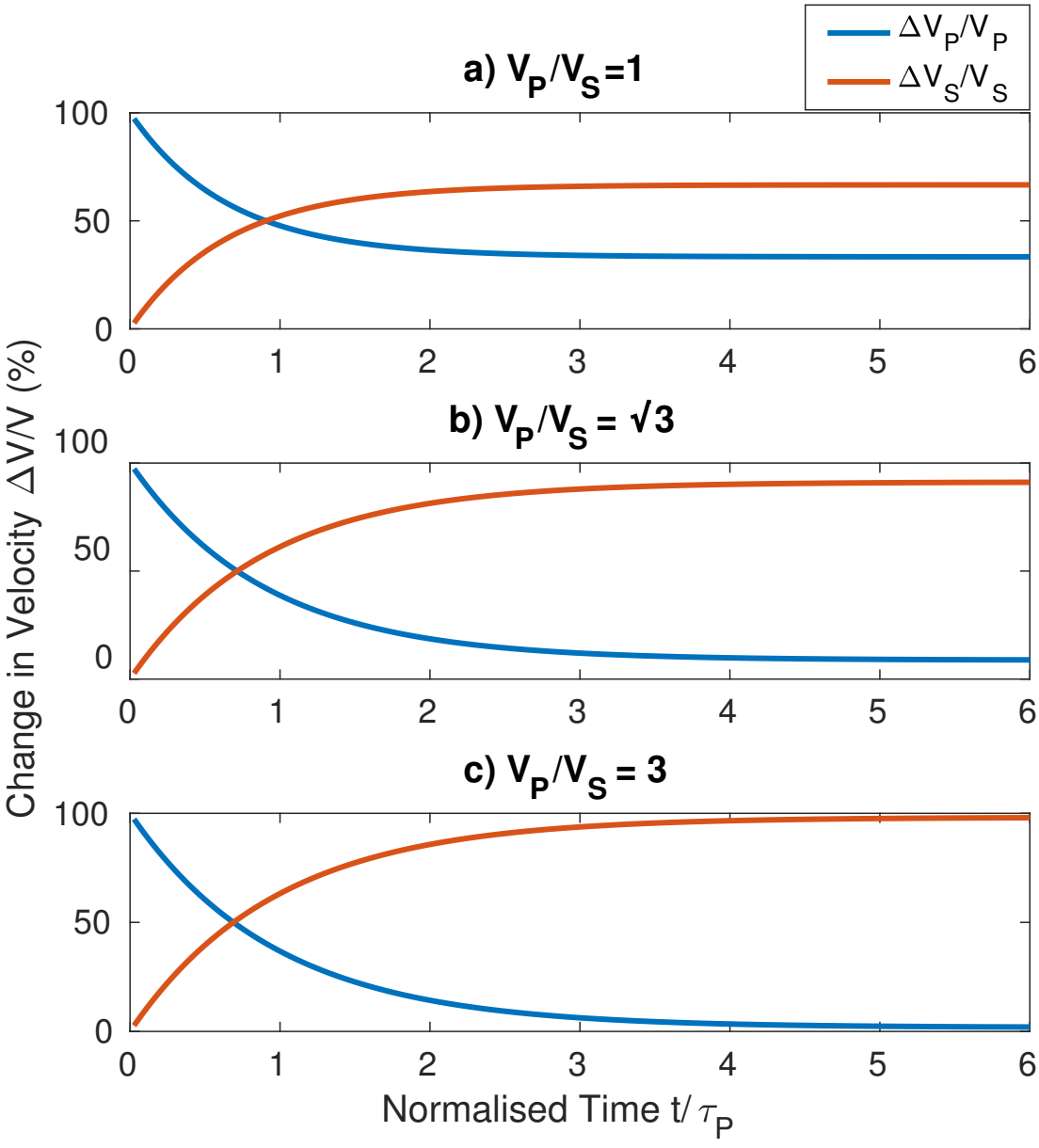

Figure 3.17: Relative proportions of changes in P-wave velocity ($\Delta V_P/V_P$) and S-wave velocity ($\Delta V_S/V_S$) which make up the change in velocity estimated from CWI ($\Delta V/V$) as a function of time along the coda, using equations 3.19 and 3.20 taken from Snieder (2002). Multiple relations are shown for media of varying V_P/V_S ratios: a) b) $V_P/V_S = 1$, b) $V_P/V_S = \sqrt{3}$, c) $V_P/V_S = 3$. Time is normalized by dividing time t by the transit time of one mean free path ($\tau_P = l_P/V_P$).

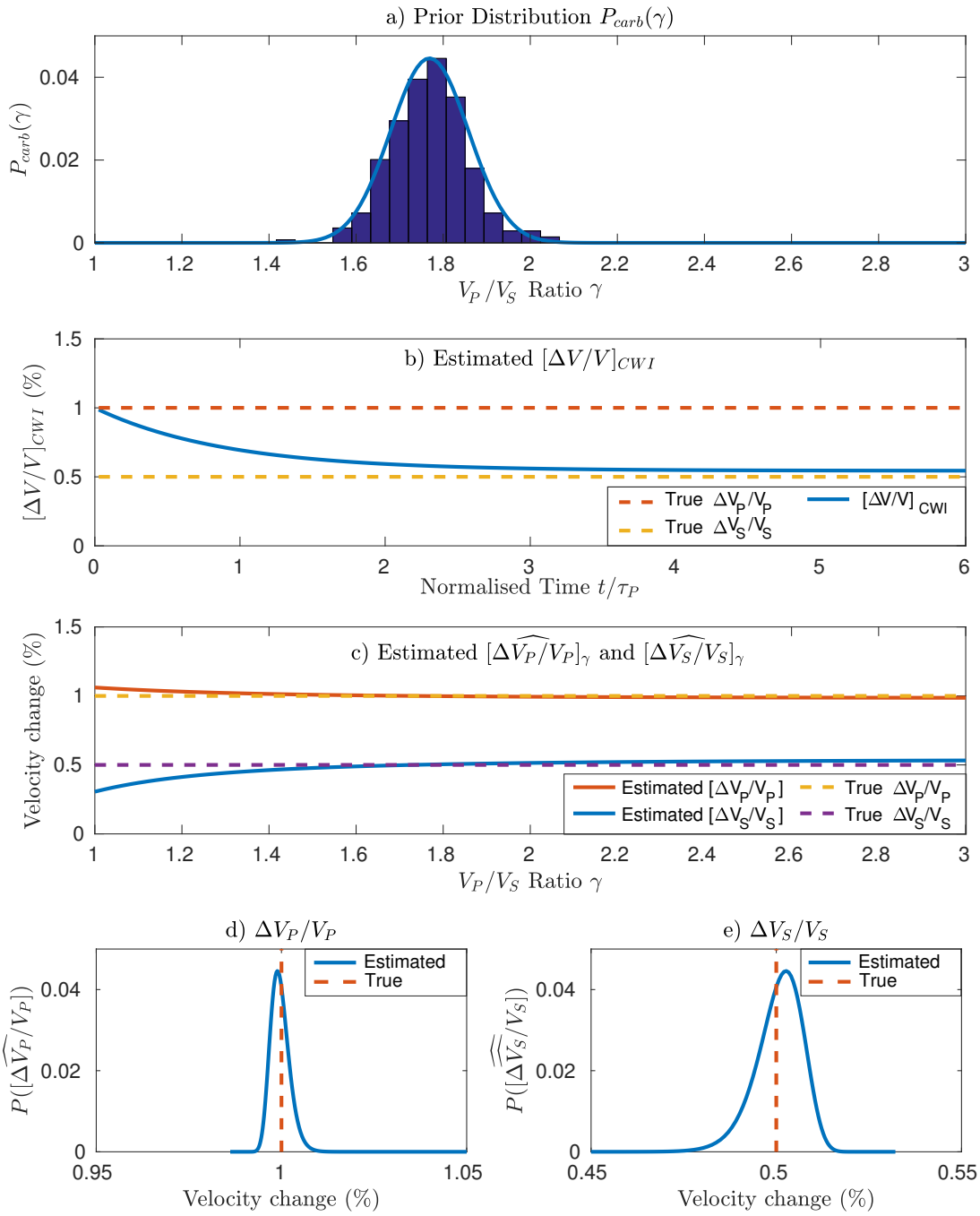

Figure 3.18: a) Prior distribution of V_P/V_S ratios from measured dry carbonate data compiled from Bakhorji (2010), Fournier *et al.* (2011) and Verwer *et al.* (2008). The curve shows the best fitting normal distribution function of the histogram. b) Synthetic $[\Delta V/V]_{CWI}$ data generated using Equation 3.21, where $\Delta V_P/V_P = 1\%$, $\Delta V_S/V_S = 0.5\%$ and $\gamma = \sqrt{3}$). c) Estimated $[\Delta\widehat{V_P/V_P}]_\gamma$ and $[\Delta\widehat{V_S/V_S}]_\gamma$ from an ordinary least squares inversion of the forward modeled $[\Delta V/V]_{CWI}$ data in panel b, as a function of the V_P/V_S ratio used in the inversion. d) and e) show the probability density functions (solid blue lines) for estimates of $\Delta V_P/V_P$ and $\Delta V_S/V_S$, where the dashed red lines represent the true changes in velocity ($\Delta V_P/V_P = 1\%$, $\Delta V_S/V_S = 0.5\%$), using samples from prior distribution in panel a and Equations 3.22 and 3.23.

One way to estimate γ would be to use the conventional experimental method to estimate V_P and V_S, but as we have shown herein, those methods are less accurate than CWI for subtle changes in the medium so it is desirable to find alternative methods. As Figure 3.17 shows, values for $q(t)$ can vary significantly depending on the V_P/V_S ratio. We can therefore refine estimates of $\Delta V_P/V_P$ and $\Delta V_S/V_S$ within a probabilistic framework, using a statistical distribution of V_P/V_S ratios rather than a single value. We illustrate this by compiling a database of 296 measured V_P/V_S ratios for dry carbonates combining data from Bakhorji (2010), Fournier *et al.* (2011) and Verwer *et al.* (2008). This data is selected purely as a demonstration of how such a distribution could be used; in practice such a distribution should be refined as the database contains samples with a large range porosities, pore structures and measurements at different confining pressures, only some of which would be relevant for our rock type or volume of interest. From the carbonate database, we create a prior distribution of V_P/V_S ratios γ for carbonate rocks $P_{carb}(\gamma)$, shown in Figure 3.18a. In order to test the method we also calculate synthetic $[\Delta V/V]_{CWI}$ data using Equation 3.21 with a change in P wave velocity of 1%, a change in S wave velocity of 0.5%, and a V_P/V_S ratio equal to $\sqrt{3}$ ($\Delta V_P/V_P = 1\%$, $\Delta V_S/V_S = 0.5\%$, $\gamma = \sqrt{3}$), which gives $[\Delta V/V]_{CWI}$ as a function of time (Figure 3.18b). The method then proceeds as follows: using the generated $[\Delta V/V]_{CWI}$ data and the known values for $q(t,\gamma)$, we invert for $[\widehat{\Delta V_P/V_P}]_\gamma$ and $[\widehat{\Delta V_S/V_S}]_\gamma$ for a range of values of V_P/V_S ratios (γ), shown in Figure 3.18c. However, given the knowledge that the sample is a carbonate, not all of these values are equally likely. We should therefore weight this set of solutions by the probability P that each V_P/V_S ratio is the one in our sample - represented by the probability distribution in Figure 3.18a. Thus we can generate probability density functions for estimates of $\Delta V_P/V_P$ and $\Delta V_S/V_S$ with the following equations:

$$P\left(\frac{\Delta V_P}{V_P}\right) = \int_{\gamma \in R_\gamma} \delta\left(\frac{\Delta V_P}{V_P} - \left[\frac{\widehat{\Delta V_P}}{V_P}\right]_\gamma\right) \cdot P_{carb}(\gamma) d\gamma, \tag{3.22}$$

$$P\left(\frac{\Delta V_S}{V_S}\right) = \int_{\gamma \in R_\gamma} \delta\left(\frac{\Delta V_S}{V_S} - \left[\frac{\widehat{\Delta V_S}}{V_S}\right]_\gamma\right) \cdot P_{carb}(\gamma) d\gamma, \tag{3.23}$$

where R_γ is the prior range of V_P/V_S ratios γ. In the case where $\Delta V_P/V_P = 1\%$ and $\Delta V_S/V_S = 0.5\%$, the resulting probability distributions for changes in P and S wave velocities are shown in Figures 3.18d and e. For both changes in P and S wave velocity, the method accurately estimates the velocity change. The probability distribution change in P wave velocity $\Delta V_P/V_P$ is relatively precise, with almost all estimates within $\pm 0.01\%$ of the true value for velocity change. The distribution of change in S wave velocity has a wider spread, though still significant precision when compared to standard methods, with the majority of estimates within $\pm 0.03\%$ of the true velocity change. From this we can see that it is possible to estimate independent changes in P and S wave velocity using CWI given the statistical distribution of V_P/V_S ratios for a rock type, and with the assumption of isotropic scattering.

3.6 Discussion

We have demonstrated that under the conditions examined here, using Coda Wave Interferometry for experimental applications can provide significant improvements over conventional methods, particularly in the accuracy and precision of estimates of changes in velocity and source location.

An important aid in the interpretation of CWI estimates is an understanding of the type of spatial average of material parameters that is implicit in CWI estimates. To examine this, a numerical experiment is conducted using the μCT derived velocity and density models of the Tivoli Travertine (Figure 3.2a). The fluid velocity (initially 1500 m/s) is perturbed by a range of values (up to a +10% perturbation), and CWI is used to estimate the velocity perturbation of the bulk medium. As the exact amount of calcite and pore fluid phases are known, as well as their properties, the change in the average properties of the medium can be calculated with various averaging methods. Here we use the Voigt upper bound M_V (Voigt, 1928):

$$M_V = \sum_{i=1}^{N} f_i M_i, \tag{3.24}$$

and the Reuss lower bound M_R (Reuss, 1929):

$$\frac{1}{M_R} = \sum_{i=1}^{N} \frac{f_i}{M_i}, \tag{3.25}$$

where f_i is the volume fraction of the ith phase and M_i is the elastic modulus of the ith phase, M can represent the bulk modulus K or the shear modulus μ. We also use the Voigt-Reuss-Hill average (Hill, 1952) $[M_V + M_R]/2$, and the Hashin-Shtrikman bounds (Hashin and Shtrikman, 1963):

$$K^{HS\pm} = K_1 + \frac{f_2}{(K_2 - K_1)^{-1} + f_1(K_1 + \frac{4}{3}\mu_1)^{-1}} \tag{3.26}$$

$$\mu^{HS\pm} = \mu_1 + \frac{f_2}{(\mu_2 - \mu_1)^{-1} + 2f_1(K_1 + 2\mu_1)/[5\mu_1(K_1 + \frac{4}{3}\mu_1)]} \tag{3.27}$$

where the subscripts 1 and 2 refer to the two phases in the medium and the upper and lower bounds are computed by interchanging which phase is termed 1 and 2 (Mavko *et al.*, 2009). The Reuss lower bound is equal to the Hashin-Shtrikman lower bound when one of the constituents is a liquid with zero shear modulus. We calculate the various averages taking the bulk and shear moduli to be $K_{calcite}$ = 129.53 GPa, $\mu_{calcite}$=35 GPa, K_{fluid} = 2.25 GPa, and μ_{fluid} = 0. A comparison of how these different measures spatially average the medium is shown in Figure 3.19. Of the different methods used, the Reuss lower bound shows the closest estimate to the measured first break velocity in Figure 3.19a, and of the CWI estimates for velocity change in Figure 3.19b.

The use of CWI estimates in current rock physics protocols is therefore possible because the appropriate information required for many rock physics models is available: the relative proportions of P and S wave velocity changes (Figure 3.18) is obtainable given

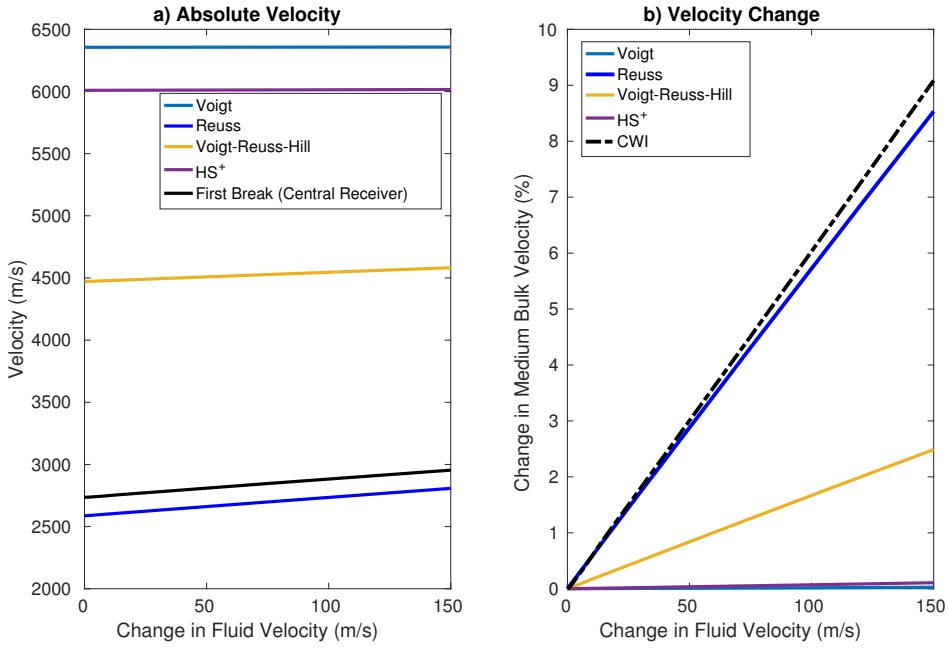

Figure 3.19: a) Calculated average velocity for the Tivoli Travertine digital rock sample following multiple perturbation of fluid velocity. The medium velocity is calculated using a range of bounding methods including the Voigt upper bound, Reuss lower bound, the Voigt-Reuss-Hill average and the Hashin-Shtrikman upper bound (HS^+), see Mavko *et al.* (2009). The velocity is also estimated using the first break method on a central receiver (black). b) The change in bulk velocity ($\Delta V/V$) as a function of fluid velocity perturbation, calculated with the multiple averages. The dotted black line is the estimate of velocity change ($\Delta V/V$) attained using CWI.

prior knowledge of V_P/V_S ratios of the medium (based for instance on rock type as in the example above), and we can infer how CWI averages the bulk velocity change properties of a medium spatially (Figure 3.19).

The method of CWI used here (Equation 3.1) is known as trace stretching and has some underlying assumptions and limitations. Namely it assumes that the velocity perturbation is uniform across the entire medium so that all arriving energy is perturbed at the same temporal rate, and therefore the trace is stretched linearly in time along the seismogram. Mikesell *et al.* (2015) provides a comparison of different methods to estimate changes in velocity for CWI, and suggests a dynamic time warping method as a solution for inhomogeneous velocity perturbations.

As we have shown, CWI is able to resolve both changes in velocity and changes in source and/or receiver locations, allowing for the estimation of relative source locations. However CWI is also able to resolve another type of perturbation on which we have not focused: the average displacement of all scatterers, δ, illustrated in Figure 3.1c (Snieder *et al.*, 2002). This value is related to the variance of travel time perturbations by

$$\sigma_\tau^2 = \frac{2\delta^2 t}{v l_\star}, \tag{3.28}$$

where $l_\star$ is the transport mean free path. It would be interesting to monitor how this parameter varies during experimental rock physics and geomechanics experiments. For example, it may be possible to monitor changes in the average distance between scattering points, which could act as a proxy measure for inter-pore distance, itself a strong control on the time of failure (Vasseur *et al.*, 2017). During the confining or varying of fluid pressure in an isotropic sample, scattering points would be displaced in all directions, and this displacement might be measured by CWI. Similar effects occur at reservoir scale where fluid injection or extraction can lead to seismically observable volumetric expansion of the reservoir. We leave this for future research.

Most of the numerical experiments presented here assume a high frequency regime as well as point sources and receivers. In one experiment where we lowered the frequency of by more than an order of magnitude we did not observe any significant differences in the method. Nevertheless, another area for the development of the CWI method is to investigate the dependence of CWI results over a broad range of frequencies, and using much larger aperture transducers such as those modelled by Li *et al.* (2018). We leave this for future research.

The work described here relates to and compliments a wide range of literature on the topic of CWI. For example, several studies suggest CWI to be an appropriate method for monitoring changes in the bulk velocity of a wide range of media (e.g., Grêt *et al.* (2006); Larose and Hall (2009); Salvermoser *et al.* (2015); Sens-Schönfelder and Wegler (2006), however the application to experimental rock physics is relatively sparse. There are also studies that describe a method for estimating inter-source distances and relative locations (Robinson *et al.*, 2013; Zhao *et al.*, 2017). Many of the previous applications of CWI assume that only one perturbation type is occurring. This paper shows the importance and possibility for combining both methods with a simultaneous estimation of both bulk velocity and source location perturbations.

There are many possible wider applications to the method presented here, outside of experimental rock physics and geoscience. As we have shown here, changes in velocity can be monitored using non-stationary sources, which allows for time-lapse monitoring without active sources. This could be of great value for monitoring areas where induced seismicity occurs, e.g., hydrocarbon extraction or CO_2 injection wells. There are also clear applications in the field of structural health monitoring, where acoustic emissions from micro-cracking can be used for monitoring the bulk properties of a material.

3.7 Conclusion

Conventional first-break methods based on manual phase-picking provide an estimate of seismic velocity that is not representative of the bulk medium in a high frequency regime

with point sources and point receivers. Such estimates of seismic velocity, changes in velocity, and source location are highly variable even for a single sample, and depend on the specific source/receiver path of the first arriving wave. They are therefore inadequate for characterizing the bulk properties of a rock sample, particularly those with complicated pore structures approximately similar size to the wavelength of the interrogating waves. By contrast, Coda Wave Interferometry is an effective method for countering these problems because coda waves sample the entire medium, and sample the same regions multiple times. CWI is shown to provide an increase in precision by an order of magnitude in the absence of noise, and to be a robust and accurate method for estimating both bulk velocity changes and perturbations of the source or receiver locations when compared with standard methods in both synthetic digital rock physics and laboratory experimental data. When noise is present, CWI remains far more accurate than conventional methods, even at very low signal-to-noise ratios. Additionally, when velocity and source/receiver location perturbations occur simultaneously CWI can still estimate velocity and source separation under some conditions: source separation estimates are mostly unaffected by the velocity perturbation, but velocity change estimates are much more sensitive and become inaccurate in the presence of larger source perturbations, possibly due to cycle-skipping. Using source separation estimates, relative locations of a cluster of sources can be estimated using a single receiver, and show higher precision and accuracy compared to conventional methods. CWI estimates a combination of changes in both P and S wave velocities, and we demonstrate a model for the equilibration of the contributions from P and S waves as a function of time, and show how the independent changes in P and S wave velocity can be measured, given probabilistic *a priori* information about the V_P/V_S ratio. Overall these results show significant potential for the use of CWI to characterize changes in porous media undergoing changes in effective stress and strain, and in temperature.

3.8 Acknowledgments

The authors would like to thank Petrobras and Shell for their sponsorship of the International Centre for Carbonate Reservoirs (ICCR), and for permission to publish this work from the 4DRP project. We are also grateful to Ian Butler, Florian Fussies, Phil Cilli, Angus Lomas, and Roseanne Clement for their helpful scientific input and comments. We also acknowledge the thoughtful and constructive reviews of Editor Douglas Schmitt and two anonymous reviewers. The MATLAB code package is available at:

`https://github.com/JonathanSingh/cwi_codes/`

The code package of Zhao and Curtis (2019) is available at:

`https://www.geos.ed.ac.uk/eip/codes.html`

Chapter 4

Unravelling coda wave interferometry: Measuring accurate changes in both P and S wave velocities

This chapter provides a more detailed description and multiple examples of the method for estimating changes in both P and S wave velocities using coda wave interferometry. In addition to this, I also demonstrate a method for estimating separate changes in fluid and solid matrix velocities. From the research questions I identified in Section 2.5, the focus of this chapter is entirely on question 3.

At the time of writing, the manuscript is in preparation for journal submission. The co-authors include Andrew Curtis and Ian Main. I acted as the lead author for this paper, and performed all of the numerical and laboratory experiments and analysis described herein.

4.1 Abstract

Measuring the seismic velocity of a medium is of great importance for many to many applications in geoscience and engineering, including rock physics experiments,

monitoring the health of concrete structures, or sub-surface fluid pressure due to hydrocarbon extraction or the injection of CO_2. Coda wave interferometry (CWI) has been used to accurately and precisely measure a change in the velocity in many of these applications. CWI uses the diffuse, multiply-scattered waves, found in the tail of the seismogram. These later arriving waves are very sensitive to small changes in a medium. Previously, CWI estimates for velocity change represent an unknown average between changes in P and S wave velocities (V_P and V_S).

Here we present a method to unravel the velocity change estimate made using CWI into independent estimates of changes in V_P and V_S individually, using CWI estimates made at multiple time windows in the coda and a scattering model for the equilibriation of P and S waves in a medium. We demonstrate the applicability of the method using a range of numerical models with increasing complexity, differing scattering properties, and a range of scales as well as in a laboratory rock physics experiment. We then derive an analytical model for the temporal equilibriation of P-to-S wave energy in a fluid saturated porous medium, and validate this model with P as S wavefield data from numerical finite-difference simulations. The model combined with many CWI estimates for velocity change at different time windows, provides accurate and precise estimates of changes in V_P and V_S. The method requires the medium to be strongly scattering, and hence is not universally applicable. For example, it fails in a westerly granite numerical model where there are few scatterers and weak impedance contrast and the accuracy of the method increases significantly when impedance contrasts are amplified for the same model geometry. For porous, fluid-saturated media, the model also allows for the inversion of changes in solid matrix velocity and fluid velocity, if the proportion of fluid in the medium is known. We demonstrate this with a random point scattering model and fluid-saturated carbonate digital rock.

These results are significant as they represent a major improvement in characterizing the evolution of subsurface properties for time lapse-monitoring.

4.2 Introduction

Accurate charecterisation of changes in the bulk seismic or acoustic velocity in a medium is important for a number of applications involving imaging and monitoring of complex porous media. Examples include estimating fluid pressure change due to fluid extraction or deformation due to stress from time lapse 4D seismic data (Guilbot and Smith, 2002; Arts *et al.*, 2004; Stork *et al.*, 2018), and laboratory rock physics (Wang, 2001; King, 1966). Coda wave interferometry (CWI) is a method for accurately and precisely measuring a *change* in velocity (Snieder *et al.*, 2002; Snieder, 2006). Specifically, CWI measures the ratio of velocity change ΔV as a fraction of the initial velocity V ($\Delta V/V$). CWI uses the diffuse, multiply scattered waves found in the tail of the seismogram after the arrival of the ballistic waves. Coda waves sample the entire medium and the same areas multiple times, therefore provide much more representative measurements of a change in bulk velocity in a medium, as well as providing an order of magnitude improvement in precision when compared to conventional methods (phase picking of first arriving waves) for measuring a bulk velocity change (Singh *et al.*, 2019).

There have been several field and laboratory applications of measuring velocity changes using CWI to date, including the monitoring of velocity changes in ice sheets (Mordret *et al.*, 2016; James *et al.*, 2017), concrete (Larose and Hall, 2009; Planès and Larose, 2013), large scale structures such as bridges (Salvermoser *et al.*, 2015), mining environments (Grêt *et al.*, 2006), volcanic regions (Sens-Schönfelder and Wegler, 2006) and associated with earthquakes (Hadziioannou *et al.*, 2011). CWI has also been used to study earthquake focal mechanisms (Robinson *et al.*, 2007), earthquake separation (Snieder and Vrijlandt, 2005; Robinson *et al.*, 2011), and relative source locations of induced micro-seismic events (Zhao *et al.*, 2017; Zhao and Curtis, 2019). There is one major limitation to the application of CWI at present: the resulting measurement of bulk velocity change is an unknown combination of changes in the P-wave (V_P) and S-wave velocity (V_S). Aki and Chouet (1975) first describe coda waves as being predominately comprised of shear waves, Snieder (2002) later uses a simple analytical model for wave scattering and conversions between P and S waves in a constant

velocity medium with uniformly distributed point scatterers, and derive the relationship between V_P/V_S ratios and the proportion of changes in V_P and V_S that contribute to the change in velocity measured by CWI at equilibrium. In a Poisson medium where $V_P = \sqrt{3}V_S$, this relationship becomes: $\Delta V/V = 0.09[\Delta V_P/V_P] + 0.91[\Delta V_S/V_S]$.

There have been several observations of the stabilization of compressional and shear energies in the coda (Margerin *et al.*, 2009), which follows a a phenomenon known as *equipartitioning* (Hennino *et al.*, 2001; Weaver, 1982, 1990). It is based on the fact that multiple scattering tends to homogenize phase space, meaning that energy ratios become time independent.

Here we use the method of Singh *et al.* (2019) for estimating the changes in P-wave and S-wave velocity independently, using CWI measurements for velocity change at multiple times along the signal, and a model for the equilibration (or equipartitioning) of P and S wave based on an extension to the model of Snieder (2002) to incorporate a fluid phase (where shear waves are not supported). We also provide a new method to separate the change in fluid velocity from the change in the solid matrix of a medium, provided an estimate of the fluid fraction, all using a single receiver. Obermann *et al.* (2013, 2016) follow a similar method, where the contributions of changes in surface and body wave velocities can be discriminated use temporal variations along the coda to localize velocity perturbations.

First, we describe the method for estimating changes in both V_P and V_S, then illustrate multiple methods for estimating the velocity change as a function of time along the signal using CWI. We then describe the analytical scattering model which provides the remaining information required for estimates of changes in both V_P and V_S. We validate the scattering model with the use of 2D elastic finite difference simulations in a range of models. We demonstrate the method for estimating the velocity change as a function of time, both numerically as well as in a laboratory rock physics experiment. Following this we estimate changes in V_P and V_S by perturbing the finite difference models, and in a second set of experiments estimate changes in matrix and pore fluid velocities. The assumptions of both CWI and the derived scattering model are that: a) the medium

exhibits strong scattering, b) scattering is isotropic, and c) scatterers are randomly distributed. We assess the performance of our method when these assumptions is contravened using a range of 2D numerical models. For the inversion of changes in P and S wave velocity we use a randomly generated point scattering medium, a digital rock based on a high resolution synchrotron x-ray microtomography volume of a Westerly granite sample and a subset of the Marmousi model. For the inversion of changes in fluid and matrix velocity we use two 2D porous models: a random point scattering model and a digital rock based on a high resolution x-ray microtomography volume of a Tivoli travertine sample (porous carbonate). In the majority of cases, our method accurately estimates changes in both P and S wave velocity, or solid matrix and pore fluid velocity changes, at least when strong scattering is occurring.

4.3 Method

We propose a method to unravel the independent changes in P and S wave velocities ($\Delta V_P/V_P$ and $\Delta V_S/V_S$) by comparing recorded signals before and after a perturbation (u_{unp} and u_{per}, respectively), at multiple times t along the signals. The perturbation of a medium's velocity cause travel-time perturbations τ of the arriving waves in recorded signal. The travel time perturbations are related to the relative velocity change $\Delta V/V$ by:

$$\frac{\tau}{t} = -\frac{\Delta V}{V}, \tag{4.1}$$

where $\Delta V/V$ is a combination of changes in both P and S wave velocities. As the proportions of P and S waves in a medium vary over time and eventually equilibriate (Snieder *et al.*, 2019), the relative proportions of changes in P and S wave velocities that contribute towards $\Delta V/V$ also vary with time t. This variation in $\Delta V/V$ as a function of time t can be expressed as:

$$\left[\frac{\Delta V}{V}\right](t) = [1 - q(t)]\left[\frac{\Delta V_P}{V_P}\right] + q(t)\left[\frac{\Delta V_S}{V_S}\right], \tag{4.2}$$

where q is the fractional proportion of the $\Delta V_S/V_S$ contribution to $\Delta V/V$ as a function of time t (thus $1-q$ is the fractional proportion of $\Delta V_P/V_P$). From Equation 4.2, $\Delta V/V$

can be measured by comparing u_{unp} and u_{per} (demonstrated in Section 4.3.1), and $q(t)$ can be estimated using an analytical model for wave scattering and equilibriation of P and S waves (described in Section 4.3.2). The remaining unknown parameters are then $\Delta V_P/V_P$ and $\Delta V_S/V_S$, which can then be estimated using an ordinary least squares inversion (described in Section 4.3.4).

4.3.1 Estimating Nonlinear Velocity Changes

Conventionally in coda wave interferometry only very late time windows are used, this is to ensure the conversions of P-to-S wave states equilibriate. Many authors have acknowledged the variation of $\Delta V/V$ estimates as a function of time along the signal (Snieder *et al.*, 2019; Mikesell *et al.*, 2015), though will only consider the late time windows that exhibit a linear relationship between travel time perturbations τ and time t, i.e., after phases are in equilibrium ($\Delta V/V$ estimates at earlier times are ignored). However, the information required to allow independent estimates of changes in P and S wave velocity lies not only in the coda, but also the first arriving waves and those is non-equilibrium (i.e., the entire waveform). Standard CWI methods are therefore not appropriate in this case.

The methods for attaining estimates of $\Delta V/V$ as a function of time along the signal can be easily adapted from CWI (the conventional methods are described in Section 4.8 and are illustrated in Figure 4.1). The commonly applied double wavelet method (Snieder *et al.*, 2002) can be extended by simply including time windows across the full signal rather than just the coda; each time window gives an independent estimate of $\Delta V/V$. The trace stretching method (Sens-Schönfelder and Wegler, 2006) is conventionally performed on much longer time windows, but still in the phase-equilibriated tail of the signal. For this method, the signals can be divided into smaller time windows, and independent stretching factors $\epsilon(t)$ calculated for each time window. This method has been shown to be more robust to noise in the data (Hadziioannou *et al.*, 2009).

A limitation to both of these methods is that they exhibit some degree of averaging of the travel time perturbation within time windows, thus not accurately characterizing

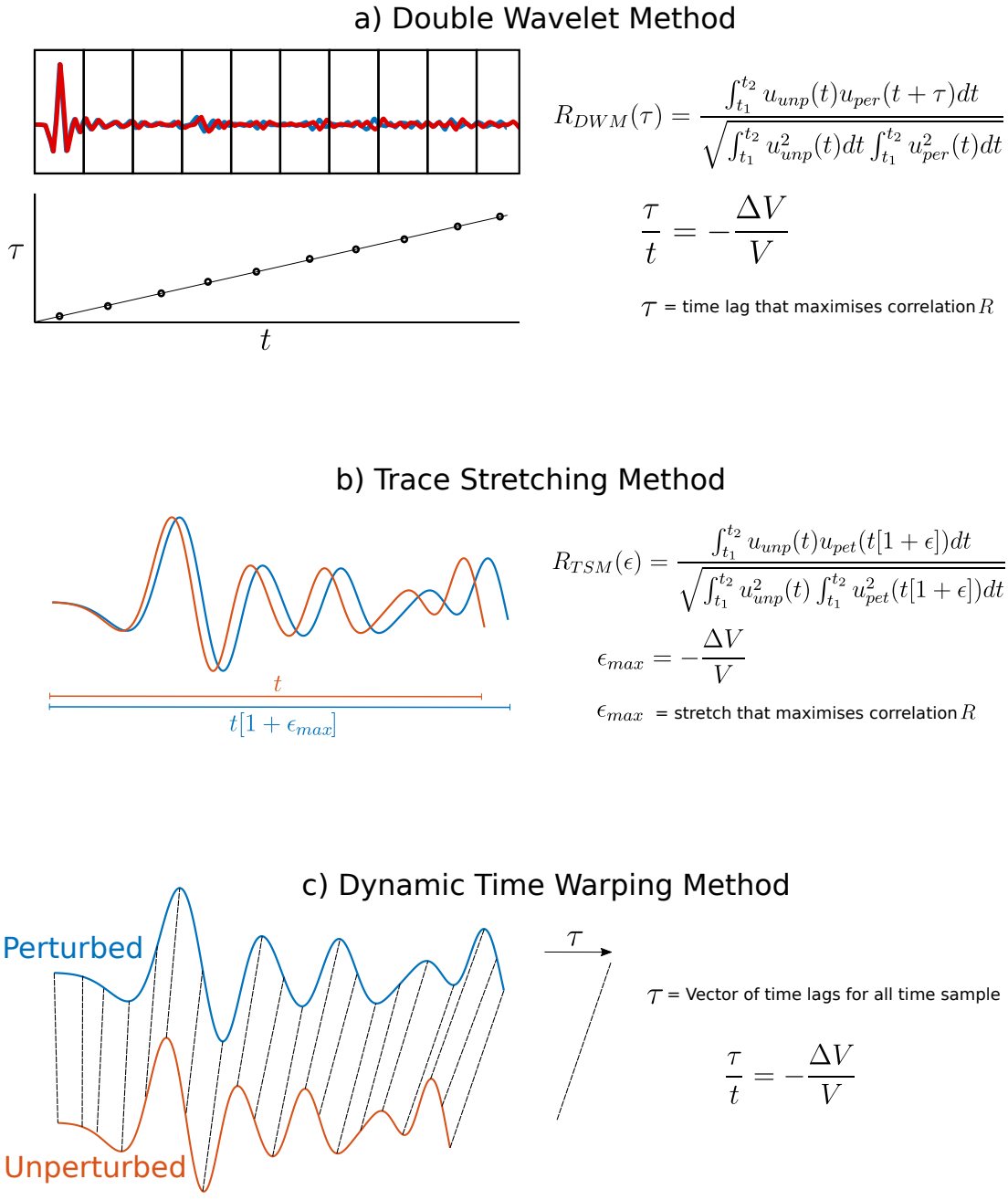

Figure 4.1: Methods for estimating a change in velocity using coda wave interferometry. a) The double wavelet method uses many time windows, finding the time lag τ for each window that maximizes correlation between the perturbed and unperturbed signals. b) The trace stretching method stretches the perturbed signal by a stretching factor ϵ, where ϵ_{max} maximizes the correlation between the stretched-perturbed and unperturbed signals. c) The dynamic time warping method applies a non-linear stretch, where a time lag τ is found for every time sample in the signal.

temporal change in $\Delta V/V$. Using a dynamic time warping algorithm (DTW) could potentially overcome this problem (Mikesell *et al.*, 2015). The method applies a nonlinear stretch of a perturbed signal to maximise similarity with the unperturbed reference signal, giving a time lag (or travel time perturbation) τ_{DTW} for every time sample in the signal. DTW is an algorithm used in time series analysis for measuring the similarity between two temporal sequences, which vary in speed (Berndt and Clifford, 1994). Mikesell *et al.* (2015) highlight the potential for DTW to be used for CWI, and compares results with the double-wavelet and trace stretching methods. Here we assume the perturbed signal $u_{per}(t)$ is equivalent to a time stretched version of the unperturbed reference signal $u_{unp}(t)$, so that

$$u_{unp}(t) \approx u_{per}(t + \tau_{DTW}), \tag{4.3}$$

where τ is a vector of time lags with a nonlinear relationship to time t. DTW estimates the vector τ_{DTW} that minimizes an error function e, which we define as the euclidean distance between u_{unp} and the time stretched perturbed signal:

$$e(t, \tau_{DTW}) = \sqrt{(u_{unp}(t) - u_{per}(t + \tau_{DTW}))^2}. \tag{4.4}$$

The next step is to accumulate these errors recursively through time, generating a distance function $d(t, \tau_{DTW})$:

$$d(t_1, \tau_{DTW}) = e(t_1, \tau_{DTW}), \tag{4.5}$$

$$d(t_1, \tau_{DTWj}) = e(t_1, \tau_{DTWj}) + min \begin{cases} d(t_{i-1}, \tau_{DTWj-1}) \\ d(t_{i-1}, \tau_{DTWj}) \\ d(t_{i-1}, \tau_{DTWj+1}) \end{cases} \tag{4.6}$$

for $i = 2, 3, \ldots, N$, where N is the number of samples in the traces and $j = 2, 3, \ldots, M - 1$, where M is the number of elements in the vector of possible time lags. The output of DTW is the warping path $w(t)$, which is set of time lags τ that both globally minimizes the error function e while satisfying the conditions: $w_1 = (1, 1)$,

$w_N = (N_{unp}, N_{per})$, and if $w_i = (a, b)$, then $w_{i-1} = (a', b')$ and where $a - a' \leq 1$ and $b - b' \leq 1$. The time lags τ_{DTW} are related to the velocity change in the same way as for the travel time perturbations τ in Equation 4.1.

Synthetic Convolutional Example

We test the double wavelet, trace stretching, and dynamic time warping methods for estimating the time-varying $\Delta V/V$ function using a pair of synthetic seismograms. We compute these signals by first convolving a randomly generated and exponentially decaying reflectively sequence with a 100 Hz ricker wavelet. The output is the unperturbed (blue) signal in Figure 4.2a. We then apply a non-linear stretch based on a P and S wave velocity perturbations of $\Delta V_P/V_P = 0.001$ and $\Delta V_S/V_S = 0.05$, and using the temporal variation of the relative contributions of each phase in Figure 4.2b. Interpolating the output signal onto the original time sampling grid used for the unperturbed signal results in the perturbed signal in Figure 4.2a. This perturbation represents the simplest case where there is no change in the signal amplitudes and no background noise is present.

The resulting estimates of $\Delta V/V$ using the double wavelet, trace stretching, and dynamic time warping methods are shown in Figure 4.2c. The trace stretching method provides the least accurate estimates of $\Delta V/V$, most likely because it requires larger time windows, and thus more averaging within each window. The assumption of linear stretching is inherent the trace stretching method. Therefore it should be avoided for estimating non-linear changes in velocity at early times in the recorded signal. The double-wavelet method provides comparatively accurate estimates, closely resembling the true $\Delta V/V$ function plotted as the dashed black line in Figure 4.2c. However due to averaging across time windows, the method fails where there are rapid temporal changes in $\Delta V/V$ ($t < 0.6$s). These times are particularly important for the estimation of $\Delta V_P/V_P$ and $\Delta V_S/V_S$. Dynamic time warping, which estimates $\Delta V/V$ for every time sample (therefore no temporal averaging), provides the greatest accuracy, almost exactly following the true $\Delta V/V$ used for computing the synthetic signals (compare dashed black line and yellow DTW filled circles in Figure 4.2c).

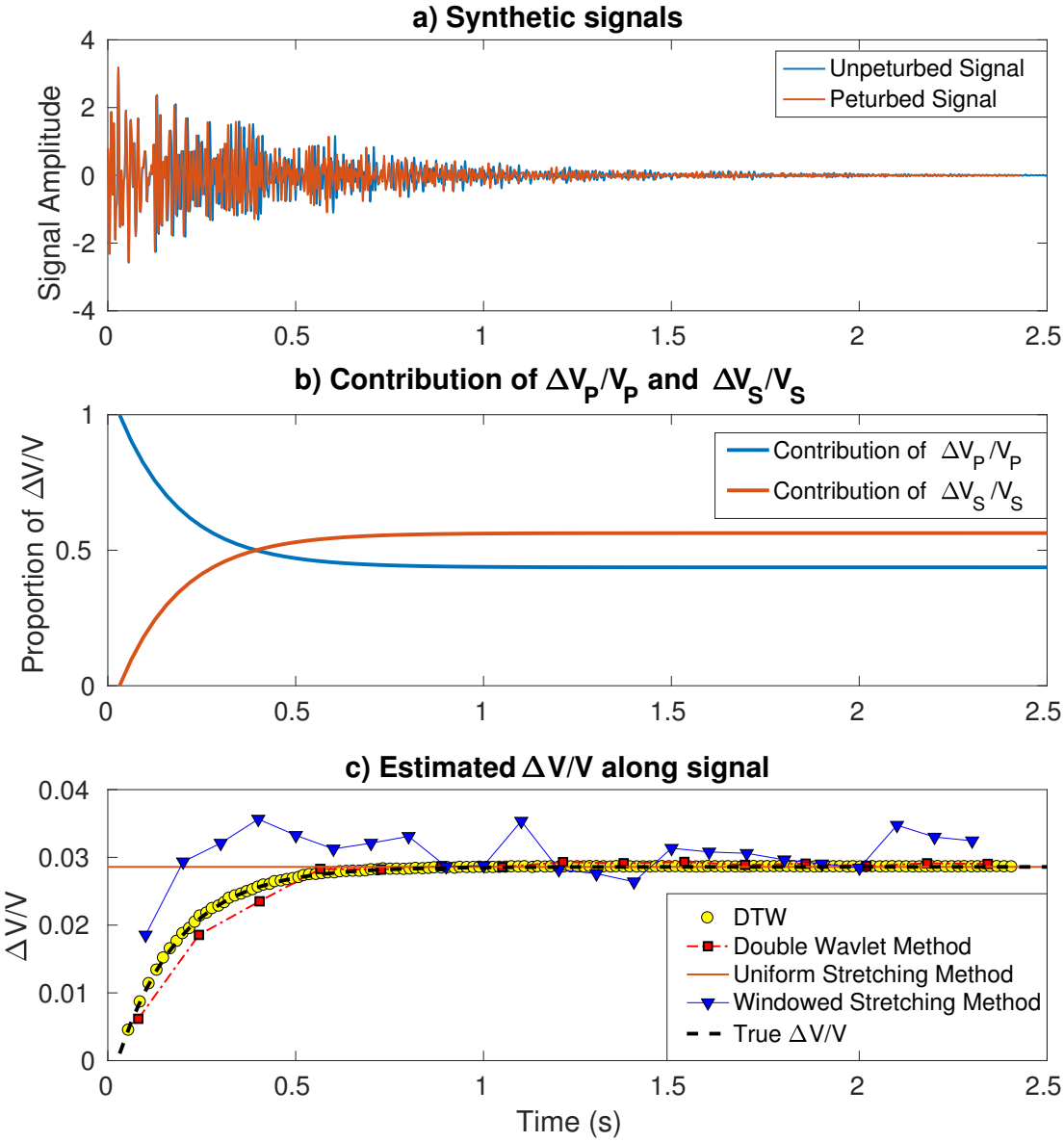

Figure 4.2: a) Unperturbed signal (blue) from the convolution of a randomly generated and exponentially decaying reflectivity series with a 100 Hz ricker wavelet. The perturbed signal (red) is the unperturbed signal following a non-linear stretch of time samples. b) The scattering model used in the generation of the perturbed signal, showing the equilibriation of proportion of P (blue) and S (red) wave velocities to the measured $\Delta V/V$. c) Comparison of methods for estimating a non-linear change in velocity, where the velocity perturbations are $\Delta V_P/V_P = 0.001$ and $\Delta V_S/V_S = 0.05$.

4.3.2 Scattering Model

The remaining required parameter in Equation 4.2 is the time-varying weighting factor q, which is the relative contribution of $\Delta V_S/V_S$ to the total $\Delta V/V$ (the contribution of $\Delta V_P/V_P$ is therefore equal to $1-q$). To estimate q we use a model for point scattering in an isotropic medium. Here we take the scattering model of Snieder (2002), who represents wave scattering and conversions as many packets of energy, either in P or S states, travelling with velocities V_P or V_S. A packet can only be in one state at a given time. When a packet of P energy travels distance a (the average distance between scatterers), it has a probability p_{PS} of converting to an S state; likewise a packet of S energy has a probability p_{SP} of converting to the P state. Over a time interval dt, a packet in the P state encounters $V_P dt/a$ scatterers, meaning that in a system with N_P and N_S packets in the P and S states, the reduction in P packets due to $P-to-S$ conversions is given by $-2p_{PS}N_P V_P dt/a$ and the increase due to $S-to-P$ conversions is given by $p_{SP}N_S V_S dt/a$. Following from this, Snieder (2002) derives the following system of differential equations:

$$\dot{N}_P = \frac{1}{a}(p_{SP}V_S N_S - 2p_{PS}V_P N_P), \tag{4.7}$$

$$\dot{N}_S = \frac{1}{a}(2p_{PS}V_P N_P - p_{SP}V_S N_S), \tag{4.8}$$

where the dot over N_P and N_S on the left side indicates a rate of change over time. Note that the factor 2 is present as there are twice as many S states, therefore should be removed in a two-dimensional medium where only one S state exists. This model assumes uniform and isotropic scattering. One major limitation to this model is the assumption that both P and S states can exist in all parts of the medium. The model therefore breaks down in the presence of fluids, which cannot support shear waves. We extend the model of Snieder (2002) to include a proportion of fluid in the medium ϕ (equivalent to the porosity in a fully saturated medium, we therefore use porosity and fluid fraction synonymously). This new model is particularly useful in laboratory rock

physics experiments, where rocks are commonly saturated with various fluids.

Consider a packet of P energy traveling through the solid matrix (P_m), when it encounters a scatterer the probability that it does not convert to an S state is equal to $1 - p_{SP}$, the remaining packets either convert to one travelling in fluid P_f, therefore the probability $p_{mf} = (1 - 2p_{SP})\phi$ or remain travelling through a solid matrix, with probability $p_{fm} = (1 - 2p_{SP})(1 - \phi)$. Using the full list of each possible conversion of energy and their associated probabilities (shown in Table 4.1) we derive the following system of differential equations:

$$\dot{N_{P_m}} = \frac{1}{a}([1-\phi]p_{SP}[N_{S_1} + N_{S_2}]V_S + [1-\phi]N_{P_f}V_P - [2p_{PS}(\phi - 2\phi p_{PS})N_{P_m}V_P]), \tag{4.9}$$

$$\dot{N_{P_f}} = \frac{1}{a}([1-2p_{PS}]\phi N_{P_m}V_P + P_{PS}\phi[N_{S_1} + N_{S_2}]V_S - [1-\phi]N_{Pf}V_P), \tag{4.10}$$

$$\dot{N_{S_1}} = \frac{1}{a}(p_{PS}N_{P_m}V_P + p_{SS}N_{S_2}V_S - p_{SP}[1-\phi]N_{S_1}V_S - p_{SP}\phi S_1 V_S), \tag{4.11}$$

$$\dot{N_{S_2}} = \frac{1}{a}(p_{PS}N_{P_m}V_P + p_{SS}N_{S_1}V_S - p_{SP}[1-\phi]N_{S_2}V_S - p_{SP}\phi S_2 V_S). \tag{4.12}$$

We assume that the proportion of energy in each state at a given time is equivalent to the proportion of the velocity change that the respective states contribute to the total velocity change measured by CWI, that is to say, for a given time:

$$[1-q] = \frac{N_P}{N_P + N_S}, \tag{4.13}$$

$$q = \frac{N_S}{N_P + N_S}, \tag{4.14}$$

where $N_P = N_{P_m} + N_{P_f}$ and $N_S = N_{S_1} + N_{S_2}$. Using this system of equations, assuming that at time $t = 0$ all energy is the the P state ($N_S = 0$), we model a range of scenarios over time. First investigating the effect of varying the V_P/V_S ratio (Figure 4.3a) and then varying the fluid fraction ϕ (Figure 4.3b). For time values to be independent of the scattering properties of the medium, time is normalized by the travel time of one

Table 4.1: Probability of each conversion type for scattering model with a fluid phase.

Conversion Type	**Probability**
P_m to P_m	$(1-\phi)(1-2P_{PS})$
P_m to P_f	$\phi(1-2P_{PS})$
P_m to S_1/S_2	P_{PS}
P_f to P_f	ϕ
P_f to P_m	$1-\phi$
S_1/S_2 to P_m	$(1-\phi)P_{SP}$
S_1/S_2 to P_f	ϕP_{SP}
S_1 to S_2/S_2 to S_1	P_{SS}
S_1 to S_1/S_2 to S_2	$1-P_{SS}-P_{SP}$

mean free path ($\tau_P = l_P/V_P$), where the mean free path l_P is defined as $l_P = a/(2P_{PS})$. In practice, the mean free path l_P can be estimated following the method of Derode *et al.* (2001), who relate the power spectrum $|\langle U(\omega\rangle|^2$ of the coherent signal $\langle u(t)\rangle$ to the scattering mean free path l_P via:

$$|\langle U(\omega\rangle|^2 = exp\bigg(-\frac{x}{l_P}\bigg), \tag{4.15}$$

where x is the distance between source and receiver locations. Examples of the application of this approach can be found in Anugonda *et al.* (2001) and Obermann *et al.* (2013).

For all combinations of V_P/V_S and ϕ the system equilibriates with a higher proportion of $\Delta V_S/V_S$ than for P wave velocity, i.e., $q > 0.5$. There are two reasons for this: S waves having twice as many possible states (S_1 and S_2), and also $V_S < V_P$ therefore encounters fewer scatterers in a given time. The latter reason also explains the large variation of q with varying V_P/V_S in Figure 4.3a, when V_P/V_S increases, the number of scatterers encountered by P waves increases relative to the number of S wave-scatterer encounters. Where porosity (fluid fraction ϕ) increases, there is a greater proportion of model for which S wave states cannot be supported, therefore q decreases (Figure

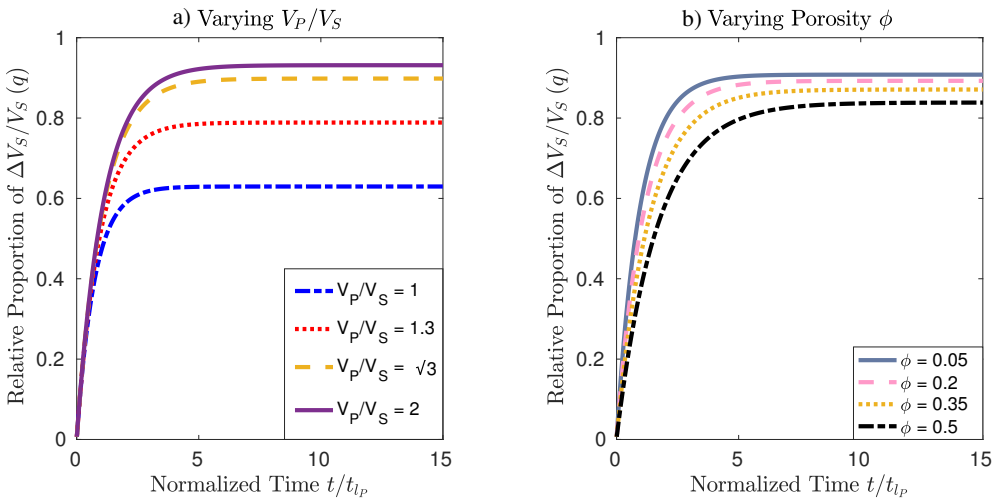

Figure 4.3: The relative proportion of $\Delta V_S/V_S$ that contributes to a CWI measurement of $\Delta V/V$ derived from the scattering model described by Equations 4.9-4.12. Showing the effect of varying a) the V_P/V_S ratio, and b) the fluid fraction (or saturated porosity).

4.3b).

4.3.3 Validation with Computed Wavefields

The scattering model described above assumes randomly distributed (uncorrelated structure) and isotropic media. In reality this is not the case. Potential uses for using CWI to monitor velocity changes are for laboratory scale rock physics experiments (where rocks exhibit correlated structures in the form of grains, pores, crystals etc.) and field scale seismic monitoring, where layering and stratification can often cause anisotropy (Alkhalifah and Tsvankin, 1995). Pacheco and Snieder (2005) show that spatial sensitivity of multiply scattered waves are not uniformly distributed, therefore the assumptions involved in the scattering model presented may not appropriate. To determine the effect of correlated structure and anisotropy on our method, we compare the predicted equilibriation of P and S waves from Equations 4.9-4.12, with the measured energy of P and S wavefields from finite difference simulations in a range of elastic media. We consider a structurally uncorrelated medium (Figures 4.4a and b) generated by inserting 2000 point velocity perturbations into a 1024×1024 grid with a 4000 m/s background velocity and 2500 kg/m^3 density. Velocity and density models for a Westerly granite sample (Figures 4.4c and d) taken from Singh *et al.*

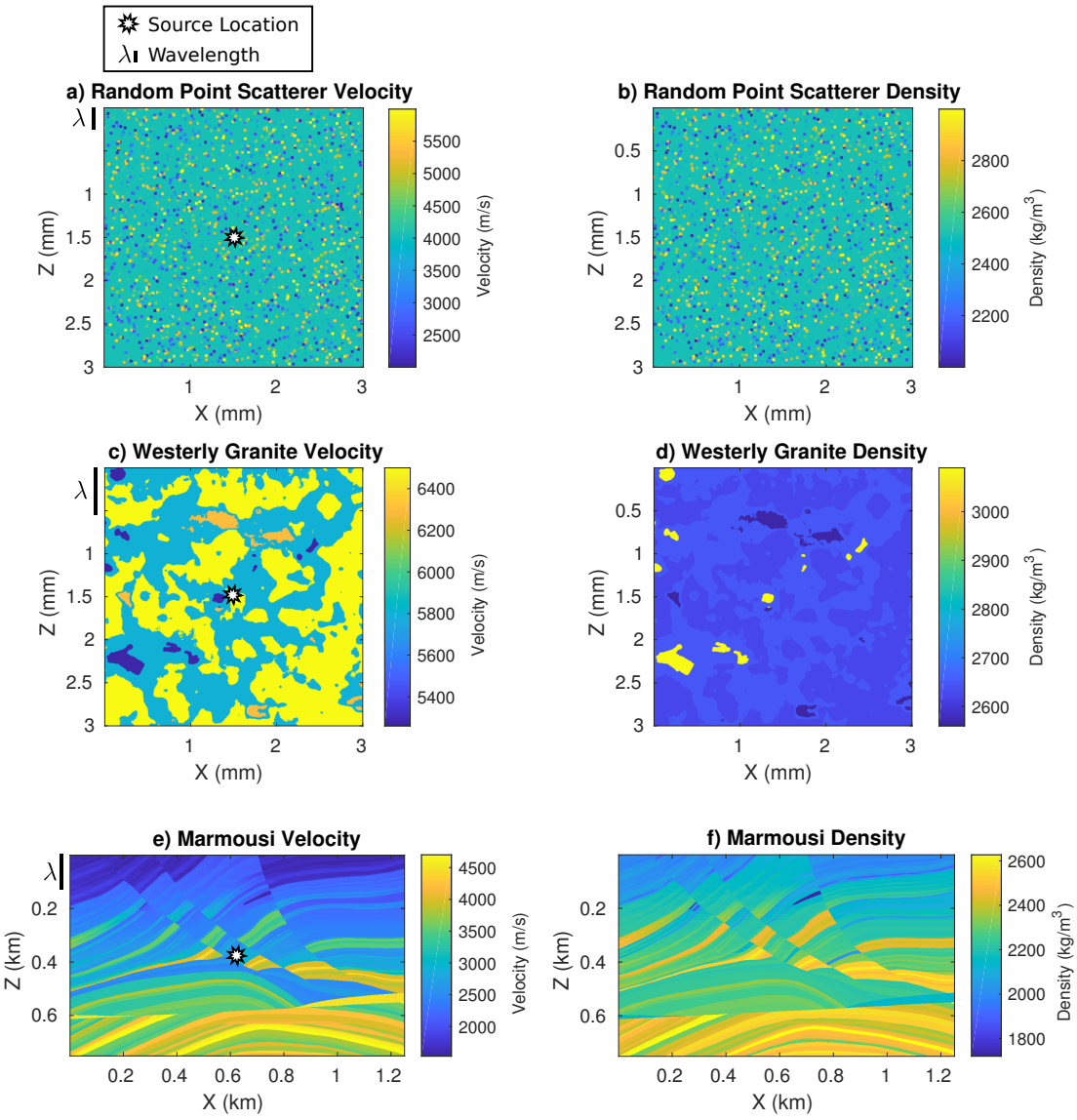

Figure 4.4: P wave velocity models (left) and density models (right) for: a-b) a randomly generated scattering model, c-d) a westerly granite digital rock, from the segmentation of a high-resolution synchrotron x-ray microtomographay volume from Singh *et al.* (2019), and e-f) a subset of the Marmousi model (Versteeg, 1994). For all models, corresponding S wave velocity models are calculated by $V_S = V_P/\sqrt{3}$. The source location for each model are shown on the left panels as a white star, and the approximate wavelength λ is labelled as a black line.

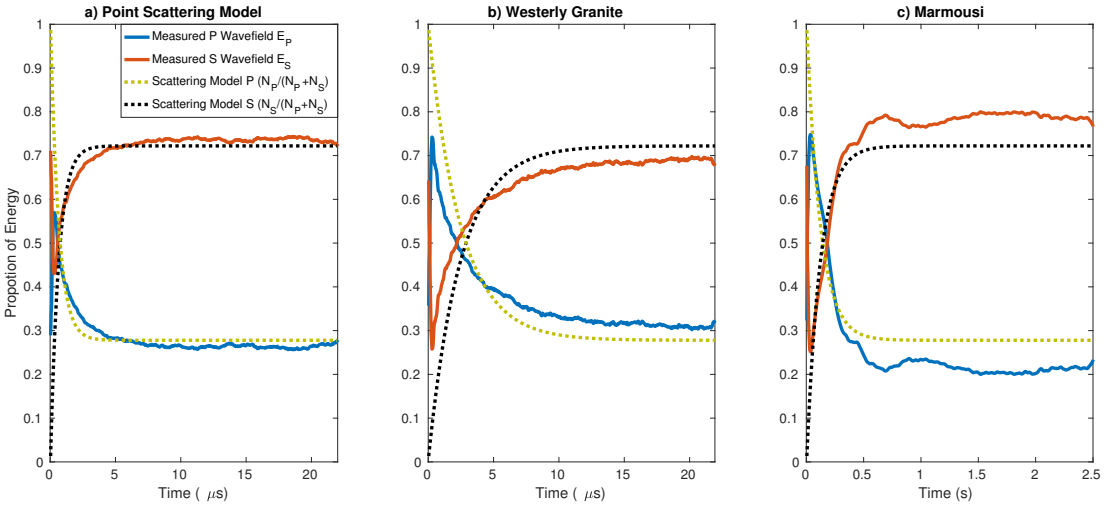

Figure 4.5: Calculated wavefield envelopes for P wave (blue) and S wave (red) phases from elastic finite difference simulations in a) the random point scattering model (Fig. 4.4a), b) Westerly Granite digital rock (Fig. 4.4b), c) a subset of the Marmousi model (Fig. 4.4c). For each figure, the predicted proportions of P and S waves using a 2D formulation of the scattering model described by Equations 4.9-4.12 and shown as dashed lines for comparison with the measured values.

(2019) are generated following the segmentation of a high-resolution synchrotron x-ray microtomography volume. Individual mineral phases are segmented, and velocity and density values for each mineral are assigned to every voxel, elastic properties from Mavko *et al.* (2009) are used for plagioclase, potassium feldspar, biotite and quartz. This model closely resembles the correlated structures of real rocks while remaining relatively isotropic. Finally we consider a subset of the Marmousi model (Figures 4.4e and f), which is often used as a standard model for a field scale demonstration, where variations in velocity and density represent different geological layers or structural units. For all models, corresponding S wave velocity models are calculated by $V_S = V_P/\sqrt{3}$, i.e., assuming a Poisson medium.

Each pixel is mapped to a regular grid of cells used as input to a two-dimensional elastic finite-difference simulation of wavefield propagation (Moczo *et al.*, 2007). We avoid instability problems caused by high-contrast discontinuities such as those between mineral phases by implementing a rotated staggered grid technique (Saenger and Bohlen, 2004). At the source locations in the centre of each model (labelled as stars in Figure 4.4), we input Ricker wavelets with a central frequencies of 10 MHz for the

random scattering and Westerly granite models and 20 Hz for the Marmousi Model (the approximate wavelengths λ are labelled as black bars in Figure 4.4). For the random scattering model and westerly granite models we use reflecting boundary conditions (to emulate laboratory core experiments) and for the Marmousi model we use absorbing boundaries.

Separate wavefields for P and S waves can be decomposed by taking the divergence and curl of the displacement vector field, respectively. The P and S wavefields ($u_P(\mathbf{x})$ and $u_S(\mathbf{x})$) are equivalent to recordings of P and S wave signals with receivers at every grid cell location $\mathbf{x}$. We then take the envelope $E(u(\mathbf{x}, t))$ for every point in the model, calculated as:

$$E_P(\mathbf{x}, s, t) = |\mathcal{H}(u_P(\mathbf{x}, s, t))|, \tag{4.16}$$

$$E_S(\mathbf{x}, s, t) = |\mathcal{H}(u_S(\mathbf{x}, s, t))|, \tag{4.17}$$

where $\mathcal{H}(f(t))$ denotes a Hilbert transform of function $f(t)$ and s is the source location. To calculate the relative proportions of P and S wavefields ($W_P(t)$ and $W_S(t)$) as a function of time t, we take the sum of each envelope for a given time and normalize by the combined sum for both P and S envelopes, that is:

$$W_P(t) = \frac{\sum_{i=1}^{N} E_P(\mathbf{x}_i, s, t)}{[\sum_{i=1}^{N} E_P(\mathbf{x}_i, s, t) + \sum_{i=1}^{N} E_S(\mathbf{x}_i, s, t)]}, \tag{4.18}$$

$$W_S(t) = \frac{\sum_{i=1}^{N} E_S(\mathbf{x}_i, s, t)}{[\sum_{i=1}^{N} E_P(\mathbf{x}_i, s, t) + \sum_{i=1}^{N} E_S(\mathbf{x}_i, s, t)]}. \tag{4.19}$$

As W_P increases to 1, (decreasing W_S), the proportion of P wave energy in the wavefield increases. W_S is the measured equivalent of q in Equations 4.13 and 4.14, and W_P is a measurement of $1 - q$. For the three models in Figure 4.4, we measure the proportions of P and S wave energy as a function of time, using source locations in the centre of each model, and calculate predicted proportions using the scattering model described by Equations 4.9-4.12 (as the simulations are in a two-dimensional medium, only one S state exists, therefore the factor 2 is removed from the scattering model equations).

We compare the measured and predicted proportions in Figure 4.5. For the point scattering model (Fig. 4.5a), the temporal rate of change as well as the final values at equilibrium are accurately charecterised by the scattering model. The westerly granite (Fig. 4.5b), exhibits a greater mismatch between modelled and measured equilibriation, in both the temporal rate of change as well as the values at equilibrium, which seems to be controlled by the difference between the proportions at the time $t = 0$ intercept. We assume $q = 0$ at $t = 0$ because the source function used in the simulations is an explosive P wave source. The estimates for the Marmousi model (which exhibits strong structural heterogeneity and anisotropy) shown in Figure 4.5c, show the rapid temporal change in phase proportions is charecterised very accurately. However there is a large variations at equilibrium and the relative proportion of S wave to P wave energy is significantly greater than that of the scattering model. We discuss the accuracy and validity of the scattering model in more detail in Section 4.5.2.

As the derived scattering model described by Equations 4.9-4.12 include a fluid fraction term ϕ, it may also be possible to predict the equilibriation of wave energy between fluid and solid matrix phases. We use two porous media models shown in Figures 4.6a and b. The first model is a randomly generated binary medium, i.e., model cells either represent quartz ($V_P = 5800$ m/s and $\rho = 2650$ kg/m^3) or pore fluid ($V_P = 1500$ m/s and $\rho = 1000$ kg/m^3), where 2000 small blocks of cells are randomly assigned to be the pore fluid phase in a background 1024×1024 constant velocity medium. The second model is a digital rock from the segmentation of a x-ray micro-tomography volume of a Tivoli travertine from Singh *et al.* (2019). Model cells are either pore fluid ($V_P = 1500$ m/s and $\rho = 1000$ kg/m^3) or calcite ($V_P = 6500$ m/s and $\rho = 2710$ kg/m^3). We use an acoustic finite difference simulation of wave propagation, with the source locations labelled on Figures 4.6a and b, and a Ricker wavelet with a central frequency equal to 1.5 MHz as the source time function.

Using the output wavefield, we measure the proportion of wave energy in the matrix

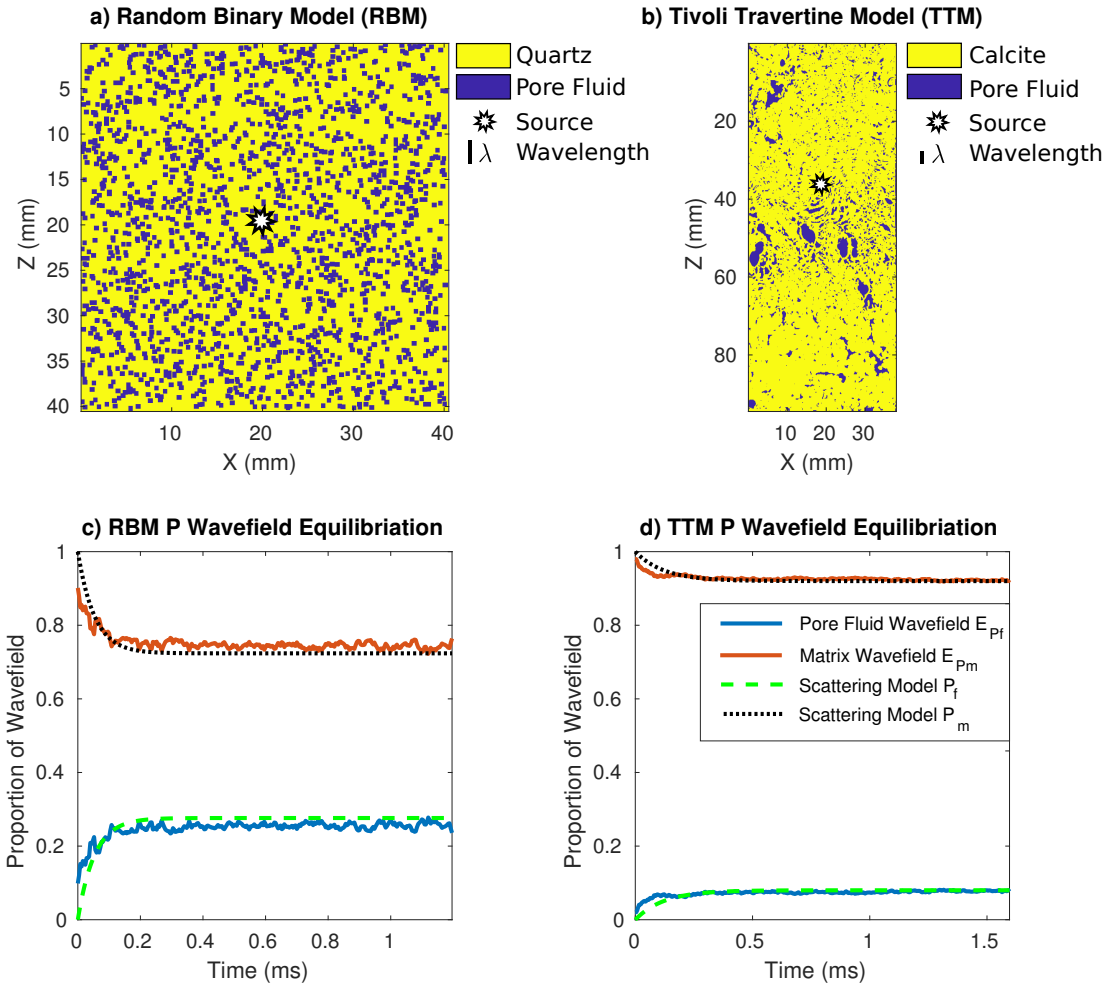

Figure 4.6: Numerical experiment for measuring the equilibraition of P waves in porous saturated media. Panel a is a model generated by adding 2000 pore fluid cells into a background quartz model. b) A digital rock from the segmentation of a x-ray micro-tomography volume of a Tivoli Travertine from Singh *et al.* (2019). The source location for each model are shown on the left panels as a white star, and the approximate wavelength λ is labelled as a black line. The lower panels compare measured proportions of wavefields in matrix (W_m) and fluid (W_f) phases from Equations 4.20 and 4.21 with predicted proportions using the scattering model described by Equations 4.9-4.12 and assuming a known porosity.

(quartz or calcite) and pore fluid phases as a function of time:

$$W_m(t) = \frac{\sum_{m=1}^{N_{matrix}} E_P(\mathbf{x}_m, s, t)}{[\sum_{m=1}^{N_{matrix}} E_P(\mathbf{x}_m, s, t) + \sum_{f=1}^{N_{fluid}} E_P(\mathbf{x}_f, s, t)]}, \tag{4.20}$$

$$W_f(t) = \frac{\sum_{f=1}^{N_{fluid}} E_P(\mathbf{x}_f, s, t)}{[\sum_{m=1}^{N_{matrix}} E_P(\mathbf{x}_m, s, t) + \sum_{f=1}^{N_{fluid}} E_P(\mathbf{x}_f, s, t)]}, \tag{4.21}$$

where x_m and x_f are model cells corresponding to matrix and fluid phases, respectively. Figures 4.6c and d compare the measured equilibriation of matrix and fluid phases with those predicted by the scattering model described by Equations 4.9-4.12, using the true porosity for each sample. Both the random binary and Tivoli travertine model results show the analytical scattering model estimations to slightly overestimate the proportion of energy in the fluid phase at equilibrium, and underestimate at early times.

4.3.4 Inversion Approach

Following the estimation of the $\Delta V/V$ as a function of time t described in Section 4.3.1 and the estimation of the equilibriation of P and S waves in a given medium q described in Section 4.3.2, there are only two remaining unknown parameters in Equation 4.2 for a given time t: $\Delta V_P/V_P$ and $\Delta V_S/V_S$, which are time independent changes in P and S wave velocities respectively. Many estimates of $\Delta V/V$ for different times gives multiple equations, the same number as there are time samples. Quantities $\Delta V_P/V_P$ and $\Delta V_S/V_S$ can then be estimated using an ordinary least squares inversion approach to solve the system:

$$d = Am, \tag{4.22}$$

where d is a matrix of measured values of $[\Delta V/V](t)$ for each time window, and A is matrix of $(1-q)$ and q values expected at each time window for a given V_P/V_S ratio γ. The resulting vector m contains estimates of $\Delta V_P/V_P$ and $\Delta V_S/V_S$ for a given V_P/V_S ratio, and we denote these estimates by $[\widehat{\Delta V_P/V_P}]_\gamma$ and $[\widehat{\Delta V_S/V_S}]_\gamma$, respectively. Clearly, in order to estimate the changes of V_P and V_S independently we need to be able to estimate $\gamma = V_P/V_S$. As CWI only provide estimates of a change in velocity, rather than the absolute velocity, estimates for γ must be made using conventional

arrival time picking methods, which are less accurate for subtle changes in the medium compared to CWI (Singh *et al.*, 2019). It is therefore desirable to take a probabilistic approach to estimate $\Delta V_P/V_P$ and $\Delta V_S/V_S$, over a range of V_P/V_S ratios. We generate a distribution $P(\gamma)$ of V_P/V_S ratios, a distribution of V_P/V_S ratios $P(\gamma)$, normally distributed around the true γ used in the finite difference models ($\gamma = \sqrt{3}$) with a standard deviation $\sigma = 0.05$ (typical error in the experimental estimation of V_P/V_S). We then generate probability density functions for estimates of $\Delta V_P/V_P$ and $\Delta V_S/V_S$ with the following equations:

$$P\left(\frac{\Delta V_P}{V_P}\right) = \int\limits_{\gamma \in R_\gamma} \delta\left(\frac{\Delta V_P}{V_P} - \left[\frac{\widehat{\Delta V_P}}{V_P}\right]_\gamma\right) \cdot P(\gamma) d\gamma, \tag{4.23}$$

$$P\left(\frac{\Delta V_S}{V_S}\right) = \int\limits_{\gamma \in R_\gamma} \delta\left(\frac{\Delta V_S}{V_S} - \left[\frac{\widehat{\Delta V_S}}{V_S}\right]_\gamma\right) \cdot P(\gamma) d\gamma, \tag{4.24}$$

where R_γ is the prior range of V_P/V_S ratios γ. In the same manner, we can estimate the change in the matrix velocity V_m independently from the fluid velocity V_f in a porous medium. In this case, A in Equation 4.22 becomes a matrix of relative proportions for fluid and matrix phases, dependent on the fraction of fluid in the medium ϕ. In the case of a fully saturated rock sample, the fluid fraction is equal to the porosity. Over the range of porosities R_ϕ, we calculate the probability density function of $\Delta V_m/V_m$ and $\Delta V_f/V_f$ with

$$P\left(\frac{\Delta V_m}{V_m}\right) = \int\limits_{\phi \in R_\phi} \delta\left(\frac{\Delta V_m}{V_m} - \left[\frac{\widehat{\Delta V_m}}{V_m}\right]_\phi\right) \cdot P(\phi) d\phi, \tag{4.25}$$

$$P\left(\frac{\Delta V_f}{V_f}\right) = \int\limits_{\phi \in R_\phi} \delta\left(\frac{\Delta V_f}{V_f} - \left[\frac{\widehat{\Delta V_f}}{V_f}\right]_\phi\right) \cdot P(\phi) d\phi. \tag{4.26}$$

We take a porosity distribution $P(\phi)$ to be normally distributed around the true porosity of each sample (random binary model $\phi_{RBM} = 0.28$ and Tivoli travertine $\phi_{TTM} = 0.11$), with a standard deviation $\sigma = 0.06$ (taken from the uncertainty analysis of porosity measurements carried out by Kharraa *et al.* (2013)).

4.4 Results

Here we present the results following the estimation of the non-linear time-varying change in velocity $\Delta V/V$ for the random scattering model (Figs. 4.4a-b) as well as a finely laminated carbonate sample in a laboratory rock physics experiment where a perturbation in velocity is applied by varying the differential stress applied to the rock.

We then present the results of two sets of inversions: one for estimating different changes in P and S wave velocity for the three numerical models in Figure 4.4, and a second experiment for estimating different changes in fluid and matrix velocity in the random binary and Tivoli travertine models (Fig. 4.6).

4.4.1 Estimated Velocity Change $\Delta V/V$ as a Function of Time from Experimental and Numerical Data

There are several methods described in Section 4.3.1, that can be used for the estimation of $\Delta V/V$. First taking the random scattering model (Figs. 4.4a-b), we simulate wave propagation before and after a perturbation where V_P and V_S are perturbed by different amounts ($\Delta V_P/V_P = 0$ and $\Delta V_S/V_S = 0.05$). Taking recorded signals from receivers co-located at the source location at the centre of each model (Figure 4.7a), we estimate the time-varying velocity change $[\Delta V/V](t)$ using the trace stretching, double wavelet and dynamic time warping CWI methods. There is no length of time windows (t_1, t_2) prescribed for the estimation of $\Delta V/V$, here we take calculate $[\Delta V/V](t)$ over a range of window lengths ranging from $t_{lP}/2$ to $5t_{lP}$ and take the mean $[\Delta V/V](t)$ across all window lengths. The resulting estimates are shown in Figures 4.7b and c. The windowed double wavelet method (Figure 4.7b) exhibits a smooth increase in $\Delta V/V$ up to around 3.4 μs. At time greater than 3.4 μs, the $\Delta V/V$ shows strong unexpected temporal variations, which we interpret as the inferred onset of the effect of cycle skipping (yellow dashed line in Fig. 4.7b). Cycle skipping is the incorrect matching of arriving waves, and is a function of the travel time perturbation τ, frequency of the signal f (or it's inverse, period T), and the length of the time windows $(t2-t1)$ used for

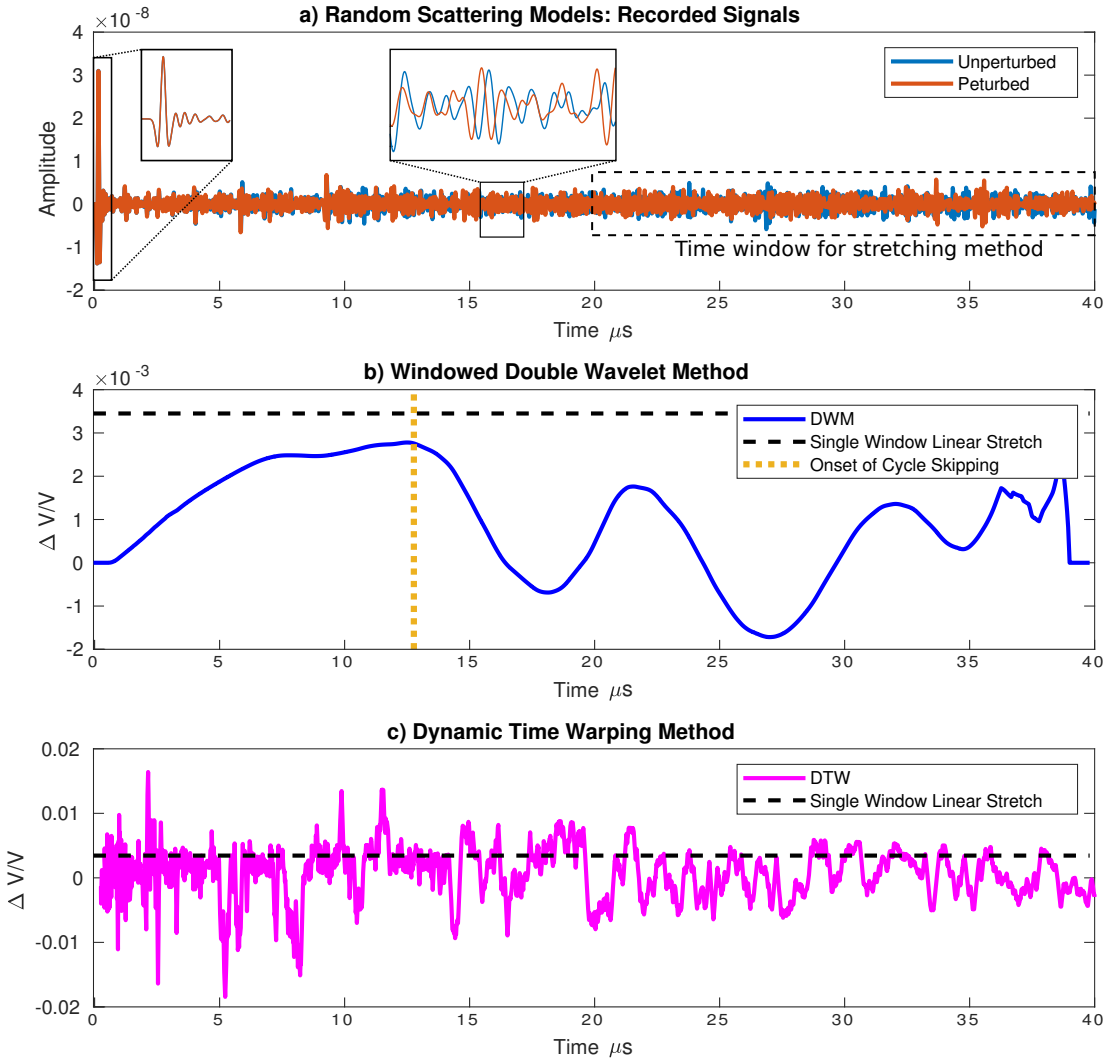

Figure 4.7: a) Example recorded signals from the Random Scattering model (Figs. 4.4a-b) before and after a velocity perturbation where P and S wave velocities are perturbed by different amounts $\Delta V_P/V_P = 0$ and $\Delta V_S/V_S = 0.005$. The dashed black box denotes the time window used for the trace stretching method. b) Estimates of the time-varying $\Delta V/V$ function using the windowed double wavelet method. The vertical green line denotes the onset of the effects of cycle-skipping where travel time perturbations become too large. c) Estimates of the time-varying $\Delta V/V$ function using the dynamic time warping method. The dashed black line in panels b and c represent the single estimate of $\Delta V/V$ using the linear stretching method.

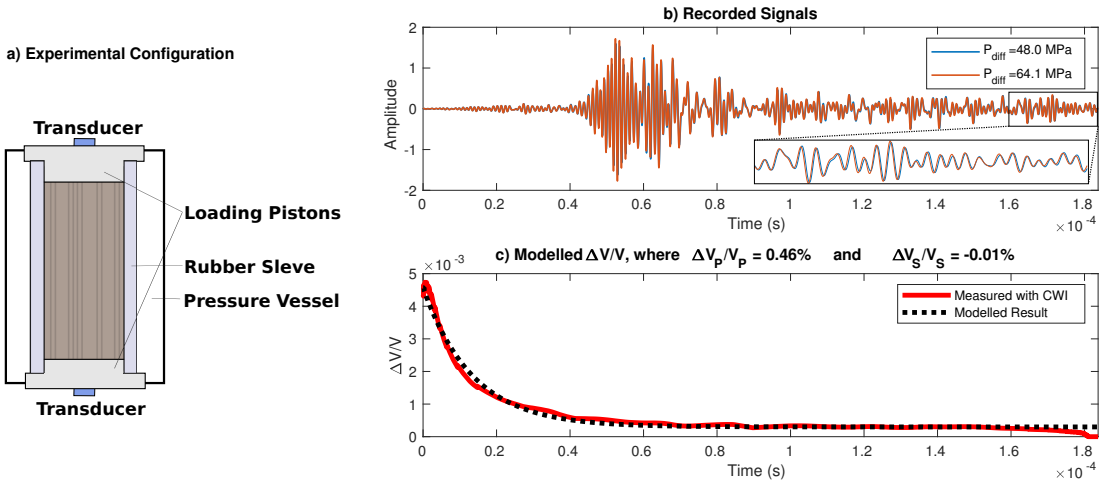

Figure 4.8: a) Experimental configuration for a triaxial rock deformation experiment, using a finely laminated carbonate sample cored parallel with sample laminations. b) Recorded signals measured at two stages of loading, where differential stress P_{diff} =48.0 MPa (blue) and 64.1 MPa (red). c) Estimated non-linear time-varying $\Delta V/V$ function (red) and the best fitting model result (black) following the inversion of $\Delta V_P/V_P$ and $\Delta V_S/V_S$.

CWI. The estimates of $\Delta V/V$ made using dynamic time warping method (Figure 4.7c) show very strong temporal variations. While this method was effective in estimating $\Delta V/V$ in the very simple example shown in Figure 4.2c, dynamic time warping appears to fail where the perturbation of the medium causes changes in the amplitude as well as arrival time of arriving waves. Therefore we only use the double wavelet and trace stretching method for the following results and discuss some areas for improvement for the dynamic time warping method in Section 4.5.1. The linear stretching method uses a much larger time window (labelled on Fig. 4.2a) and arriving waves for the perturbed and unperturbed signals are essentially matched with the stretching function, thus the method is less susceptible to cycle skipping. It is possible to combine the estimates of $\Delta V/V$ made using the double wavelet method before the onset of cycle skipping, with those made using the trace stretching method (after equilibriation).

While the two-dimensional numerical simulations performed in this study are undoubtedly useful for testing CWI, it is also important to examine the behaviour of real rock experiments. Therefore, we estimate $\Delta V/V$ following a velocity perturbation induced by varying differential stress in a laboratory experiment, illustrated in Figure 4.8a. A

36.5 mm diameter, 75 mm length core of a fine grained laminated carbonate was held at 35 MPa confining pressure, and a differential stress was applied with a strain rate of $3 \times 10^{-5}\text{s}^{-1}$. We record full waveforms using the transducer configuration shown on Figure 4.8a, at two stages of loading: differential stress P_{diff}=48.0 MPa and 64.1 MPa (recorded signals shown in Figure 4.8b). The sensors used are PZT sensitive to displacement tangential to the sensor face, with a central frequency of 700 kHz and a contact area of 20 mm^2. The amplitude of the pulse spike is 500 V with approximate signal rise time of 0.3 μs and total duration of 2.8 μs, the sampling period is 40 ns. The estimate of the time-varying $\Delta V/V$ function made using the double wavelet method is shown in Figure 4.8c and very closely resembles the best fitting forward model using the scattering model for equilibriation. The smooth transition from a high-to-low $\Delta V/V$ indicates that $\Delta V_P/V_P > \Delta V_S/V_S$, while the true values of $\Delta V_P/V_P$ and $\Delta V_S/V_S$ are not known, the close fit to the best fitting scattering model suggests our method is valid for three-dimensional real rock experiments.

4.4.2 Estimating $\Delta V_P/V_P$ and $\Delta V_S/V_S$ from Numerical Data

Taking the three models shown in Figure 4.4, as well as a version of the Westerly granite where impedance contrasts are strongly enhances (models compared in Figure 4.9), we simulate wave propagation before and after a perturbation where V_P and V_S are perturbed by different amounts ($\Delta V_P/V_P = 0$ and $\Delta V_S/V_S = 0.05$). Using the recorded signals from receivers co-located at the source location at the centre of each model, we estimate the time-varying $\Delta V/V$ function. We also estimate a single velocity change $\Delta V/V$ at late time (after equilibriation) with the trace stretching method. For the random scattering model (Fig. 4.10) and Westerly granite model (Fig. 4.11), a combination of the double wavelet and linear trace stretching methods is used as input into the inversion for $\Delta V_P/V_P$ and $\Delta V_S/V_S$ (d in Equation 4.22), using a piece-wise cubic interpolation between the $\Delta V/V$ at the onset of cycle skipping to the estimate of $\Delta V/V$ made using the trace stretching method at the centre of the time window used (shown as the blue curve in Figs. 4.10a and 4.11a). The high contrast Westerly granite model and the Marmousi model estimates exhibit smooth increases in $\Delta V/V$

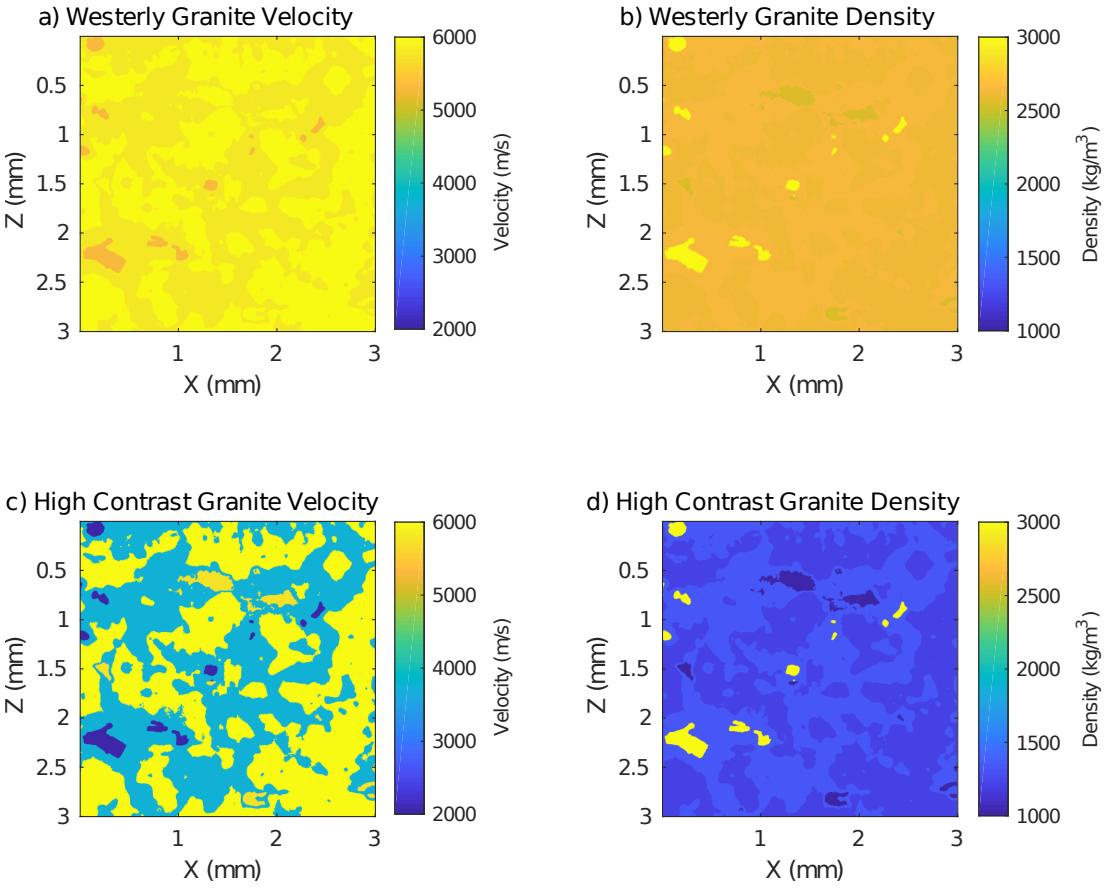

Figure 4.9: Velocity and density model comparison using realistic values for Westerly Granite (a and b) and a case where impedance contrasts are significantly stronger to increase scattering strength (c and d)

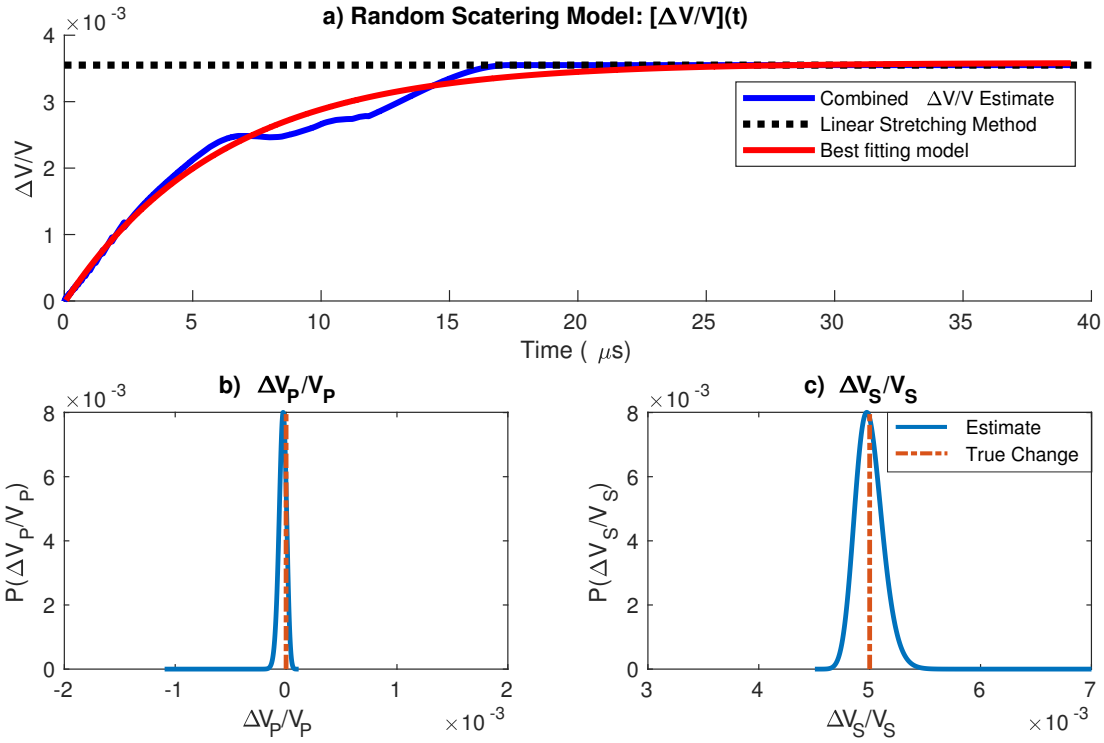

Figure 4.10: a) Estimates of velocity change $\Delta V/V$ as a function of time t following a perturbation in the random scattering model (Figs. 4.4a-b). Estimates are made using the double wavelet method (blue), as well as a single $\Delta V/V$ estimate made using the CWI stretching method (black). The solid red line shows the $\Delta V/V$ calculated by forward modelling the best fitting $\Delta V_P/V_P$ and $\Delta V_S/V_S$ values into Equation 4.2. The lower panels are the resulting $\Delta V_P/V_P$ estimates (b) and $\Delta V_S/V_S$ estimates (c), compared with the true velocity perturbations (red dashed) used as input into the finite difference simulations ($\Delta V_P/V_P = 0$ and $\Delta V_S/V_S = 0.05$).

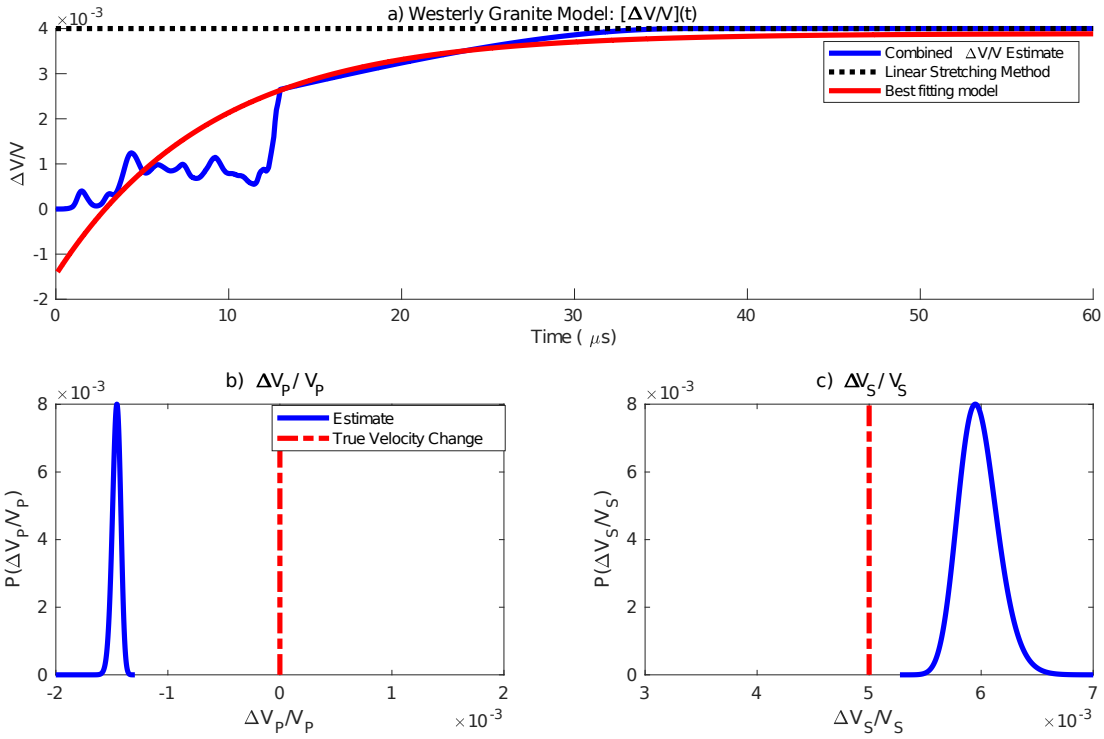

Figure 4.11: a) Estimates of velocity change $\Delta V/V$ as a function of time t following a perturbation in the Westerly granite model (Figs. 4.4c-d and 4.9a-b). Estimates are made using the double wavelet method (blue), as well as a single $\Delta V/V$ estimate made using the CWI stretching method (black). The solid red line shows the $\Delta V/V$ calculated by forward modelling the best fitting $\Delta V_P/V_P$ and $\Delta V_S/V_S$ values into Equation 4.2. The lower panels are the resulting $\Delta V_P/V_P$ estimates (b) and $\Delta V_S/V_S$ estimates (c), compared with the true velocity perturbations (red dashed) used as input into the finite difference simulations ($\Delta V_P/V_P = 0$ and $\Delta V_S/V_S = 0.05$).

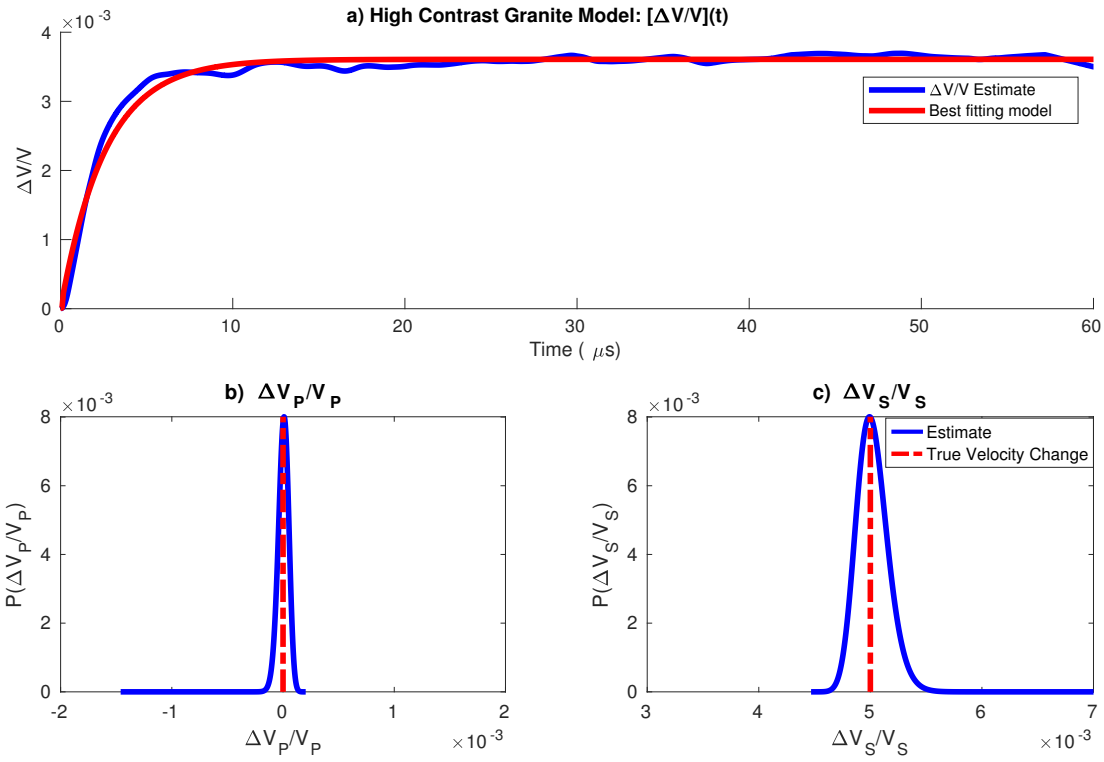

Figure 4.12: a) Estimates of velocity change $\Delta V/V$ as a function of time t following a perturbation in the Westerly granite model with exaggerated impedance contrasts to increase scattering strength (Figs. 4.9c-d). Estimates are made using the double wavelet method (blue), as well as a single $\Delta V/V$ estimate made using the CWI stretching method (black). The solid red line shows the $\Delta V/V$ calculated by forward modelling the best fitting $\Delta V_P/V_P$ and $\Delta V_S/V_S$ values into Equation 4.2. The lower panels are the resulting $\Delta V_P/V_P$ estimates (b) and $\Delta V_S/V_S$ estimates (c), compared with the true velocity perturbations (red dashed) used as input into the finite difference simulations ($\Delta V_P/V_P = 0$ and $\Delta V_S/V_S = 0.05$).

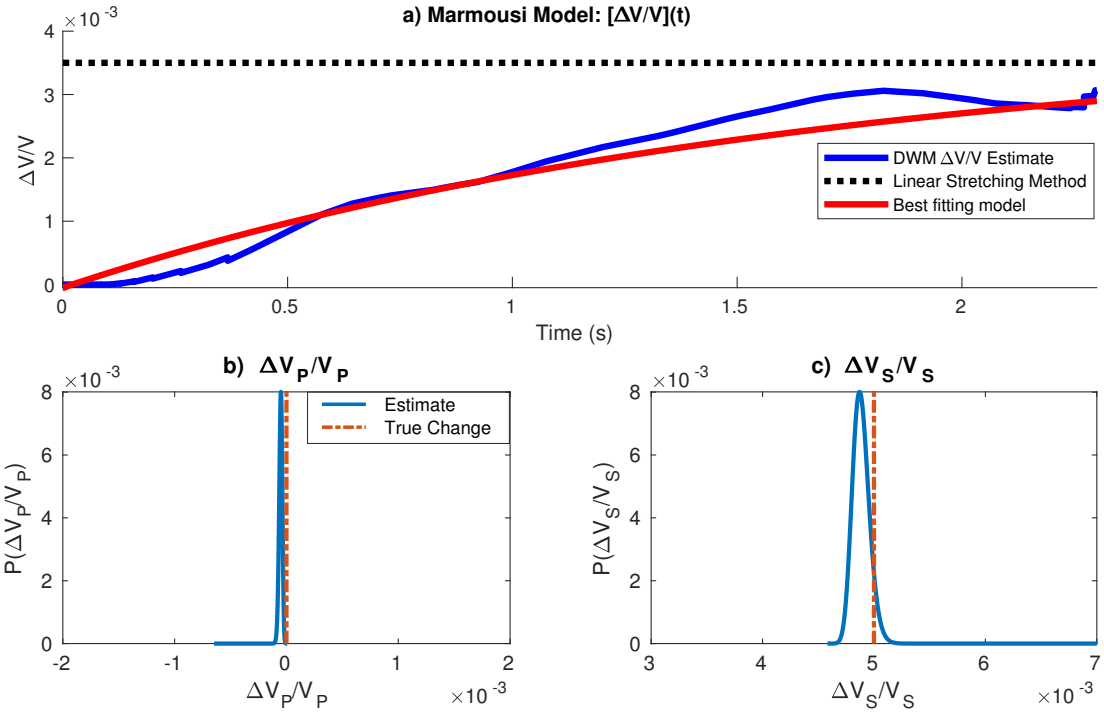

Figure 4.13: a) Estimates of velocity change $\Delta V/V$ as a function of time t following a perturbation in the Marmousi model (Figs. 4.4e-f). Estimates are made using the double wavelet method (blue), as well as a single $\Delta V/V$ estimate made using the CWI stretching method (black). The solid red line shows the $\Delta V/V$ calculated by forward modelling the best fitting $\Delta V_P/V_P$ and $\Delta V_S/V_S$ values into Equation 4.2. The lower panels are the resulting $\Delta V_P/V_P$ estimates (b) and $\Delta V_S/V_S$ estimates (c), compared with the true velocity perturbations (red dashed) used as input into the finite difference simulations ($\Delta V_P/V_P = 0$ and $\Delta V_S/V_S = 0.05$).

as a function of time (Figs. a and 4.11a), there is no strong variations in $\Delta V/V$ at later times, thus do not show any effects of cycle skipping on the double wavelet method. Therefore for the Marmousi and high contrast Westerly granite models, we only use the double wavelet method as input into the inversion (blue curve in Figs. a and 4.13a). Using the scattering model for equilibration of P-to-S waves described by Equations 4.9-4.12 as A in Equation 4.22, we invert for $\Delta V_P/V_P$ and $\Delta V_S/V_S$ over a distribution of V_P/V_S ratios $P(\gamma)$. Using such a distribution illustrates the sensitivity of estimates for $\Delta V_P/V_P$ and $\Delta V_S/V_S$ to errors in the estimate of γ. The results are shown in the lower panels of Figures 4.10, 4.11, and 4.13.

For all models, the estimates of $\Delta V_P/V_P$ are more precise (narrower probability distribution) than those for $\Delta V_S/V_S$. These estimates are more constrained by early times in the signal (where the analytical scattering model predicts the medium is dominated by P waves), which results in less variation as the V_P/V_S ratio varies. The random scattering model estimates for $\Delta V_P/V_P$ and $\Delta V_S/V_S$ (Figs. 4.10b and c) are accurate, very close to the true velocity changes used in the wave propagation simulations. We take the estimates of $\Delta V_P/V_P$ and $\Delta V_S/V_S$ at the distribution peaks, as input into Equation 4.2, forward modelling the best fitting $\Delta V/V$ (shown as a red curve in Fig. 4.10a), the CWI estimates for $\Delta V/V$ are consistent with the best fitting model, suggesting the scattering model is appropriate and the CWI method is effective in this medium. The random isotropic nature of this model follows the assumptions of the CWI method, thus the results estimates reflect the best case scenario of random and isotropic strong scattering. The estimates made for the Westerly granite model (Figs. 4.11b and c) are comparatively inaccurate compared to the high contrast Westerly granite model (Figs. 4.4.2b and c). The Westerly model contravenes the assumptions of CWI in that the number of scatterers in the medium is low, and the impedance contrasts between mineral phases are small, therefore strong scattering does not occur. This causes the double wavelet method to fail ($<13\ \mu s$ in Fig. 4.11a), and the following calculations of $\Delta V_P/V_P$ and $\Delta V_S/V_S$ are therefore inaccurate. In this medium, the forward model of the peak estimates of $\Delta V_P/V_P$ and $\Delta V_S/V_S$ (red curve in Fig. 4.11a) shows little resemblance to the estimated $\Delta V/V$ using CWI, indicating the failure

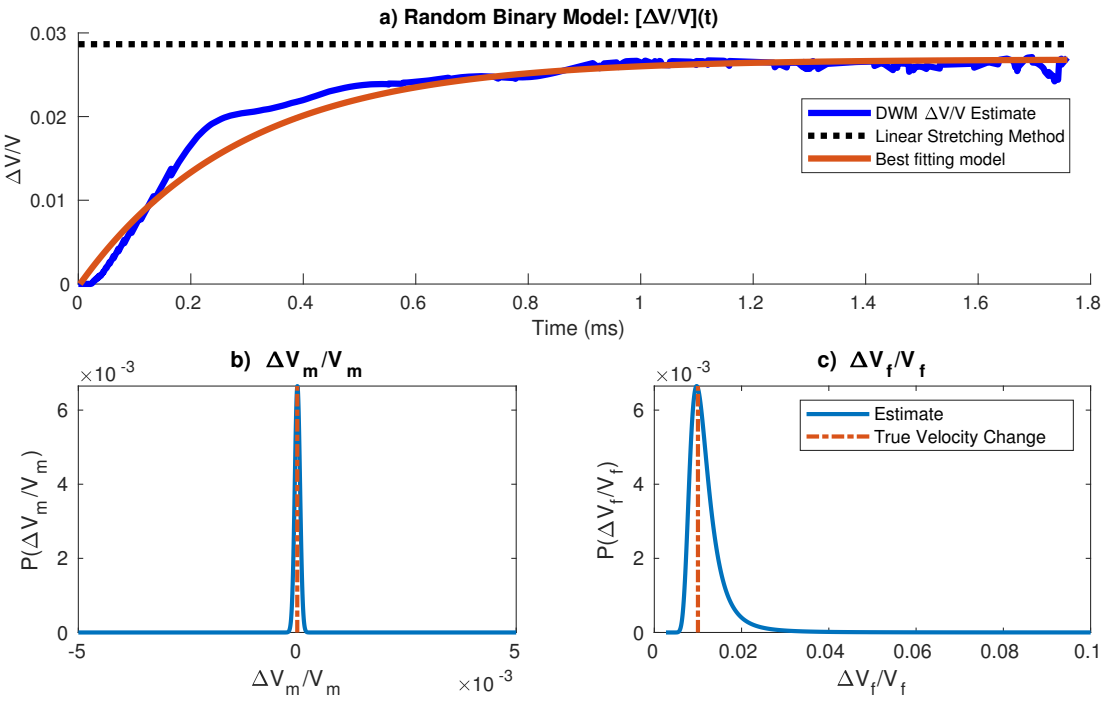

Figure 4.14: a) Estimates of velocity change $\Delta V/V$ as a function of time t for the random scattering model (Fig. 4.6a). Estimates are made using the double wavelet method (blue) as well as a single $\Delta V/V$ estimate made using the CWI stretching method (black). The solid red line shows the $\Delta V/V$ calculated by forward modelling the best fitting $\Delta V_m/V_m$ and $\Delta V_f/V_f$. The lower panels are inversion results for the estimation of the change in matrix velocity $\Delta V_m/V_m$ (b) and the change in fluid velocity $\Delta V_f/V_f$ (c) using the scattering model over a distribution of fluid fraction (blue) compared with the true velocity changes (red).

of either the scattering model, or the CWI method. Estimates for velocity change made for the Marmousi model (Figs. 4.13b and c) are accurate despite the structural heterogeneity and anisotropy in the medium. This suggests that the estimated $\Delta V_P/V_P$ and $\Delta V_S/V_S$ is not so dependent on the assumption of isotropic scattering, but rather the presence of strong scattering to allow for sufficient equilibriation.

4.4.3 Estimating a Fluid Velocity Change from Numerical Data

Here we take the two porous medium models shown in Figures 4.6a and b: the random binary model and Tivoli travertine mode, as input to a 2D acoustic finite difference simulation of wave propagation. We perturb the velocity model used in for the simulation where only the fluid phases are perturbed ($\Delta V_m/V_m = 0$ and

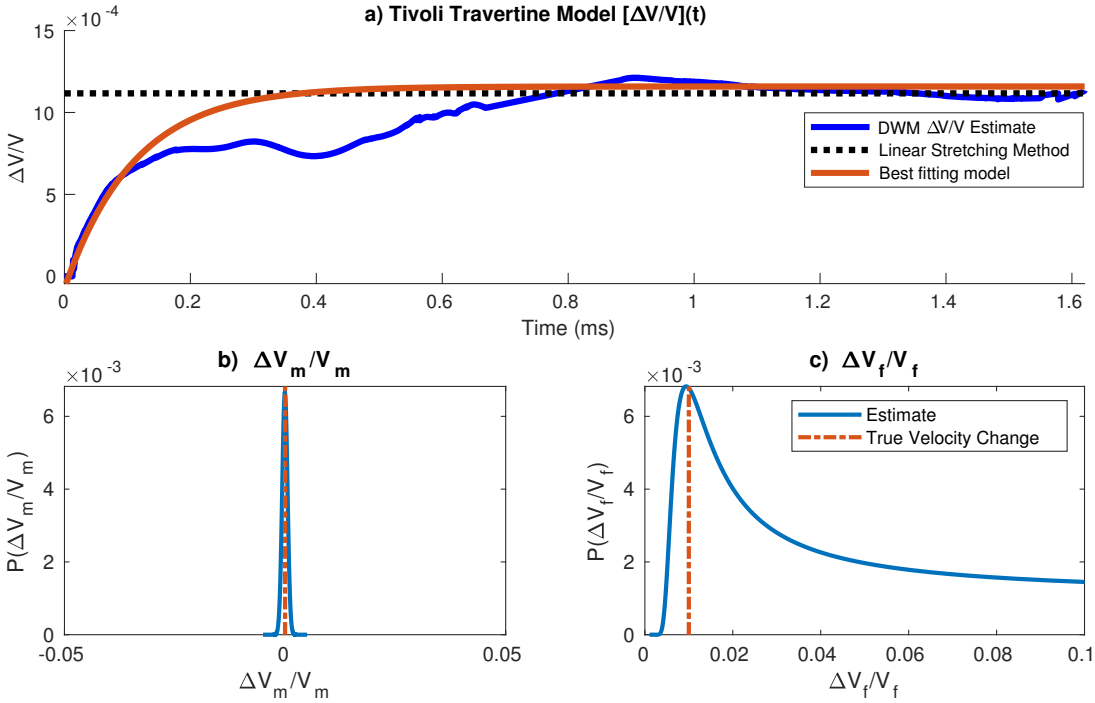

Figure 4.15: a) Estimates of velocity change $\Delta V/V$ as a function of time t for the Tivoli travertine model (Fig. 4.6b). Estimates are made using the double wavelet method (blue) as well as a single $\Delta V/V$ estimate made using the CWI stretching method (black). The solid red line shows the $\Delta V/V$ calculated by forward modelling the best fitting $\Delta V_m/V_m$ and $\Delta V_f/V_f$. The lower panels are inversion results for the estimation of the change in matrix velocity $\Delta V_m/V_m$ (b) and the change in fluid velocity $\Delta V_f/V_f$ (c) using the scattering model over a distribution of fluid fraction (blue) compared with the true velocity changes (red).

$\Delta V_f/V_f = 0.01$). Taking the recorded signals from the same source and receiver locations for the perturbed and unperturbed media, we estimate $\Delta V/V$ as a function of time t using the double wavelet and linear trace stretching methods, shown in Figures 4.14a and 4.15a. The estimates of $\Delta V/V$ using the double wavelet method exhibit an increase to a constant value at late times, with no strong temporal variations, thus do not show the effects of cycle skipping. The results are in good agreement with the predicted equilibriation from the scattering model. We therefore use only the estimates of the double wavelet method as input to the inversion for changes in matrix velocity $\Delta V_m/V_m$ and fluid velocity $\Delta V_f/V_f$.

We invert for the velocity changes following Equations 4.25 and 4.26, using the analytical scattering model for equilibration between solid and fluid phases (Equations 4.9-4.12), and over distribution of fluid fractions $P(\phi)$. The resulting distribution of estimates for $\Delta V_m/V_m$ and $\Delta V_f/V_f$ are shown in the lower panels of Figures 4.14 and 4.15. The estimates for $\Delta V_m/V_m$ and $\Delta V_f/V_f$ in the random binary model (Figs. 4.14b and c) are both accurate and precise. We take the estimates of $\Delta V_m/V_m$ and $\Delta V_f/V_f$ at the distribution peaks and forward modelling using the analytical scattering model to calculate $\Delta V/V$ as a function of time (red curve in Fig. 4.14a). This closely resembles the $\Delta V/V$ measured by the CWI double wavelet method. The random binary model contains very little/no correlated structure, therefore is close to the assumption of the scattering model (Section 4.3.2), namely that the medium consists of randomly distributed point scatterers.

The Tivoli travertine model exhibits much more correlation of structures (there is variation between densely cemented regions and highly porous regions in Fig. 4.6b). As the medium moves away from idealised random point scatterers, the analytical scattering model becomes less appropriate. The distribution of velocity change estimates in the Tivoli travertine model (Figs. 4.15b and c) remain accurate despite the deviation from uncorrelated structure. However, there is a loss in precision of $\Delta V_f/V_f$ estimates, which is due to the porosity distribution $P(\phi)$ extending to a zero porosity case ($\phi = 0$). As ϕ decreases, the $\Delta V_f/V_f$ required to account for the measured $\Delta V/V$

increases, when $\phi = 0$, $\Delta V_f/V_f$ becomes infinite. Therefore this approach leads to a loss in precision at very low porosities. The best fitting forward model shows close resemblance to the $\Delta V/V$ measured by the CWI double wavelet method at early times and late times (after equilibrium), though fits poorly between 0.1-0.8 ms, most likely due to the non-uniform nature of the medium. Generally these results highlight the strong potential for this method to be used in core scale experiments, at least in the case where strong scattering occurs.

4.5 Discussion

We have demonstrated an extension of coda wave interferometry, which is capable of resolving very small changes in a medium to a far greater degree of accuracy and precision, so that changes in both P and S wave velocities can be measured independently. This greatly improves the applicability and relevance to many real world problems laboratory and field scale problems. There are however several limitations and areas for future research to be considered.

4.5.1 Limitations to the estimation of $\Delta V/V$ as a function of time

The method presented here consists of multiple stages. The first is the estimation of a non-linear velocity change as a function of time along the entire signal. Singh *et al.* (2019) show that the first arriving waves, which only sample along a specific (fastest source-to-receiver) path, are generally less representative of the changes in a medium compared to measurements using coda waves. The method presented here includes these early arriving waves, which take very simple paths, therefore we cannot expect the same precision and accuracy offered by conventional CWI. However, the new ability to separate velocity changes into independent changes in V_P and V_S may be worth this loss in accuracy and precision. We use the double wavelet method for estimating $\Delta V/V$ at multiple time windows along the signals, which introduces errors associated with the averaging of temporal variations within the time windows. We initially suggest dynamic time warping to be an appropriate method, as an estimate of $\Delta V/V$ is made for every

time sample in the signal, however when used on more realistic data we see very strong temporal variations. This is due to two effects: the presence of cycle-skipping and the variation of signal amplitudes following a perturbation in velocity. Both of these effects can contaminate the results. To improve results, a combination of methods and a limit on the possible time lags allowed in the dynamic time warping algorithm, such as those applied by (Hale, 2013), would better constrain the estimates of velocity change. We leave this for future research. Another major limitation we identify is the dependence on the strength of scattering. By comparing the Westerly granite sample with the high contrast version of the Westerly granite, we see that weak impedance contrasts leads to the absence of strong scattering, contravening the assumptions of CWI, thus the methods presented here fail in this case.

4.5.2 Limitations to the scattering model for equilibriation

The second part to the method presented here is the estimation of equilibriation of P-to-S waves in the medium. Figures 4.5 and 4.6 compare the equilibraition of P-to-S waves and solid matrix to pore fluids, measured from wavefield intensities, and estimated using the scattering model described in Section 4.3.2. There are several differences between the measured and predicted equilibriation. A major difference is the clear mismatch between predicted and measured proportions of P and S waves at early times, which is particularly visible in for the westerly granite (Fig. 4.5b). The wavefield intensities suggest a much higher than expected proportion of S waves shortly after $t = 0$, this could be non-random distribution of scatterers in the medium (in the case of the Westerly granite model, scatterers are mineral phase boundaries). If source and receiver locations are in areas of locally concentrated scatterers, we expect more scattering, therefore more phase conversion, in a given time. Therefore we expect this effect to vary depending on source and receiver configuration. Another difference between predicted and measured equilibration is the mismatch between P and S wave proportions after equilibrium is reached. This effect most clearly visible in the Marmousi model (Fig. 4.5b). It is not clear where the inaccuracy in the scattering model stems from, the model for the simplest case of the random scattering model generates accurate results

(Fig. 4.5a). This suggest errors are a function of the incorrect assumption of isotropic and randomly distributed scatterers, however the following inversion remains accurate.

The inversion approach used here assumes the correct estimation of the scattering mean free path l_P, describing the degree of scattering in the medium (therefore the time required for the system to reach equilibrium). While our current inversion implementation requires a correct estimate of l_P, a joint inversion for l_P, $\Delta V_P/V_P$ and $\Delta V_S/V_S$, could also be implemented, providing the signal length is long enough for proportion of P and S waves to reach equilibrium.

In all the inversion examples presented here for the numerical data, we use two dimensional finite difference simulations, where wave propagation is confined to a single plane, and only one possible S wave state can exist. In reality waves propagate in three dimensions, so we expect stronger scattering, and greater difference between P and S waves at equilibrium. Therefore we expect the coda wave interferometry method to perform better than in the 2D models tested here. This is supported by the smooth curve exhibited by the estimation of $\Delta V/V$ in Figure 4.8 for the laboratory experiment using a laminated carbonate sample.

4.5.3 Relation to other studies and wider applications

There are strong similarities with the method presented here and that of Obermann *et al.* (2013, 2016), who charecterise the time-dependent relationship between measurements from the coda and the contributions of both surface and bulk (body) waves, allowing the depth localization of a velocity perturbation. They formulate the modelled relative velocity change $\Delta V/V^{theo}(d,t)$ measured at time t and depth d to be:

$$\left[\frac{\Delta V}{V}\right]^{theo}(d,t) = \alpha(t)\left[\frac{\Delta V}{V}\right]^{Surf}(d) + (1-\alpha(t))\left[\frac{\Delta V}{V}\right]^{Bulk}(d,t), \tag{4.27}$$

where $[\Delta V/V]^{Surf}$ and $[\Delta V/V]^{Bulk}$ are the relative velocity changes of the surface and bulk waves and α is the partition coefficient. However, the equipartition of compressional and shear wave energy is not taken into account in the inversion. Combining

Equation 4.27 with Equation 4.2 would give an expression for the contributions of changes in bulk and surface waves as well as changes in compressional and shear waves, a similar inversion approach could be performed using CWI measurements made at multiple time windows (as in Equation 4.22). There is therefore strong potential to combine the time-dependent model for α from Obermann *et al.* (2013) with the time-dependent model presented here, to charecterise the changes in V_P and V_S, as well as localising the perturbation in terms of its depth and distance from the source-to-receiver path. We leave this for future work.

There are several potential uses for the method presented here that are applicable outside of geoscience. In medical imaging, specifically in elastography, the separation of bulk and shear moduli is important in the mapping of soft-tissue stiffness (Gennisson *et al.*, 2013). These methods could also be used for improving ultrasonic charecterisation of defects in non-destructive testing.

4.6 Conclusion

Measurements of a change in velocity made using coda waves have previously been limited to an unknown combination of changes in P and S wave velocities. We provide a method for estimating both changes in P and S wave velocity independently, using estimates for velocity change at multiple times along the entire signal, and a scattering model for equilibriation of P and S waves in a medium. We show dynamic time warping and double wavelet methods to be effective in characterizing a simple change in velocity (where amplitudes of the signal do not change). Dynamic time warping is more sensitive to cycle-skipping, but the double wavelet method introduces errors due to averaging within time windows. We extend the scattering model of Snieder (2002) to incorporate a fluid fraction, where S waves cannot exist. This models estimates the equilibriation of P to S waves over time, as well as the equilibriation of the proportion of waves in the solid matrix to pore fluid. Using wavefields from finite difference simulations in a range of media with increasing structure at both the laboratory core scale and field scale, we show the analytical scattering model to be accurate in both the temporal

changes in P and S wave proportions, as well as the final proportions of P and S waves at equilibrium. We estimate changes in P and S wave velocity and changes in matrix in fluid and matrix velocity in a probabilistic framework. We accurately estimate changes P and S wave velocity while retaining the additional precision when compared to conventional methods of phase picking first arriving waves, which was previously unavailable using coda wave interferomerty. This greatly improves the applicability and relevance for many real-world problems such as those in experimental rock physics, or field-scale monitoring projects.

4.7 Acknowledgments

The authors would like to thank Petrobras and Shell for their sponsorship of the International Centre for Carbonate Reservoirs (ICCR), and for permission to publish this work from the 4DRP project.

4.8 Appendix: Conventional methods for Coda Wave Interferometry

One method for estimating a change in velocity is known as the 'Double Wavelet Method' (DWM), where the coda of a unperturbed and perturbed signals (u_{unp} and u_{per}) are divided into multiple time windows with start time t_1, end times t_2, and central time t. For each time window, a cross correlation function is applied using the perturbed and unperturbed signals:

$$R_{DWM}(\tau) = \frac{\int_{t_1}^{t_2} u_{unp}(t)u_{per}(t+\tau)dt}{\sqrt{\int_{t_1}^{t_2} u_{unp}^2(t)dt \int_{t_1}^{t_2} u_{per}^2(t)dt}} \tag{4.28}$$

The travel time perturbation τ is equivalent to the time lag that maximizes the

correlation coefficient R_{DWM}, and relates to the velocity perturbation by:

$$\frac{\tau}{t} = -\frac{\Delta V}{V}. \tag{4.29}$$

Another method to estimate the change in velocity is known as the 'Trace Stretching Method' (TSM) (Sens-Schönfelder and Wegler, 2006), where the perturbed waveform is assumed to be a time-stretched version of a reference waveform; this follows if one assumes that a velocity perturbation is uniform across the entire medium, so all arriving energy is perturbed at the same temporal rate. The time axis of the perturbed signal is stretched by a range of stretching factors (ϵ) and compute the correlation coefficient R_{TSM} between $u_{unp}(t)$ and the stretched version of the perturbed waveform $u_{per}(t[1+\epsilon])$ over a given time window (t_1, t_2):

$$R_{TSM}(\epsilon) = \frac{\int_{t_1}^{t_2} u_{unp}(t) u_{pet}(t[1+\epsilon])dt}{\sqrt{\int_{t_1}^{t_2} u_{unp}^2(t) \int_{t_1}^{t_2} u_{pet}^2(t[1+\epsilon])dt}} \tag{4.30}$$

The optimum stretching factor ϵ_{max} that maximizes the correlation coefficient (for which $R = R_{max}$), is related to the ratio of the change in velocity ΔV to the original velocity V) by:

$$\epsilon_{max} = -\frac{\Delta V}{V}. \tag{4.31}$$

Chapter 5

Monitoring elastic properties during triaxial deformation of oriented finely laminated carbonates using coda waves

The focus of this chapter is on the interpretation of changing seismic velocity during the experimental deformation of rock cores. I provide a laboratory application to the methods described in the previous two chapters for estimating both changes in P and S wave velocity using coda wave interferometry. I use this information as input to a rock physics model for calculating crack density during the triaxial deformation of two finely laminated carbonate samples. I use complementary first-break method results to investigate anisotropy within the samples. From the research questions I identified in Section 2.5, this chapter seeks to answer questions 4 and 5.

At the time of writing, the manuscript is in preparation for journal submission. The co-authors include Alexis Cartwright-Taylor, Andrew Curtis and Ian Main. I acted as the lead author for this paper, and performed all of the laboratory experiments and analysis described herein.

5.1 Abstract

The characterisation of elastic properties and how they evolve during brittle deformation is of great importance for many applications across geoscience and engineering. Coda wave interferometry (CWI) is a method to measure accurate and precise changes in seismic velocity. It utilises the diffuse multiple scattered waves that are very sensitive to small changes in a medium. Previously the estimate of velocity change made using CWI has used an unknown weighted average between the changes in bulk compressional (P) and shear (S) wave velocities.

Here we demonstrate a method where CWI estimates are combined with an analytical scattering model that accounts for the equilibriation of P and S waves over time, allowing the estimation of both changes in P and S wave velocity independently. This allows for the calculation of changes in the P-to-S wave velocity ratio and changes in the inverted crack density. We demonstrate the method using the triaxial deformation of two finely laminated Aptian carbonates, cored parallel and perpendicular to the laminations allowing the investigation of structural anisotropy. The parallel-cored sample exhibits a 36% higher Young's modulus and a 19.9% higher peak stress than the perpendicular cored sample. The increase in velocity (due to stress induced pore closure of pores and pre-existing microcracks) estimated by the conventional first-break method is greater than CWI in the parallel core, and lower than CWI in the perpendicular core. This reflects the contrast between the directional measurement provided by the first break (sampling along the fastest path), and the isotropic average provided by CWI (as the scattered waves eventually travel in all directions). The data suggest pre-existing microcracks are oriented at a high angle to laminations.

These results represent a major improvement in the methods surrounding experimental rock physics, as information regarding the anisotropy of a sample can be attained even where velocities are only measured in one orientation.

5.2 Introduction

Fractures are ubiquitous in the Earth's lithosphere (Bonnet *et al.*, 2001), and the study of fractures is important for a wide range of geological and engineering applications, such as the underground storage of hazardous waste (Green and Mair, 1983), management of groundwater resources (Singhal and Gupta, 2010), CO_2 storage and sequestration (Iding and Ringrose, 2010), geothermal engineering projects (Watanabe and Takahashi, 1995), and the extraction of hydrocarbons (Medeiros *et al.*, 2007). The presence of fractures strongly influence the elastic properties of rocks (Nur and Simmons, 1969; Nur, 1971; O'Connell and Budiansky, 1974; Crampin, 1981; Sayers and Kachanov, 1995; Guéguen and Palciauskas, 1994). In many cases, changes in seismic velocity have been used as a precursor to system-scale failure (Volti and Crampin, 2003; Gao and Crampin, 2004). Here we consider the case of triaxial deformation experiments (Paterson and Wong, 2005), where samples are deformed uniaxially under hydrostatic stress conditions. During these experiments, seismic velocity initially increases due to pressure-induced closure of pores and pre-existing microcracks, then velocities decrease at the onset of dilatancy due to microcracking (Jaeger *et al.*, 2009; Guéguen and Palciauskas, 1994).

In these experiments, velocity is conventionally measured axially, in the direction of loading (Sammonds *et al.*, 1989; Ayling *et al.*, 1995; Schubnel *et al.*, 2006), by taking picking the travel times of the first arriving compressional (P) and shear (S) waves. Recently, coda wave interferometry (CWI) has been used to measure a change in velocity with higher precision and and accuracy compared to conventional methods (Snieder *et al.*, 2002; Snieder, 2006; Singh *et al.*, 2019). The method uses the multiply scattered coda waves, that sample the entire medium many times, thus providing a representative isotropic average of the rock properties. The estimate of velocity change using CWI has previously been made using an unknown weighted average of the changes in P and S waves, limiting the applicability of CWI.

Here we demonstrate the first laboratory application of the recently developed method

of Singh *et al.* (2019) for estimating changes in both P and S wave velocity by combining CWI with an analytical scattering model that describes the conversions and equilibriation of P and S waves in a medium. We hypothesise that measurements made from the coda can be used in conjunction with axial first-break measurements to understand any anisotropy present in the samples, utilising the directional information for the first-break, and the isotropic average that is inherent to CWI. We show how CWI estimates for changes in P and S wave velocities can be used to monitor the compressional-to-shear wave velocity ratio (a key parameter for lithology and fluid prediction methods, e.g., Duffaut and Landrø (2007)), and invert for changes in crack density.

First we describe the geological properties of the two carbonate samples studies here, and describe the experimental methodology and apparatus. We then summarise the theory of CWI and demonstrate how it can be coupled with an analytical scattering model to provide estimates for changes in both P and S wave velocity. We measure the static elastic (i.e., Young's modulus) and dynamic elastic properties (i.e., P and S wave velocities) during deformation and compare the results of the CWI analysis with those of the conventional method. We then invert for changes in crack density and describe how CWI can be used in conjunction with conventional first-break methods to understand anisotropy in the media.

5.3 Method

5.3.1 Sample Characterization

The cores studied here are dry Aptian laminated limestones from the Crato formation, outcropping in the Araripe Basin, North-East Brazil. These rocks are finely laminated lacustrine carbonates (Neumann, 1999), and are of particular interest as they are close analogues to the Barra Velha Formation in the Pre-Salt layer offshore Brazil - a significant hydrocarbon reservoir (Catto, 2015).

Table 5.1: Sample Details

Sample	Orientation to bedding	Length	Diameter	Porosity ϕ
CL1	Parallel	75.44 mm	36.50 mm	7.18%
CL2	Perpendicular	74.50 mm	36.44 mm	2.50%

The main petrographic characteristics observed in these samples are fine grained matrix (micrite or mudstone), which consists of 1 to 4 μm-diameter crystals of low-Magnesium calcite, similar to most lacustrine calcareous muds (Miranda *et al.*, 2016; Scholle and Ulmer-Scholle, 2003). Scanning electron micropscope (SEM) analyses conducted by Miranda *et al.* (2016) show Crato formation laminite samples exhibit an intergranular primary porosity and some secondary porosity such as vugs and moldic structures. Sillicon and Iron replacement of some pores due to the interaction with meteoric water during the post-depositional diagenetic stage is observed. There are multiple fracture systems found in the formation: shear fractures dipping 55°, and vertical opening-mode fractures filled mainly by recrystallized calcite (Miranda *et al.*, 2014). These calcitic veins exhibit zero porosity and are impermeable. The laminated limestones porosities are found to range from 4% to 22% with an average of 12% and permeability values ranging from 0 to 0.09 mD with an average of 0.004 mD (Miranda *et al.*, 2016).

We take two core samples, one cored parallel to the laminations (and a high angle to the pre-existing fractures) and one cored perpendicular to the laminations (and a low angle to pre-existing fractures). The effective (or connected) porosity is measured using the triple-weight method, where we measure the mass of the dry samples (m_{dry}) after oven drying, the mass of the water saturated samples (m_{sat}), and mass of saturated samples immersed in water (m_{imm}). The porosity is then estimated as $\phi = (m_{sat} - m_{dry})/(m_{sat} - m_{imm})$. The sample dimensions and effective porosity are shown in Table 5.1.

5.3.2 Laboratory Apparatus

We use the two Crato formation laminites described above for dry triaxial compression experiments varying the differential stress applied to the sample and measuring the strain and seismic velocities. Such experiments are conducted to simulate the natural stress states within the Earth's crust. We use a conventional triaxial Hoek cell (Figure 5.1), which deforms sample uniaxially under hydrostatic stress conditions (i.e., two of the three principal stresses are equal). The pressure vessel allows the application of a confining pressure, which is held constant at 30 MPa. The load is applied through the pistons inserted at each end of the cell. The axial stress σ_1 is calculated as $\sigma_1 = F/A$, where F is the force applied by the pistons and A is the cross-sectional area of the sample and the intermediate and principal stresses $\sigma_2 = \sigma_3$ are equal to the radial confining pressure. The differential stress σ is calculated as $\sigma = \sigma_1 - \sigma_3$. Loading is applied axially with a strain rate $\dot{\epsilon} = 3 \times 10^{-5}\ s^{-1}$, to a peak stress and sample failure.

Axial displacement is measured using two linear variable displacement transducers (LVDTs). Linear strain ϵ is then calculated as the ratio of the change in length δl as a function of the initial length l_0, i.e., $\epsilon = \delta l / l_0$.

To characterise the extent of damage within the samples following the triaxial deformation, we image the samples before and after loading using high-resolution x-ray microtomography (μCT). These three-dimensional images have voxel sizes and thus maximum resolution of 37.5 μm^3.

Conventional Velocity Measurements

To measure P-wave velocity we use Glaser-type conical piezoelectric sensors sensitive to displacement normal to the sensor face (McLaskey and Glaser, 2012). These wide-band sensors are calibrated against theoretical displacement time history and have an almost flat displacement response spectrum in the 20 kHz to 1 MHz frequency band. This means that, in this frequency band, they are essentially displacement sensors and their voltage output is linearly proportional to the surface normal displacement.

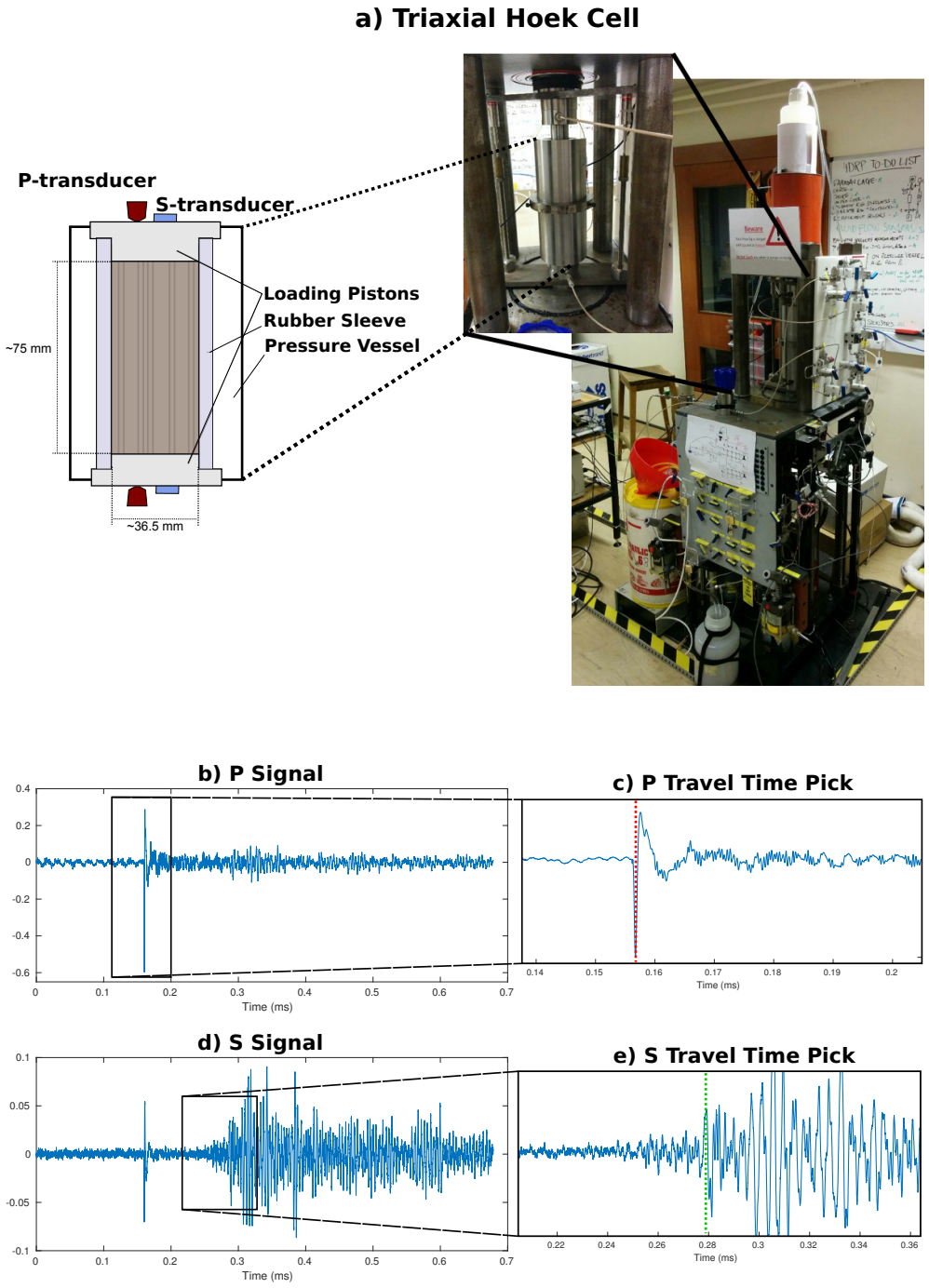

Figure 5.1: a) Triaxial rock deformation rig, for applying confining, fluid, and loading stresses on a 36.5 mm diameter sample while measuring differential stress, axial strain, and P and S wave velocities. Dimensions are approximate to account for variations between samples. b) Example signal recorded using transducers sensitive to displacement perpendicular to the sensor face (P sensor). c) Example travel time pick (first-maximum) on P sensor. d) Example signal recorded using transducer sensitive to displacement tangential to the sensor face (S signal). e) Example S wave travel time pick.

Aperture effects are reduced due to the relatively small 0.5 mm sensor contact area. We used an Itasca Image pulser-amplifier system with operating frequency range of 100 kHz to 1 MHz and pre-amp gain of 40 dB, which switches between all transducers in an ultrasonic array, allowing each to act as both a transmitter and a receiver. The amplitude of the pulse spike is 500 V with approximate signal rise time of 0.3 μs and total duration of 2.8 μs, the sampling period is 40 ns. The output recorded waveform at each receiver is a stack of received waveforms from 25 source pulses with a pulse repetition frequency of 20 kHz (as the pulse repetition is high, we assume no loss in phase resolution). We measure S wave velocity using sensors with PZT sensitive to displacement tangential to the sensor face, with a central frequency of 700 kHz and a contact area of 20 mm^2. Example recordings using the perpendicular (P) and tangential (S) sensors, as well as example picks for the P and S wave arrival times are shown in Figures 5.1b-e. The conventional method for measuring the P and S wave velocities is to measure the arrival time of the first arriving P and S waves (specifically, we take the arrival time of the first maximimum), and assume a straight path between the source and receiver to calculate velocity.

5.3.3 Coda Wave Interferometry

Coda Wave Interferometry (CWI) is a method for accurately and precisely measuring a *change* in velocity (Snieder *et al.*, 2002; Snieder, 2006). CWI uses the diffuse, multiply scattered waves found in the tail of the seismogram, Coda waves sample the entire medium and the same areas multiple times, therefore provide much more representative measurements of a change in bulk velocity velocity of a medium, as well as providing an order of magnitude improvement in precision when compared to conventional methods (phase picking of first arriving waves) for measuring a bulk velocity change (Singh *et al.*, 2019).

We estimate the velocity change by taking unperturbed and perturbed signals (u_{unp} and u_{per}) and subdivide into multiple time windows with start time t_1, end times t_2, and central time t. For each time window, a cross correlation function is computed using the perturbed and unperturbed signals:

$$R(\tau) = \frac{\int_{t_1}^{t_2} u_{unp}(t) u_{per}(t+\tau) dt}{\sqrt{\int_{t_1}^{t_2} u_{unp}^2(t) dt \int_{t_1}^{t_2} u_{per}^2(t) dt}}. \tag{5.1}$$

The time lag τ that maximises the correlation coefficient R for a given time t relates to the velocity perturbation ΔV as a fraction of the original velocity V by:

$$\frac{\tau}{t} = -\frac{\Delta V}{V}. \tag{5.2}$$

There is no length of time windows (t_1, t_2) prescribed for the estimation of $\Delta V/V$, here we take calculate $[\Delta V/V](t)$ over a range of window lengths ranging from 0.01 ms to 0.2 ms and take the mean $[\Delta V/V](t)$ across all window lengths.

There are many advantages to using CWI for measuring changes in velocity using CWI: the process is automatic, and more accurate and precise than the conventional first-break method Singh *et al.* (2019). However, the estimate of velocity change given by CWI ($\Delta V/V$) reflects an unknown combination of changes in P and S wave velocities ($\Delta V_P/V_P$ and $\Delta V_S/V_S$, respectively), therefore it is not possible to compare standard CWI results with conventional P and S-wave results. However, the relative proportions of P and S waves in a medium change over time (Snieder *et al.*, 2019), and equilibrate to a constant energy ratio (a phenomenon known as equipartitioning (Hennino *et al.*, 2001; Weaver, 1982, 1990; Margerin *et al.*, 2009)), therefore the relative contributions of $\Delta V_P/V_P$ and $\Delta V_S/V_S$ to the measured $\Delta V/V$ also vary with time and stabilize in the coda. This variation in $\Delta V/V$ as a function of time t can then be used to infer $\Delta V_P/V_P$ and $\Delta V_S/V_S$, using the relation:

$$\left[\frac{\Delta V}{V}\right](t) = [1 - q(t)]\left[\frac{\Delta V_P}{V_P}\right] + q(t)\left[\frac{\Delta V_S}{V_S}\right], \tag{5.3}$$

where $q(t)$ is the fractional proportion of the $\Delta V_S/V_S$ contribution to $\Delta V/V$ (thus $1 - q(t)$ is the fractional proportion of $\Delta V_P/V_P$).

Singh *et al.* (2019) demonstrate a model for estimating the function q, adapting the analytical scattering model of Snieder (2002). The model assumes that at the beginning

of a recording, the signal is comprised of only P wave energy, thus the measurement of $\Delta V/V$ reflects only the change in P wave velocity $\Delta V_P/V_P$. As time t increases, the proportion of P and S waves equilibriate, and the rate that this occurs depends on the scattering properties of the medium and the proportions of P and S waves after equilibrium depends on the V_P/V_S ratio. The model for the amount of P wave energy (N_P) and S wave energy (N_S) as a function of time can be described by the following differential equations:

$$\dot{N}_P = \frac{1}{a}(p_{SP}V_S N_S - 2p_{PS}V_P N_P), \tag{5.4}$$

$$\dot{N}_S = \frac{1}{a}(2p_{PS}V_P N_P - p_{SP}V_S N_S), \tag{5.5}$$

where the dot denotes a rate of change over time, a is the average distance between scatterers, p_{SP} and p_{PS} are the probabilities of S-to-P and P-to-S conversions occurring at a scatterer. The probabilities of conversions and inter-scatter distance a relate to the mean free path l_P, which is defined as $l_P = a/(2P_{PS})$. In some cases, the mean free path l_P can be estimated by relating the power spectrum $|\langle U(\omega\rangle|^2$ of the coherent signal $\langle u(t)\rangle$ to the scattering mean free path l_P (Derode *et al.*, 2001; Anugonda *et al.*, 2001; Obermann *et al.*, 2013):

$$|\langle U(\omega\rangle|^2 = exp\bigg(-\frac{x}{l_P}\bigg), \tag{5.6}$$

where x is the distance between source and receiver locations. We assume that for a given time t, the contribution of $\Delta V_S/V_S$ and $\Delta V_P/V_P$ is equal to the proportion of S and P waves in the medium i.e., $q = N_S/(N_P + N_S)$ and $1 - q = N_P/(N_P + N_S)$.

The remaining unknown parameters in Equation 5.3 are $\Delta V_P/V_P$ and $\Delta V_S/V_S$, which are time independent changes in P and S wave velocities respectively. Many estimates of $\Delta V/V$ measured at different times results in multiple solutions to Equation 5.3, the same number as there are time samples. Quantities $\Delta V_P/V_P$ and $\Delta V_S/V_S$ can then be estimated using an ordinary least squares inversion approach to solve the system:

$$d = Am, \tag{5.7}$$

where d is a matrix of measured values of $[\Delta V/V](t)$ for each time window, and A is matrix of $(1-q)$ and q values expected at each time window for a given V_P/V_S ratio γ. The resulting vector m contains estimates of $\Delta V_P/V_P$ and $\Delta V_S/V_S$.

An important measurement in experimental rock physics and the interpretation of the mechanical properties of a material is the ratio of compressional-to-shear wave velocity $\gamma = V_P/V_S$. The estimated changes in P and S wave velocity can be used to calculate the fractional change in γ:

$$\frac{\Delta\gamma}{\gamma} = \frac{(1+\Delta V_P/V_P)}{(1+\Delta V_S/V_S)} - 1. \tag{5.8}$$

One of assumptions underlying the CWI method is that small perturbations are occurring, and that there are no changes in the ray paths or addition of any new scatterers. In the differential stress experiments conducted here, samples are deformed under high stress, therefore major changes occur including the addition of fracture networks in the medium, contravening the assumption of CWI. To limit extent of changes occurring in the recorded signals, we use a moving reference trace method, where the velocity change from the initial reference trace (u_0) to any other recorded waveform during deformation (u_n) can be calculated as

$$[\Delta V/V]_{u_0u_n} = [\Delta V/V]_{u_0u_s} + [\Delta V/V]_{u_su_n}, \tag{5.9}$$

where $[\Delta V/V]_{u_iu_j}$ is the stretching factor of trace u_j relative to u_i, $s = k\lfloor n/k \rfloor$, n is the trace number, k is the user-selected step size of the moving reference trace, and $\lfloor \ldots \rfloor$ denotes a floor function, which outputs the greatest integer less than or equal to the argument. Here we use a range of k values of 1-3 and take the average of the three estimates for each recording.

5.3.4 Crack Density Models

Using the absolute V_P and V_S measurements made using the conventional method of picking first arrivals, as well as the CWI measurements for velocity changes $\Delta V_P/V_P$ and $\Delta V_S/V_S$, we asses the damage occurring the samples using a crack density model. Here we use the self-consistent model of O'Connell and Budiansky (1974), who developed a general description of crack damage and its effect on the elastic properties of rocks. The model assumes the crack density is low, so cracks are far apart and hence crack interaction is negligible, and also that the location and orientation of cracks in the rock is random uniform and isotropic. For the case of randomly oriented and penny-shaped cracks, the crack density ρ_C is defined as:

$$\rho_C = N\langle a^3 \rangle = (3\phi/4\pi)\langle a \rangle, \tag{5.10}$$

where $a \approx b \ll c$ (a and b are the major axes of the ellipsoidal crack and c is the crack aperture), $\langle a^3 \rangle$ is therefore the mean crack radius, N is the number of cracks per unit volume, $\langle \alpha \rangle$ is the mean crack aspect ratio (c/a), and ϕ is the volume of cracks per unit volume. Crack density can be estimated from the effective (or measured) bulk modulus K_{eff} and Poisson ratio ν_{eff} (O'Connell and Budiansky, 1974):

$$\rho_C = \frac{9}{16}\frac{(1-2\nu_{eff})}{(1-\nu_{eff}^2)}\left(1 - \frac{K_{eff}}{K^*}\right), \tag{5.11}$$

where K^* is the bulk modulus of the crack-free rock (see also Ayling *et al.* (1995) and Stanchits *et al.* (2006) for the application of this method). We take K^* to be the maximum measured bulk modulus ($K^* = 49.4$ GPa), where we assume all cracks are closed.

As CWI provides a change in velocities, rather than an absolute velocity, to estimate the change in crack density we first take the initial values of bulk modulus K_0 and Poisson ratio ν_0 using the P and S wave velocities measure from first arrivals:

$$K_0 = \rho(V_{P0}^2 + \frac{4}{3}V_{S0}^2), \tag{5.12}$$

and

$$\nu_0 = \frac{1}{2}\frac{\gamma_0^2 - 2}{\gamma_0^2 - 1}, \tag{5.13}$$

where ρ is the sample density, and V_{P0}, V_{S0} and γ_0 are the initial measurements of P wave velocity, S wave velocity, and the V_P/V_S ratio, respectively. Using the CWI estimates of $\Delta V_P/V_P$ and $\Delta V_S/V_S$, the bulk modulus and Poisson ratio can be estimated using CWI:

$$K_{CWI} = \rho\left(\left(V_{P0} + V_{P0}\frac{\Delta V_P}{V_P}\right)^2 + \frac{4}{3}\left(V_{S0} + V_{S0}\frac{\Delta V_S}{V_S}\right)^2\right), \tag{5.14}$$

and

$$\nu_{CWI} = \frac{1}{2}\frac{(\gamma_0 + \gamma_0[\Delta\gamma/\gamma])^2 - 2}{(\gamma_0 + \gamma_0[\Delta\gamma/\gamma])^2 - 1}. \tag{5.15}$$

The crack density ρ_C can be estimated with Equation 5.11 where $K_{eff} = K_{CWI}$ and $\nu_{eff} = \nu_{CWI}$. To avoid any of the inaccuracies of using the conventional first-break method for measuring velocity, we consider only the change in crack density $\Delta\rho_C$ as a fraction of the initial crack density ($\Delta\rho_C/\rho_C$).

5.4 Results

5.4.1 Mechanical Deformation

The measured axial strain ϵ and differential stress during the experimental deformation of the two Crato formation laminite samples (CL1 and CL2), as well as the estimated absolute velocity using the conventional first-break method, are shown in Figure 5.2 and some key mechanical features are noted in Table 5.2. Figures 5.2a and b show the relationship between stress and strain for CL1 and CL2, which are cored parallel and perpendicular to laminations, respectively. We observe different geomechanical behaviour, due to the different orientations of the cores relative to the laminations in the samples. The static dynamic properties, i.e., the Young's modulus, are measured by taking the ratio of changing stress to strain in the quasi-linear elastic phase of deformation (the gradient of the linear portion of the stress strain curve), and is higher for CL1 (30 GPa) compared to CL2 (22 GPa). CL1 also reaches a higher peak

differential stress (319 MPa) compared to CL2 (266 MPa). The geological properties (e.g., porosity and mineralogy) of each lamination will vary depending on varying environmental factors during deposition. Therefore the stiffness will also vary between lamination, resulting in mechanical anisotropy. The sample that is cored parallel with the laminations (CL1) is supported by the stiffest laminations within the sample, thus exhibiting a higher Young's modulus and peak stress. The static elastic properties of the sample cored perpendicular with the laminations (CL2) are dominated by the softer laminations, thus the sample exhibits a higher strain, lower peak stress and lower Young's modulus.

Table 5.2: Summary of geomechanical results

Sample	P_{eff} (MPa)	ϵ (s^{-1})	Young's modulus (GPa)	Peak Stress (MPa)
CL1	30.0	3×10^{-5}	30.2	293.0
CL2	30.0	3×10^{-5}	22.4	237.6

The dynamic elastic properties (i.e., P and S wave velocities) initially increase at the early stages of deformation (Figs 5.2c and d), attributed to the closure of pores and pre-exising microcracks (Guéguen and Palciauskas, 1994; Paterson and Wong, 2005). As strain increases, a drop in V_S and subsequent drop in V_P is observed. There are many cases in the literature of V_P and V_S decreasing at the onset of microcracking, where the stress-strain curve begins to flatten to a zero gradient (Birch, 1960; Walsh, 1965; O'Connell and Budiansky, 1974; Sammonds *et al.*, 1989; Schubnel *et al.*, 2006). While the observed trends in P and S wave velocity follow what is expected from the literature quoted, the form of the strain-velocity curves shows high temporal variability, particularly in V_P, where there are large steps in velocity between contiguous strain measurements. Such strong variations are not expected in the case of a constant loading or creep experiment. The conventional first-break method is more susceptible to contamination by noise, so can exhibit errors, especially when compared to CWI (Singh *et al.*, 2018, 2019).

We also charecterise the deformation of the two samples, shown as photographs in Figures 5.3a and b, and compare pre- and post-deformation μCT data sliced normal

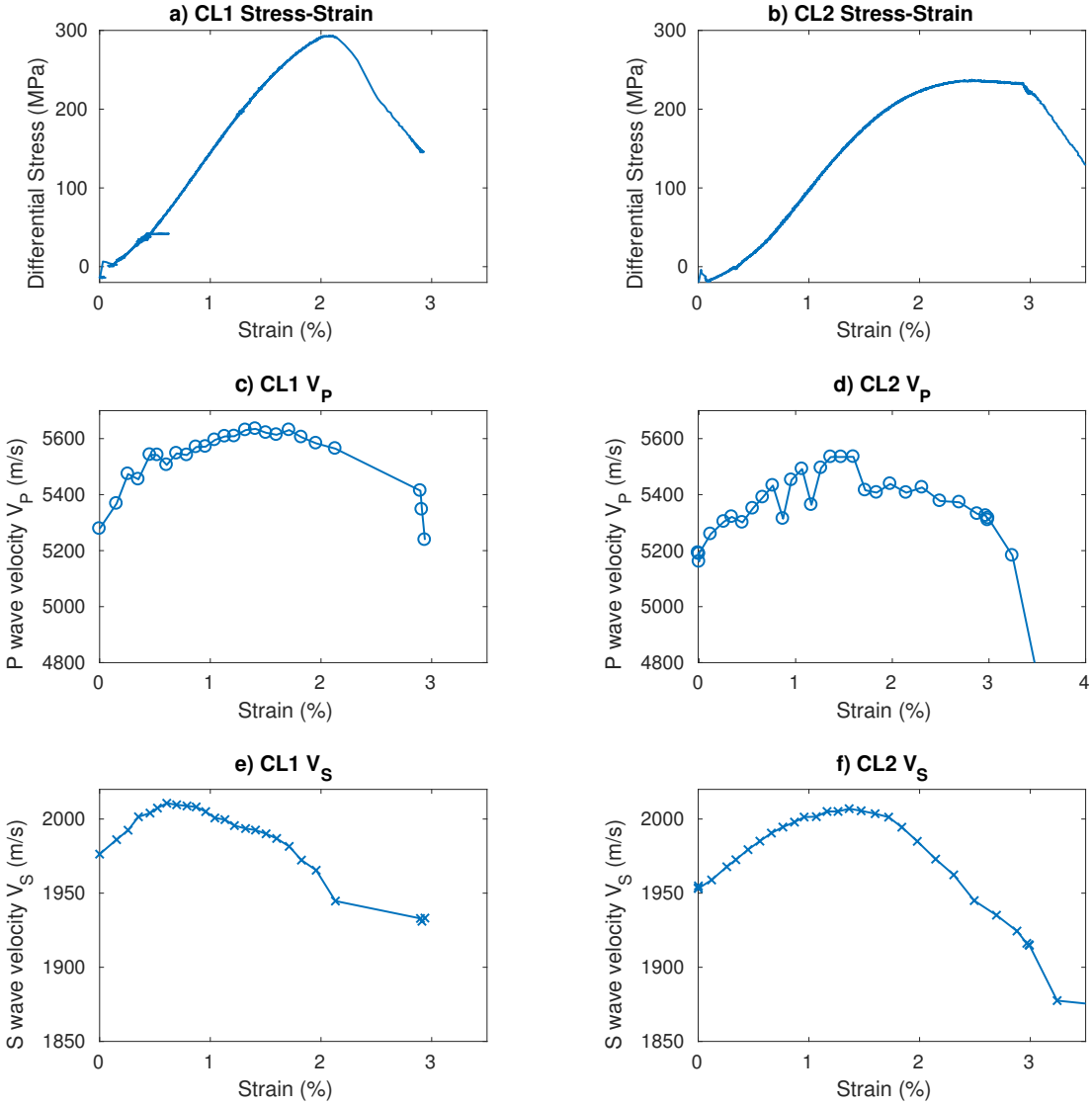

Figure 5.2: a-b) Differential stress as a function of strain in a constant loading experiment (strain rate $=3\times10^{-5}$ s^{-1}). c-d) Measured absolute compressional (blue) and shear (red) wave velocities using the conventional first-break method, plotted as a function of strain. The left are right panels are for samples CL1 and CL2, cored parallel and perpendicular to laminations, respectively.

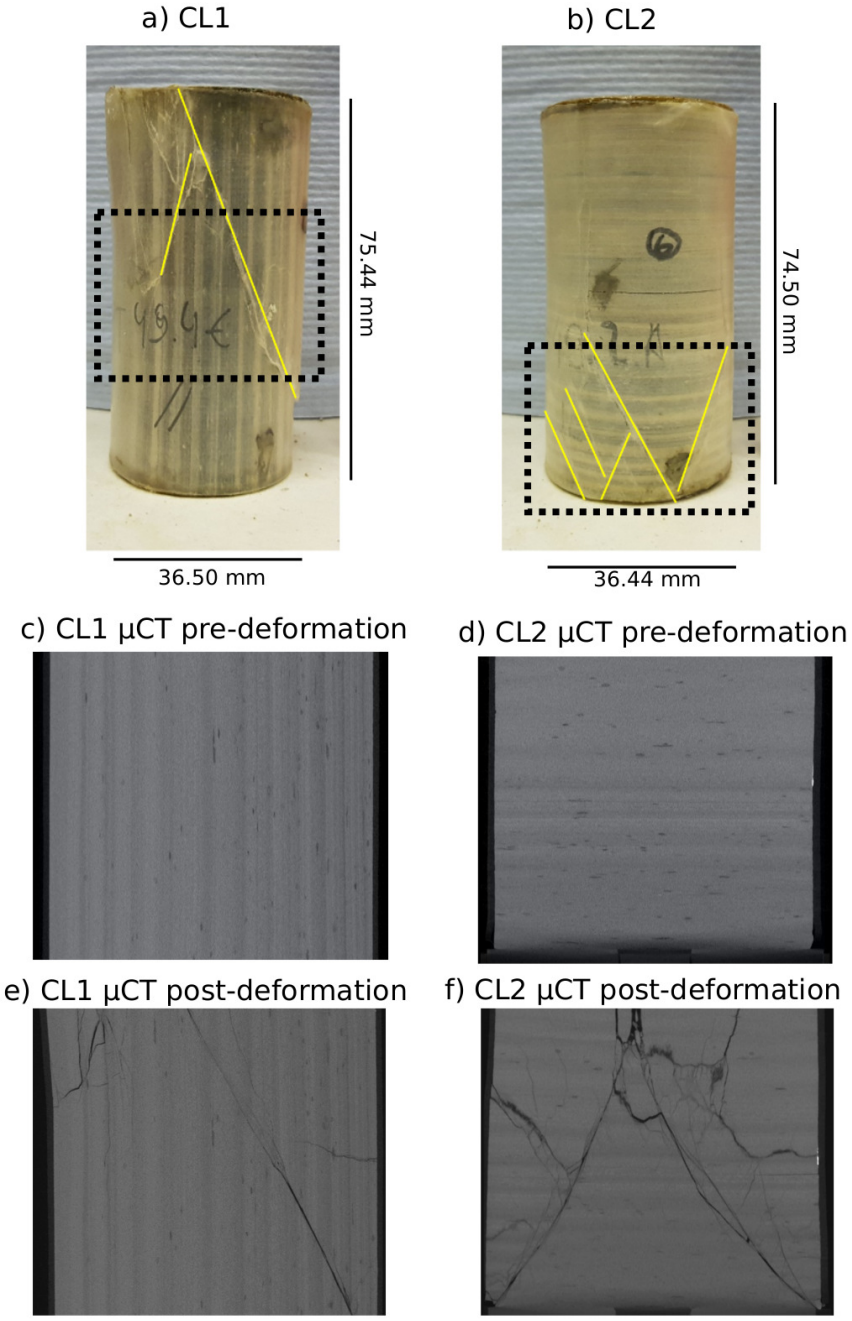

Figure 5.3: Post-deformation photographs of CL1 (a) and CL2 (b), with slices through microtomography (μCT) volumes shown as dashed black boxes. The fracture exposed at the core surface are highlighted with yellow lines. c and d) The pre-deformation μCT slices perpendicular to the strike of the dominant fracture. e and f) The post deformation μCT slices perpendicular to the strike of the dominant fracture.

to the strike of the dominant fractures in Figures 5.3c-f. The deformation in CL1 is dominated by a single fracture plane whereas CL2 exhibits many conjugate fractures. The angle of fracture planes θ to the direction of axial loading is consistent between the two samples ($\theta = 27°$ for CL1 and $\theta = 28°$ for CL2), meaning that despite the different orientations of the samples, the fundamental failure mode of individual cracks remains the same. This is possibly due to the relatively uniform mineralogy in the samples dominating the fracture angles.

5.4.2 Dynamic Elastic Property Changes from Coda Wave Interferometry

As described in Section 5.3.3, the estimation of the fractional changes in P and S wave velocity ($\Delta V_P/V_P$ and $\Delta V_S/V_S$) require the estimation of $\Delta V/V$ using CWI at multiple time windows along the signal, as well as a model that describes the equilibriation of P and S waves in a given medium. We demonstrate this processes in Figure 5.4. First we take two recorded signals measured at two stages of loading (differential stress $P_{diff} = 48$ and 64.1 MPa, plotted in Fig. 5.4a). We estimate the inter-scatter distance and input into the scattering model described by Equations 5.4 and 5.5, which gives the estimated relative contributions of $\Delta V_P/V_P$ and $\Delta V_S/V_S$ to the measured CWI estimate of $\Delta V/V$ (Fig. 5.4b). We also estimate $\Delta V/V$ as a function of time using Equations 5.1 and 5.2 at multiple time windows, plotted as the red curve in Figure 5.4c, which shows a high $\Delta V/V$ at early times when the medium is dominated by P waves, and equilibriation to a much lower $\Delta V/V$, where S waves are dominant. We invert for independent velocity changes using Equation 5.7 and find $\Delta V_P/V_P = 0.46\%$ and $\Delta V_S/V_S = -0.01\%$. By forward modelling these estimates into Equations 5.3 using the scattering model in Fig. 5.4b, we estimate the equivalent modelled $\Delta V/V$ as a function of time, based on the final estimates of $\Delta V_P/V_P$ and $\Delta V_S/V_S$ (plotted as a dashed black line in Figure 5.4c). The residuals between the forward modelled and measured $\Delta V/V$ curves are plotted in Figure 5.4d. The residuals as a function of time are not randomly distributed around zero, rather they show some coherence in the error structure indicating the residuals are not independent. This is likely due to

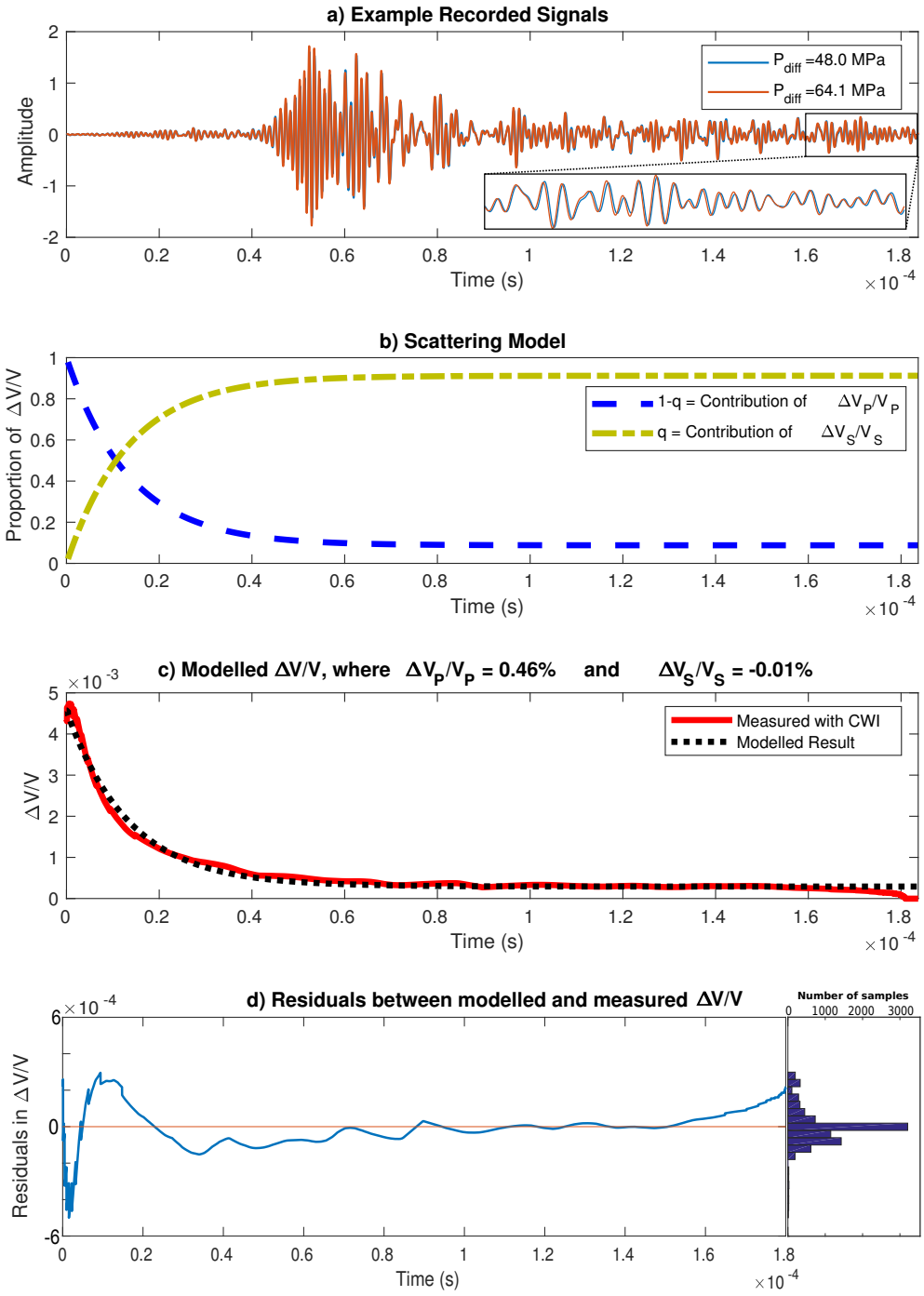

Figure 5.4: Demonstration of the Coda Wave Interferometry methods for estimating separate changes of P and S wave velocities. a) Example recorded signals using the S-sensors (sensitive to tangential displacement) at recording at stages of loading: differential stress P_{diff}=48 MPa (blue) and 64.1 MPa (red). b) Time dependent relative contributions of $\Delta V_P/V_P$ and $\Delta V_S/V_S$ to the $\Delta V/V$ measured by CWI, derived using the scattering model described by Equations 5.4 and 5.5. c) Recorded $\Delta V/V$ as a function of time (solid red), and the best fitting model result (dashed black) from taking the q values from panel b and estimated velocity changes $\Delta V_P/V_P = 0.46\%$ and $\Delta V_S/V_S = -0.01\%$.

the assumption of the scattering model that scatterers are randomly distributed and isotropic, which is not the case for the samples considered here. However, the measured and modelled functions of $\Delta V/V$ overall are in good agreement, suggesting that both the scattering model, as well as estimates for $\Delta V_P/V_P$ and $\Delta V_S/V_S$ are appropriate.

We repeat this processes for all the recorded signals (using the moving reference trace method described by Equation 5.9) giving an estimates of $\Delta V_P/V_P$ and $\Delta V_S/V_S$ as a function of strain. This also allows the calculation of the change in compressional-to-shear wave velocity ratio $\gamma = V_P/V_S$ from Equation 5.8. The resulting estimates are shown for both Crato formation laminite samples in Figure 5.5. The general trend of the changes in P wave velocity (Figs. 5.5a and b) and S wave velocity (5.5c and d) are in good agreement with the absolute velocity measurements shown in Figure 5.2. However the CWI estimates exhibit a much smoother response to strain, suggesting the method is less susceptible to errors and mis-picking due to the contamination of noise.

5.4.3 Crack Density

Using the conventional first-break measurements for absolute velocity (Figure 5.2), and the CWI measurements for velocity change (Figure 5.5), we first calculate the change in bulk modulus (Figures 5.6a and b) and Poisson ratio (Figures 5.6c and d), then using Equation 5.11 we invert for crack density. The resulting changes in crack density $\Delta\rho_C/\rho_C$ are shown in Figures 5.6e and f. There are a few differences between the conventional first-break method and the CWI method results (red and blue curves in Figure 5.6, respectively). First, the estimates made using CWI are smoother and do not show strong temporal variations, most likely because the CWI method is more robust to ambient background noise (Singh *et al.*, 2019). Second, the estimated changes in dynamic elastic properties, and thus the estimated changes in crack density $\Delta\rho_C/\rho_C$, are different for CWI and first-break methods, and the differences are not consistent between the two samples. For CL1 the measurements made using the first-break method are more sensitive to strain, where bulk modulus K and Poisson ratio ν increase and ρ_C decreases by a greater amount compared to the measurements made using CWI.

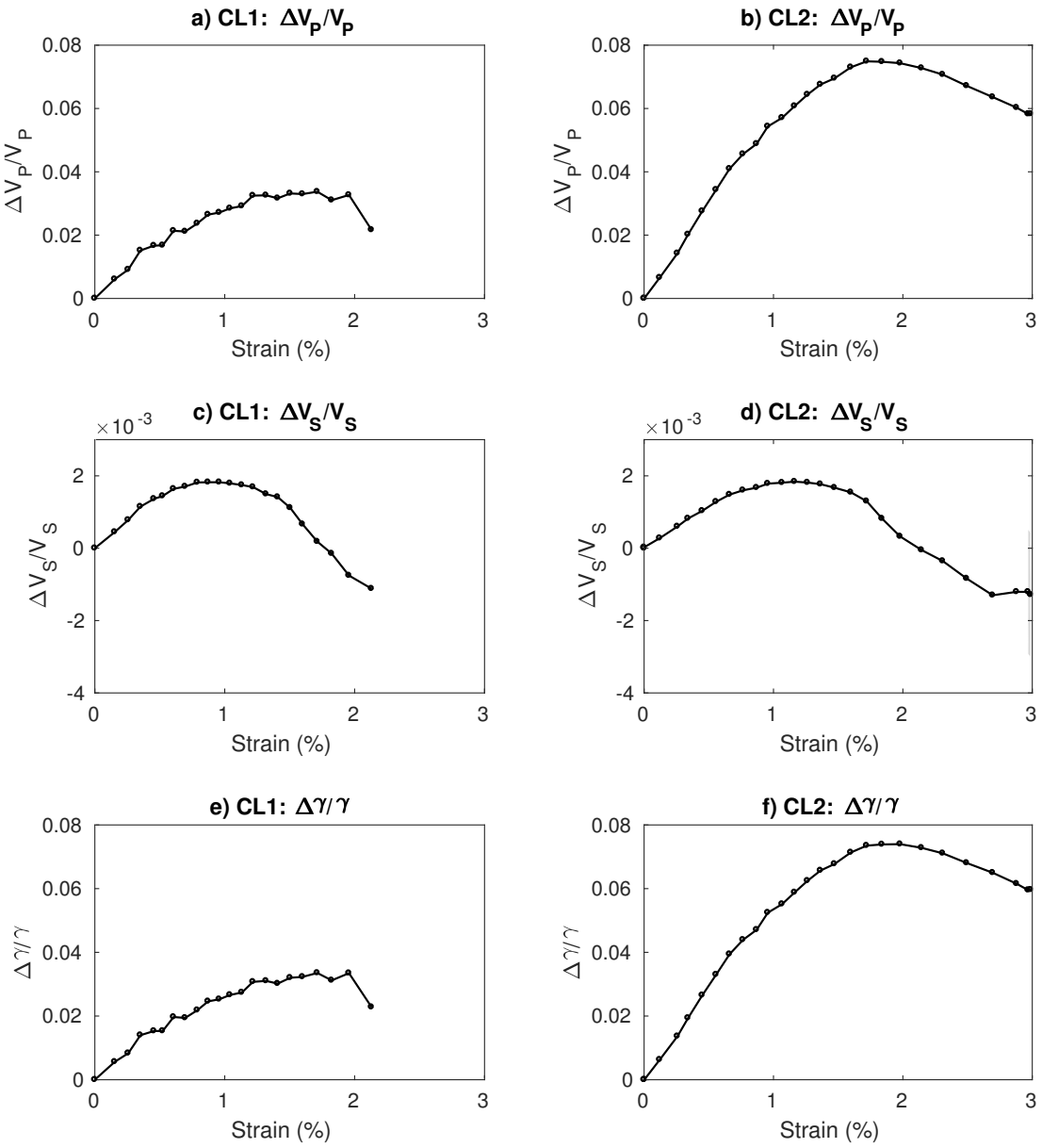

Figure 5.5: Estimated changes in P wave velocity (a-b) and S wave velocity (c-d), using CWI. e-f) Calculated change in the P-to-S velocity ratio $\Delta\gamma/\gamma$, where $\gamma = V_P/V_S$. The left are right panels are for samples CL1 and CL2, cored parallel and perpendicular to laminations, respectively.

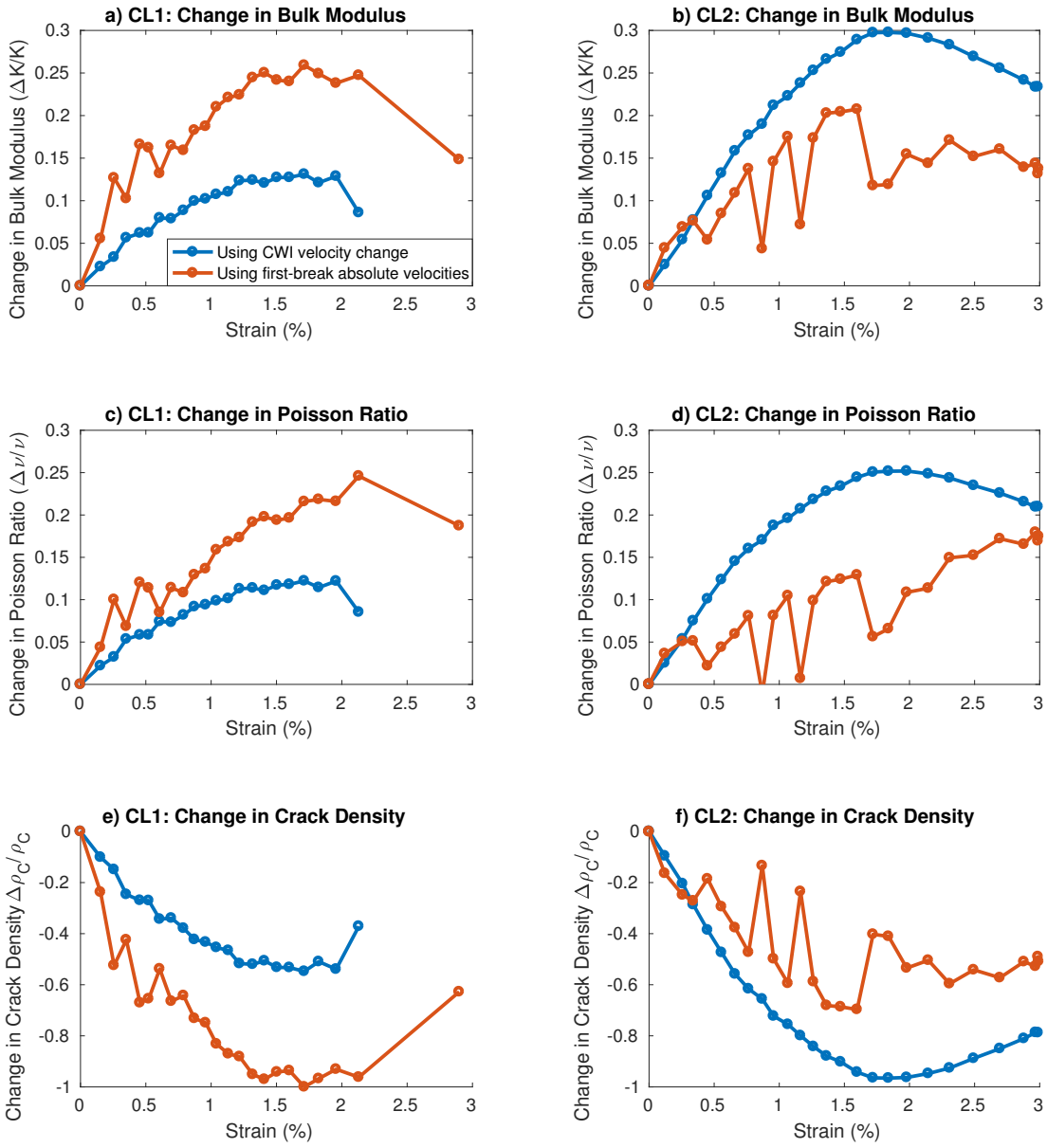

Figure 5.6: Estimated changes in bulk modulus $\Delta K/K$ (a and b), the change in Poisson ratio $\Delta\nu/\nu$ (c and d), and the calculated change in crack density $\Delta\rho_C$ (e and f) using CWI and first break methods (blue and red curves, respectively).

The opposite occurs for CL2, where CWI measurements appear to be more sensitive to changes in axial strain.

The difference in measurements made using CWI and first-break methods most likely results from differences in the directionality inherent to the methods. Coda waves by nature, sample the entire medium in *all* directions, thus the estimate from CWI are an isotropic average of the entire medium. In contrast the first break method samples only in the direction of the propagating wave, in this case transducers are measuring velocity approximately axially along the sample.

Initially, the main mechanism for a change in velocity is the closure of pores and pre-existing microcracks (Guéguen and Palciauskas, 1994; O'Connell and Budiansky, 1974). We therefore suggest that the difference in measurements made using CWI and first break methods during the closure phase is caused by the preferential closing of microcracks with a dominant orientation. In CL1, the first-break measurements are more sensitive than CWI, suggesting pore and microcrack closure is mostly in the axial direction. In CL2, the CWI measurements are more sensitive, suggesting that pore closure is stronger in a non-axial orientation, or even that there is some fracture opening in the axial direction. This is supported by the fracture charecterisation of the Crato formation laminites carried out by (Miranda *et al.*, 2014), who document several fracture sets dipping at high angles to the laminations. As there are no fractures visible in the pre-deformation μCT data, the pre-existing fractures are likely to be below the resolution of the images (fracture apertures are less than 37.5 μm).

5.5 Discussion

Here we show CWI provides more robust estimates of changes in both the P and S wave velocities during the deformation of two oriented structurally anisotropic samples than conventional first-break methods. The estimated changes in dynamic elastic properties using CWI can also provide complementary information when used alongside the estimates made using the conventional first-break method, where information on

the anisotropy in the medium can be attained more robustly. The information provided is not a full diagnosis of anisotropy, i.e., the full compliance (or it's inverse stiffness) tensor can not be estimated, unless there were a full suite of transducers oriented in three orthogonal directions. The method here only provides a comparison between the direction along the (fastest) first-arrival path and the average across all directions. This information has previously not been available using a single-orientation experimental configuration, as is common in many experimental rock physics laboratories.

CWI is limited in its ability to resolve strong changes occurring in the medium, such as new fracture planes or some scatterers being removed (e.g., due to pore closure). The strengths of CWI however lies in its ability to provide accurate and precise estimates of small changes, such as the deformation that occurs at low strains. The CWI estimates should then be used with caution when high strains and strong deformation occurs.

We invert for changes in crack density using the model of O'Connell and Budiansky (1974). The model assumes cracks are dilute, non-interacting, randomly distributed and randomly oriented. The evidence from our experiments, as well as the analysis of Miranda *et al.* (2014) suggests fracture sets in our samples have a strong preferred orientation at high angles to the laminations. At late stages of deformation, the coalasence of microcracks begins along the dominant fracture planes (Paterson and Wong, 2005; Lennartz-Sassinek *et al.*, 2014), at these stages cracks are in close proximity therefore interact with each other. The crack density model is therefore not valid in this case.

The results here compliment the work of Volti and Crampin (2003) and Gao and Crampin (2004), where changes in seismic velocity are observed at the regional tectonics scale as a precursor to system scale failure. Similar results are found at the laboratory scale, where velocities decrease at the onset of dilatancy due to the formation of microcracks (Jaeger *et al.*, 2009; Guéguen and Palciauskas, 1994). However, these studies use only the first arriving waves in their estimation of velocity, which as can be biased in areas of strong heterogeneity (Singh *et al.*, 2019). Our results yield similar results using both the first arrivals as well as the seismic coda. In many laboratory

scale experiments, velocity is conventionally measured axially, in the direction of loading (Sammonds *et al.*, 1989; Schubnel *et al.*, 2006). The experiments conducted here follow the same approach, the difference is that by using CWI as well as the direct arrival, material properties from waves travelling in all directions can be estimated as well as in the direction of the source-to-receiver path.

This study only considers the application of CWI for estimating a bulk velocity change. There is potential to use CWI to also estimate the relative locations of acoustic emmisions during deformation (Robinson *et al.*, 2013; Zhao *et al.*, 2017). As the processes of fracturing itself generates acoustic emissions, which can be used as passive sources for estimating the change in velocity. Other applications include the improved accuracy and charecterisation of crack density for structural health monitoring of engineering structures, e.g., Salvermoser *et al.* (2015) uses conventional CWI, though could be extended so that changes in P and S wave velocities can be used in the charecterisation of the material properties.

5.6 Conclusion

We study the static and dynamic elastic properties of two low-porosity Aptian laminated carbonates from the Crato formation, NE Brazil. The samples are cored in orthogonal direction, parallel and perpendicular to laminations, allowing the investigation of mechanical anisotropy. We estimate the Young's modulus of the parallel sample to be around 31% higher than the perpendicular core. We test and validate the method of Singh *et al.* (2019) for estimating changes in P and S wave velocity that combines coda wave interferometery and an analytical scattering model describing the conversions between P and S waves in an isotropic and random point-scattering medium. We compare this method with the conventional method of picking the travel times of the first arriving waves to calculate velocity, and show the new method to be comparatively robust in the presence of ambient background noise. We demonstrate how measurements from CWI can be used to calculate change is the V_P/V_S ratio, the bulk modulus, and Poisson's ratio, and use these properties to invert for the changing crack density

during deformation. As coda waves scatter in all directions and throughout the entire medium, the estimates of CWI represent an isotropic average, whereas the first-arrival velocity only represent a single direction in along the path of wave propagation. The estimates of velocity change for CWI and first-breaks, particularly how the estimates differ, can be used in the interpretation of any anisotropy in the samples. The data here suggests the preferential closing of pores perpendicular to the laminations, most likely pre-existing fractures at high angles to the laminations/bedding. This is supported by the known orientations of fracture sets reported for the Crato formation. CWI can therefore be used in conjunction with existing methods to provide previously unavailable information regarding the anisotropy of the sample. These findings mark a significant improvement and large potential for use in laboratory rock physics experiments.

5.7 Acknowledgments

The authors would like to thank Petrobras and Shell for their sponsorship of the International Centre for Carbonate Reservoirs (ICCR), and for permission to publish this work from the 4DRP project. We also thank Ian Butler and Michael Flynn for their valuable scientific and technical support.

Chapter 6

Digital rock physics in four dimensions: simulating cementation and its effect on seismic velocity

The focus of this chapter is on the interpretation of changing seismic velocity due to changes in porosity during cementation in rocks. I use a range of models generated from the process-based simulation of cementation in digital carbonate rocks and numerical finite-difference methods to estimate seismic velocity. I then statistically compare two competing rock physics models. From the research questions I identified in Section 2.5, this chapter seeks to answer questions 6 and 7.

This paper has been submitted to my project sponsors for approval to submit to Geophysical Journal International. The co-authors include Phil Cilli, Ola Hosa and Ian Main. I acted as lead author for this paper. My contribution to the work described are the simulations of wavefield propagation for the estimation of velocity (Section 6.3.2), the inversions using various rock physics models (Section 6.3.3), and the statistical testing of each model (Section 6.3.4), as well as the analysis of the results. The process-based simulation of the digital rocks, described in Section 6.3.1, was performed by Ola Hosa. The rock physics model of Cilli and Chapman (2019) is fundamental to this

chapter. Their paper is currently in preparation for submission. A summary of their model is available in a shorter conference abstract (Cilli and Chapman, 2018).

6.1 Abstract

Porosity exerts a strong control on the mechanical and hydraulic properties of rocks, but cannot be imaged directly from the surface. Therefore understanding the relationship between seismic velocity and porosity is a fundamental goal of many rock physics models. However, the geological processes that control porosity, such as cementation, will often occur over very long timescales, making the experimental calibration of velocity-porosity trends challenging. In contrast, simulating such geological processes numerically in 3D digital rocks and digitally estimating elastic properties from the 3D volumes allows for velocity-porosity trends to be characterized in a reasonable time frame.

Here we first simulate initial deposition of two carbonate sediments under gravity - grainstone (near spherical grains) and coquina (shell fragments), and then simulate their cementation. These simulations output a set of 3D volumes (or digital rocks) of varying controlled porosity with otherwise constant and known mineral and grain phases. Combining these models with the known velocity and densities of the relevant constitutive phases, we generate a set of velocity and density models corresponding to each stage of cementation. These models are then used as input to a 3D acoustic staggered-grid finite difference simulation of wavefield propagation, from which we estimate bulk seismic velocity and calculate the estimated bulk modulus.

The resulting bulk modulus show realistic trends with porosity, all within the physical limits imposed by the Hashin-Shtrikman bounds. We observe anisotropy in the measured velocity (and bulk modulus) consistent with structural anisotropy due to the settling of elongate grains under gravity. We also observe a critical porosity effect in the coquina samples, where there is a sudden drop in bulk modulus as porosity increases above 30%, attributed to the complex ray paths though convex grain shapes. We use the

resulting bulk velocity-porosity trends to test competing rock physics models, including one that accounts for varying effective pore aspect ratio with porosity. By inverting our digital elastic measurements for effective pore aspect ratio, we find our modelled rocks follow a power-law relationship between effective pore aspect ratio and porosity. The inversion results from digital rocks are also consistent with those obtained from a suite of laboratory carbonate grainstones. Finally, we investigate the effect of structural anisotropy from the resulting rock fabrics on the resulting elastic properties in three orthogonal directions using a sensitivity analysis. The results show the optimal model to be relatively insensitive to the degree of anisotropy in the fabric. Our approach paves the way to use the new rock physics model to link observed changes in effective pore aspect ratio to changes in porosity due to a wider range of geological processes, for example fracturing, dissolution and compaction.

6.2 Introduction

Geophysical properties such as seismic velocity and electrical resistivity, depend strongly on porosity, and the form of this relationship is fundamental to applications of imaging and modelling natural processes in the solid Earth. Specific examples include, the characterization and monitoring of geomechanical processes such as compaction (Zimmer, 2004) or elucidating the process of rock fracturing (Pyrak-Nolte *et al.*, 1990). Seismic velocity is often used to monitor hydraulic processes where spatio-temporal changes in the seismic velocity may be caused by fluid flow and/or changes in effective stress during subsurface injection or production (Arts *et al.*, 2004; Brown, 2002; Guilbot and Smith, 2002; Stork *et al.*, 2018). Seismic velocity is also sensitive to diagentic processes, such as cementation or dissolution (Dvorkin and Nur, 1996; Fabricius, 2003; Weil *et al.*, 2011).

Diagenesis is any physical, chemical, or biological alteration of sediments to form a sedimentary rock (Bathurst, 1972; Tucker and Wright, 2009). It strongly influences reservoir quality, with strong controls on porosity (Bjørlykke *et al.*, 1989; Moore, 1989), permeability (Bloch *et al.*, 2002; Nadeau, 1998), and wettability (Barclay and

Worden, 2000). Understanding diagenetic processes, and how geophysical properties relate to them, is therefore important for hydrocarbon production, CO_2 injection, and groundwater resource management. However, measuring geophysical properties associated with diagenetic processes can be very challenging, even in a controlled laboratory environment. Diagenesis often occurs over very long timescales and in extreme conditions making it impractical to reproduce in the laboratory. In some experiments, microbial-induced calcite precipitation has been shown to accelerate cementation (Karol and Berardinelli, 2003; Saneiyan *et al.*, 2018), but these methods require elaborate and expensive experimental apparatus. This practical problem is a prime motivation for using digital rocks, where geological or diagenetic processes such as cementation can be simulated in principle over any time scale. A digital rock is a three-dimensional representation of a rock fabric, where individual phases within a rock (e.g., each mineral component and pore space/fluid) is known for each voxel in three dimensions (see Andrä *et al.* (2013a,b) for an extensive review of digital rock physics). Digital rock models are far more flexible and far less expensive to run than laboratory experiments, and can be used to test hypotheses and establish trends of evolving geophysical properties including specific diagentic processes. Digital rock physics begins with a starting model from a three-dimensional image, most commonly obtained from high resolution x-ray micro-tomography, where data is segmented into individual phases (e.g., grain, pore, cement). Bulk rock properties can then be estimated, such as permeability (Martys *et al.*, 1999; Keehm, 2003), seismic velocity (Saenger *et al.*, 2000; Saenger, 2008; Arns *et al.*, 2002), thermal conductivity (Wiegmann and Zemitis, 2006) and electrical resistivity (Liu *et al.*, 2009; Zhan *et al.*, 2010). Rather than the x-ray imaging of real rocks, here we simulate rock deposition and cementation to form digital rocks.

There are several examples of process-based simulation of cementation in digital rocks, including isopachous and syntaxial cementation in both sandstones (Mousavi and Bryant, 2012; Latief *et al.*, 2010) and carbonates (Biswal *et al.*, 2007; Mousavi *et al.*, 2012). However, the physical properties investigated during cementation are most commonly transport properties such as permeability and electrical conductivity

(e.g., Keehm *et al.* (2001)); to date there have been no applications of process-based cementation modelling for the estimation of elastic properties using digital rocks.

In order to interpret a change in the measured seismic velocity, a suitable rock physics model is required. There is an abundance of methods used in rock physics for the modelling of elastic moduli-porosity or velocity-porosity data. Empirical methods, such as Eberhart-Phillips *et al.* (1989); Gardner *et al.* (1974); Han *et al.* (1986), are entirely based on empirical matches to trends in observed data. Thus, any inference of physical significance from using such models can be unreliable. Bounding models (Voigt, 1889; Reuss, 1929; Hashin and Shtrikman, 1963) and bounding average models (Hill, 1952) recognize the uncertainty of elastic moduli for a given porosity and therefore give a range of moduli, where the exact value depends on geometric factors of the medium. However, these bounds can be far too broad for many practical applications. Inclusion-based models such as Eshelby (1957); Mori and Tanaka (1973); Kuster and Toksöz (1974); Berryman (1992) assume an unrealistic, ellipsoidal inclusion shape embedded into a background material, but having this physics-based approach generally leads to more intuitive interpretation and model results that more closely match real-rock scenarios. Conventionally, inclusion models assume a constant inclusion shape to characterize an elastic modulus-porosity trend; recently Cilli and Chapman (2019) explored the potential for a variable inclusion aspect ratio related to porosity by a power law, which proved a better fit to existing elastic moduli-porosity data than models which ignore the scaling of inclusion aspect ratios with porosity.

Here, we develop a process-based model for deposition and cementation in digital rocks, combined with the finite-difference simulation of wave propagation, and show that it is an effective method of developing understanding of changes in elastic properties. In addition we compare the Cilli-Chapman analytical rock physics model for a material with ellipsoidal inclusions with a commonly-used competing model. We compare these models using a statistical model selection method known as the corrected Akaike information criteria AIC_C (Akaike, 1973; Hurvich and Tsai, 1989), for their ability to capture the effects of varying cementation, cement type, and initial rock fabric without

over-fitting. We also investigate the effect of underlying anisotropy on the relationship between porosity and elastic properties.

In this study, we describe the method used for generating digital rocks, including the simulated deposition of the primary grains under gravity, followed by cementation. Following this we demonstrate the method of estimating the bulk seismic velocity and elastic modulus using a rotated-staggered-grid finite-difference numerical simulation (Saenger and Bohlen, 2004). We introduce the two existing inclusion models used for elastic moduli-porosity trends, and describe the method for selecting the most appropriate model (AIC_C), which is particularly important for comparing models with different numbers of model parameters. We compare results for grainstone (ellipsoidal grains) and coquina (shelly fragments) digital rocks, with two different types of cementation, and also investigate the effect of the initial structural anisotropy on the evolution of the elastic properties with cementation. Finally, we validate the model by comparing results from synthetic digital grainstone rocks with those of laboratory measured elastic data from Fournier *et al.* (2011).

6.3 Method

The methods used in this paper consist of a three part modelling approach. First is the process-based modelling of initial deposition and subsequent cementation to generate a suite of digital rocks. Anisotropy in the fabric is introduced due to the ellipticity of the clasts, and horizontal settling due to gravity. For a random horizontal orientation this results in bulk transverse isotropy. Secondly we model wavefield propagation through each digital rock to estimate bulk elastic properties. Finally we statistically compare the modelling performance of the Cilli-Chapman model (variable inclusion aspect ratio) and the commonly used differential effective medium theory model (constant inclusion aspect ratio) to the measured elastic data using the corrected Akaike information criterion.

6.3.1 Deposition and Cementation of Digital Rocks

To generate digital rock models with different cement types, we follow the methodology described in detail by Hosa and Wood (2017). The process first involves the analysis of thin-section images, so that a realistic distribution of grain shapes and sizes are used for the initial deposition. The deposition and initial packing of grains is generated in a process-based simulation of grains falling and settling on one another in a 3D space under gravity. The model allows for heterogenous shapes and sizes in the grains, modelled with normal distributions. In this study we investigate two grain shapes: ellipsoidal grains and shells, representing those of end-member carbonate facies such as carbonate grainstones and coquinas respectively. The initial rock fabrics from the resulting deposition and settling due to gravity are shown as the high porosity slices (panels a and d) in Figures 6.2, 6.3 and 6.4. The initial porosity for coquina ($\phi = 90\%$) is much higher than that of the grainstone ($\phi = 38\%$), which is a result of the difference in the geometries. Wadell (1932) defines the sphericity ψ as: $\psi = S_{sphere}/S_{grain}$, where S_{sphere} is the surface area of a sphere with the same volume of the grain, and S_{grain} is the actual surface area of the grain. Deviations from $\psi = 1$ (decreasing sphericity) results in higher porosity. The average sphericities for coquina and grainstone are $\psi_C = 0.04$ and $\psi_G = 0.14$, respectively.

After the simulation of the process of deposition, the resulting volume containing the grains is cropped and voxelized into a 300^3 voxel domain. The voxel sizes are 10 μm^3 for the grainstones and 0.1 mm^3 for the coquina, so the digital rock samples have the dimensions $3 \times 3 \times 3$ mm and $30 \times 30 \times 30$ mm, respectively. We then model calcite cement growth. The model considers two different grain types: polycrystalline and monocrystalline, which develop different types of early marine calcite cement - isopachous and syntaxial, respectively (Figure 6.1). The syntaxial cement, which is associated with monocrystalline grains, is modelled in the shape of a parallelepiped (a prism whose all six faces are all parallelograms) and approximates the rhombohedral crystal form of calcite, which is a common calcite crystal form. In nature, syntaxial cement grows rapidly until euhedral crystal faces are reached (epitaxial growth) and

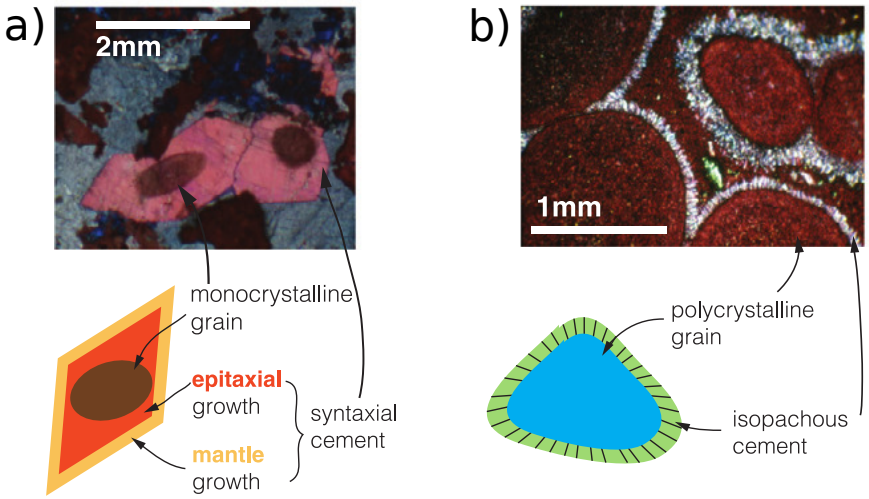

Figure 6.1: a) Thin-section image and schematic illustrations of syntaxial cement growth, where cement grows in the rhomobohedral crystal form of calcite, associated with monocrystalline (single crystal) grains b) Thin-section image and schematic illustrations of isopachous cement growth, where cement is precipitated evenly around polycrystalline grains. Figure adapted from Hosa and Wood (2017).

approximate crystal form of calcite is achieved. The growth on the euhedral surfaces proceeds at a slower pace (mantle growth). Our method models the first, rapid stage of syntaxial growth. Isopachous cement, which develops on polycrystalline grains (consisting of many small crystals), is modeled as a layer of cement precipitated evenly around the grains. For both cement types, cementation progressed iteratively by adding a 1-voxel thick layer of cement in each iteration.

The modelled process of deposition and cementation for generation of digital rocks is greatly simplified compared to real-world scenarios, and has several underlying assumptions: several processes are ignored such as the agitation of deposited material and re-arrangement of deposited grains due to compaction, therefore initial porosities prior to cementation are unrealistically high. This is not considered to be a problem as the focus of this study is on the *change* in porosity and how seismic velocity responds. The cementation method used here assumes fully saturated media, that cementation is uniform throughout the rock, and cement grows on all grains. In reality, not all pore space is accessible by percolating fluids, and cementation is linked to the fluid

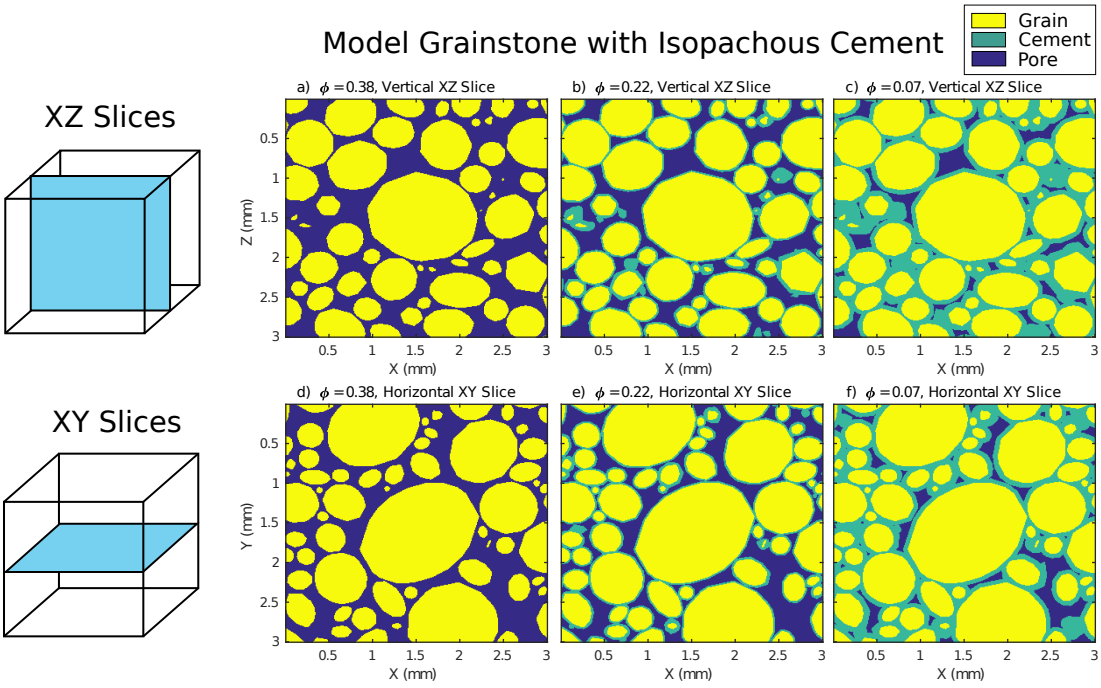

Figure 6.2: Example vertical (a-c) and horizontal (d-f) slices through digital rock models at varying degrees of cementation. The model uses a grainstone morphology prior to cementation, which does not change with time (yellow clasts), and a isopachous cement type that grows with time (green) into the pore space (blue).

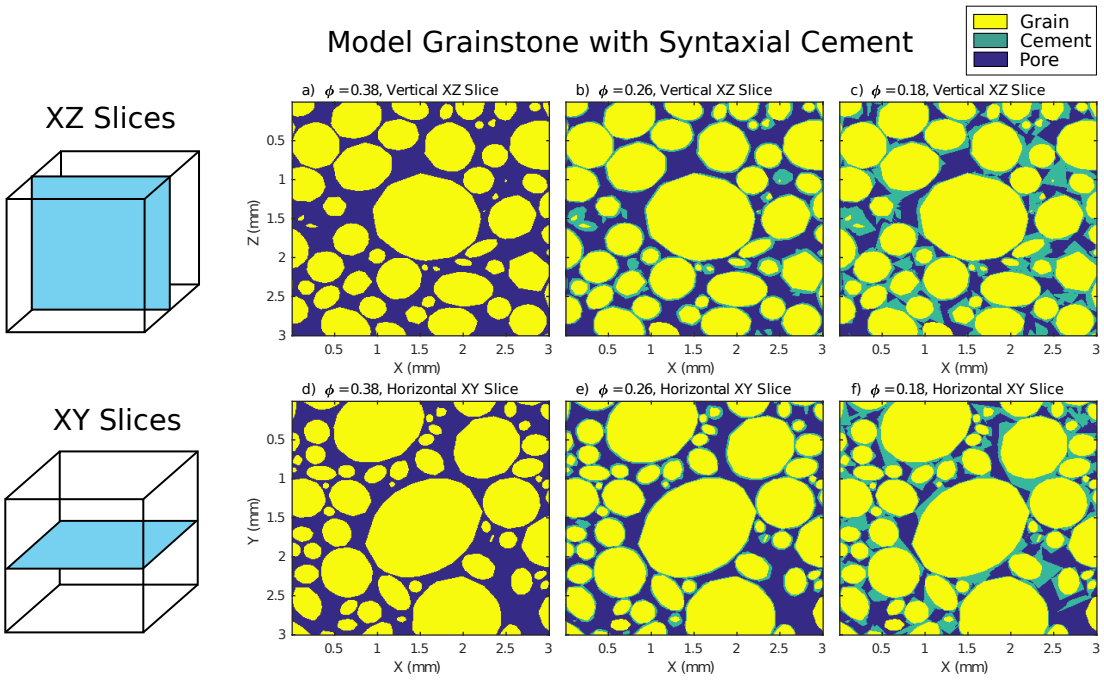

Figure 6.3: Example vertical (a-c) and horizontal (d-f) slices through digital rock models at varying degrees of cementation, using a grainstone morphology prior to cementation and a isopachous cement type, which does not change with time (yellow clasts), and a syntaxial cement type that grows with time (green) into the pore space (blue).

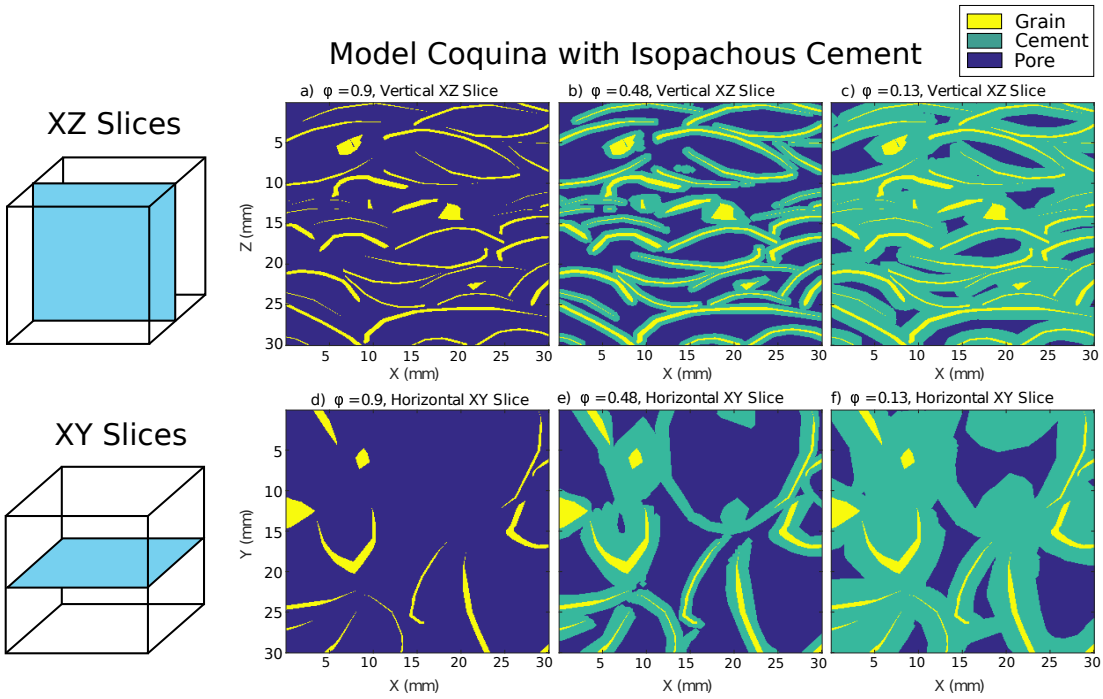

Figure 6.4: Example vertical (a-c) and horizontal (d-f) slices through digital rock models at varying degrees of cementation, using a coquina morphology prior to cementation and a isopachous cement type, which does not change with time (yellow clasts), and a syntaxial cement type that grows with time (green) into the pore space (blue).

dynamics within the pore space. The current implementation of our method includes the continuation of precipitation in pores even after they are cut off from the percolating pore space. In reality, some sub-resolution porosity would likely allow the percolation of pore fluids but not to the extent we allow in our models.

To examine the effect of cement type, we generate a range of digital rock models using the same starting grainstone fabric assuming either polycrystalline or monocrystalline grains, therefore modeling both isopachous and syntaxial cementation. Representative slices through the grainstone models are shown in Figures 6.2 and 6.3. We also examine the effect of varying the initial rock deposition, where we use shell fragments representing a coquina, and model isopachous cementation. Two-dimensional slices through these models are shown in Figure 6.4. The sections show horizontal alignment of elongate grains, and thus some emergent anisotropy. This may be due to finite size effects, for larger samples we might expect transverse isotropy in the fabric due to sedimentation under gravity. We quantify the degree of anisotropy DOA (Harrigan and Mann, 1984) of the initial fabrics prior to cementation as:

$$DOA = 1 - \frac{min(\lambda)}{max(\lambda)}, \tag{6.1}$$

where $min(\lambda)$ and $max(\lambda)$ are the minimum and maximum eigenvalues of the data cloud obtained by mean intercept length analysis. Mean intercept length analysis determines the number of matrix voxels that intersect with a set of oriented rays sent through the volume at different angles. The mean number of intersecting voxels as a function of angle forms the data cloud then used in eigenvalue analysis. When $DOA = 0$, the fabric is perfectly isotropic, and the increases to $DOA = 1$, the fabric exhibits stronger anisotropy. Both coquina and grainstone initial fabrics exhibit some emergent structural anisotropy. The details of the ranges of models for each rock type are documented in Table 6.1.

Table 6.1: Range of Digital Rock Models, where N is the number of models

Initial Fabric	Cement	N	Porosity Range	Degree of Anisotropy
Grainstone	Isopachous	6	6.6-38%	0.51
Grainstone	Syntaxial	20	18-38%	0.51
Shells	Isopachous	21	0.1-90%	0.55

6.3.2 Estimating Elastic Properties

The digital rock models described in Table 6.1, where every voxel has an assigned phase (either pore fluid, calcite grain or cement), are converted into corresponding 3D models of local velocity and density (assuming isotropic mineralogy for each phase). At this stage of the modelling we assume the properties of the precipitated cement to be the same as those of the calcite grains. The local velocity and density of calcite is taken from Mavko *et al.* (2009), to be $V_P = 6500$ m/s and $\rho = 2710$ kg/m^3. We take the pore fluid velocity and density to be $V_P = 1500$ m/s and $\rho = 1000$ kg/m^3. Each voxel is mapped to a regular grid of cells used as input to a three-dimensional finite-difference (FD) simulation of wavefield propagation (Moczo *et al.*, 2007). The FD method discretizes the wave equation on a grid and replaces spatial derivatives by FD operators using neighboring points. High-contrast discontinuities such as those between pores and mineral phases may cause instability problems on a staggered grid. We avoid these difficulties by implementing a rotated staggered grid technique (Saenger and Bohlen, 2004). We assume both point receivers and point sources as well as perfect transducer coupling, and use Ricker wavelets with central frequencies of 40 MHz and 4 MHz for the source time function in the grainstones and coquinas, respectively. The output is a set of synthetic seismograms from user-selected source and receiver locations. We treat these synthetic signals as if they were recorded in the laboratory, and estimate the bulk velocity from the origin time of the source signal, the arrival time of the first maximum (picked manually) and the known source-to-receiver distance. In order to measure any velocity anisotropy in the samples, we use three pairs of sources and receivers placed on opposite faces in orthogonal directions allowing for three measurements of velocity (V_P^X, V_P^Y, V_P^Z). We use the empirical relationship of Pickett (1963), which linearly

relates P and S wave velocities in carbonates, to estimate S wave velocity from the P wave velocity (i.e., $V_S = f(V_P)$). The bulk and shear moduli are then calculated using the following equations:

$$K = \rho\left(V_P^2 - \frac{4}{3}V_S^2\right) \tag{6.2}$$

$$\mu = \rho V_S^2 \tag{6.3}$$

The density ρ is known for each model by taking the volumetric average of densities for all voxel phases in each model. The resulting estimates for P-wave velocities are shown in Figure 6.5, where each subplot either represent a different initial rock fabric (coquina or grainstone), or a different type of cementation (isopachous or syntaxial). In each plot the bulk velocity lies between that of the pore fluid and the assumed local velocity of the grains and cement. For the coquina facies (Figure 6.5a) we see a dramatic drop in bulk velocity V_P at a critical porosity of $\phi_C \approx 30\%$. The trend then flattens asymptotically to a lower bound, equivalent to the velocity of the pore fluid (1500 m/s). This most likely reflects a critical porosity effect; due to the thin and convex shape of the shells used coquina deposition (Fig. 6.4a) there are very few grain-to-grain contacts at high porosity, thus the rock is effectively fluid-supported (i.e., a suspension). As cementation increases and porosity decreases below a critical porosity ($\phi < \phi_c$), the number of grain-to-grain contacts increases so that the rock becomes grain supported, and the velocity rapidly increases. The diagrams show bulk velocities measured in three directions. These synthetic data exhibit a drop in velocity at different porosities depending on orientation of the measurement. The initial fabric of grainstones use grain shapes which are much rounder than the shelly fragments of the coquina, and there are many grain-to-grain contacts. Consequently these digital rocks are always below ϕ_c and the curves in Figs. 6.5b and c exhibit a much smoother response to increasing cementation. We see an exponential trend for isopachous cementation (Fig. 6.5b) and a more linear one for syntaxial cementation, which is measured over a narrow porosity range (Fig. 6.5c). Both grainstone samples exhibit anisotropy, where V_P^Z (measured in the direction of the vertical axes in the upper panels of Figs. 6.2 and 6.3) is approx. 500 m/s faster than V_P^X and V_P^Y, as expected from the horizontal alignment in the fabric. The coquina facies also exhibits anisotropy, most notably in the critical porosity ϕ_C.

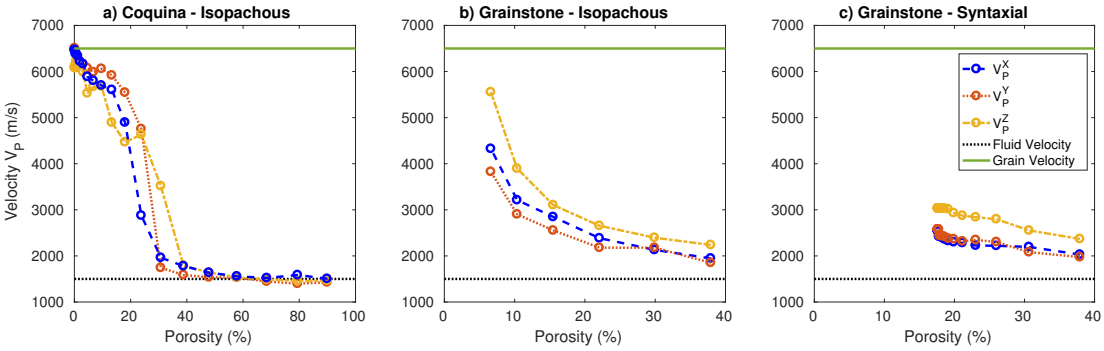

Figure 6.5: Bulk velocity-porosity trends measured in three orthogonal components: V_P^X (blue), V_P^Y (red), V_P^Z (green), for a) Coquina (shelly fragments) with isopachous cementation, b) Grainstone (ellipsoids) with isopachous cementation, c) Grainstone with syntaxial cementation. The lower bound of fluid velocity (1500 m/s) and upper bound of calcite grain and cement velocity (6500 m/s) are denoted by horizontal lines.

6.3.3 Rock Physics Modeling

Modelled elastic data estimated from synthetic digital rocks also provides an opportunity to test and validate existing analytical rock physics models. Here we test two existing analytical rock physics models: conventional differential effective medium theory (DEMT) as of Berryman (1992) and the Cilli-Chapman (CC) model (Cilli and Chapman, 2019). In conventional DEMT, a small volume of spheroidal inclusions with aspect ratio α and known elastic properties, are iteratively added into an initially homogeneous background medium with known elastic properties. After each iteration of added inclusions, the average properties of the average composite are calculated and used as background medium properties for the next iteration. When the the inclusion volume added per iteration becomes infinitesimally small, the elastic DEMT model can be described by the following differential equations:

$$(1-y)\frac{d}{dy}[K^*(y)] = (K_2 - K^*(y))P^{(*2)} \tag{6.4}$$

$$(1-y)\frac{d}{dy}[\mu^*(y)] = (\mu_2 - \mu^*(y))Q^{(*2)} \tag{6.5}$$

with initial conditions $K^*(0) = K_1$ and $\mu^*(0) = \mu_1$, where K_1 and μ_1 are the inclusion bulk and shear moduli; K^* and μ^* are the rock's effective bulk and shear moduli; y is the

inclusion volume fraction (i.e., porosity); P and Q are α-dependent geometric factors (Berryman, 1980) and their superscript denotes they are to be calculated with ellipsoids of phase 2 embedded in the effective background material. Thus, the estimated effective moduli K^*_{DEMT} and μ^*_{DEMT} are functions of the bulk and shear moduli of the two phases, the porosity, and the inclusion aspect ratio. There are several assumptions and limitations to the application of the DEMT method, for example that the bulk rock is assumed to be isotropic and inclusion shapes are idealized randomly-oriented ellipsoids. Also, the processes of incrementally adding inclusions to a background matrix is also entirely non-physical but rather a thought experiment, and does not represent the actual evolution of a rock's porosity.

In real rocks, pores are not ideal ellipsoids, and hence the inclusion aspect ratio is simply a parameter that quantifies the contribution of a rock's pore space architecture to the rock's overall elastic moduli. To make this distinction between the theoretical model inclusion aspect ratio and its applied physical interpretation, Fournier *et al.* (2011, 2014, 2018) refer to the applied DEMT parameter α as 'equivalent' pore aspect ratio (EPAR). Similarly, Cilli and Chapman (2019) synonymously label it the 'effective' pore aspect ratio. The EPAR for a given sample can be estimated by minimising the misfit between measured bulk modulus K_{meas} and the forward modelled moduli using Equations 6.4 and 6.5:

$$\Psi(\alpha) = ||K_{meas} - K^*_{DEMT}(K_1, \mu_1, K_2, \mu_2, y, \alpha)||_2. \tag{6.6}$$

The EPAR is estimated by finding the aspect ratio α that minimises Ψ, where the bulk and shear moduli of the two phases (K_1, μ_1, K_2, μ_2) and the porosity (y) are known.

Cilli and Chapman (2019) investigated how a rock's effective pore and grain aspect ratio (EPAR and EGAR) parameters changed with porosity for seven public domain datasets for elastic and electrical properties of carbonate rocks and concluded that these parameters vary with porosity as a power law, of the form:

$$\alpha = \Gamma \phi^{\xi} \,. \tag{6.7}$$

In the case of elastic modelling, where α represents EPAR, Equation 6.7 shows the model $\alpha = \Gamma =$ constant in the case of $\xi = 0$, consistent with the typical DEMT modelling approach.

By substituting Equation 6.7 into Equations 6.4 and 6.5, the resultant bulk and shear moduli, K^*_{CC} and μ^*_{CC}, can be calculated as functions of the bulk and shear moduli of the two phases, the porosity, and two parameters Γ and ξ. The Cilli-Chapman model uses an extra model parameter than the standard, constant-α DEMT model, so its effectiveness cannot be compared to the standard method on the residuals alone. Cilli and Chapman (2019) use log-relative likelihood analysis that justifies the extra parameter used in fitting the data.

Given our digitally measured velocities and porosities, as well as the known fluid and matrix elastic moduli, we inverted Equations 6.4 and 6.5 to estimate the EPAR of every rock sample. We inverted for the model parameters by minimising the misfit between each sample's measured (from Equation 6.2) and modelled bulk modulus. We display the inverted EPARs for each data set as a function of porosity on a log-log scale in Figure 6.6, and fit a line of best fit through each data set's inversion results. We calculated a close approximation $\{\Gamma_0, \xi_0\}$ of the true model parameters $\{\Gamma, \xi\}$ by the gradient and constant of these lines. As the inversion for each sample's EPAR was porosity-dependent, parameters $\{\Gamma_0, \xi_0\}$ are not necessarily equal to $\{\Gamma, \xi\}$. We thus performed a non-linear global optimisation to find the solution $\{\Gamma, \xi\}$ which minimise the l_2-norm misfit of all samples by directly substituting Equation 6.7 into Equations 6.4 and 6.5 with starting point $\{\Gamma_0, \xi_0\}$.

We use this inversion technique for four suite of bulk modulus-porosity data: 1) synthetically generated grainstones with syntaxial cementation, 2) synthetic grainstones with isopachous cementation, 3) synthetic coquinas with isopachous cementation, and

4) a subset of real-rock laboratory measured grainstone data from Fournier *et al.* (2011). This subset laboratory data consists of 80 outcrop samples, all exhibiting grainstone texture and with almost pure calcitic mineralogy. There is no presence of any inter-granular, inter-crystalline, or moldic porosity in these samples, consistent with the definition of the grainstone end-member model examined here. In principle, these textures could be examined in future work.

6.3.4 Comparing Competing Models

Following from the inversions using both the constant-α differential effective medium theory model and the variable-α Cilli-Chapman model, it is then necessary to test these competing models. Here we use the corrected Akaike information criterion (AIC_C) (Akaike, 1973; Hurvich and Tsai, 1989), which is a statistical tool used for model selection based on information theory. The conventional AIC method penalizes models with more modelling parameters (more complex models) and favours models with smaller misfits, thus dealing with the trade-off between data fit and model simplicity. This is necessary here because the conventional DEMT and the Cilli-Chapman models require different numbers of model parameters.

Let k be the number of parameters for a model, and $\hat{L}$ be the estimated likelihood function of the model (goodness of fit). The AIC value for a particular model is:

$$AIC = 2k - 2\ln(\hat{L}). \tag{6.8}$$

When the number of samples n is small, AIC becomes biased to models with more model parameters (McQuarrie and Tsai, 1998). As the datasets used here are relatively small, to therefore avoid this risk of over-fitting, we use the corrected Akaike Information Criterion AIC_C (Hurvich and Tsai, 1989; Cavanaugh *et al.*, 1997), defined as:

$$AIC_C = AIC + \frac{2k^2 + 2k}{n - k - 1}. \tag{6.9}$$

The absolute AIC_C value generally has little indication of the validity of a model (Burnham and Anderson, 2004); rather the difference between AIC_C values (ΔAIC_C) for competing models is the significant measure, where $\Delta AIC_C = AIC_C^{DEMT} - AIC_C^{CC}$.

Burnham and Anderson (2003) provide a practical rule-of-thumb method for the interpretation of ΔAIC_C values, suggesting that: if $\Delta AIC_C < 2$, the variable-α CC model has "insufficient" evidence to accept as the best model; if $4 < \Delta AIC_C < 7$, the CC model has "good" evidence and constant-α DEMT has considerably less evidence as the best model; and if $\Delta AIC_C > 10$, the variable-α CC has "compelling" evidence to be the best model (constant-α DEMT has negligible evidence). Here we use an extra category for where $7 < \Delta AIC_C < 10$, the CC model has "substantial" evidence.

6.4 Results

We employ these guidelines for interpreting ΔAIC_C values and provide all inversion results, including the output parameters Γ and ξ from the Cilli-Chapman model and α_{DEMT} from conventional differential effective medium theory, summarized in Table 6.2.

6.4.1 Grainstone

In order to test both the differential effective medium theory and Cilli-Chapman models described above, we first use elastic moduli estimated for grainstone samples using both syntaxial and isopachous cementation, as well as the laboratory measured grainstone data from Fournier *et al.* (2011). The results for both inversion techniques are shown as model fits to the data in Figure 6.6. The grainstone samples with syntaxial cementation (Figures 6.6a and b) show a strong power-law relationship between EPAR and porosity (plotting linearly on a log-log scale). The data points for bulk modulus clearly cross-cut the forward modeled line (dashed red) using DEMT, which assumes a constant aspect ratio for all porosities. The Cilli-Chapman model (variable aspect ratio) provides a significant improvement in data fit in these cases. This improvement is expected

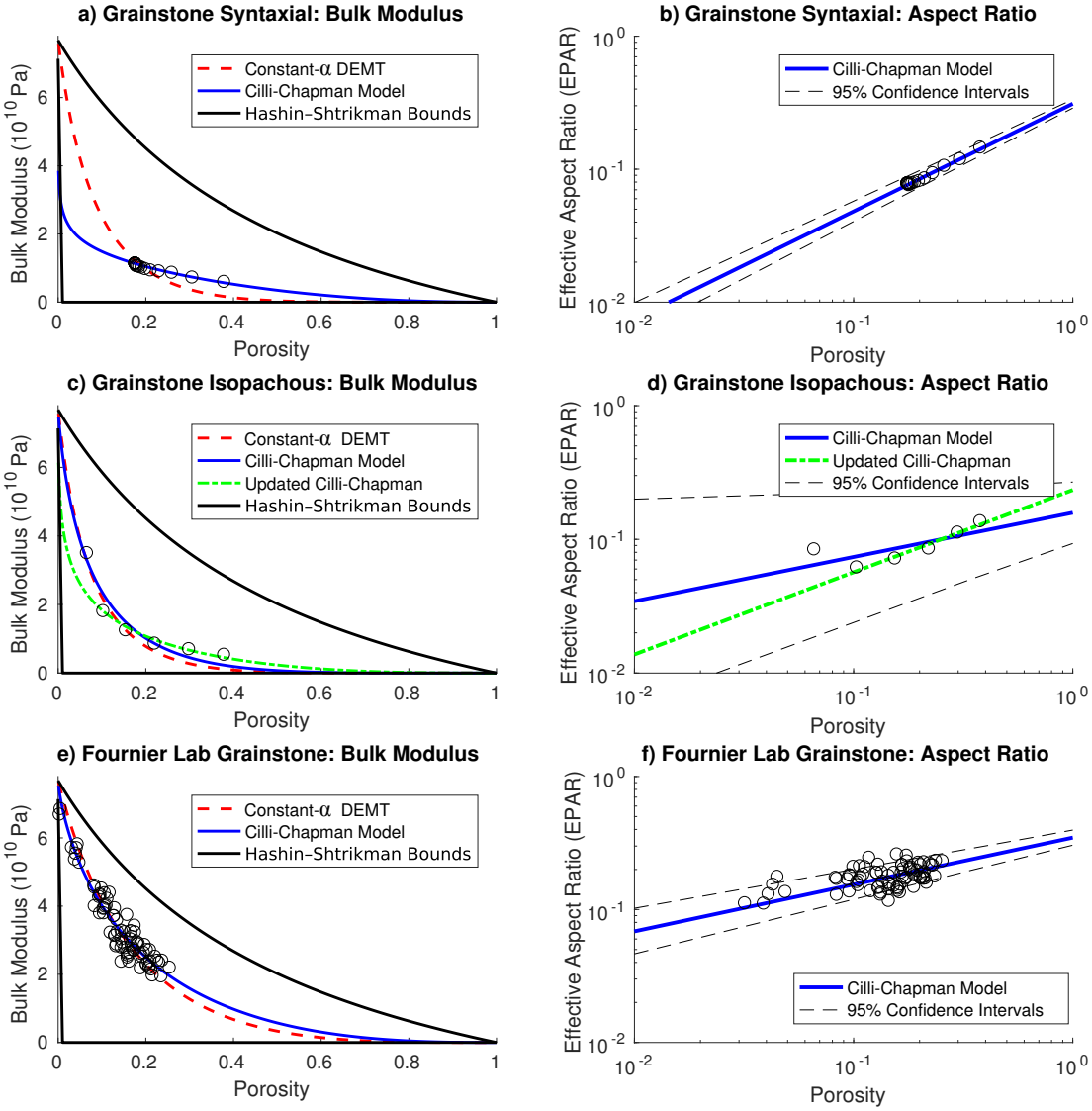

Figure 6.6: Rock physics modelling results for grainstone data. The left panels are the modelled bulk modulus trends using a constant-α DEMT model (dashed red) and the variable-α Cilli-Chapman model (solid blue). The right panels show inverted EPAR as a function of porosity. The figure shows results for: a-b) syntaxial cementation, c-d) isopachous cementation, e-f) laboratory measured grainstone data from Fournier *et al.* (2011). For the isopachous cementation data (c-d), we include an updated model (green), where the low porosity is rejected in the regression as the data point has Cook's distance d_C equal to 2.650, well above the recommended threshold $d_C > 1$ (Cook and Weisberg, 1982).

Table 6.2: Comparison of model inversion results

Figure	Data	ϕ Range	n	Γ	ξ	α_{DEMT}	ΔAIC_C	Preferred Model	Evidence
6(a-b)	Grainstone Syntaxial	18-37%	20	0.301	0.791	0.08	51.3	$\xi > 0$	Compelling
6(c-d)	Grainstone Isopachous	6.6-37%	6	0.014	0.139	0.07	-3.80	$\xi = 0$	Good
6(c-d)	Grainstone Isopachous (High ϕ range)	10.4-37%	5	0.213	0.562	0.07	9.13	$\xi > 0$	Substantial
6(e-f)	Fournier Lab Grainstones	0.4-26%	80	0.227	0.238	0.17	17.9	$\xi > 0$	Compelling
7	Coquina Isopachous	0.01-90%	21	0.359	0.147	0.23	-9.03	$\xi = 0$	Substantial
7	Coquina Isopachous (2x ϕ ranges)	0.01-21% 21-90%	13 8	0.727 0.844	0.279 1.757	0.23	53.9	$\xi > 0$	Compelling

to some degree, as the Cilli-Chapman model uses an additional modeling parameter, therefore an addition degree of freedom. As shown in Table 6.2, despite the additional modeling parameter, the Cilli-Chapman model has compelling evidence as the best model ($\Delta AIC_C = 51.3$).

Grainstone samples using isopachous cementation shows a similar trend (Figures 6.6c and d), where there is clear variation of EPAR with changing porosity. However the lowest porosity sample ($\phi = 6.6\%$) clearly does not follow the trend exhibited by the other samples. According to AIC_C, there is good evidence that DEMT is the best model to describe the data ($\Delta AIC_C = -3.8$). The low porosity sample can be identified as 'highly influential' to the model according to Cook's distance, which is a statistical measure used to identify the influence of individual data points when performing least-squares regression (Cook, 1977). Cooks distance of the $\phi = 6.6\%$ sample is $d_C = 2.65$, well above the recommended threshold for a sample to be considered highly influential, where $d_C > 1$ (Cook and Weisberg, 1982). This does not necessarily give grounds to reject the sample from the inversion, but indicates the data point should be examined more closely, and possibly indicates the limits of using digital rock physics at such low porosities (this is further discussed in Section 6.5.2). For comparison, Figures 6.6c and d include inversion results using Cilli-Chapman model for both the full porosity range (blue) and one excluding the low porosity sample (green). Where the low porosity value is excluded $\Delta AIC_C = 9.13$, which suggests stronger evidence for the Cilli-Chapman model as the preferred model.

Figures 6.6e and f show inversion results for the laboratory measured 'real-rock' grainstone data. Compared with the synthetic digital rock results, the EPAR-porosity relationship exhibits a similar Γ value, but a significantly lower ξ value (gradient of best fit line through log-log EPAR-porosity plot). When ξ is small, the Cilli-Chapman model closer resembles the constant-aspect ratio DEMT model. Despite the small variation in models, the improvement in data fit is regarded as statistically significant, where $\Delta AIC_C = 17.9$, due to the large number of data points. The difference between digital rock simulations and laboratory results is discussed in Section 6.5.1.

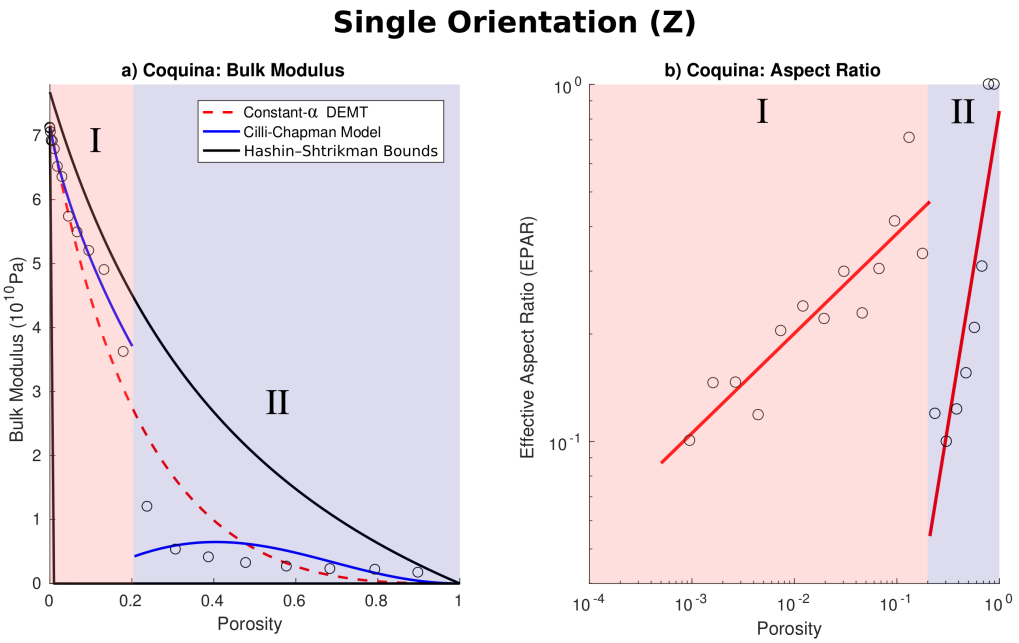

Figure 6.7: Rock physics model comparison for Coquina samples, using bulk modulus inferred from velocities measured perpendicular to shell orientation (Z direction, vertical direction in Figures 6.4a-c). a) Bulk modulus-porosity trend for a constant-α DEMT model (dashed red) and the variable-α Cilli-Chapman model (solid blue) separated into two separate porosity ranges (critical porosity $\phi_c = 0.21$) with two power-law relationships. b) Inverted aspect ratio α (circles) and two linear trend-lines: I) $\phi < 0.21$ and II) $\phi > 0.21$. Porosity range I is below critical porosity ($\phi < 0.21$) and exhibits the previously observed power-law (linear on log-log scale) relationship. Stage II is above critical porosity ($\phi > 0.21$), where inverted aspect ratio values drop initially, then increase to $\alpha = 1$.

6.4.2 Coquina

The estimated bulk modulus and the inverted Effective Pore Aspect Ratio (EPAR) values for the Coquina samples, using the same method as in Section 6.4.1 are shown in Figure 6.7. This data is using the velocity measurements taken only in the direction perpendicular to shell orientations (V_P^Z in Figure 6.5a and the vertical direction in Figures 6.4a-c). The coquina samples contain a very large porosity range ($\phi = 0.1 - 90\%$), and exhibit much more complex pore shapes in comparison with those in the grainstone samples. There appears to be two distinct EPAR-porosity trend-lines, separated into stages: I) $\phi < 0.21$ and II) $\phi > 0.21$ in Figure 6.7b. This is interpreted as a critical porosity effect, where above a given porosity ϕ_C the rock can be

treated as fluid supported, which also explains the abrupt drop in bulk modulus where $\phi > 0.21$ in Figure 6.4a. Below this threshold the rock is grain or clast-supported. When the full range of porosity samples are included in the inversion the constant-α DEMT model is statistically much stronger ($\Delta AIC_C = -9.03$) than a single power law relationship. However, when two separate inversion are performed for porosities both above and below $\phi_C = 0.21$, where two power law relationships doubles the number of model parameters, $\Delta AIC_C = 53.9$, which suggests strong evidence for the two stage Cilli-Chapman model as the most appropriate.

The EPAR of a rock is related to its solid frame's stiffness. When $\alpha = 0$, the frame is as weak as possible and the rock's moduli coincide with the lower Hashin-Shtrikman (Hashin and Shtrikman, 1963) and Reuss (Reuss, 1929) bounds (Norris, 1985). A fluid-filled porous rock with a measured porosity above its critical porosity is, in effect, a suspension of solid material in a background of fluid and has elastic moduli coinciding with the lower Hashin-Shtrikman bound. In the case of the Coquina samples (Figure 6.7), we see the rock's EPAR increasing with porosity in stage I, implying the matrix is becoming relatively more stiff as porosity increases. At the interface between stage I and stage II, however, the inverted EPARs plummet as the rock passes its critical porosity and becomes significantly softer. In stage II the rock is acting approximately as a suspension. We notice the Coquina's measured bulk modulus does not go exactly to the Hashin-Shtrikman lower bound, but rather seems to stay at an approximately constant value for all porosities above the critical porosity. The way in which the digital rocks have been generated, involves the deposition of falling grains and settling due to gravity, where grain-to-grain contacts must be present. Therefore the media cannot be true suspensions under gravity, though a critical porosity effect is still observed during dynamic wave propagation. Figure 6.4 shows that even at 90% porosity, there are some load-bearing connected paths of matrix material from one side of the digital rock to the other under gravity. We speculate that if connected paths like this exist over all porosities, the bulk modulus will be higher than the Hashin-Shtrikman lower bound, as observed in Figure 6.7. The bulk modulus remains approximately constant in the high porosity samples of Figure 6.7 while the upper and lower Hashin-Shtrikman bounds

converge with increasing porosity. The bulk modulus is hence becoming closer to the upper Hashin-Shtrikman bound with increasing porosity in stage II, which is the cause of the observed increasing EPAR with porosity in this stage.

Both models are constructed assuming background medium, with spheroidal inclusions with a given aspect ratio α embedded within. Therefore using either DEMT or Cilli-Chapman models in suspensions, where the porosity is higher than the critical porosity ϕ_C, does not follow any physical intuition and does not allow for physical interpretation. It may therefore be more appropriate to consider a separate rock physics models for suspensions (e.g., Wood (1941)) in stage II.

6.4.3 Anisotropy

In the previous section measurements from a single orientation were used as input to the rock physics inversions for coquina samples. This was done to prevent the smoothing out of the critical porosity effect, as each orientation exhibits it's own distinct critical porosity. The difference in orientations is visible in Figure 6.5a, where velocity abruptly drops at different porosities for each of the three orientations, to approximately the velocity of the pore fluid (1500 m/s). Using an average of all orientations for bulk modulus as input data to the rock physics inversions results in a different trend than that observed in the single-orientation inversion. Figure 6.8 shows the inversion results using an average bulk modulus, where the inverted EPARs as a function of porosity appears to follow three separate power-law trends lines at different porosity stages: I) <11.5%; I+II) 11.4-41.75%; II) >41.75%. Stage I can be physically interpreted in the same way as before, where the medium is grain supported during wave propagation, and exhibits the usual power-law relationship between porosity and aspect ratio. Stage I+II is an intermediate phase, where two orientations exhibit a critical porosity effect. This intermediate stage is an artifact of the averaging across the three orthogonal directions. In stage II, moduli from all orientations are close to the lower bound therefore all orientations can be treated as a suspension during dynamic wave propagation, thus stage II exhibits a similar aspect ratio-porosity trend to stage II for the single-orientation coquina inversion in Figure 6.7b.

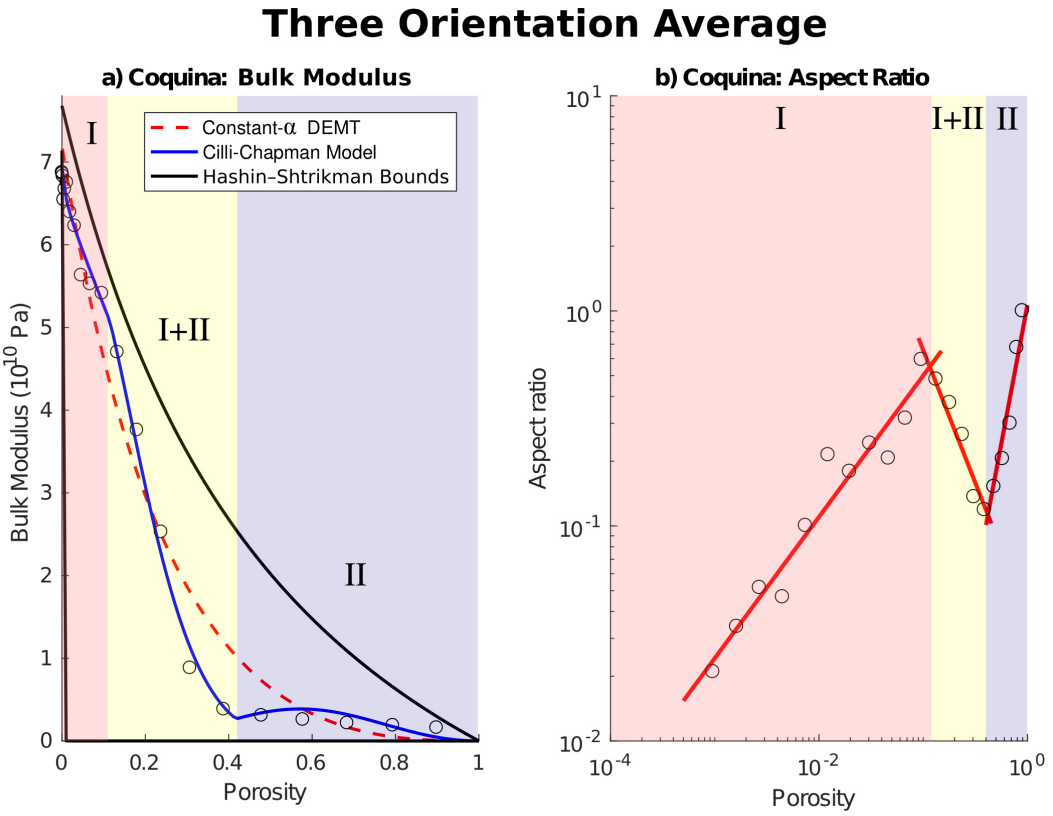

Figure 6.8: Rock physics model comparison for Coquina samples, using data averaged across three orthogonal orientations. a) Bulk modulus-porosity trend for a constant-α DEMT model (dashed red) and the variable-α Cilli-Chapman model (solid blue) separated into stages at different porosity ranges: I) <11.5%; I+II) 11.4-41.75%; II) >41.75%, where the intermediate stage is an artifact of averaging across different critical porosities exhibited by each orientation (Fig. 6.5a). b) Inverted aspect ratio α (circles) and three linear trend-lines.

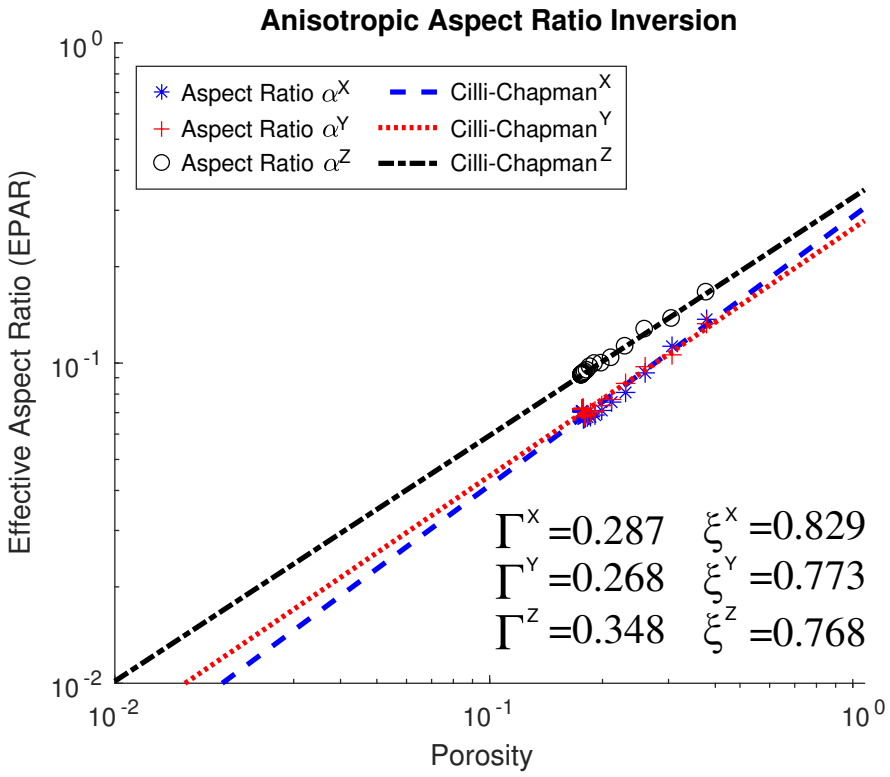

Figure 6.9: Inverted aspect ratio α as a function of porosity, for grainstones with syntaxial cementation. Measurements are made using elastic data measured in three orthogonal directions (the input velocity measurements are shown in Figure 6.5c). Γ (aspect ratio α at the porosity ϕ=1 intersect) and ξ (gradient of the trend-line on log-log scale) for each orientation are labelled.

Figure 6.5b and c highlight elastic anisotropy in the initial fabric of the grainstones, where velocity measured in the Z direction (vertical direction in Figures 6.3 and 6.2a-c) is approximately 500 m/s faster than V_P^X and V_P^Y. To further understand the effect of anisotropy on the rock physics model inversions, we invert for the independent EPAR parameters $(\alpha_X, \alpha_Y, \alpha_Z)$ using bulk modulus calculated from the three separate orientations, using the grainstone samples with syntaxial cementation. The resulting inverted EPAR as a function of porosity are shown in Figure 6.9. The results are consistent with a bulk seismic anisotropy that is traversly isotropic, where $V_P^Z > V_P^X \approx V_P^Y$ leading to $\alpha^Z > \alpha^X \approx \alpha^Y$ at all porosities in Figure 6.9. This is consistent with the input model fabric due to sedimentation under gravity. Interestingly the effect of anisotropy is only on the Γ parameter in the Cilli-Chapman model (the theoretical inclusion aspect ratio α where porosity $\phi = 1$), whereas ξ (the gradient of the trend-line on a log-log scale) is approximately constant, independent of orientation and anisotropy. In this case, if bulk modulus is inferred from measured velocity along a single orientation (as is often the case in laboratory experiments), then the estimated ξ parameter can be assumed to be representative of the entire medium.

6.5 Discussion

6.5.1 Comparison of modelled and real data

When comparing the synthetic data from modelled digital rocks and those of the 'real' laboratory measured grainstones, a significant difference between the inverted power-law relationships is observed (Figure 6.6), particularly the values of ξ (in Equation 6.7). This value denotes the gradient of the aspect ratio-porosity trend-line on a log-log graph, and reflects the sensitivity of the EPAR to porosity changes. We interpret the high ξ values for digital rocks to be a product of considering cementation to be the only process occurring, essentially ignoring other physical effects. This results in much smoother trends with lower variance in the synthetic data compared to the data from real rocks. As porosity increases, the digital rocks show increasing EPAR, meaning the rock frame becomes relatively stiffer. However in reality, other physical

effects also operate as porosity increase, such as the stiffness of grain contacts. Rocks with high porosity can be poorly consolidated, these samples would exhibit relatively low stiffness, therefore a low inverted EPAR. These different processes occurring and acting against each other essentially reduce the sensitivity of the effective pore EPAR to porosity (reducing ξ). A digital rock model incorporating changes in both cementation and grain contact stiffness could overcome this observed difference, but we leave this for future work.

6.5.2 Digital rocks at low porosity

In real rocks, pore structures are found to be fractals, i.e., the geometric features of the pore space are similar across all scales. At the smallest scales the estimation of physical properties of porous rocks are hampered by the resolution of the 3D images, mainly due to the presence of unresolved microporosity. In digital rocks that attempt to emulate real ones, the smallest possible pore is equivalent to a single voxel with a cubic shape. Therefore digital rocks cannot replicate the fractal dimensions of a real rock, and particularly at low porosities, the pore shapes become unrealistic. This could be an explanation for the outlier result for the low porosity sample ($\phi = 6.6\%$) of the grainstones using isopachous cementation seen in Figures 6.6e and d, which exhibits an EPAR higher than expected assuming a power-law relationship. As porosity decreases due to cementation, individual pore shapes become more cubic (closer to a sphere where $\alpha = 1$) and therefore relatively stiff. The inversion results from the laboratory measured grainstones (Figures 6.6e and f) do not show this increase of EPAR at lower porosities indicating the phenomenon is an artifact of the finite bandwidth scaling of the digital rock. This can somewhat be overcome by increasing the resolution of the digital rocks, therefore increasing the porosity range where digital rock microstructure remains valid.

6.5.3 Critical porosity and beyond

Digital rock physics provides an insight into the elastic properties of media that either do not often occur in nature, or would be challenging to produce in laboratory experiments,

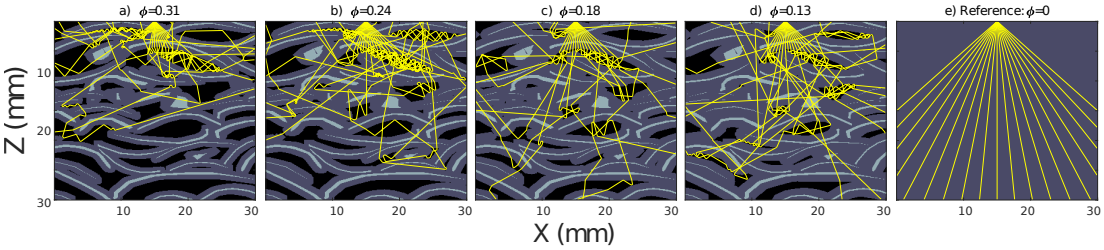

Figure 6.10: 2D ray tracing (Margrave, 2000) results using the vertical slices through the center of coquina models with increasing cementation, over the porosity range that exhibits an abrupt increase in seismic velocity. Rays originate from the center-top of the models, and are shown for a 90° aperture with 5° intervals. Rays terminate when they leave the bounds of the velocity model.

such as the very high porosity of the initial coquina model prior to cementation. This has allowed us to observe critical porosity effects associated with a transition from grain-supported to fluid-supported textures during dynamic wave propagation. The critical porosity ϕ_C is generally defined as a threshold when porosity $\phi > \phi_C$, the medium can be treated as a fluid supported suspension, and when $\phi < \phi_C$ the medium is grain supported. However, we have previously stated that grain-to-grain contacts exist across all porosities under static load, though a critical porosity effect is still observed. To explore this further we take vertical slices through the center of four volumes, over the porosity range that exhibits the abrupt change in bulk modulus. We use the slices, converted into velocity models (following the same method described in Section 2.4), as input into the ray-tracing software of Margrave (2000). This method takes a fan of rays from a user-selected source location, and calculates the ray path, which terminates when it leaves the bounds of the model. This process is to illustrate the difference in ray path complexity, rather than calculate absolute ray paths, as our finite-difference simulations are not limited to a 2D plane. The output shown in Figure 6.10 gives an idea of how waves travel through each model. At high porosity (Figure 6.10a) waves take very complex paths, with many internal reverberations. For a ray to traverse the full length of the medium (necessary for the measurement of seismic velocity with conventional experimental geometries) would require to take a complex path through grain and cement, or travel through a large amount of pore fluid. Contrast this with a lower porosity model (Figure 6.10d), where rays are transmitted through the full length of the model, and paths are considerably simpler (fewer reflections). Therefore

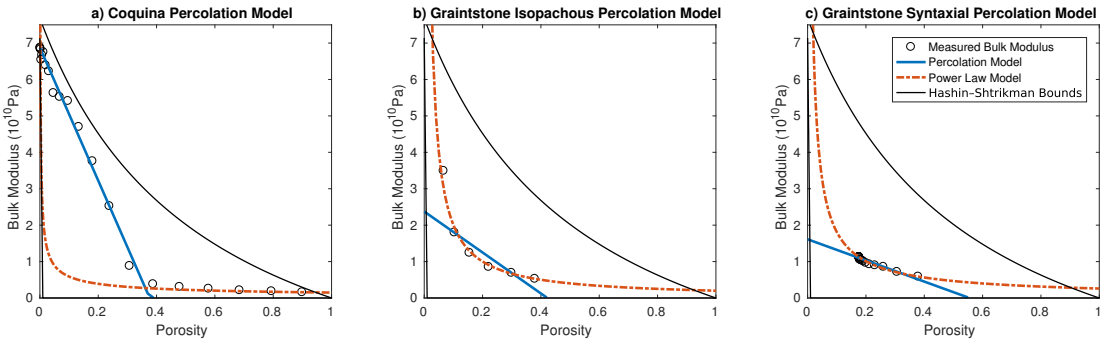

Figure 6.11: Comparison of some alternative empirical models for fitting bulk modulus-porosity data: a percolation model using Equation 6.10 (blue) and power law model using Equation 6.11 (red) for the coquina (a), grainstones with isopachous (b) and syntaxial cement (c). The black lines represent the Hashin-Shtrikman bounds.

the critical porosity reflects the transition between direct tortuous paths between the source and receiver on opposite sample boundaries. Independently, Walker *et al.* (2016) observe a step increase in the number of force chains at a critical stress when simulating simple shear in 3D media. In principle this could provide another possible explanation for critical porosity effect observed in the coquina, if it can be demonstrated to occur also under static gravitational load.

6.5.4 Alternative Models

In this study we carry out an in-depth comparison of two physics-based rock physics inclusion models: conventional differential effective medium theory (Berryman, 1992) and the Cilli-Chapman model (Cilli and Chapman, 2019). While it would not be feasible to statistically test all existing rock physics models, we believe it is worthwhile considering some empirical models, which give complementary insight into physical processes. Models arising from percolation theory (Stauffer and Aharony, 2014), where bulk modulus K_{perc} can be modeled as:

$$K_{perc} = K_{max}\left(\frac{|\phi_c - \phi|}{\phi_c}\right)^m, \tag{6.10}$$

Where K_{max} is the maximum measured bulk modulus, and m is a fitting parameter. Given the power-law nature of the Cilli-Chapman model, we also consider a simple

empirical power law model for bulk modulus K_{pl}:

$$K_{pl} = K_0 \left(\frac{\phi}{\phi_0} \right)^n, \tag{6.11}$$

where ϕ_0 is the initial (highest) porosity, K_0 is the initial (lowest) measured bulk modulus, and n is a fitting parameter. We invert for ϕ_c and m in Equation 6.10 and n in Equation 6.11 to find the best fitting models. We compare these models to the estimated bulk modulus data in Figure 6.11. First we note that the percolation model performs relatively well for the coquina data below critical porosity (Fig. 6.11a), exhibiting a near-linear trend. Percolation theory describes the connectivity of a network across a medium, where at a certain porosity threshold (or critical porosity), the connected network spans the entire medium. This physical process closely resembles the interpreted critical porosity effect observed in the coquina samples. The power law model performs well at porosities above ϕ_c though is clearly not appropriate at low porosities. The percolation model fails to fit the data for the grainstone with isopachous cement (Fig. 6.11b), however the power law model fits the data relatively well. The grainstone with syntaxial cement data (Fig. 6.11c) spans a narrow porosity range, thus both percolation and power law models fit the data well; there is not sufficient data to effectively asses the models. These empirical models can sometimes show impressive fits to the measured data, however offer limited ability to infer any physical significance. With the exception of one outlier noted above, the physics-based approach of the inclusion models considered here provides a more complete description of the data, and does allow for a physical interpretation of the results observed at the bulk scale.

The work described here strongly compliments the work of Cilli and Chapman (2018), where the power-law relationship between porosity and equivalent pore aspect ratio is first described using the public domain laboratory datasets of (Bakhorji, 2010), (Fournier *et al.*, 2011) and (Verwer *et al.*, 2008). The experimental data is measured with a range of different lithologies, in different laboratories and in different external conditions. Despite these differences, the observation here are the same as those recorded in the laboratory suggesting that the power-law relationship relates to the

underlying physics of changing porosity and its effect on elastic properties.

The use of effective medium theory models for elastic properties are exceptionally broad across many different disciplines, thus so are the application of the findings in this study. For example, the need for models that describe how elastic properties relate to volume fraction are used in material science and engineering (Sun *et al.*, 2007; Gubernatis and Krumhansl, 1975), medical imaging (Potsika *et al.*, 2014), the design of meta-materials (Wu *et al.*, 2007).

6.6 Conclusion

Measuring geophysical properties associated with geological processes, such as the measurement of seismic velocity during rock cementation, is very challenging in a laboratory environment. Such experiments require elaborate equipment and can require very long timescales making them expensive in terms of cost and time. By contrast, digital rock physics is an effective method for the estimation of seismic velocity as cementation is occurring, while remaining cheap, fast, and without the use of any intricate and complex laboratory equipment. The method could easily be extended to the study of other geological processes such as compaction, dissolution, or fracturing. The results presented here show realistic bulk modulus-porosity trends for a range of carbonate morphologies and cementation types. We observe anisotropy in the measured velocity (and elastic modulus) due to structural anisotropy caused by the settling of elongate grains under gravity. We also observe a critical porosity effect in the coquina samples, where bulk modulus above 30% porosity drops to the approximately the lower Reuss and Hashin-Shtrikman bounds. Digital rock physics also allows for the quantitative testing of competing rock physics models. For modelling bulk modulus-porosity data, a variable-aspect ratio model is statistically stronger than the conventionally used single-aspect ratio differential effective medium (DEMT) model for both grainstone and coquina digital rocks. The variable-aspect ratio model also remains robust to anisotropy where the conventional DEMT method fails. There are strong similarities between simulated data and real laboratory measured data for grainstones,

validating both the digital rock physics approach, as well as the variable aspect ratio rock physics model. Our results also highlight a significant critical porosity effect for the anisotropic 'shelly' fragments between phases that provide more direct or more tortuous path between the source and receiver at different stages of cementation.

6.7 Acknowledgments

The authors would like to thank Petrobras and Shell for their sponsorship of the International Centre for Carbonate Reservoirs (ICCR), and for permission to publish this work from the 4DRP, VSP, and RockType II projects. We also thank Rachel Wood, Mark Chapman and Satyan Singh for their helpful scientific input and support.

Chapter 7

Discussion

7.1 Introduction

Across all scientific research, making new discoveries generally leads to a whole series of new scientific questions or hypotheses to test. In this chapter I highlight some of these new questions, based on some of the current limitations to the methods used in this thesis, and present some possible areas for future work to address them. I have already included more specific discussions relating to each chapter topic in Chapters 3-6. To avoid repetition, here I address the more general questions facing coda wave interferometry and digital rock physics, drawing on experience from the work presented in the whole thesis and the wider literature.

7.2 Coda Wave Interferometry

7.2.1 Dependence on absolute measurements

In Chapter 3, I show that the accuracy and precision of estimates for a change in bulk velocity significantly increases when using CWI, which measures the relative velocity change directly, compared with the conventional first-break method which measures the

absolute velocities to calculate the velocity change. The fact that CWI only provides an estimate for relative changes in velocity rather that absolute velocity is not a significant concern for many applications, such as those relating to the interpretation of 4D seismic data where there is a dynamic dependence of velocity on changes in external properties (Landrø and Stammeijer, 2004).

However, there are some cases where an absolute velocity is desirable. An example occurs in Chapter 5 of this thesis, where the absolute P and S wave velocities are used for the inversion of crack density following the self-consistent model of O'Connell and Budiansky (1974). For the case of randomly oriented and penny-shaped cracks, the crack density ρ_C is defined as:

$$\rho_C = N\langle a^3 \rangle = (3\phi/4\pi)\langle a \rangle, \tag{7.1}$$

where $a \approx b \ll c$ (a and b are the major axes of the ellipsoidal crack and c is the crack aperture), $\langle a^3 \rangle$ is the mean crack radius, N is the number of cracks per unit volume, $\langle \alpha \rangle$ is the mean crack aspect ratio (c/a), and ϕ is the volume of cracks per unit volume. Crack density can be estimated from the effective (or measured) bulk modulus K_{eff} and Poisson's ratio ν_{eff} (O'Connell and Budiansky, 1974):

$$\rho_C = \frac{9}{16}\frac{(1-2\nu_{eff})}{(1-\nu_{eff}^2)}\left(1 - \frac{K_{eff}}{K^*}\right), \tag{7.2}$$

where K^* is the bulk modulus of the crack-free rock. In Chapter 5, I use the initial absolute measurements of V_P and V_S from the first-break method, then calculate the absolute velocity using the estimated velocity changes from CWI. However, in some conditions the estimation of absolute P and S wave velocities can be inaccurate (as shown in Chapter 3). To illustrate the dependence of the initial estimates of the elastic properties on the estimated change in crack density $\Delta\rho_C/\rho_C$, I take a velocity perturbation of a 2% increase in the P wave velocity and a 1% decrease in the S wave velocity ($\Delta V_P/V_P = 0.002$, $\Delta V_S/V_S = -0.001$) and calculate the change in crack density $\Delta\rho_C/\rho_C$ over a range of initial P wave velocities varying between 4000-6000 m/s. The S wave velocity ($V_S = 3000$ m/s) and density (2000 kg/m^3) remain constant.

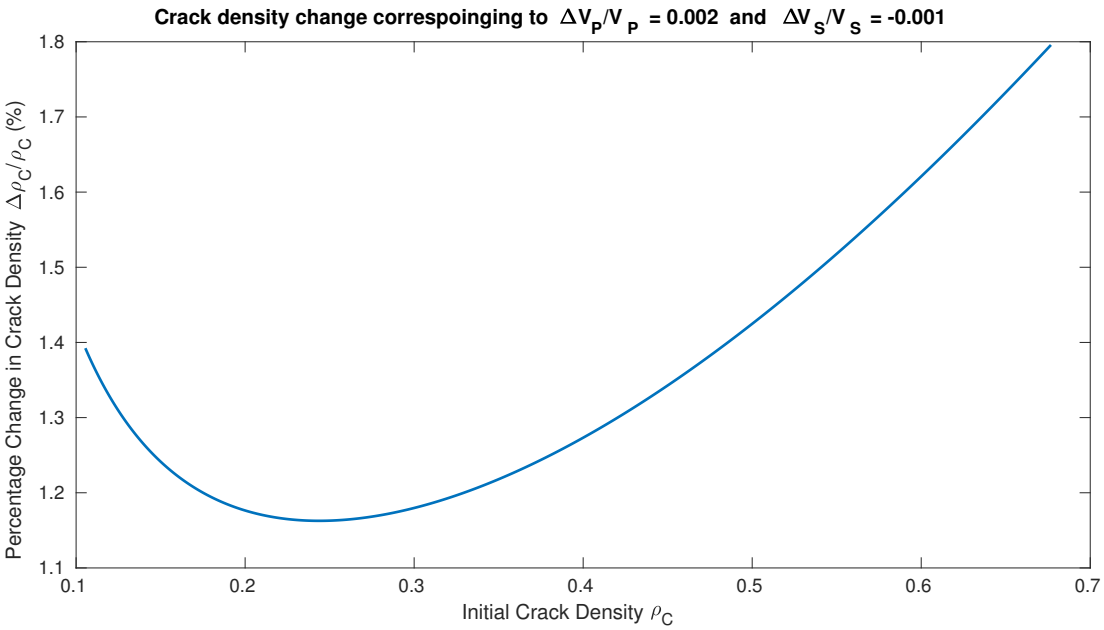

Figure 7.1: The calculated change in crack density ($\Delta\rho_C/\rho_C$) using velocity perturbations of a 2.0% increase in V_P and 1.0% decrease in V_S ($\Delta V_P/V_P = 0.002$, $\Delta V_S/V_S = -0.001$), plotted as a function of the assumed initial crack density ρ_C.

Using Equation 7.2, the data is equivalent to a range of initial crack densities ρ_C= 0.11-0.68. The calculated change in crack density ($\Delta\rho_C/\rho_C$) is plotted as a function of the initial crack density (ρ_C) in Figure 7.1. There is a clear non-linear dependence on the initial elastic moduli used in calculating the change in crack density, meaning that the errors in the first-break method still influence the estimate of the change in crack density even when the change in velocity is measured using CWI.

In Chapter 3, I also present a new method for the estimation of P and S wave velocities using CWI (further described in Chapter 4). This method also requires estimates of absolute measurements in the medium (rather than relative measurement), specifically the V_P/V_S ratio and the average inter-scatterer distance a.

Rather than using the initial absolute measurements of V_P and V_S from the first-break method, a more appropriate approach would be to use a weighted distribution of initial elastic moduli, which accounts for the uncertainty and variability of the first break method, but does not fully remove the dependence on absolute measurements.

A beneficial future study would be to measure the sensitivity of estimates in changing P and S wave velocities to estimates of V_P/V_S and inter-scatterer distance a. For any calculations involving such absolute measurements, a suitable approach would be to use a distribution of values (such as the distribution of V_P/V_S used in Chapter 3), accounting for the uncertainty in estimates.

7.2.2 Strength of scattering

In CWI it is commonly assumed that strong scattering is occurring. If not then CWI estimates for velocity change may be inaccurate. In Chapter 4, the Westerly Granite digital rock used contained weak impedance contrasts, and the length scale of the material heterogeneities were larger than the dominant wavelength. Mavko *et al.* (2009) breaks down the different scattering regimes based on the ratio of seismic wavelength λ to the diameter of the scattering heterogeneity d_s. Roughly speaking there are three domains:

- Rayleigh scattering, where $\lambda > d_s$;
- stochastic/Mie scattering, where $\lambda \approx d_s$;
- diffusion scattering, where $\lambda < d_s$;

When $\lambda \gg d_s$, the heterogeneous medium behaves like an effective homogeneous medium, and scattering effects may be negligible and conventional first break methods are more representative of the medium. At the other limit, when $\lambda \ll d_s$ the heterogeneous medium may be treated as a piecewise homogeneous medium (i.e., following ray theory). The focus of this thesis is on high-frequency laboratory experiments. Therefore, the majority of the laboratory and numerical experiments performed within this thesis use wavelengths much smaller that the scattering heterogeneities (ray theory and diffusion scattering), and in some cases they are approximately equal in length (stochastic scattering). Vlastos *et al.* (2007) use numerical simulations of wave propagation through these scattering regimes, studying the wavefields and spectral components. Another useful future study would be to investigate the performance of CWI

and conventional methods, in similar experiments, varying signal frequency, as well as varying the amount of scattering points (i.e., gradually increasing the number of point scatterers in the medium), particularly into the Rayleigh scattering and effective medium regimes, where the performance of CWI is expected to deteriorate.

7.2.3 Anisotropy

Another limitation of CWI is the assumption of an isotropic medium (and isotropic scattering). This means that any estimate for velocity change made using CWI represents an unknown weighted average of the change in velocity in all directions. This will not be appropriate for anisotropic media, for example due to layers or micro-crack alignment.

In Chapter 5, I compare estimates for velocity change using CWI with those made using the first-break method. Using the directionality implicit to the two methods, information about the anisotropy can be attained (specifically in Chapter 5, the data suggests fractures are present at high angles to the laminations within the samples). However, the results in Chapter 3 imply that the first-break method can be highly susceptible to errors due to the presence of background noise and provide unrepresentative and potentially biased results. Therefore, using these estimates to attain information about any anisotropy should be carried out with caution. A more appropriate method may be to extend the approach for separating changes in P and S wave velocities (outlined in Chapter 4) to account for variations with respect to orientation.

To illustrate this proposed method, I perform a proof-of-concept numerical experiment here, taking a structurally anisotropic layered medium (Figure 7.2a) and a isotropic homogeneous medium (Figure 7.2b). These models are used in a 2D elastic rotated-staggered-grid finite-difference simulation of wave propagation with reflecting boundary conditions, and 30 Hz ricker wavelet sources at central source locations. The measured wavefield $\mathbf{W}$ is a vector of displacement, therefore can be separated into horizontal (W_x) and vertical (W_z) components. For every model point $\mathbf{x}$, I take the envelope

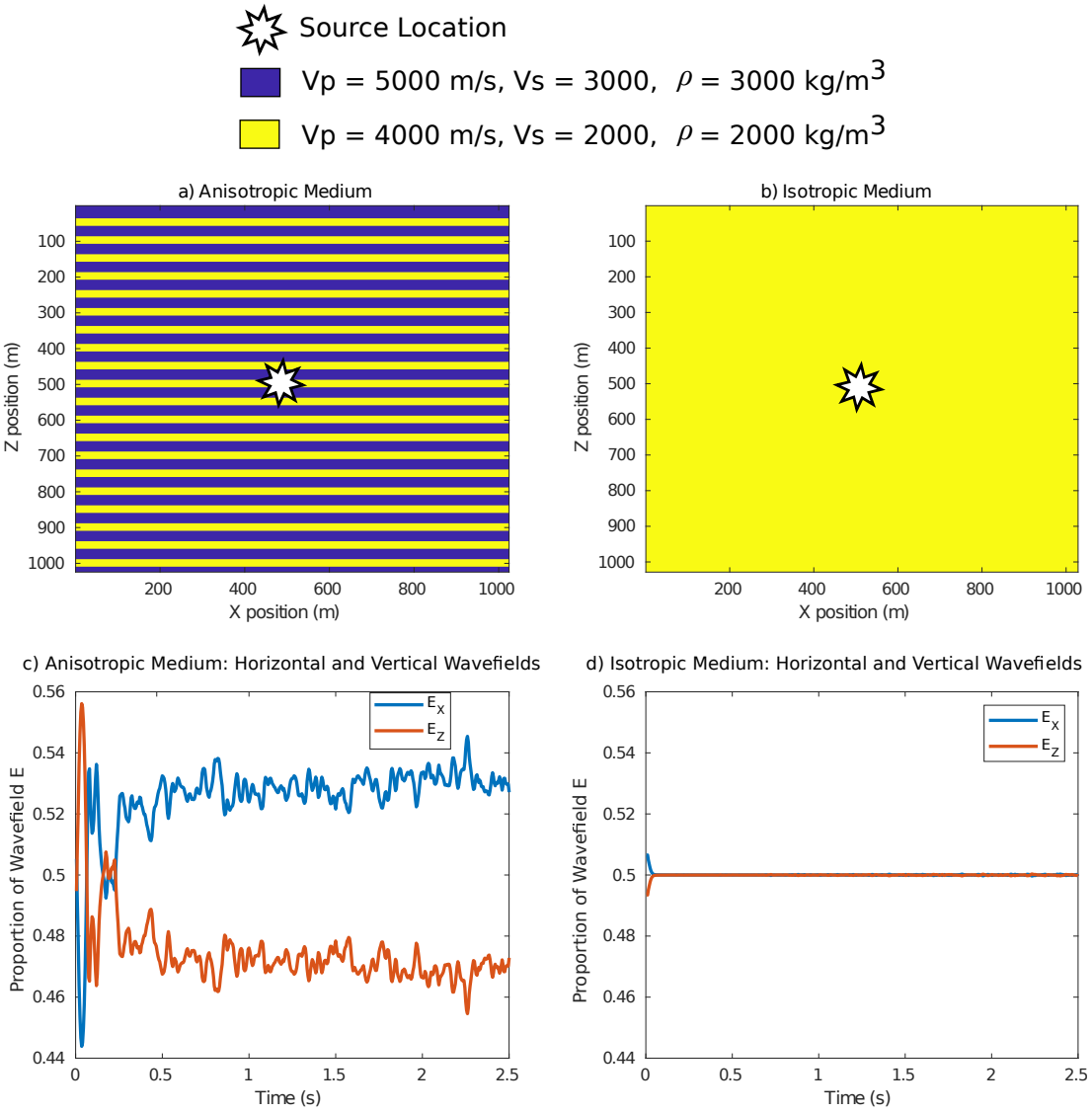

Figure 7.2: a) Structurally anisotropic two-phase model where each phase has different elastic properties. b) Structurally isotropic and homogeneous model with uniform elastic properties. c and d) the relative proportion of the wavefields of horizontal E_X (blue) and vertical E_Z (red) displacement to the total displacement wavefield for each of the models, calculated from Equations 7.3 and 7.4.

$(e(\mathbf{x}, t))$ for every point in the model, calculated as:

$$e_x(\mathbf{x}, t) = |\mathcal{H}(W_x(\mathbf{x}, t))|, \tag{7.3}$$

$$e_z(\mathbf{x}, t) = |\mathcal{H}(W_z(\mathbf{x}, t))|, \tag{7.4}$$

where $\mathcal{H}(f(t))$ denotes a Hilbert transform of function $f(t)$ and t is time. The relative proportion of the horizontal and vertical envelopes are calculated as $E_x = e_x/(e_x + e_z)$ and $E_z = e_z/(e_x + e_z)$. The resulting calculations for the proportions of vertical and horizontal displacements for the two models are shown in Figures 7.2c and d. There is a clear temporal variation in E_x and E_z for the structurally anisotropic model, whereas E_x and E_z are almost exactly equal and constant for the isotropic model. Note that the numerical examples here does not use a true anisotropic velocity model, but the model is structurally anisotropic, i.e., the compliance tensors are symmetric.

If the temporal variation between the horizontal and vertical wavefields is known, separate estimates for independent changes in velocity for both horizontal and vertical travelling waves can be made using CWI estimates for velocity change at multiple time windows. This method is essentially the same as that described in Chapter 4 for estimating relative proportions of compressional and shear waves, but taking the relative contribution of vertical and horizontal travelling waves as a function of time instead. This approach requires some prior information regarding the anisotropy of the medium and a model for the temporal change in the proportion of horizontal and vertical travelling waves. The model could be estimated using such numerical simulations as shown here, or by incorporating into an analytical scattering model that allows for different velocities and probabilities of a wave converting to a different phase depending on the direction of travel. I leave this for future research.

7.3 Digital Rock Physics

Chapter 6 contains a detailed discussion regarding the specific application of digital rock physics applied to process-based modelling of cementation. To avoid repetition, here I discuss the limitations in the field of digital rock physics from a wider perspective.

One of the major questions regarding this method is how close digital rocks resemble 'real' rocks, or more importantly how close are the estimated effective properties of digital rocks to those measured in the laboratory. In the majority of digital rock physics applications, the voxel sizes (maximum resolution) is on the order of microns. Therefore, any features below this size cannot be resolved. As the elastic properties of rocks are heavily influenced by very small structures such as fractures and grain contacts, conventional digital rocks cannot fully charecterise the elastic properties (Dvorkin *et al.*, 2011). There are many attempts to calibrate digital rock estimates with real rocks, for example Madonna *et al.* (2012) use a single scaling factor for the calibration of computed moduli to effective 'real' moduli. This approach is limited as any established scaling factor is only appropriate for the specific samples studies (a similar limitation to the empirical rock physics models described in Chapter 2.3.2). Therefore, applying such corrections for the prediction of elastic properties from digital rocks should be carried out with caution.

I believe the strengths of digital rock physics are not its it predictive ability, but in its repeatability. Heraclitus once said "you could not step twice into the same river"; this is a thought-provoking challenge to many rock physics experiments. In conventional laboratory rock physics, no two rock cores are exactly the same. Even when cored from a homogeneous medium there will be some differences at a small scale. This is a limitation of conventional experiments, which seek to keep all variables the same, and vary one dependent variable, e.g., varying the effect of confining pressure on a rocks strength. Digital rock physics allows a unique approach where digital rocks can be exactly the same, allowing for truly repeatable experiments, and the isolation of a single variable or process that can be varied and its effect can be determined. Therefore, there is great potential for process based modelling of digital rocks, where physical properties can be estimated over a wide range of geological processes, such as cementation (as in Chapter 6), or mechanical loading and fracturing (Tang, 1997), compaction (Katsman *et al.*, 2005), or dissolution (Kang *et al.*, 2003). These are the natural next steps for research within this field.

Chapter 8

Conclusion

8.1 Introduction

In this chapter I summarise the main findings presented in this thesis. In Section 2.5, I identified a series of research questions formed from the gaps I had identified in the current literature, and which act as the motivation for this thesis. My main findings are summarised below in the form of answers to these specific questions.

8.2 Research Questions and Answers

1. *For experimental rock physics, how do estimates for velocity change and source separation vary between coda wave interferometry (CWI) and conventional first arrival methods?*

Conventional first-break methods based on manual phase-picking provide an estimate of seismic velocity that is not representative of the bulk medium in a high frequency regime with point sources and point receivers. Such estimates of seismic velocity, changes in velocity, and source location are highly variable even for a single sample, and depend on the specific source-to-receiver path of the first arriving wave. They are therefore

inadequate for characterizing the bulk properties of a rock sample, particularly those with complicated pore structures approximately similar size to the wavelength of the interrogating waves. By contrast, coda wave interferometry is an effective method for countering these problems because coda waves sample the entire medium, and sample the same regions multiple times. CWI is shown to provide an increase in precision by an order of magnitude in the absence of noise, and to be a robust and accurate method for estimating both bulk velocity changes and perturbations of the source or receiver locations when compared with standard methods in both synthetic digital rock physics and laboratory experimental data. When noise is present, CWI remains far more accurate than conventional methods, even at very low signal-to-noise ratios. In addition, using source separation estimates, relative locations of a cluster of sources can be estimated using a single receiver, and show higher precision and accuracy compared to conventional methods.

2. *Can CWI estimates of velocity change and source separation be jointly estimated when both perturbations occur simultaneously?*

When velocity and source location perturbations occur simultaneously, CWI can estimate velocity and source separation under the conditions of small source separations (relative to the wavelength). Source separation estimates are mostly unaffected by the velocity perturbation, but velocity change estimates are much more sensitive and become inaccurate in the presence of larger source perturbations, possibly due to cycle-skipping.

3. *Can the estimate of velocity change provided by CWI be unravelled further into estimates of changes in V_P and V_S or changes in fluid velocity and solid matrix velocity?*

I extend the scattering model of Snieder (2002) to incorporate a fluid fraction, where shear waves are not supported. This models estimates the equilibriation of P to S waves

over time, as well as the equilibriation of the proportion of waves in the solid matrix to pore fluid. Estimates of separate changes in P and S wave velocity can be made by taking many estimates of velocity change made using CWI for different time windows along the signal, combined with the analytical scattering model and given probabilistic *a priori* information about the V_P/V_S ratio of the medium. In a similar way, providing probabilistic *a priori* information about the fluid fraction in the medium, estimates of separate changes in the fluid velocity and matrix velocity can also be made.

4. *Can CWI be used in conventional rock physics models, e.g., for the inversion of crack density?*

Measurements of changes in P and S wave velocities from CWI can be used to calculate changes in the V_P/V_S ratio, the bulk and shear moduli, and Poisson's ratio. I demonstrate the inversion of changing crack density during the triaxial deformation of laminated carbonates. The results are in good agreement with previous rock deformation theory, where crack density initially increases due to pore and micro-crack closure, and eventually decrease at the onset of micro-cracking through to macroscopic failure.

5. *What are the implications of the implicit isotropic averaging of CWI compared to the directionality of the first-break method?*

As coda waves scatter in all directions and throughout the entire medium, the CWI estimates of a change in velocity represent an isotropic average of the medium, whereas the first-arrival velocity only represent a single direction along the path of wave propagation. The estimates of velocity change for CWI and first-breaks, particularly how the estimates differ, can be used in the interpretation of any anisotropy in the samples. The data from two oriented finely laminated carbonates of the Crato formation suggests preferential closing of pores perpendicular to the laminations, most likely pre-existing fractures at high angles to the laminations/bedding. This is supported by the

known orientations of fracture sets reported for the Crato formation (Miranda *et al.*, 2014). CWI can therefore be used in conjunction with existing methods to provide previously unavailable information regarding the anisotropy in a medium.

6. *Using process based simulation of digital rocks, what is the effect of cementation on seismic velocity?*

Digital rocks show realistic velocity-porosity (and bulk modulus-porosity) trends for a range of carbonate morphologies and cementation types, all falling within the Hashin-Shtrikman bounds for bulk modulus. Anisotropy is measured in the velocity due to the structural anisotropy caused by the settling of elongate grains under gravity, even when the individual grains shapes are near spherical. In the coquina samples, which have long convex grain shapes, there is a critical porosity effect, where elastic modulus drops above 30% porosity to the approximately the lower Reuss and Hashin-Shtrikman bounds.

7. *What is the most appropriate rock physics model for digital carbonate rocks?*

For modelling bulk modulus-porosity data from digital grainstones (spherical grains) and coquinas (shelly-fragment grains), a variable-aspect ratio model is statistically stronger than the conventionally used single-aspect ratio differential effective medium model for both grainstone and coquina digital rocks. The variable-aspect ratio model also remains robust to anisotropy where the conventional differential effective medium method fails. There are strong similarities between simulated data and real laboratory measured data for grainstones, validating both the digital rock physics approach, as well as the variable aspect ratio rock physics model.

8.3 Final Remarks

The findings of this thesis have been encouraging for the use of both coda wave

interferometry and digital rock physics in conventional rock physics workflows. The improvements presented here are not only limited to experimental rock physics but can be in principle extended to field-scale surface seismic data. These innovations represent significant improvements in our ability to characterize the evolution of properties of media across all scales for a variety of applications across geoscience and engineering.

Appendix A

CWI MATLAB Code Package: User Guide

A.1 Introduction

This guide accompanies Singh *et al.* (2019): *Coda Wave Interferometry for Velocity Monitoring and Acoustic Source Location in Experimental Rock Physics*, which can be downloaded from `https://github.com/JonathanSingh/cwi_codes/`. Contained in this package are a suite of well-commented MATLAB functions for estimating the changes in the bulk velocity of a medium, the small change in source or receiver locations, or the joint estimation of velocity and source/receiver location changes when both occur simultaneously. This code package can be used in conjunction with the codes of Zhao and Curtis (2019), available at `https://www.geos.ed.ac.uk/eip/codes.html`. These codes provide methods for the estimation of relative source locations in a cluster of sources. By combining these two code packages, estimates of the relative locations of a cluster of sources can be made as well as any velocity perturbations that occur in the medium, all using a single receiver. Users can execute all function contained in the package by running a single script: $examples\_running\_script.m$, which demonstrates

the implementation of all the functions and how they can edited to suit the users requirements. First we cover the theory of Coda Wave Interferometry (CWI) and how it can be used to estimated changes in the velocity of a medium, a change in the location of a source or receiver, and the random displacement of scatterer locations. We then provide an overview of the code package contents and explain each code with examples for their implementation.

A.2 Theory

CWI allows small changes in velocity, the displacement of source or receiver locations, or movement of scatterers to be monitored (Snieder *et al.*, 2002; Sens-Schönfelder and Wegler, 2006; Snieder, 2006). These different perturbations and their effect on recorded signals are illustrated in Figure A.1. First we consider the effect of a velocity perturbation (ΔV in Figure A.1a), where the direct arriving wave between a source and receiver would only sample the perturbation once (or not at all), whereas the multiply reflected waves sample the perturbation many times. Therefore the change in arrival times for later arriving waves (t3,t4) is much larger than for the first arrival (t1,t2). The second perturbation type is a displacement of the source or receiver location (source displacement in Figure A.1b): in this case, the difference in ray paths before and after the perturbation is the path between the source and the first scattering point (blue arrows in Figure A.1b). Paths would be both shortened and lengthened depending on the location of the first scatterer, which is reflected by the advancement and retardation of peaks highlighted by red and blue arrows. The extent to which these travel times are perturbed (their variance) is directly proportional to the (small) displacement of the source. The third perturbation type is the displacement of all scattering points (yellow circles in Figure A.1c): in this case, all paths between scattering points are perturbed (both shortened and lengthened) and similarly to the previous case, the statistics of travel time perturbations are related to the displacement of scattering points. All three perturbation types can be monitored by using a cross correlation of the unperturbed (u_{unp}) and perturbed (u_{per}) waveforms - the waveforms from the source recorded by the receiver before and after the change or displacement takes place.

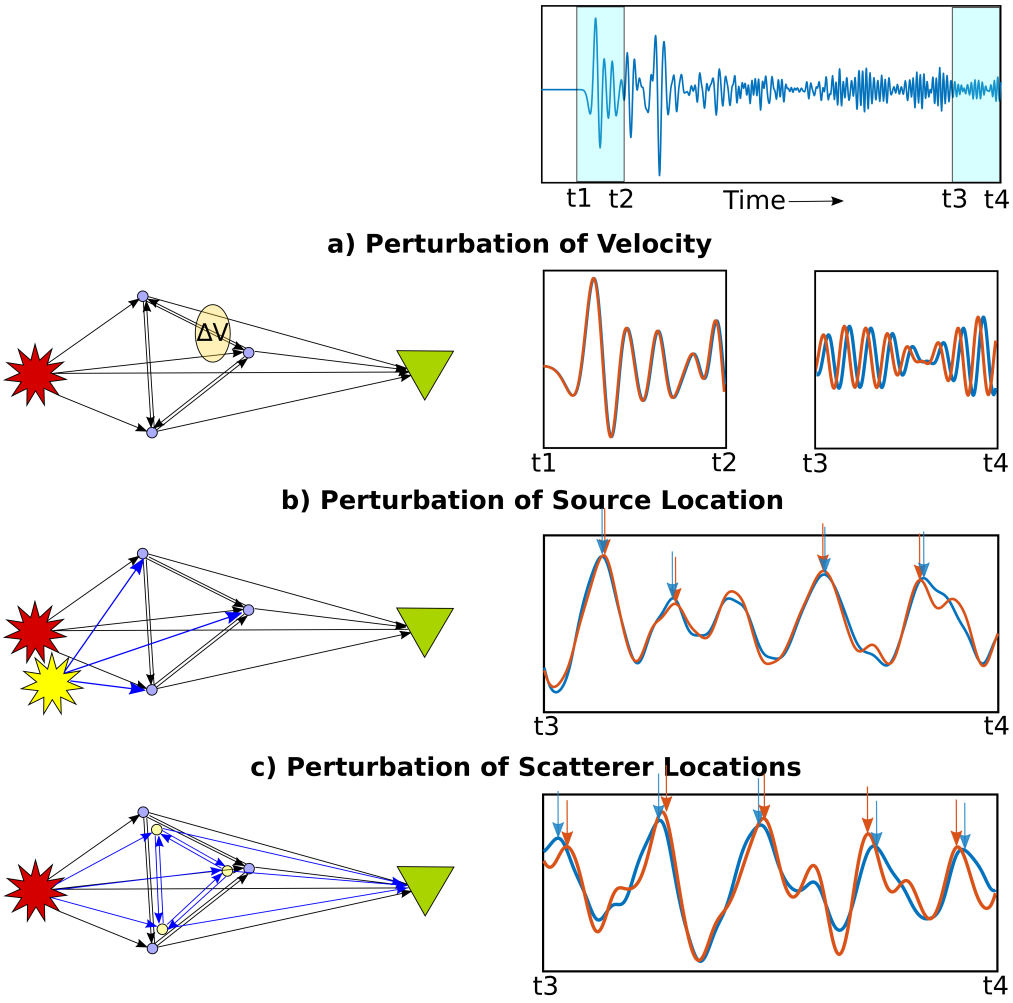

Figure A.1: Illustrations of different perturbation types and their effects on coda waves. The cartoons (left) represent a scattering medium, with a source (star), receiver (triangle), and point scatterers (circles). Ray paths between the source and receiver, including multiple reverberations, are represented as black arrows. A velocity perturbation (a) is represented as a yellow ellipse, which has a velocity different to the background medium. New ray paths that are introduced due to source location (b) and scatterer location (c) perturbations are represented as blue arrows. Example recorded signals (right) at early (t1,t2) and late (t3,t4) time windows for each perturbation type are shown before and after each perturbation takes place (blue and red, respectively). Differences in travel times of arriving energy for b) and c) are highlighted with vertical arrows.

The method we use to estimate the change in velocity is known as trace stretching (Sens-Schönfelder and Wegler, 2006), where the perturbed waveform is assumed to be a time-stretched version of a reference waveform; this follows if one assumes that a velocity perturbation is uniform across the entire medium, so all arriving energy is perturbed at the same temporal rate. We stretch the time axis of the perturbed signal by a range of stretching factors (ϵ) and compute the correlation coefficient R between $u_{unp}(t)$ and the stretched version of the perturbed waveform $u_{per}(t[1+\epsilon])$ over a given time window (t_1, t_2):

$$R^{(t_1,t_2)}(\epsilon) = \frac{\int_{t_1}^{t_2} u_{unp}(t) u_{per}(t[1+\epsilon])dt}{\sqrt{\int_{t_1}^{t_2} u_{unp}^2(t)dt \int_{t_1}^{t_2} u_{per}^2(t[1+\epsilon])dt'}} \tag{A.1}$$

The optimum stretching factor ϵ_{max} that maximizes the correlation coefficient (for which $R = R_{max}$), is related to the ratio of the change in velocity ΔV to the original velocity V) by

$$\epsilon_{max} = -\frac{\Delta V}{V} \tag{A.2}$$

(Sens-Schönfelder and Wegler, 2006). That method also assumes that the velocity changes are small to avoid cycle skipping in the calculation of R in equation A.1. In cases where the medium changes significantly, such as during material deformation where new scattering paths are introduced due to fracturing, it may not be appropriate to use a constant reference trace (u_{unp}) for all recorded waveforms during deformation. We propose the use of a moving reference trace, where the optimum stretching factor from the initial reference trace (u_0) to any other recorded waveform during deformation (u_n) can be calculated as

$$\epsilon_{u_0 u_n} = \epsilon_{u_0 u_s} + \epsilon_{u_s u_n} \tag{A.3}$$

where $s = k\lfloor n/k \rfloor$, n is the trace number, k is the user-selected step size of the moving reference trace, and $\lfloor \ldots \rfloor$ denotes a floor function, which outputs the greatest integer less than or equal to the input.

CWI allows the joint estimation of both a velocity perturbation and the displacement r of the source/receiver location to be made from a single receiver. This is because

velocity perturbation information is retrieved from the consistent phase information along the waveforms, whereas the source or receiver separation is related to the variance of inconsistent phase perturbations and hence to the maximum value of the cross correlation value (R_{max}) in equation A.1 (Figure A.1). Snieder (2006) derives the relationship between the maximum cross-correlation and the variance of the travel time perturbation (σ_τ^2) as

$$R_{max} = 1 - \frac{1}{2}\bar{\omega}^2\sigma_\tau^2 \tag{A.4}$$

where $\bar{\omega}^2$ is the dominant mean squared frequency in the recorded waveform. When a source or receiver is displaced by distance r, one can estimate separation r from the variance of the travel time perturbation

$$\sigma_\tau^2 = \frac{(\frac{6}{\alpha^8} + \frac{7}{\beta^8})}{7(\frac{2}{\alpha^6} + \frac{3}{\beta^6})} r^2 \tag{A.5}$$

where α and β are estimates of the representative P- and S-wave velocities of the medium. In a two-dimensional acoustic medium this relationship simplifies to:

$$\sigma_\tau^2 = \frac{1}{2\alpha^2} r^2. \tag{A.6}$$

The estimates of source separation for a cluster of sources can be used to estimate relative locations of all sources within the cluster with a single receiver (Zhao *et al.*, 2017). CWI is also able to resolve another type of perturbation on which we do not focus: the average displacement of all scatterers, δ, illustrated in Figure A.1c (Snieder *et al.*, 2002). This value is related to the variance of travel time perturbations by

$$\sigma_\tau^2 = \frac{2\delta^2 t}{v l_\star} \tag{A.7}$$

where $l_\star$ is the transport mean free path. An estimate for δ can be made using the output of the *cwi_sep.m* function and the equation above.

A.3 Package Contents

A.3.1 Functions

- **cwi_stretch_vel.m**: for estimating a velocity change, using the CWI stretching technique (Equation A.1). The function initially searches through stretching factors equivalent to a range of 10% to -10% velocity changes, then searches at fine increments of 0.005% changes in velocity. If a wider search range is required, the user should edit the $s\_factors$ variable.

  Inputs:

  - $sig1$: Reference signal recorded prior to a perturbation
  - $sig2$: Signal recorded after a perturbation

  Output:

  - $epsilon$: Stretching factor which maximizes correlation (equal to $-\Delta V/V$)

- **cwi_sep.m**: for estimating the separation between a pair of sources or a pair of receivers using coda wave interferometry. The function uses Equation A.4 to estimate and output the variance of travel time perturbations σ_τ^2, which is related to the displacement of source location by Equations A.5 and A.6.

  Inputs:

  - $sig1$: Reference signal recorded prior to a perturbation
  - $sig2$: Signal recorded after a perturbation
  - dt: Sampling interval time in seconds - must be the same for both signals
  - win_start: Index of sig1 and sig2 corresponding to the start of the desired time window
  - win_end: Index of sig1 and sig2 corresponding to the end of the desired time window

  Output:

  - *variance*: Variance of travel time perturbations. Proportional to the separation and the velocity of the medium (Equations A.5 and A.6).

- **cwi_stretch_vel_and_sep.m**: for joint estimation of changes in velocity and source location, when both occur simultaneously.

  Inputs:

  - *sig*1: Reference signal recorded prior to a perturbation
  - *sig*2: Signal recorded after a perturbation
  - *dt*: Sampling interval time in seconds - must be the same for both signals
  - *win_start*: Index of sig1 and sig2 corresponding to the start of the desired time window
  - *win_end*: Index of sig1 and sig2 corresponding to the end of the desired time window

  Output:

  - *variance*: Variance of travel time perturbations. Proportional to the separation and the velocity of the medium (Equations A.5 and A.6).
  - *epsilon*: Stretching factor which maximizes correlation (equal to $-\Delta V/V$)

- **mov_ref_trace.m**: a function for combining estimates of velocity change from coda wave interferometry (*epsilon* from *cwi_stretch_vel.m*), employing a moving reference trace (Equation A.3)- with a user selected step size. Velocity changes are required to be combined into a NxN matrix, where N is the number of signals.

  Inputs:

  - *epsilon_matrix*:
  - *k*: Step size for moving reference trace

  Output:

  - *dv_mrt*: 1xN vector of cumulative velocity change.

A.3.2 Scripts and Data

- **examples_running_script.m**: Full script for loading in example data and using all functions for changes in velocity, source location, both perturbation types occurring simultaneously, and the combination of multiple velocity changes using a moving reference trace. This script also generates a series of plots, all contained in this report.

- **fluid_change_data.mat**: example data generated from finite difference simulation of a wavefield through a Tivoli Travertine, where pore fluid velocity is perturbed by 100 m/s.

- **source_change_data.mat**: example data generated at an array of source locations, represented a fracture plane occurring in the Tivoli Travertine digital rock.

- **source_and_vel_data.mat**: example generated for a range of source locations, and a range of velocity perturbations occurring simultaneously.

- **mrt_example_data.mat**: example CWI data from laboratory experiment of the deformation of a laminated carbonate core. Used for the demonstration of the moving reference trace method.

A.4 Codes and Example

We demonstrate the use of all function listed above in the *examples_running_script.m* script, using appropriate example data. We generate example data using finite difference simulation of wavefield propogation through a model based on a x-ray micro-tomography slice through a Tivoli Traverine core (shown in Figure A.2). Here we demonstrate the use of each function and describe how they can be edited to be used different data sets. All figures shown in this user guide are also generated as part of the *examples_running_script.m* script.

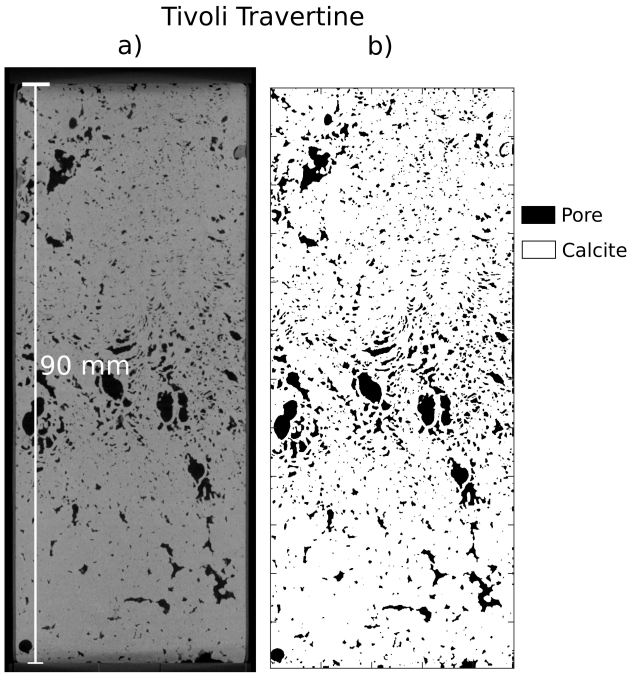

Figure A.2: a) X-ray micro-tomography slice of a Tivoli Travertine core. b) The equivalent model of segmented phases, in this case we assume two phases, calcite and pore fluid. The elastic properties of calcite and water are used in the finite difference simulations of wave propogation to generate the example data sets used in this guide.

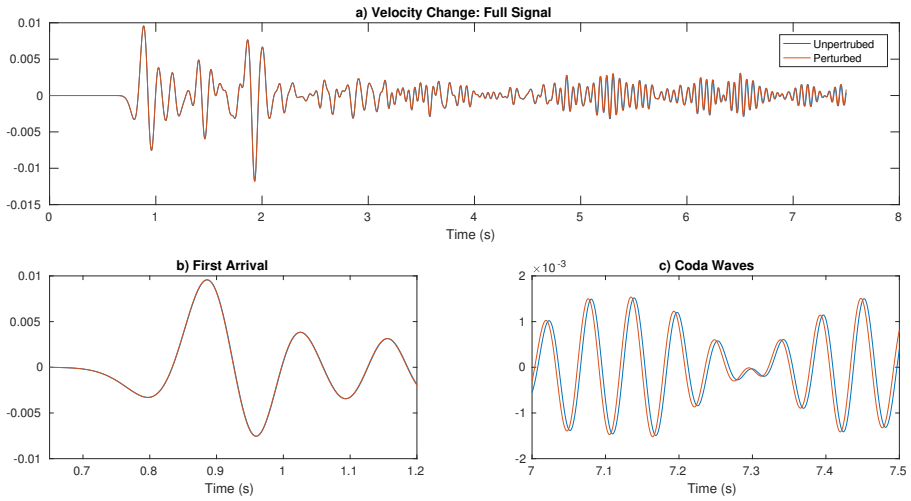

Figure A.3: Example data generated from finite difference simulation of a wavefield through a Tivoli Travertine, before (blue) and after pore fluid velocity is perturbed by 1.5 m/s (red). Comparison is shown for a) the full signal, b) the first arriving waves and c) the coda waves.

A.4.1 Estimating a change in velocity

The first example data set was generated from finite difference simulation of a wavefield through a Tivoli Travertine, where pore fluid velocity is perturbed by range of velocities up to 100 m/s. The data can be loaded into MATLAB with the following lines

```
load('example_data/fluid_change_data.mat')
```

The example data is plotted in Figure A.3, comparing signals before and after a velocity perturbation. The lower panels highlight how the coda waves are more sensitive to small changes in velocity when compared against first arriving waves. CWI can be performed on the example data set with the by computing the following:

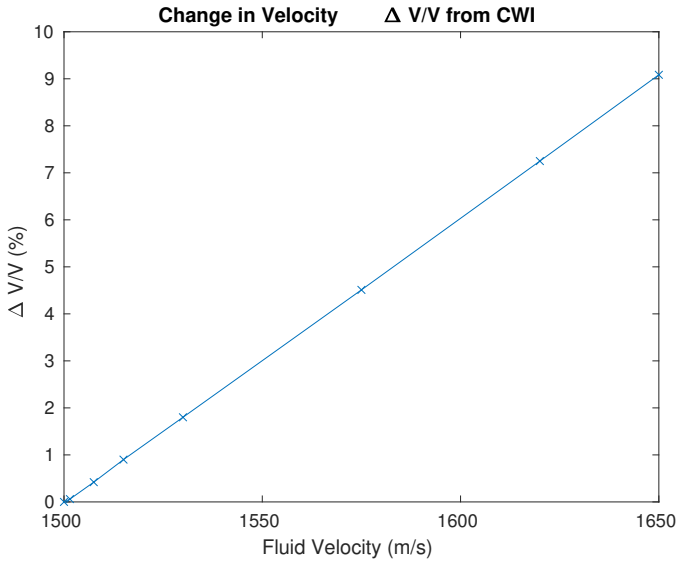

Figure A.4: Estimates of velocity change ($\Delta V/V$) using CWI, as a function of pore fluid velocity in a Tivoli Travertine digital rock.

```
% Unperturbed signal:
sig1 = fluid_change_data(:,1);
% Loop through all signals performing CWI
for i = 1:size(fluid_change_data,2)
    % Perturbed signal:
    sig2 = fluid_change_data(:,i);
    % CWI stretching method for velocity change
    epsilon=cwi_stretch_vel(sig1,sig2);
    % Velocity change dV/V = - epsilon:
    dV(i) = -epsilon;
end
```

The output **dV** is a vector of velocity change estimates between the reference signal (sig1) and every other signal in the data set (plotted in Figure A.4). If the user requires to apply this method on different data sets, the $fluid\_change\_data$ variable can replaced with an $l \times N$ matrix, where l is the length of the signals and N is the number of signals.

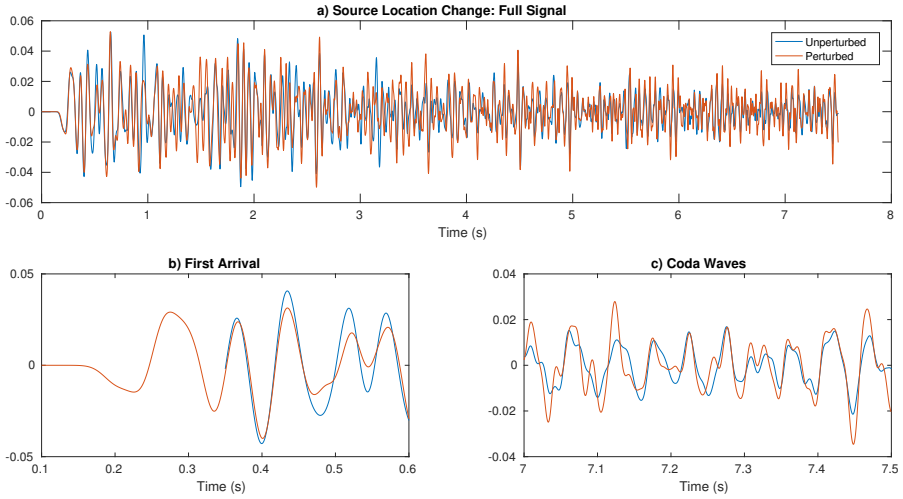

Figure A.5: Example data generated from finite difference simulation of a wavefield through a Tivoli Travertine, before (blue) and after the source location is perturbed by 0.001λ (red). Comparison is shown for a) the full signal, b) the first arriving waves and c) the coda waves.

A.4.2 Estimating a source location perturbation

The second example data set is for the estimation of a change in source location, i.e., inter source distance. Example data can be loaded from *source_change_data.m*, a pair of signals are compared in Figure A.5, from this we see that the perturbation causes a change in the correlation of the coda waves, but is not a coherent shift of the travel times as seen for the velocity perturbation in Figure A.3. The data is from an array of source locations occurring along a plane in the Tivoli Traverine digital rock sample (shown in Figure A.6). To perform CWI to estimate the source separation, first find the variance of travel time perturbations, then the source location perturbation can be estimated using Equation A.6. This is achieved be executing the following:

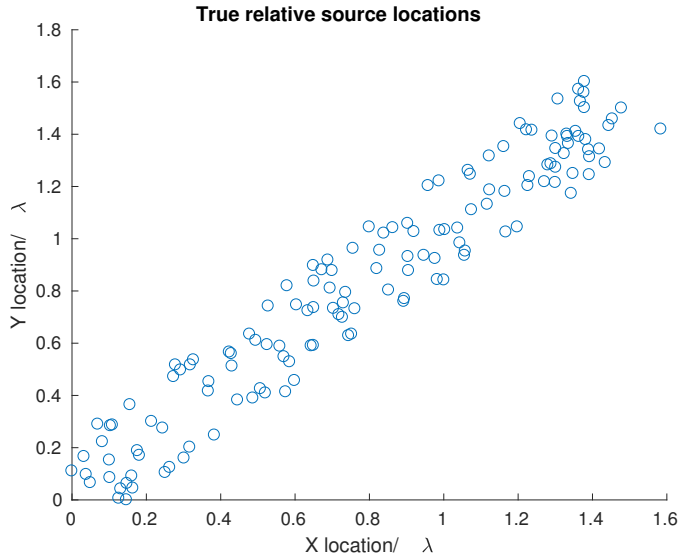

Figure A.6: Relative locations of a cluster of sources used to generate the example data for estimating source separation using CWI.

```
% Required parameters:
N = size(source_change_data,1); % Number of signals
win_start = 100000; % Index for start time window
win_end = 150000; % Index for end of time window
dt = 5e-5; % Sampling interval
vel = 2200; % velocity of the medium
lambda = 67; % dominant wavelength in the signal
% Assign reference signal:
sig1 = source_change_data(1,:);
% Loop through all sources:
for i = 1:N
    % Perturbed signal for varying source location
    sig2 = source_change_data(i,:);
    % Perform CWI to estimate variance of travel time perturbations
    [var] = cwi_sep(sig1,sig2,dt,win_start,win_end);
    % Calculate inter-source separation using relationship between
    % velocity and variance of travel time perturbations.
    sep_cwi(i) = sqrt(2*vel^2.*var)/lambda; % Normalised by dominant wavelength
end
```

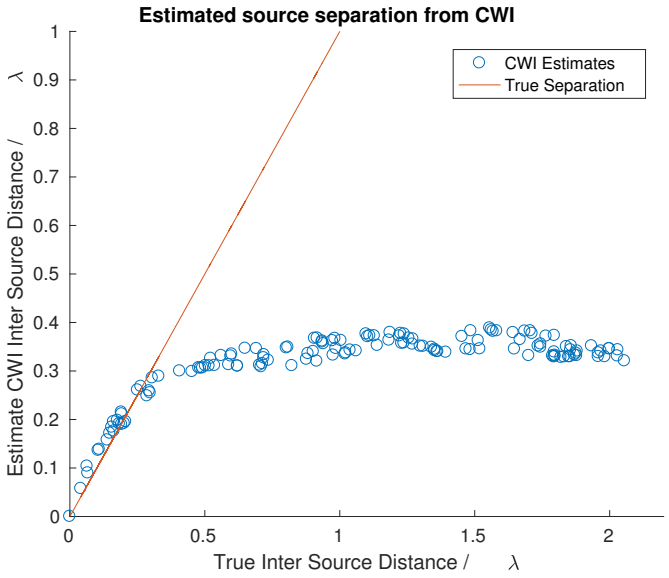

Figure A.7: Estimated source separation between a single source, and every other source in the cluster (circles) plotted as a function of the true source separation. The red line shows the true separations for reference.

The output *sep_cwi* is a vector of estimated inter source separations, normalised by the dominant wavelength in the signal. The resulting estimates are plotted as a function of true separation in Figure A.7. The variance *var* can also be used to estimate the average displacement of scatterers (using Equation A.7) though we do not illustrate this use in the package. To use a different data set, change the *source_change_data* variable to an $N \times l$ matrix, where l is the length of the signals and N is the number of signals.

Note: the output from this function can be used in conjunction with publicly available codes of Zhao and Curtis (2019), for the relocation of relative source locations, using a single receiver.

A.4.3 Estimating simultaneous source location and velocity perturbations

The third example data set is synthetically generated using finite difference wavefield simulation, where signals are generated at an array of source locations, and source

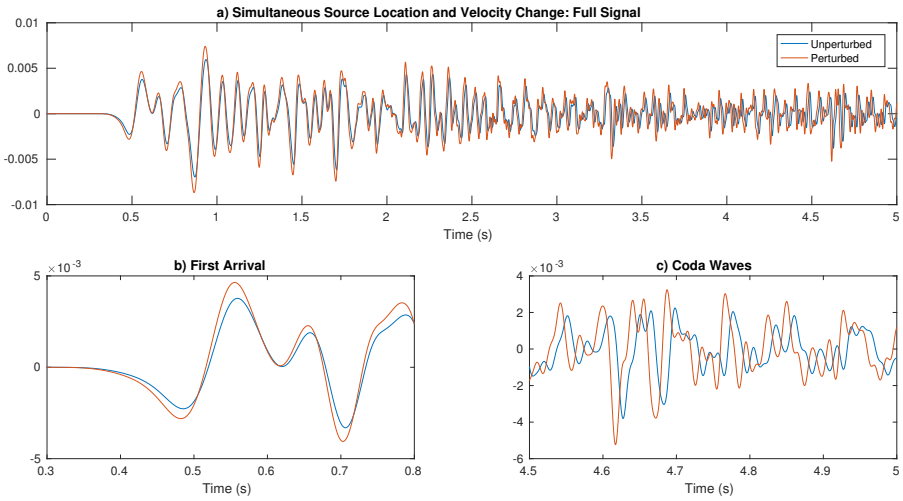

Figure A.8: Example data generated from finite difference simulation, before (blue) and after the simultaneous perturbation of source location by 0.05λ and velocity by 0.2 % (red). Comparison is shown for a) the full signal, b) the first arriving waves and c) the coda waves.

locations survey are repeated with a range of velocity perturbations occurring simultaneously. Example signals are compared in Figure A.8, where a source location perturbation of 0.04λ and a velocity perturbation of 0.2% have occurred. The data is loaded from *source_and_vel_data.m*, and is a 6×10 matrix, representing the 6 different velocity models, and 10 different source locations used. To estimate both the change in velocity and source location, use the *cwi_stretch_vel_and_sep.m* function, demonstrated below:

```
% Required parameters:
dt = 5e-5; % Sampling interval
win_start = 500; % Index for start time window
win_end = 100000; % Index for end of time window
dt = 5e-5; % Sampling interval
vel = 3500; % velocity of the medium
% Assign reference signal:
sig1 = source_and_vel_data(:,1,1);
% Loop through all all velocity perturbations and source location changes
for i = 1:6 % Number of velocity models
    for j = 1:10 % Number of source locations
        % Assign perturbed signal
        sig2 = source_and_vel_data(:,i,j);
        % CWI for simultaneous changes in velocity and source location
         [eps,var]=cwi_stretch_vel_and_sep(sig1,sig2,dt,win_start,win_end);
        % Velocity change = -epsilon:
        vel_change_cwi(i,j) = eps;
        % Calculate inter-source separation using relationship between
        % velocity and variance of travel time perturbations:
        sep_cwi(i,j) = sqrt(2*vel^2.*var)/67;
    end
end
```

The output is a pair of matrices, one represents the velocity change estimates *vel_change_cwi_mat* and the other source location change estimates *sep_cwi* for all combinations of velocity and source location changes. The estimates of both source location and velocity changes are plotted against their true changes in Figure A.9.

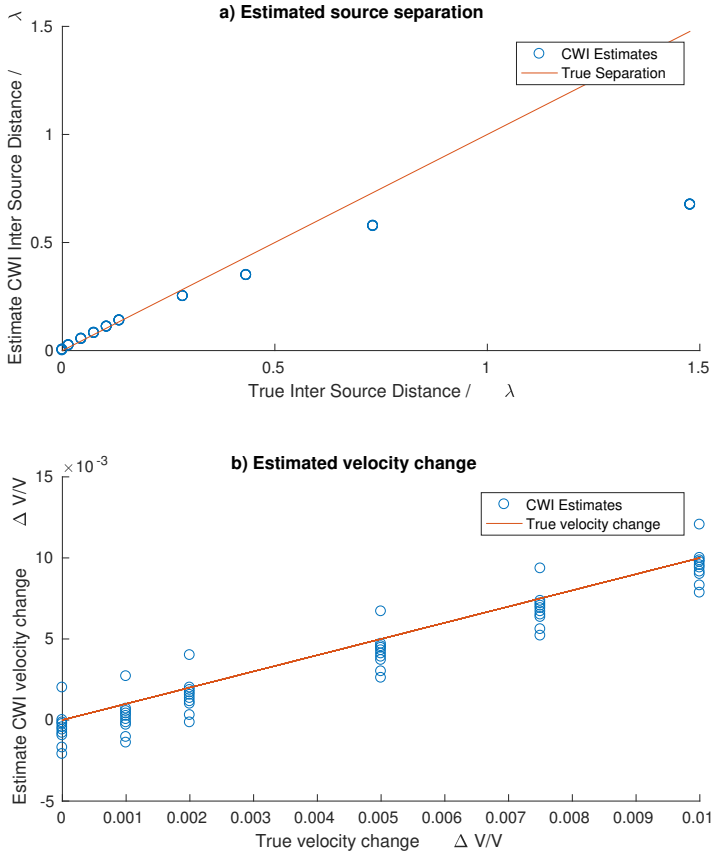

Figure A.9: a) Estimates of source separation with simultaneous velocity perturbation. b) Estimates of velocity perturbation with simultaneous source location perturbations. CWI estimates plotted as circles, and the true solutions are represented as red lines.

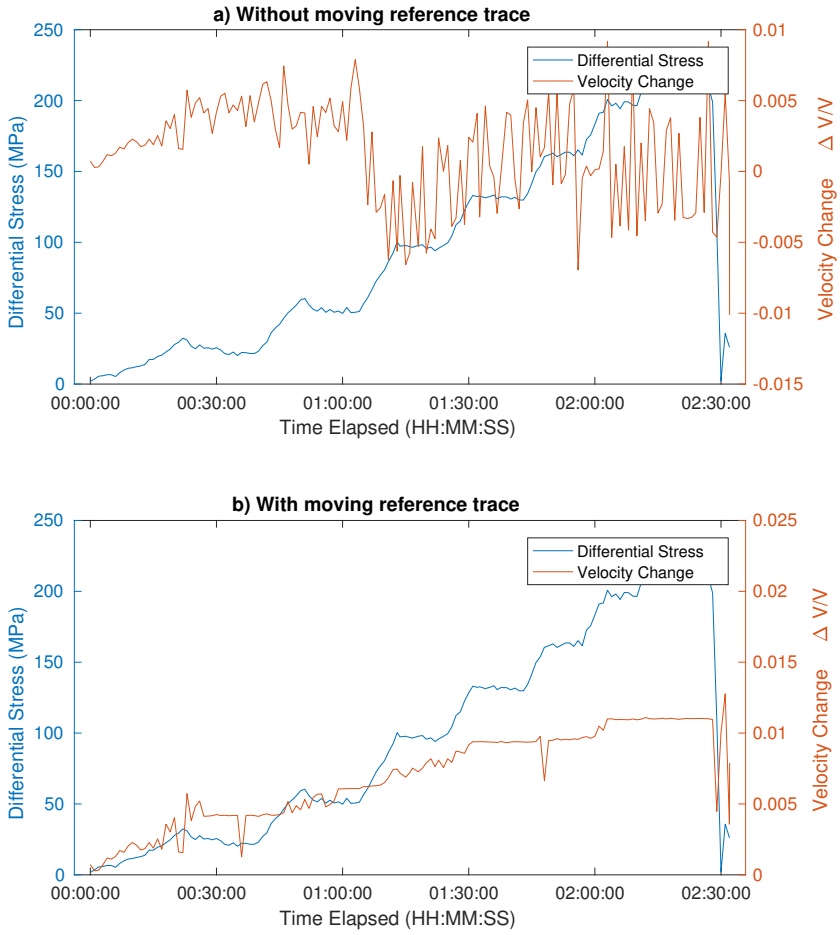

Figure A.10: Velocity change $\Delta V/V$ measured by CWI (red lines) for a finely laminated carbonate rock during experimental deformation by increasing differential stress (blue lines), with corresponding stress values labelled on the left axes. a) Estimates of velocity change from CWI are calculated using a single reference signal measured prior to deformation. b) Estimates of velocity change from CWI use multiple reference signals. In this case, the reference signal is reassigned every 32 surveys. This ensures that the velocity changes remain within the working range of CWI.

A.4.4 Combining estimates of velocity change using the moving reference trace function

The final example is for implementing the moving reference trace method. The function $mov\_ref\_trace.m$ requires an $N \times N$ matrix of estimates of velocity change. Where the row index indicates the reference trace used for CWI, and the column index indicates the index of the perturbed signal for CWI. This matrix can be generated from the following script:

```
% Take the output of cwi_stretch_vel in a nested for loop
% signals:Nxl matrix, where N is the number of signals and l is the signal length
 for i = 1:N
     for j = i:N % only cells where j>i are required, as matrix is symmetric
         % estimate velocity change using CWI
         epsilon=cwi_stretch_vel(signals(i,:),signals(j,:));
         % write into an NxN matrix
         epsilon_matrix(i,j)=epsilon;
     end
 end
```

An example matrix can be loaded from $mrt\_example\_data.mat$, which is laboratory data collected during the deformation of a laminated carbonate core sample. The step size k indicates the step size of the moving reference trace, and depends on the rate of change between the signals. Example data is loaded, and moving reference trace function is executed with the following script:

```
% Load epsilon matrix: Experimental deformation of a laminated carbonate
load('example_data/mrt_example_data.mat')
% Step size for moving reference trace
k = 32;
% Use mov_ref_trace.m function
[dv_mrt] = mov_ref_trace(epsilon_matrix,k);
```

The output vector dv_mrt is the cumulative velocity change $\Delta V/V$, shown in Figure A.10. To apply this method to a different data set, edit the *signals* variable, to be a $N \times l$ matrix, where N is the number if signals, and l is the length of the signals.

Appendix B

Conference Proceedings

B.1 SEG 2018 Annual Meeting Technical Program Expanded Abstract

Title: Accurate estimates of simultaneous seismic velocity changes and interfracture-source distances from coda wave interferometry

Authors: Jonathan Singh, Andrew Curtis, Ian Main

Abstract: Coda Wave Interferometry (CWI) is a potential source of new information on simultaneous changes in seismic velocity and the locations of earthquakes induced by subsurface engineering projects. Here we investigate the sensitivity of CWI to the contamination of recorded signals by measurement noise, and the robustness of estimates of simultaneous changes in the mediums velocity and the locations of induced acoustic emissions, as analogues of larger scale earthquakes. We conduct numerical experiments with finite-difference modelling in media constructed using real-rock x-ray micro-tomography volumes, and generate realistic synthetic ambient noise based on the frequency-domain characteristics of laboratory-measured noise. CWI is shown to be more accurate and reliable in estimating changes in velocity and source location

compared to conventional phase picking methods in heterogeneous media, particularly in the presence of noise. When simultaneous perturbations of velocity and source locations occur, CWI estimates of source perturbation remain accurate in the presence of a velocity perturbation. However, estimates of velocity perturbation exhibit errors of up to 0.5% in the presence of source perturbations of around one wavelength. These results demonstrate the potential of CWI to be used to characterize the response of rocks to stress during laboratory deformation experiments, and with suitable scaling to field-scale applications.

Full extended abstract: https://doi.org/10.1190/segam2018-2995402.1

B.2 American Geophysical Union, Fall Meeting 2018

Title: Digital Rock Physics in Four Dimensions: Simulating Geological Processes and Estimating the Response of Geophysical Properties

Authors: Jonathan Singh, Phil Cilli, Ian Main

Abstract: Understanding the relationship between geophysical properties (e.g., seismic velocity and electrical resistivity) and porosity is fundamental to many rock physics models. However, the geological processes that dominate the formation of porosity, such as cementation and dissolution, will often occur over very long timescales, making the experimental calibration of velocity-porosity trends challenging. Simulating such geological processes in 3D digital rocks and estimating elastic properties from the 3D volumes allows for velocity-porosity trends to be characterized without the long times required for laboratory experiments. Here we simulate deposition of two carbonate clastic rocks, grainstone (near spherical grains) and coquina (shelly fragments), then simulate both cementation and dissolution. These simulations output a set of 3D volumes representing rocks of varying porosity with known mineral and grain phases. Using the spatial phase information, combined with known velocity and densities of the relevant phase properties (we assume all mineral grains to be calcite, and porosity is fully saturated with fresh water) we create velocity and density models corresponding

to each stage of cementation and dissolution. We then estimate seismic velocity from simulated wavefield propagation through each medium using the 3D staggered-grid finite difference method.

We use these estimated velocity-porosity trends to test the elastic model of Cilli and Chapman (2018), which extends differential effective medium theory with the claim that a rock's effective pore aspect ratio changes by power law with porosity. Inverting our digital elastic measurements for effective pore aspect ratio, we find our modelled rocks do follow this power-law relationship. This validates the new rock physics model. Moreover, we see different effective pore aspect ratio-porosity trends for different rock types. This discovery paves the way to use the new rock physics model to link observed changes in effective pore aspect ratio to changes in porosity due to a wider range of geological processes, for example fracturing or compaction.

Cilli, P. and Chapman, M. (2018, June). Modelling the Elastic and Electrical Properties of Rocks with Complex Pore Geometries. Paper presented at 80th EAGE Conference and Exhibition, Copenhagen, Denmark

B.3 European Geosciences Union General Assembly 2019

Title: Estimating seismic velocity changes and relative source locations simultaneously from coda wave interferometry

Authors: Jonathan Singh, Andrew Curtis, Ian Main

Abstract: Coda Wave Interferometry (CWI) is a method for observing and quantifying changes in a medium, which uses the diffuse, multiply-scattered waves, found in the tail of the seismogram. These later arriving waves are very sensitive to small changes in a medium. CWI is a potential source of new information on simultaneous changes in seismic velocity and the relative locations of earthquakes induced by subsurface engineering projects, regional stress changes, or by the earthquakes themselves. When compared against conventional methods, CWI provides significant improvements in

the accuracy and precision of estimates of both changes in velocity and relative source locations. When simultaneous perturbations of velocity and source locations occur, CWI estimates remain accurate. As CWI provides an estimate for the separation between two sources, we use CWI on a cluster of sources to estimate their relative locations, all using a single seismic receiver.

CWI estimates for velocity change represent an average between changes in P and S wave velocities (VP and VS). We present a method to unravel the changes in VP and VS individually, using CWI estimates made at multiple time windows in the coda and prior knowledge of the medium. We demonstrate the method and results in rock physics data from a laboratory experiment.

These results are significant as they represent a major improvement in characterizing the evolution of subsurface properties and microseismicity for a variety of applications including a range of problems in subsurface engineering and time lapse-monitoring.

Appendix C

Rig Operating Procedure Experimental Protocol

As part of the work carried out within this thesis, I assisted in the setting up of Edinburgh rock physics laboratory, including the formation of the experimenal protocol described below.

The Figures C.1 and C.2 illustrate the configureation of all valves for the rock physics rig and fluid board. The experimental protocol is as follows:

1. Remove fluid flow board:
   (a) Remove connectors for Omega pore fluid pressure sensors
   (b) Undo two cap screws at top of board with allen key attached to rig
   (c) Place board safely on ISCO trolley
   (d) Coil sensor cables and store on DAQ trolley hook
2. Return ram to top of its stroke with hand pump (to ensure that as little oil as possible is used to deform the rock to avoid large displacement of ram due to oil expansion on failure):

(a) Check all valves are closed

(b) Open required valves - the only valves that should be open for this are: Hand pump, A3, B3, B2, B1, Ram top

(c) Pump the hand pump slowly (handle is on floor below hand pump) until ram is at top of stroke (this may take a while as the top of the ram may be full of air!). N.B. If air comes out of header tank then it is nearly empty and needs refilling; take it off the top and fill from big barrel using large syringe or funnel

(d) Close all the valves!

3. Assemble sample

(a) Ensure sample preparation procedure is complete (e.g., sonicate, measure length, porosity, density, benchtop velocity etc.)

(b) Put the fritt filter into the hole in the top of both mushroom platens

(c) Put a melinex disk on top (with ultrasonic gel)

(d) Put the fluid distribution disk on top of that (with ultrasonic gel)

(e) Put the grey semi-circular spacer disks on top of mushroom part of base platen

(f) Carefully slide the vessel over the top of the platen and rest it on the grey spacers

(g) Smear ultrasonic gel or shear wave couplant on ends of sample

(h) Slide the rock sample into the vessel

(i) Pop the other melinex disk on top of the rock (with gel)

(j) Slide the top platen into the top of the vessel

4. Inside the frame:

(a) Ensure that the metal spacer on the base is centred inside the inner o-ring

(b) Place the LVDT bottom plate on top of the metal spacer and ensure it is centred

(c) Prepare AE/Velocity Transducer

i. Apply ultrasonic gel to the transducer contacts

ii. Pop the transducers into the transducer platens secured with an o-ring

iii. Put the cushion on the back of the transducers and secure with sellotape to ensure good contact

(d) Put the bottom AE transducer platen onto the bottom LVDT plate (which should be on top of a small aluminum spacer in the middle of the rig) - make sure that the cable is pointing towards the AE kit out the back of the frame (so there is space to connect the fluid flow board)

(e) Lift the vessel into the frame and align with bottom spacer ensure stack is centred and both pore fluid pipes point out the front of the frame

(f) Place the top AE transducer platen on top of the top mushroom platen

(g) Lift the top LVDT plate onto the stack

(h) Ensure the LVDTs nestle in the brass dips well in to their movement range (approx. 1/4 to 1/2 way)

(i) Place two metal spacers on top of the LVDT plate ensure whole stack is fully centred! (N.B. If sample >95mm then only one spacer will fit)

5. Using hand pump, drive ram down to just touch top of stack (this stops the pistons rising up when confining pressure is applied):

(a) Make sure all valves are closed

(b) Open the following valves: Hand pump, A3, B3, B2, A2, Ram, bottom

(c) Pump with handle slowly and gently, watching gap close and stop pumping as soon as there is no light visible through the gap

(d) Close ram bottom valve

(e) Equalise pressure in hand pump by cracking open the wheel on the side of the hand pump and then closing it again

(f) Close all the valves

6. Connect the AE sensors to the PAD amplifiers make sure bottom sensor is connected to channel 1 and top sensor is connected to channel 2

7. Synchronise the two acquisition computers with time server 129.215.7.254: Go to PC time and date settings > select internet time tab > change settings > input server info > update now (may need to press it twice) > ok

8. Acoustic acquisition set-up (record AEs and velocities while confining the sample):

   (a) Switch on Richter unit and open CecchiLeach

   (b) Change BSF storage directory to required path

   (c) Initialise communications

   (d) Check settings

   (e) START acquisition

9. Mechanical data acquisition set-up:

   (a) Open LabVIEW > open multi graphs shared variable project

   (b) Open VI multi graphs draft 9 DAQ correct units

   (c) Start program by clicking on white arrow in top left corner

   (d) Press start DAQ is running

   (e) Check signals look reasonable

10. Apply small confining pressure for centring (< 200 psi limit of low pressure release valve):

    (a) Check the confining fluid vessel connection to the confining pressure piping

    (b) Make sure black refill valve on pump is closed

    (c) Double check that A3 is closed

    (d) Open the following valves: High pressure, Low pressure (labelled always off), Centre, B5, B4, D4

    (e) On ISCO pump control:

        i. Press CONST PRESS key

        ii. Set pressure at 200psi with number pad

        iii. Press ENTER

iv. Press RUN

v. Watch the LP gauge

vi. Pressure will take time to build as there will be air in the vessel due to making and breaking the confining fluid pipe connection check for leaks when pressure shoulders off, but may just be compressing the air inside the vessel.

vii. When LP gauge reads c.200 psi (confining/effective pressures read 1.3 MPa on Labview), close Centre valve and stop pump (same switch as Run)

viii. Close HP and LP valves

ix. Monitor Pc relaxation due to oil cooling allow to equilibrate while continuing with rest of setup

x. Remove grey spacers from the bottom of the stack

11. Flush sample through using only pump not whole fluid flow system! (May not always be necessary)

12. Connect fluid flow board to rig:

(a) Attach board to steel frame with cap screws and allen key attached to rig

(b) Connect the white cables to the pressure gauges - green to green and red to red!

(c) Connect grey cable with bayonet connector to differential pressure gauge (DPG)

(d) Put back pressure regulator (BPR) on top of front panel

(e) Connect PEEK flexible connections:

i. From output filter with label saying to BPR to the BPR

ii. From top connection that says to rock to top piston connection

iii. From bottom connection that says to rock to bottom piston connection

iv. From connection that says to ISCO to the ISCO pump needle valve connection

(f) Ensure that all 11 valves on board and 2 ISCO valves are all closed

13. Fluid flow data acquisition set-up:

    (a) N.B. Ensure mechanical DAQ has already been started

    (b) Open VI fluid flow DAQ

    (c) Start program by clicking on white arrow in top left corner

    (d) Press start DAQ is running

    (e) Check signals seem reasonable if not shut down labview completely and try again! Otherwise, check cables and DAQ connections and sensor connections

14. At this stage, a small confining pressure should be first applied without using the intensifier (i.e., less than the desired effective pressure (Pc minus Pp) but at least 5 MPa more than the desired Pp. Then apply the required pore fluid pressure. Then, using the intensifier, increase the confining pressure to achieve the desired Peff.

15. Apply confining pressure without using bladder accumulator or intensifier (<25 MPa):

    (a) Make sure black refill valve on pump is closed

    (b) Double check that A3, HP and LP are closed

    (c) Open HP valve and run pump at 30% of 400 ml/hr until pressure in pipes before Centre valve (as seen on LP gauge on rig) reaches same as pressure on 1241 (remember that labview DAQ is in MPa and LP gauge is in psi and bar!)

    (d) Close LP valve and open Centre

    (e) Continue pumping at 30% of 400 ml/hr until desired confining pressure is reached

    (f) Once pressure is reached close D4, stop pump, and monitor pressure on GEMS

    (g) Close HP and Centre

16. Apply confining pressure with bladder accumulator but without intensifier (<25 MPa):

    (a) Make sure black refill valve on pump is closed

    (b) Double check that A3, HP and LP are closed

    (c) Open HP valve and run pump at 30% of 400 ml/hr until pressure in pipes before Centre valve (as seen on LP gauge on rig) reaches same as pressure on 1241 (remember that labview DAQ is in MPa and LP gauge is in psi and bar!)

    (d) Close LP valve and open Centre

    (e) Continue pumping at 30% of 400 ml/hr until confining pressure reaches bladder accumulator gas pressure

    (f) Once pressure is reached:

        i. Stop pump

        ii. Close HP and Centre

        iii. Open D5

        iv. Monitor pressure on GEMS and 1241

        v. If the pressure drops, re-pump to point where p1241 pressure-time graph starts to roll over and then increases linearly at a slower rate this is the pressure inside the BA and the oil and gas pressures are now equal

17. Apply pore fluid pressure (sample should have been fully vacuum-saturated prior to assembly):

    (a) Check that the PEEK connections are connected as per instructions above on fluid flow system

    (b) Make sure drain from BPR goes into beaker next to drain bottle

    (c) Open round black Swagelok valve on ISCO pump

    (d) Then, on fluid flow board, open the following valves to allow fluid to enter the rock at both ends: A, C, D, E, F, G, H, I, J,

    (e) Wind down BPR almost completely so doesnt crack while applying pressure

(f) On ISCO control, set pump rate to 60% of 150 ml/hr

(g) Run ISCO pump (switches from right to left: operate - deliver - pump - run)

(h) Fluid pipes will fill with water

(i) Once pressure on both pressure sensors start to rise, monitor pressure until desired pressure is reached, slowing the flow rate on ISCO pump as necessary to ensure that the fluid pressure entering the rock never approaches or overtakes the confining pressure

(j) Once desired pressure is reached, switch off pump and monitor whether pressure is dropping there are two main reasons it will drop - i) there are leaks, and ii) fluid is flowing into the rock

(k) Fix any leaks and wait for pressure to equilibrate

(l) Run pump again until desired pressure is reached

(m) Repeat above three points until fluid pressure remains steady at desired level

(n) Once at desired level set maximum pressure (press red maximum button and turn dial above it) to 40 psi above the run pressure and leave the pump in run mode it will automatically run and stop to maintain that pressure

(o) For undrained test (constant pore fluid volume), close valves A and J

(p) For drained test (constant pore fluid pressure): and set BPR such that it cracks at just over desired pressure

(q) Check confining pressure (NB need to use BA and intensifier to maintain constant confining pressure during tests thus ensuring constant effective pressure)

18. Apply confining pressure using bladder accumulator with intensifier (required for >25 MPa):

(a) Ensure all valves are closed, except D4 and D5 they must remain OPEN.

(b) Open the following valves: High pressure, Centre, B5, Int 2 LP

(c) Ensure both C4 and B4 are closed otherwise intensifier wont work

(d) Run the pump for a short time, pumping oil into the LP end of the intensifier and monitoring the intensifier LVDT this should rise, showing that pressure is building in the HP side of the intensifier.

(e) After about 30 seconds of pumping, stop the pump.

(f) Open Int 2 HP monitor the pressure on the GEMS, it should be about 3 times the pressure on the 1241.

(g) Pressurise the LP end of the intensifier to the pressure at which bladder accumulator is maintained

i. On main ISCO pump control start on 20% of 400 ml/hr

ii. Check switch positions from right to left - operate - deliver - pump - run

iii. Check for pressure increase on p1241 and if all looks good then increase pump rate a little to about 50% of 400 ml/hr

iv. Monitor p1241 until pressure gets to BA2 charge value

v. Open D5

vi. If the pressure drops, re-pump to point where p1241 pressure-time graph starts to roll over and then increases linearly at a slower rate this is the pressure inside the BA and the oil and gas pressures are now equal

(h) Bleed BA to 75-80% of required run pressure (low pressure side required Pc/3):

i. Connect BA bleed valve to gas inlet with all valves and stoppers on the bleed valve closed

ii. Check gas loader valve is closed

iii. Gently crack valve A1 on front panel

iv. Crack gas loader valve very gently until pressure starts to appear on the gauge of the bleed valve

v. Once that pressure is stable, with care open knurled knob

vi. allow pressure to reduce to the desired value monitored on both gauge and p1241 sensor

vii. Shut the knurled knob and shut A1

viii. Bleed any excess gas from bleed valve and disconnect it from the gas inlet

ix. N.B. if BA pressure is lower than required pressure you will need to re-pressurise the BA

(i) Check the following valves are open: High pressure, Centre, B5, Int 2 LP, Int 2 HP, D4, D5,

(j) Ensure B4 and C4 are closed otherwise intensifier wont work

(k) Run the pump, slowly at first and then faster

(l) N.B. if the p1241 pressure increases but the GEMS pressure doesnt, then the intensifier is likely at the end of its stroke.

(m) Monitor pressure on GEMS and p1241 until desired Pc is reached

(n) Close centre valve and HP valve

(o) Stop pump

19. Ensure BPR valve and pipe are pressurised during loading:

(a) Open BPR valve at top of ram

(b) Set the BPR pressure control to something really high

20. Load sample:

(a) Stop set-up acquisition programs, write to excel and save files with appropriate names

(b) Re-start LabView and then acquisition programs for loading/unloading experiment

(c) Ensure Centre valve is closed

(d) Open: High Pressure, A3, B3, B2, A2, Ram Bottom, BRP valve,

(e) Run pump at 20% of 400 ml/h and gently turn to up desired flow rate (100% of 400 ml/hr is approx. 10-5 s-1 strain rate but need to check actual stress rate), 35% of 150 ml/hour = 1e-5

(f) Stop set-up acquisition programs, write to excel and save files with appropriate names (see next step)

21. Run permeability test

    (a) Pause loading

    (b) Close BPR valve

    (c) Close F

    (d) Open J (if undrained test)

    (e) Run fluid flow pump at 60% of 150 ml/hour with max fluid pressure setting about 5% above run pressure

    (f) Adjust BPR in decrease direction so top pressure is less than bottom pressure by about 5%. This ensures that dP is within 10% of confining pressure and average Pp remains at the run pressure.

    (g) Leave to run for full LVDT extension

    (h) Close J (for undrained test)

    (i) Open F

    (j) Pump should remain in run mode the whole time - if pressure drops, the pump will run to return fluid pressure to original run pressure

    (k) Screw LVDT back to starting position

    (l) Open BPR valve

22. Controlled unload

    (a) Leave Pp pump running to maintain fluid pressure

    (b) Close A2, B2, A3, B3, ram bottom

    (c) Make sure ram top is closed

    (d) Make sure BPR valve is open

    (e) Set the BPR controller to match pressure in top of ram

    (f) Turn BPR controller down at slow rate to approximately match the loading rate

23. At the end of test:

(a) Press stop on fluid flow VI

(b) Press write to excel

(c) Excel file will pop up in task bar

(d) Click on it - save as

(e) Save it to your personal data directory with a suitable name

(f) Press stop on mechanical data VI

(g) Press write to excel

(h) Excel file will pop up in task bar

(i) Click on it - save as

(j) Save it to your personal data directory with a suitable name

(k) Press STOP acquisition on CecchiLeach

(l) Close communications

24. Dismantle sample:

(a) Re-start acquisition programs for dismantling

(b) Release the pore fluid pressure by winding out the BPR (if both valves A and J are shut for undrained test, open valve J first)

(c) Check status of confining pressure valve system: Centre valve should be closed , D4 should be open, D5 should be open, B4 and B5 should be open, unless intensifier was used, in which case B4 should be closed

(d) Put the grey spacers back under the vessel

(e) Drain the pore fluid pressure by cracking the BPR until all pressure released

(f) Close D5

(g) Close Int2 HP and Int2 LP

(h) Open C4 to drain very slowly (mm at a time)

(i) Open C5 to drain

(j) Monitor pressure on LabView

(k) While confining pressure is slowly decreasing, ram pressure should also decrease slowly if not, crack open RAM top (mm at a time) and monitor slow pressure drop on LabView

(l) Once the pressure has dropped, close all of the valves apart from C4 and D4 (to allow confining oil to completely drain)

(m) Close all valves on the fluid flow board

(n) If necessary release pressure in the ISCO pump by cracking the big black valve at the back of the pump

(o) Disconnect fluid pipes from to BPR, to ISCO and to rock connections

(p) Disconnect cables from pressure sensors and DPG

(q) Remove fluid flow board

25. Drive the RAM back upwards by opening the following: HP, A3, B3, B2, B1, RAM top,

    (a) Drive the pump forward

    (b) Make sure the black valve to the pump is closed

    (c) Ensure pump control is set to 20% full range to start

    (d) The switches on the control should be set to Operate Deliver Pump and Run

    (e) Ramp the pump up to 100% full range

26. Once ram has returned, stop pump if necessary and close all the valves!

27. Remove fluid flow board from side of the rig and unplug the fluid flow pump

28. Disconnect the fluid flow pipes from mushroom platens

29. Remove the metal spacer and the top LDVT plate from the stack

30. Remove the top AE sensor from the stack

31. Disconnect the confining pressure connection at the back of the vessel

32. Slide the vessel onto the top of the front panel

33. Wipe down the AE sensors to remove the remaining gel

34. Pull out the top piston from the vessel and wipe it down

35. Lift the vessel off the bottom piston and rest the vessel on the steel block so as not to stress the confining pressure connections

36. Remove and wipe down the melinex disks (one may still be on top the sample) and wash the rock dust off the fluid distribution plate

37. Put all components back in the red box

38. Push the sample out with the grey tube NB, may need to core slightly smaller samples and heat shrink them to preserve deformation features. May also need to suck oil out of the vessel to allow sample to slide out easily

39. Tidy everything up, clean out pressure vessel and wipe surfaces

40. N.B. never exceed the desired Peff (Peff = Pc Pp); i.e., if want Pp = 10 MPa and Pc = 40 MPa, desired Peff = 30 MPa. So, take Pc to max 30 MPa first, then flood with fluid and raise Pp to 10 MPa, then raise Pc to 40 MPa to ensure that Peff never exceeds 30 MPa

41. N.B. never overpressure the system make sure Pp << Pc (max 90%) in case of locally high Pp

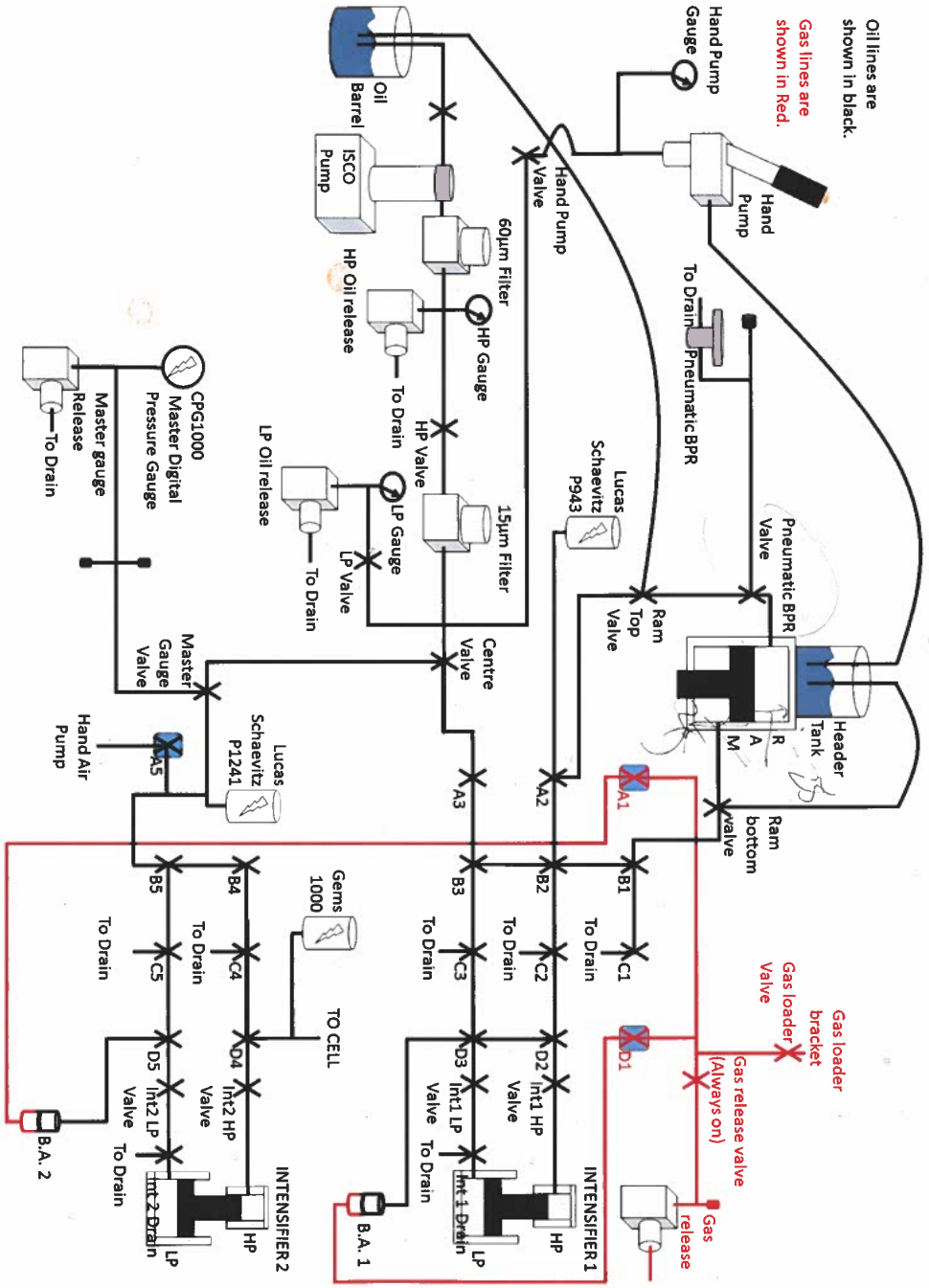

Figure C.1: 4DRP Rock physics rig schematic

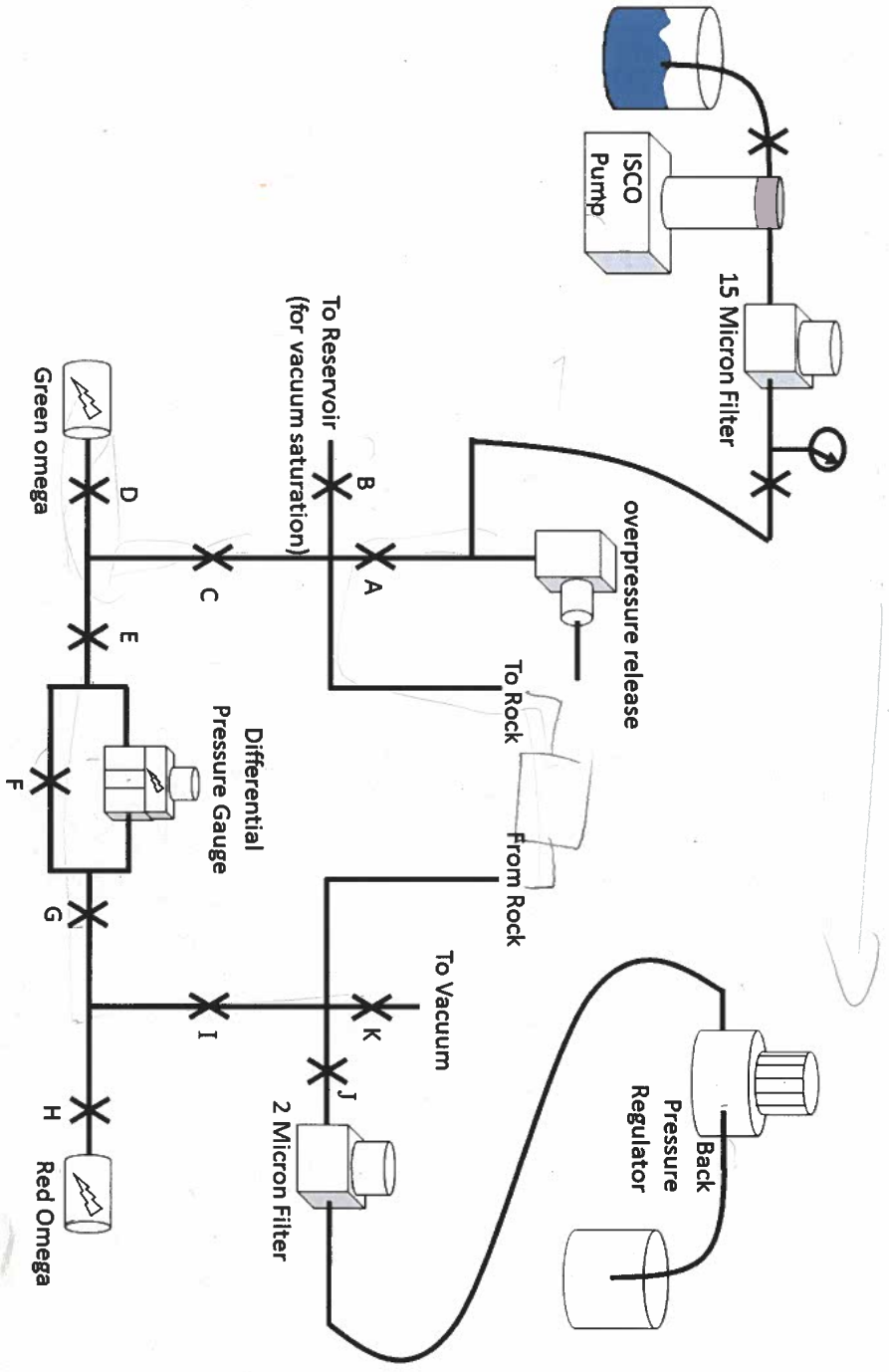

Figure C.2: 4DRP Rock physics rig: pore fluid system for measurement of permeability and/or holding constant pore pressure.

Appendix D

Sample preparation procedure

1. Core, grind, sonicate and dry
2. Mark orientations (red for X-dir, black for Z-dir and blue for Y-dir)
3. Measure dry mass and volume
4. Dab silver paint marks on rock to ensure can match up for CT scan registration
5. Coat with heat shrink
6. Measure dry mass and dimensions with heat shrink
7. CT scan with red line 90 deg to camera
8. Measure dry bench top velocities (ensure S1 = X-dir)
9. Saturate
10. Measure saturated mass and submerged mass
11. Measure saturated benchtop velocities
12. Re-saturate and run experiments with fully saturated samples
13. Compare bench top bulk and shear moduli with bench top porosity and density

References

Akaike, H. (1973). Maximum likelihood identification of gaussian autoregressive moving average models. *Biometrika*, **60**, 255–265.

Ake, J., Mahrer, K., OConnell, D. and Block, L. (2005). Deep-injection and closely monitored induced seismicity at Paradox Valley, Colorado. *Bulletin of the Seismological Society of America*, **95**, 664–683.

Aki, K. and Chouet, B. (1975). Origin of coda waves: source, attenuation, and scattering effects. *Journal of Geophysical Research*, **80**, 3322–3342.

Alkhalifah, T. and Tsvankin, I. (1995). Velocity analysis for transversely isotropic media. *Geophysics*, **60**, 1550–1566.

Allstadt, K. and Malone, S.D. (2014). Swarms of repeating stick-slip icequakes triggered by snow loading at Mount Rainier volcano. *Journal of Geophysical Research: Earth Surface*, **119**, 1180–1203.

Andrä, H., Combaret, N., Dvorkin, J., Glatt, E., Han, J., Kabel, M., Keehm, Y., Krzikalla, F., Lee, M., Madonna, C. *et al.* (2013a). Digital rock physics benchmarks Part I: Imaging and segmentation. *Computers & Geosciences*, **50**, 25–32.

Andrä, H., Combaret, N., Dvorkin, J., Glatt, E., Han, J., Kabel, M., Keehm, Y., Krzikalla, F., Lee, M., Madonna, C. *et al.* (2013b). Digital rock physics benchmarks part II: computing effective properties. *Computers & Geosciences*, **50**, 33–43.

Anugonda, P., Wiehn, J.S. and Turner, J.A. (2001). Diffusion of ultrasound in concrete. *Ultrasonics*, **39**, 429–435.

Arns, C.H., Knackstedt, M.A., Pinczewski, W.V. and Garboczi, E.J. (2002). Computation of linear elastic properties from microtomographic images: Methodology and agreement between theory and experiment. *Geophysics*, **67**, 1396–1405.

Arts, R., Eiken, O., Chadwick, A., Zweigel, P., Van der Meer, L. and Zinszner, B. (2004). Monitoring of CO2 injected at Sleipner using time-lapse seismic data. *Energy*, **29**, 1383–1392.

Ayling, M.R., Meredith, P.G. and Murrell, S.A. (1995). Microcracking during triaxial deformation of porous rocks monitored by changes in rock physical properties, i. elastic-wave propagation measurements on dry rocks. *Tectonophysics*, **245**, 205–221.

Baker, D.R., Mancini, L., Polacci, M., Higgins, M., Gualda, G., Hill, R. and Rivers, M. (2012). An introduction to the application of x-ray microtomography to the three-dimensional study of igneous rocks. *Lithos*, **148**, 262–276.

Bakhorji, A.M. (2010). *Laboratory measurements of static and dynamic elastic properties in carbonate*. Ph.D. thesis, University of Alberta, Edmonton, Alberta , Canada.

Barclay, S. and Worden, R. (2000). Effects of reservoir wettability on quartz cementation in oil fields. *Quartz Cementation in Sandstones*, 103–117.

Bass, J.D. (1995). Elasticity of minerals, glasses, and melts. *Mineral physics & crystallography: a handbook of physical constants*, **2**, 45–63.

Bathurst, R.G. (1972). *Carbonate sediments and their diagenesis*, vol. 12. Elsevier.

Berndt, D.J. and Clifford, J. (1994). Using dynamic time warping to find patterns in time series. In *Proceedings of the 3rd International Conference on Knowledge Discovery and Data Mining*, 359–370, AAAI Press.

Berryman, J.G. (1980). Long-wavelength propagation in composite elastic media II. ellipsoidal inclusions. *The Journal of the Acoustical Society of America*, **68**, 1820–1831.

Berryman, J.G. (1992). Single-scattering approximations for coefficients in Biots equations of poroelasticity. *The Journal of the Acoustical Society of America*, **91**, 551–571.

Betz, O., Wegst, U., Weide, D., Heethoff, M., Helfen, L., Lee, W.K. and Cloetens, P. (2007). Imaging applications of synchrotron x-ray phase-contrast microtomography in biological morphology and biomaterials science. I. general aspects of the technique and its advantages in the analysis of millimetre-sized arthropod structure. *Journal of Microscopy*, **227**, 51–71.

Birch, F. (1960). The velocity of compressional waves in rocks to 10 kilobars: 1. *Journal of Geophysical Research*, **65**, 1083–1102.

Biswal, B., Øren, P.E., Held, R., Bakke, S. and Hilfer, R. (2007). Stochastic multiscale model for carbonate rocks. *Physical Review E*, **75**, 061303.

Bjørlykke, K., Ramm, M. and Saigal, G.C. (1989). Sandstone diagenesis and porosity modification during basin evolution. *Geologische Rundschau*, **78**, 243–268.

Bloch, S., Lander, R.H. and Bonnell, L. (2002). Anomalously high porosity and permeability in deeply buried sandstone reservoirs: Origin and predictability. *AAPG bulletin*, **86**, 301–328.

Bonnet, E., Bour, O., Odling, N.E., Davy, P., Main, I., Cowie, P. and Berkowitz, B. (2001). Scaling of fracture systems in geological media. *Reviews of Geophysics*, **39**, 347–383.

Boschetti, F., Dentith, M.D. and List, R.D. (1996). A fractal-based algorithm for detecting first arrivals on seismic traces. *Geophysics*, **61**, 1095–1102.

Brace, W., Paulding Jr, B. and Scholz, C. (1966). Dilatancy in the fracture of crystalline rocks. *Journal of Geophysical Research*, **71**, 3939–3953.

Brillouin, L. (1960). *Wave propagation and group velocity*. Academic Press.

Brown, L.T. (2002). *Integration of rock physics and reservoir simulation for the interpretation of time-lapse seismic data at Weyburn field, Saskatchewan*. Ph.D. thesis, Colorado School of Mines. Arthur Lakes Library.

Burnham, K.P. and Anderson, D.R. (2003). *Model selection and multimodel inference: A practical information-theoretic approach*. Springer Science & Business Media.

Burnham, K.P. and Anderson, D.R. (2004). Multimodel inference: understanding AIC and BIC in model selection. *Sociological methods & research*, **33**, 261–304.

Castagna, J.P., Batzle, M.L. and Eastwood, R.L. (1985). Relationships between compressional-wave and shear-wave velocities in clastic silicate rocks. *Geophysics*, **50**, 571–581.

Catto, B. (2015). *Laminitos microbiais no membro Crato (neoaptiano), Bacia do Araripe, nordeste do Brasil*. Ph.D. thesis, Universidade Estadual Paulista (UNESP).

Cavanaugh, J.E. *et al.* (1997). Unifying the derivations for the Akaike and corrected Akaike information criteria. *Statistics & Probability Letters*, **33**, 201–208.

Chen, K.H., Bürgmann, R. and Nadeau, R.M. (2013). Do earthquakes talk to each other? Triggering and interaction of repeating sequences at Parkfield. *Journal of Geophysical Research: Solid Earth*, **118**, 165–182.

Christensen, N.I. (1966). Shear wave velocities in metamorphic rocks at pressures to 10 kilobars. *Journal of Geophysical Research*, **71**, 3549–3556.

Christensen, N.I. and Mooney, W.D. (1995). Seismic velocity structure and composition of the continental crust: A global view. *Journal of Geophysical Research: Solid Earth*, **100**, 9761–9788.

Christensen, R.M. (2012). *Mechanics of composite materials*. Courier Corporation.

Cilli, P. and Chapman, M. (2018). Modelling the elastic and electrical properties of rocks with complex pore geometries. In *80th EAGE Conference and Exhibition 2018*.

Cilli, P.A. and Chapman, M. (2019). The power-law relation between inclusion aspect ratio and porosity: Implications for elastic and electrical modeling. *In Preparation*.

Cleary, M.P., Lee, S.M. and Chen, I.W. (1980). Self-consistent techniques for heterogeneous media. *Journal of the Engineering Mechanics Division*, **106**, 861–887.

Cloetens, P., Ludwig, W., Boller, E., Peyrin, F., Chlenker, M. and Baruchel, J. (2002). 3d imaging using coherent synchrotron radiation. *Image Analysis & Stereology*, **21**, S75–S85.

Cnudde, V. and Boone, M. (2013). High-resolution x-ray computed tomography in geosciences: A review of the current technology and applications. *Earth-Science Reviews*, **123**, 1–17.

Cook, R.D. (1977). Detection of influential observation in linear regression. *Technometrics*, **19**, 15–18.

Cook, R.D. and Weisberg, S. (1982). *Residuals and influence in regression*. New York: Chapman and Hall.

Cowan, M., Page, J. and Weitz, D. (2000). Velocity fluctuations in fluidized suspensions probed by ultrasonic correlation spectroscopy. *Physical review letters*, **85**, 453.

Crampin, S. (1981). A review of wave motion in anisotropic and cracked elastic-media. *Wave motion*, **3**, 343–391.

Derode, A., Tourin, A. and Fink, M. (2001). Random multiple scattering of ultrasound. II. Is time reversal a self-averaging process? *Physical Review E*, **64**, 036606.

Dodge, D.A., Beroza, G.C. and Ellsworth, W. (1995). Foreshock sequence of the 1992 Landers, California, earthquake and its implications for earthquake nucleation. *Journal of Geophysical Research: Solid Earth*, **100**, 9865–9880.

Douglas, A. (1967). Joint epicentre determination. *Nature*, **215**, 47.

Duffaut, K. and Landrø, M. (2007). Vp/Vs ratio versus differential stress and rock consolidation - A comparison between rock models and time-lapse AVO data. *Geophysics*, **72**, C81–C94.

Dvorkin, J. and Nur, A. (1996). Elasticity of high-porosity sandstones: Theory for two North Sea data sets. *Geophysics*, **61**, 1363–1370.

Dvorkin, J., Derzhi, N., Diaz, E. and Fang, Q. (2011). Relevance of computational rock physics. *Geophysics*, **76**, E141–E153.

Earle, P.S. and Shearer, P.M. (1994). Characterization of global seismograms using an automatic-picking algorithm. *Bulletin of the Seismological Society of America*, **84**, 366–376.

Eberhart-Phillips, D., Han, D.H. and Zoback, M.D. (1989). Empirical relationships among seismic velocity, effective pressure, porosity, and clay content in sandstone. *Geophysics*, **54**, 82–89.

Ellsworth, W.L. (2013). Injection-induced earthquakes. *Science*, **341**, 1225942.

Ervin, C.P., McGinnis, L., Otis, R. and Hall, M. (1983). Automated analysis of marine refraction data: A computer algorithm. *Geophysics*, **48**, 582–589.

Eshelby, J.D. (1957). The determination of the elastic field of an ellipsoidal inclusion, and related problems. *Proceedings of the Royal Society London A*, **241**, 376–396.

Fabricius, I.L. (2003). How burial diagenesis of chalk sediments controls sonic velocity and porosity. *AAPG bulletin*, **87**, 1755–1778.

Fehler, M., Roberts, P. and Fairbanks, T. (1988). A temporal change in coda wave attenuation observed during an eruption of Mount St. Helens. *Journal of Geophysical Research: Solid Earth*, **93**, 4367–4373.

Fournier, F., Leonide, P., Biscarrat, K., Gallois, A., Borgomano, J. and Foubert, A. (2011). Elastic properties of microporous cemented grainstones. *Geophysics*, **76**, E211–E226.

Fournier, F., Léonide, P., Kleipool, L., Toullec, R., Reijmer, J.J., Borgomano, J., Klootwijk, T. and Van Der Molen, J. (2014). Pore space evolution and elastic properties of platform carbonates (Urgonian limestone, Barremian–Aptian, SE France). *Sedimentary Geology*, **308**, 1–17.

Fournier, F., Pellerin, M., Villeneuve, Q., Teillet, T., Hong, F., Poli, E., Borgomano, J., Léonide, P. and Hairabian, A. (2018). The equivalent pore aspect ratio as a tool for pore type prediction in carbonate reservoirs. *AAPG Bulletin*, **102**, 1343.

Frankel, A. (1991). High-frequency spectral falloff of earthquakes, fractal dimension of complex rupture, b value, and the scaling of strength on faults. *Journal of Geophysical Research: Solid Earth*, **96**, 6291–6302.

Frohlich, C. and Brunt, M. (2013). Two-year survey of earthquakes and injection/production wells in the Eagle Ford Shale, Texas, prior to the Mw4.8 20 October 2011 earthquake. *Earth and Planetary Science Letters*, **379**, 56–63.

Fung, Y.c. (1965). Foundations of solid mechanics(book on deformation and motion of elastic and plastic solids including variational calculus and tensor analysis). *Englwood Cliffs, N. J., Prentice-Hall, Inc.., 1965. 525 P.*

Fusseis, F., Xiao, X., Schrank, C. and De Carlo, F. (2014). A brief guide to synchrotron radiation-based microtomography in (structural) geology and rock mechanics. *Journal of Structural Geology*, **65**, 1–16.

Gao, Y. and Crampin, S. (2004). Observations of stress relaxation before earthquakes. *Geophysical Journal International*, **157**, 578–582.

Gardner, G., Gardner, L. and Gregory, A. (1974). Formation velocity and density - the diagnostic basics for stratigraphic traps. *Geophysics*, **39**, 770–780.

Gennisson, J.L., Deffieux, T., Fink, M. and Tanter, M. (2013). Ultrasound elastography: principles and techniques. *Diagnostic and interventional imaging*, **94**, 487–495.

Got, J.L., Fréchet, J. and Klein, F.W. (1994). Deep fault plane geometry inferred from multiplet relative relocation beneath the south flank of Kilauea. *Journal of Geophysical Research: Solid Earth*, **99**, 15375–15386.

Green, A. and Mair, J. (1983). Subhorizontal fractures in a granitic pluton: Their detection and implications for radioactive waste disposal. *Geophysics*, **48**, 1428–1449.

Grêt, A., Snieder, R. and Özbay, U. (2006). Monitoring in situ stress changes in a mining environment with coda wave interferometry. *Geophysical Journal International*, **167**, 504–508.

Gubernatis, J.E. and Krumhansl, J.A. (1975). Macroscopic engineering properties of polycrystalline materials: Elastic properties. *Journal of Applied Physics*, **46**, 1875–1883.

Guéguen, Y. and Palciauskas, V. (1994). *Introduction to the Physics of Rocks*. Princeton University Press.

Guilbot, J. and Smith, B. (2002). 4-D constrained depth conversion for reservoir compaction estimation: Application to Ekofisk field. *The Leading Edge*, **21**, 302–308.

Gusev, A. and Lemzikov, V. (1985). Properties of scattered elastic waves in the lithosphere of Kamchatka: parameters and temporal variations. *Tectonophysics*, **112**, 137–153.

Hadziioannou, C., Larose, E., Coutant, O., Roux, P. and Campillo, M. (2009). Stability of monitoring weak changes in multiply scattering media with ambient noise correlation: Laboratory experiments. *The Journal of the Acoustical Society of America*, **125**, 3688–3695.

Hadziioannou, C., Larose, E., Baig, A., Roux, P. and Campillo, M. (2011). Improving temporal resolution in ambient noise monitoring of seismic wave speed. *Journal of Geophysical Research: Solid Earth*, **116**.

Hale, D. (2013). Dynamic warping of seismic images. *Geophysics*, **78**, S105–S115.

Hallbauer, D., Wagner, H. and Cook, N. (1973). Some observations concerning the microscopic and mechanical behaviour of quartzite specimens in stiff, triaxial compression tests. In *International Journal of Rock Mechanics and Mining Sciences & Geomechanics Abstracts*, vol. 10, 713–726, Elsevier.

Han, D.h., Nur, A. and Morgan, D. (1986). Effects of porosity and clay content on wave velocities in sandstones. *Geophysics*, **51**, 2093–2107.

Harrigan, T. and Mann, R. (1984). Characterization of microstructural anisotropy in orthotropic materials using a second rank tensor. *Journal of Materials Science*, **19**, 761–767.

Hashin, Z. and Shtrikman, S. (1963). A variational approach to the theory of the elastic behaviour of multiphase materials. *Journal of the Mechanics and Physics of Solids*, **11**, 127–140.

Hatherly, P. (1982). A computer method for determining seismic first arrival times. *Geophysics*, **47**, 1431–1436.

Hayward, T.W. and Bostock, M.G. (2017). Slip behavior of the Queen Charlotte plate boundary before and after the 2012, MW 7.8 Haida Gwaii earthquake: Evidence from repeating earthquakes. *Journal of Geophysical Research: Solid Earth*, **122**, 8990–9011.

Heckmeier, M. and Maret, G. (1997). Dark speckle imaging of colloidal suspensions in multiple light scattering media. In *Optical Methods and Physics of Colloidal Dispersions*, 12–16, Springer.

Hennino, R., Trégourès, N., Shapiro, N., Margerin, L., Campillo, M., Van Tiggelen, B. and Weaver, R. (2001). Observation of equipartition of seismic waves. *Physical review letters*, **86**, 3447.

Herwanger, J.V. and Horne, S.A. (2009). Linking reservoir geomechanics and time-lapse seismics: Predicting anisotropic velocity changes and seismic attributes. *Geophysics*, **74**, W13–W33.

Hill, R. (1952). The elastic behaviour of a crystalline aggregate. *Proceedings of the Physical Society. Section A*, **65**, 349.

Hornby, B.E. (1998). Experimental laboratory determination of the dynamic elastic properties of wet, drained shales. *Journal of Geophysical Research: Solid Earth*, **103**, 29945–29964.

Hosa, A. and Wood, R. (2017). Quantifying the impact of early calcite cementation on the reservoir quality of carbonate rocks: A 3D process-based model. *Advances in water resources*, **104**, 89–104.

Hurvich, C.M. and Tsai, C.L. (1989). Regression and time series model selection in small samples. *Biometrika*, **76**, 297–307.

Iassonov, P., Gebrenegus, T. and Tuller, M. (2009). Segmentation of x-ray computed tomography images of porous materials: A crucial step for characterization and quantitative analysis of pore structures. *Water Resources Research*, **45**.

Iding, M. and Ringrose, P. (2010). Evaluating the impact of fractures on the performance of the In Salah CO2 storage site. *International Journal of Greenhouse Gas Control*, **4**, 242–248.

Jaeger, J.C., Cook, N.G. and Zimmerman, R. (2009). *Fundamentals of rock mechanics*. John Wiley & Sons.

James, S., Knox, H., Abbott, R. and Screaton, E. (2017). Improved moving window cross-spectral analysis for resolving large temporal seismic velocity changes in permafrost. *Geophysical Research Letters*, **44**, 4018–4026.

Jin, A. and Aki, K. (1986). Temporal change in coda Q before the Tangshan earthquake of 1976 and the Haicheng earthquake of 1975. *Journal of Geophysical Research: Solid Earth*, **91**, 665–673.

Jin, A. and Aki, K. (1991). Case 7A: Observational and physical bases for the coda Q^{-1} precursor. *Evaluation of Proposed Earthquake Precursors*, **32**, 33–53.

Jouini, M.S., Vega, S. and Al-Ratrout, A. (2015). Numerical estimation of carbonate rock properties using multiscale images. *Geophysical Prospecting*, **63**, 405–421.

Kaestner, A., Lehmann, E. and Stampanoni, M. (2008). Imaging and image processing in porous media research. *Advances in Water Resources*, **31**, 1174–1187.

Kalam, M.Z. (2012). Digital rock physics for fast and accurate special core analysis in carbonates. In *New Technologies in the Oil and Gas Industry*, IntechOpen.

Kang, Q., Zhang, D. and Chen, S. (2003). Simulation of dissolution and precipitation in porous media. *Journal of Geophysical Research: Solid Earth*, **108**.

Kanu, C. and Snieder, R. (2015). Time-lapse imaging of a localized weak change with multiply scattered waves using numerical-based sensitivity kernel. *Journal of Geophysical Research: Solid Earth*, **120**, 5595–5605.

Karimpouli, S. and Tahmasebi, P. (2016). Conditional reconstruction: An alternative strategy in digital rock physics. *Geophysics*, **81**, D465–D477.

Karimpouli, S., Khoshlesan, S., Saenger, E.H. and Koochi, H.H. (2018). Application of alternative digital rock physics methods in a real case study: a challenge between clean and cemented samples. *Geophysical Prospecting*, **66**, 767–783.

Karol, R.H. and Berardinelli, C. (2003). *Chemical grouting and soil stabilization*. CRC Press.

Katsman, R., Aharonov, E. and Scher, H. (2005). Numerical simulation of compaction bands in high-porosity sedimentary rock. *Mechanics of materials*, **37**, 143–162.

Keehm, Y. (2003). Computational rock physics: Transport properties in porous media and applications. *Ph. D. thesis, Stanford University*.

Keehm, Y., Mukerji, T. and Nur, A. (2001). Computational rock physics at the pore scale: Transport properties and diagenesis in realistic pore geometries. *The Leading Edge*, **20**, 180–183.

Kharraa, H.S., Al-Amri, M.A., Mahmoud, M. and Okasha, T. (2013). Assessment of uncertainty in porosity measurements using NMR and conventional logging tools in carbonate reservoir. In *SPE Saudi Arabia Section Technical Symposium and Exhibition*, Society of Petroleum Engineers.

King, M.S. (1966). Wave velocities in rocks as a function of changes in overburden pressure and pore fluid saturants. *Geophysics*, **31**, 50–73.

Knackstedt, M.A., Latham, S., Madadi, M., Sheppard, A., Varslot, T. and Arns, C. (2009). Digital rock physics: 3D imaging of core material and correlations to acoustic and flow properties. *The Leading Edge*, **28**, 28–33.

Kuster, G.T. and Toksöz, M.N. (1974). Velocity and attenuation of seismic waves in two-phase media: Part i. theoretical formulations. *Geophysics*, **39**, 587–606.

Landrø, M. and Stammeijer, J. (2004). Quantitative estimation of compaction and velocity changes using 4D impedance and traveltime changes. *Geophysics*, **69**, 949–957.

Larose, E. and Hall, S. (2009). Monitoring stress related velocity variation in concrete with a $2\times\ 10^{-5}$ relative resolution using diffuse ultrasound. *The Journal of the Acoustical Society of America*, **125**, 1853–1856.

Latief, F., Biswal, B., Fauzi, U. and Hilfer, R. (2010). Continuum reconstruction of the pore scale microstructure for Fontainebleau sandstone. *Physica A: Statistical Mechanics and its Applications*, **389**, 1607–1618.

Lee, H.B. (1975). Accuracy limitations of hyperbolic multilateration systems. *IEEE Transactions on Aerospace and Electronic Systems*, 16–29.

Lennartz-Sassinek, S., Main, I., Zaiser, M. and Graham, C. (2014). Acceleration and localization of subcritical crack growth in a natural composite material. *Physical Review E*, **90**, 052401.

Li, W., Schmitt, D.R., Zou, C. and Chen, X. (2018). A program to calculate pulse transmission responses through transversely isotropic media. *Computers & geosciences*, **114**, 59–72.

Liu, X., Sun, J. and Wang, H. (2009). Numerical simulation of rock electrical properties based on digital cores. *Applied Geophysics*, **6**, 1–7.

Lobkis, O.I. and Weaver, R.L. (2001). On the emergence of the Greens function in the correlations of a diffuse field. *The Journal of the Acoustical Society of America*, **110**, 3011–3017.

Lobkis, O.I. and Weaver, R.L. (2003). Coda-wave interferometry in finite solids: Recovery of P-to-S conversion rates in an elastodynamic billiard. *Physical review letters*, **90**, 254302.

Lockner, D. (1993). The role of acoustic emission in the study of rock fracture. *International Journal of Rock Mechanics and Mining Sciences & Geomechanics Abstracts*, **30**, 883–899.

Lockner, D., Byerlee, J., Kuksenko, V., Ponomarev, A. and Sidorin, A. (1992). Observations of quasistatic fault growth from acoustic emissions. *International Geophysics*, **51**, 3–31.

Madonna, C., Almqvist, B.S. and Saenger, E.H. (2012). Digital rock physics: numerical prediction of pressure-dependent ultrasonic velocities using micro-CT imaging. *Geophysical Journal International*, **189**, 1475–1482.

Makse, H.A., Gland, N., Johnson, D.L. and Schwartz, L.M. (1999). Why effective medium theory fails in granular materials. *Physical Review Letters*, **83**, 5070.

Margerin, L., Campillo, M., Van Tiggelen, B. and Hennino, R. (2009). Energy partition of seismic coda waves in layered media: Theory and application to pinyon flats observatory. *Geophysical Journal International*, **177**, 571–585.

Margerin, L., Planès, T., Mayor, J. and Calvet, M. (2015). Sensitivity kernels for coda-wave interferometry and scattering tomography: theory and numerical evaluation in

two-dimensional anisotropically scattering media. *Geophysical Journal International*, **204**, 650–666.

Margrave, G.F. (2000). New seismic modelling facilities in MATLAB. Tech. rep., CREWES Research Report 12.

Margrave, G.F. (2007). Methods of seismic data processing. *Geophysics*, **557**, 657.

Martys, N.S., Hagedorn, J.G., Goujon, D. and Devaney, J.E. (1999). Large-scale simulations of single-and multicomponent flow in porous media. In *Developments in X-Ray Tomography II*, vol. 3772, 205–214, International Society for Optics and Photonics.

Mason, W.P. and McSkimin, H. (1947). Attenuation and scattering of high frequency sound waves in metals and glasses. *The Journal of the Acoustical Society of America*, **19**, 464–473.

Mavko, G., Mukerji, T. and Dvorkin, J. (2009). *The rock physics handbook: Tools for seismic analysis of porous media*. Cambridge university press.

McLaskey, G.C. and Glaser, S.D. (2012). Acoustic emission sensor calibration for absolute source measurements. *Journal of Nondestructive Evaluation*, **31**, 157–168.

McQuarrie, A.D. and Tsai, C.L. (1998). *Regression and time series model selection*. World Scientific.

Medeiros, F., Ozkan, E., Kazemi, H. *et al.* (2007). Productivity and drainage area of fractured horizontal wells in tight gas reservoirs. In *Rocky Mountain Oil & Gas Technology Symposium*, Society of Petroleum Engineers.

Mikesell, T.D., Malcolm, A.E., Yang, D. and Haney, M.M. (2015). A comparison of methods to estimate seismic phase delays: Numerical examples for coda wave interferometry. *Geophysical Journal International*, **202**, 347–360.

Mindlin, R. (1949). Compliance of elastic bodies in contact. *Journal of Applied Mechanics, American Society of Mechanical Engineers*, **16**, 259–268.

Miranda, T., Barbosa, J., Gale, J., Marrett, R., Gomes, I., Neumann, V., Matos, G., Correia, O. and Alencar, M. (2014). Natural fracture characterization in Aptian carbonates, Araripe basin, NE Brazil. In *76th EAGE Conference and Exhibition 2014*.

Miranda, T., Barbosa, J., Gomes, I., Soares, A., Santos, R., Matos, G., McKinnon, E., Neumann, V. and Marrett, R. (2016). Petrophysics and petrography of Aptian tight carbonate reservoir, Araripe basin, NE Brazil. In *78th EAGE Conference and Exhibition 2016*.

Moczo, P., Robertsson, J.O. and Eisner, L. (2007). The finite-difference time-domain method for modeling of seismic wave propagation. *Advances in Geophysics*, **48**, 421–516.

Molyneux, J.B. and Schmitt, D.R. (1999). First-break timing: Arrival onset times by direct correlation. *Geophysics*, **64**, 1492–1501.

Molyneux, J.B. and Schmitt, D.R. (2000). Compressional-wave velocities in attenuating media: A laboratory physical model study. *Geophysics*, **65**, 1162–1167.

Moore, C.H. (1989). *Carbonate diagenesis and porosity*, vol. 46. Elsevier.

Mordret, A., Mikesell, T.D., Harig, C., Lipovsky, B.P. and Prieto, G.A. (2016). Monitoring southwest Greenlands ice sheet melt with ambient seismic noise. *Science advances*, **2**, e1501538.

Mori, T. and Tanaka, K. (1973). Average stress in matrix and average elastic energy of materials with misfitting inclusions. *Acta metallurgica*, **21**, 571–574.

Mousavi, M.A. and Bryant, S.L. (2012). Connectivity of pore space as a control on two-phase flow properties of tight-gas sandstones. *Transport in porous media*, **94**, 537–554.

Mousavi, M.A., Prodanovic, M. and Jacobi, D. (2012). New classification of carbonate rocks for process-based pore-scale modeling. *SPE Journal*, **18**, 243–263.

Nadeau, P.H. (1998). An experimental study of the effects of diagenetic clay minerals on reservoir sands. *Clays and Clay Minerals*, **46**, 18–26.

Neumann, V. (1999). *Estratigrafía, sedimentología, geoquímica y diagénesis de los sistemas lacustres Aptienses-Albienses de la Cuenca de Araripe (Noreste de Brasil). 1999*. Ph.D. thesis, Tesis (Doctorado), Universidad de Barcelona, Barcelona 244p.

Nichols, D.E. (1996). Maximum energy traveltimes calculated in the seismic frequency band. *Geophysics*, **61**, 253–263.

Norris, A.N. (1985). A differential scheme for the effective moduli of composites. *Mechanics of materials*, **4**, 1–16.

Nur, A. (1971). Effects of stress on velocity anisotropy in rocks with cracks. *Journal of Geophysical Research*, **76**, 2022–2034.

Nur, A. and Simmons, G. (1969). Stress-induced velocity anisotropy in rock: An experimental study. *Journal of Geophysical Research*, **74**, 6667–6674.

Nye, J.F. *et al.* (1985). *Physical properties of crystals: their representation by tensors and matrices*. Oxford university press.

Obermann, A., Planès, T., Larose, E., Sens-Schönfelder, C. and Campillo, M. (2013). Depth sensitivity of seismic coda waves to velocity perturbations in an elastic heterogeneous medium. *Geophysical Journal International*, **194**, 372–382.

Obermann, A., Planès, T., Hadziioannou, C. and Campillo, M. (2016). Lapse-time-dependent coda-wave depth sensitivity to local velocity perturbations in 3-d heterogeneous elastic media. *Geophysical Journal International*, **207**, 59–66.

O'Connell, R.J. and Budiansky, B. (1974). Seismic velocities in dry and saturated cracked solids. *Journal of Geophysical Research*, **79**, 5412–5426.

Olhoeft, G.R. (1981). Electrical properties of rocks. *Physical properties of rocks and minerals*, **2**, 257–297.

Pacheco, C. and Snieder, R. (2005). Time-lapse travel time change of multiply scattered acoustic waves. *The Journal of the Acoustical Society of America*, **118**, 1300–1310.

Paterson, M.S. and Wong, T.f. (2005). *Experimental rock deformation-the brittle field*. Springer Science & Business Media.

Peraldi, R. and Clement, A. (1972). Digital processing of refraction data study of first arrivals. *Geophysical Prospecting*, **20**, 529–548.

Pickett, G.R. (1963). Acoustic character logs and their applications in formation evaluation. *Journal of Petroleum technology*, **15**, 659–667.

Planès, T. and Larose, E. (2013). A review of ultrasonic coda wave interferometry in concrete. *Cement and Concrete Research*, **53**, 248–255.

Poirier, J.P. (1985). *Creep of crystals: high-temperature deformation processes in metals, ceramics and minerals*. Cambridge University Press.

Potsika, V.T., Grivas, K.N., Protopappas, V.C., Vavva, M.G., Raum, K., Rohrbach, D., Polyzos, D. and Fotiadis, D.I. (2014). Application of an effective medium theory for modeling ultrasound wave propagation in healing long bones. *Ultrasonics*, **54**, 1219–1230.

Poupinet, G., Ellsworth, W. and Frechet, J. (1984). Monitoring velocity variations in the crust using earthquake doublets: An application to the Calaveras fault, California. *Journal of Geophysical Research: Solid Earth*, **89**, 5719–5731.

Press, W.H., Flannery, B.P., Teukolsky, S.A. and Vetterling, W.T. (1986). *Numerical Recipes: The Art of Scientific Computing*. Cambridge University Press.

Price, D., Angus, D., Garcia, A. and Fisher, Q. (2017). Probabilistic analysis and comparison of stress-dependent rock physics models. *Geophysical Journal International*, **210**, 196–209.

Pyrak-Nolte, L.J., Myer, L.R. and Cook, N.G. (1990). Transmission of seismic waves across single natural fractures. *Journal of Geophysical Research: Solid Earth*, **95**, 8617–8638.

Ratdomopurbo, A. and Poupinet, G. (1995). Monitoring a temporal change of seismic velocity in a volcano: Application to the 1992 eruption of Mt. Merapi (Indonesia). *Geophysical research letters*, **22**, 775–778.

Raymer, L., Hunt, E., Gardner, J.S. *et al.* (1980). An improved sonic transit time-to-porosity transform. In *SPWLA 21st Annual Logging Symposium*, Society of Petrophysicists and Well-Log Analysts.

Reuss, A. (1929). Berechnung der fließgrenze von mischkristallen auf grund der plastizitätsbedingung für einkristalle. *ZAMM-Journal of Applied Mathematics and Mechanics/Zeitschrift für Angewandte Mathematik und Mechanik*, **9**, 49–58.

Robein, E. (2003). *Velocities, Time-Imaging, and Depth-Imaging in Reflection Seismics: Principles and Methods*. EAGE.

Robinson, D., Snieder, R. and Sambridge, M. (2007). Using coda wave interferometry for estimating the variation in source mechanism between double couple events. *Journal of Geophysical Research: Solid Earth*, **112**, B12302.

Robinson, D., Sambridge, M. and Snieder, R. (2011). A probabilistic approach for estimating the separation between a pair of earthquakes directly from their coda waves. *Journal of Geophysical Research*, **116**, B04309.

Robinson, D.J., Sambridge, M., Snieder, R. and Hauser, J. (2013). Relocating a cluster of earthquakes using a single seismic station. *Bulletin of the Seismological Society of America*, **103**, 3057–3072.

Rossetto, V., Margerin, L., Planes, T. and Larose, E. (2011). Locating a weak change using diffuse waves: Theoretical approach and inversion procedure. *Journal of Applied Physics*, **109**, 034903.

Ruff, L.J. (2002). State of stress within the earth. *International Handbook of Earthquake & Engineering Seismology*, 539–558.

Saenger, E.H. (2008). Numerical methods to determine effective elastic properties. *International Journal of Engineering Science*, **46**, 598–605.

Saenger, E.H. and Bohlen, T. (2004). Finite-difference modeling of viscoelastic and anisotropic wave propagation using the rotated staggered grid. *Geophysics*, **69**, 583–591.

Saenger, E.H., Gold, N. and Shapiro, S.A. (2000). Modeling the propagation of elastic waves using a modified finite-difference grid. *Wave motion*, **31**, 77–92.

Saenger, E.H., Enzmann, F., Keehm, Y. and Steeb, H. (2011). Digital rock physics: Effect of fluid viscosity on effective elastic properties. *Journal of Applied Geophysics*, **74**, 236–241.

Saenger, E.H., Madonna, C., Osorno, M., Uribe, D. and Steeb, H. (2014). Digital carbonate rock physics. In *SEG Technical Program Expanded Abstracts 2014*, 2915–2919, Society of Exploration Geophysicists.

Sahimi, M. (2011). *Flow and transport in porous media and fractured rock: from classical methods to modern approaches*. John Wiley & Sons.

Salvermoser, J., Hadziioannou, C. and Stähler, S.C. (2015). Structural monitoring of a highway bridge using passive noise recordings from street traffic. *The Journal of the Acoustical Society of America*, **138**, 3864–3872.

Sammonds, P., Ayling, M., Meredith, P., Murrell, S., Jones, C. *et al.* (1989). A laboratory investigation of acoustic emission and elastic wave velocity changes during rock failure under triaxial stresses. In *ISRM International Symposium*, International Society for Rock Mechanics and Rock Engineering.

Sammonds, P., Meredith, P. and Main, I. (1992). Role of pore fluids in the generation of seismic precursors to shear fracture. *Nature*, **359**, 228.

Sams, M., Neep, J., Worthington, M. and King, M. (1997). The measurement of velocity dispersion and frequency-dependent intrinsic attenuation in sedimentary rocks. *Geophysics*, **62**, 1456–1464.

Saneiyan, S., Ntarlagiannis, D., Werkema Jr, D.D. and Ustra, A. (2018). Geophysical methods for monitoring soil stabilization processes. *Journal of applied geophysics*, **148**, 234–244.

Sato, H. (1988). Temporal change in scattering and attenuation associated with the earthquake occurrence - A review of recent studies on coda waves. *Pure and applied geophysics*, **126**, 465–497.

Sato, H., Fehler, M.C. and Maeda, T. (2012). *Seismic wave propagation and scattering in the heterogeneous earth*, vol. 484. Springer.

Saxena, N. and Mavko, G. (2016). Estimating elastic moduli of rocks from thin sections: Digital rock study of 3D properties from 2D images. *Computers & Geosciences*, **88**, 9–21.

Sayers, C. and Kachanov, M. (1995). Microcrack-induced elastic wave anisotropy of brittle rocks. *Journal of Geophysical Research: Solid Earth*, **100**, 4149–4156.

Scholle, P.A. and Ulmer-Scholle, D.S. (2003). *A Color Guide to the Petrography of Carbonate Rocks: Grains, Textures, Porosity, Diagenesis, AAPG Memoir 77*, vol. 77. AAPG.

Scholz, C.H., Sykes, L.R. and Aggarwal, Y.P. (1973). Earthquake prediction: a physical basis. *Science*, **181**, 803–810.

Schubnel, A., Benson, P.M., Thompson, B.D., Hazzard, J.F. and Young, R.P. (2006). Quantifying damage, saturation and anisotropy in cracked rocks by inverting elastic wave velocities. In *Rock Damage and Fluid Transport, Part I*, 947–973, Springer.

Sell, K., Saenger, E.H., Falenty, A., Chaouachi, M., Haberthür, D., Enzmann, F., Kuhs, W.F. and Kersten, M. (2016). On the path to the digital rock physics of gas hydrate-bearing sediments-processing of in situ synchrotron-tomography data. *Solid Earth*, **7**, 1243.

Sens-Schönfelder, C. and Wegler, U. (2006). Passive image interferometry and seasonal variations of seismic velocities at Merapi Volcano, Indonesia. *Geophysical research letters*, **33**, L21302.

Shearer, P. (1999). *Introduction to Seismology*. Cambridge University Press.

Singh, J., Curtis, A. and Main, I. (2018). Accurate estimates of simultaneous seismic velocity changes and interfracture-source distances from coda wave interferometry. In *SEG Technical Program Expanded Abstracts 2018*, 2897–2901, Society of Exploration Geophysicists.

Singh, J., Curtis, A., Zhao, Y., Cartwright-Taylor, A. and Main, I. (2019). Coda wave interferometry for accurate simultaneous monitoring of velocity and acoustic source locations in experimental rock physics. *Journal of Geophysical Research, doi:10.1029/2019JB017577*.

Singhal, B.B.S. and Gupta, R.P. (2010). *Applied hydrogeology of fractured rocks*. Springer Science & Business Media.

Snieder, R. (2002). Coda wave interferometry and the equilibration of energy in elastic media. *Physical review E*, **66**, 046615.

Snieder, R. (2006). The theory of coda wave interferometry. *Pure and Applied Geophysics*, **163**, 455–473.

Snieder, R. and Page, J. (2007). Multiple scattering in evolving media. *Physics today*, **60**, 49.

Snieder, R. and Vrijlandt, M. (2005). Constraining the source separation with coda wave interferometry: Theory and application to earthquake doublets in the Hayward fault, California. *Journal of Geophysical Research: Solid Earth*, **110**.

Snieder, R., Grêt, A., Douma, H. and Scales, J. (2002). Coda wave interferometry for estimating nonlinear behavior in seismic velocity. *Science*, **295**, 2253–2255.

Snieder, R., Duran, A. and Obermann, A. (2019). Locating velocity changes in elastic media with coda wave interferometry. *Seismic Ambient Noise*, 188–217.

Stanchits, S., Vinciguerra, S. and Dresen, G. (2006). Ultrasonic velocities, acoustic emission characteristics and crack damage of basalt and granite. *Pure and Applied Geophysics*, **163**, 975–994.

Stauffer, D. and Aharony, A. (2014). *Introduction to percolation theory*. Taylor & Francis.

Stein, S. and Wysession, M. (2009). *An introduction to seismology, earthquakes, and Earth structure*. John Wiley & Sons.

Stock, S. (2008). Recent advances in x-ray microtomography applied to materials. *International Materials Reviews*, **53**, 129–181.

Stork, A.L., Allmark, C., Curtis, A., Kendall, J.M. and White, D.J. (2018). Assessing the potential to use repeated ambient noise seismic tomography to detect CO2 leaks: Application to the Aquistore storage site. *International Journal of Greenhouse Gas Control*, **71**, 20–35.

Sun, Z., Garboczi, E.J. and Shah, S.P. (2007). Modeling the elastic properties of concrete composites: Experiment, differential effective medium theory, and numerical simulation. *Cement and Concrete Composites*, **29**, 22–38.

Tang, C. (1997). Numerical simulation of progressive rock failure and associated seismicity. *International Journal of Rock Mechanics and Mining Sciences*, **34**, 249–261.

Toksöz, M., Johnston, D.H. and Timur, A. (1979). Attenuation of seismic waves in dry and saturated rocks: I. laboratory measurements. *Geophysics*, **44**, 681–690.

Tosaya, C. and Nur, A. (1982). Effects of diagenesis and clays on compressional velocities in rocks. *Geophysical Research Letters*, **9**, 5–8.

Tucker, M.E. and Wright, V.P. (2009). *Carbonate sedimentology*. John Wiley & Sons.

Twiss, R.J. and Moores, E.M. (1992). *Structural geology*. Macmillan.

Vasseur, J., Wadsworth, F.B., Heap, M.J., Main, I.G., Lavallée, Y. and Dingwell, D.B. (2017). Does an inter-flaw length control the accuracy of rupture forecasting in geological materials? *Earth and Planetary Science Letters*, **475**, 181–189.

Versteeg, R. (1994). The marmousi experience: Velocity model determination on a synthetic complex data set. *The Leading Edge*, **13**, 927–936.

Versteeg, R.J. (1993). Sensitivity of prestack depth migration to the velocity model. *Geophysics*, **58**, 873–882.

Verwer, K., Braaksma, H. and Kenter, J.A. (2008). Acoustic properties of carbonates: Effects of rock texture and implications for fluid substitution. *Geophysics*, **73**, B51–B65.

Vlastos, S., Liu, E., Main, I., Schoenberg, M., Narteau, C., Li, X. and Maillot, B. (2006). Dual simulations of fluid flow and seismic wave propagation in a fractured network: effects of pore pressure on seismic signature. *Geophysical Journal International*, **166**, 825–838.

Vlastos, S., Liu, E., Main, I.G. and Narteau, C. (2007). Numerical simulation of wave propagation in 2-D fractured media: scattering attenuation at different stages of the growth of a fracture population. *Geophysical Journal International*, **171**, 865–880.

Voigt, W. (1889). Ueber die beziehung zwischen den beiden elasticitätsconstanten isotroper körper. *Annalen der physik*, **274**, 573–587.

Voigt, W. (1928). *Lehrbuch der kristallphysik*, vol. 962. Teubner Leipzig.

Volti, T. and Crampin, S. (2003). A four-year study of shear-wave splitting in Iceland: 1. Background and preliminary analysis. *Geological Society, London, Special Publications*, **212**, 117–133.

Wadell, H. (1932). Volume, shape, and roundness of rock particles. *The Journal of Geology*, **40**, 443–451.

Waldhauser, F. and Ellsworth, W.L. (2000). A double-difference earthquake location algorithm: Method and application to the northern hayward fault, california. *Bulletin of the Seismological Society of America*, **90**, 1353–1368.

Waldhauser, F. and Ellsworth, W.L. (2002). Fault structure and mechanics of the Hayward fault, California, from double-difference earthquake locations. *Journal of Geophysical Research: Solid Earth*, **107**.

Walker, D.M., Tordesillas, A. and Kuhn, M.R. (2016). Spatial connectivity of force chains in a simple shear 3D simulation exhibiting shear bands. *Journal of Engineering Mechanics*, **143**, C4016009.

Walsh, J. (1965). The effect of cracks on the compressibility of rock. *Journal of Geophysical Research*, **70**, 381–389.

Walton, K. (1987). The effective elastic moduli of a random packing of spheres. *Journal of the Mechanics and Physics of Solids*, **35**, 213–226.

Wang, W., Kravchenko, A., Smucker, A. and Rivers, M. (2011). Comparison of image segmentation methods in simulated 2D and 3D microtomographic images of soil aggregates. *Geoderma*, **162**, 231–241.

Wang, Z. (2001). Fundamentals of seismic rock physics. *Geophysics*, **66**, 398–412.

Watanabe, K. and Takahashi, H. (1995). Fractal geometry characterization of geothermal reservoir fracture networks. *Journal of Geophysical Research: Solid Earth*, **100**, 521–528.

Weaver, R.L. (1982). On diffuse waves in solid media. *The Journal of the Acoustical Society of America*, **71**, 1608–1609.

Weaver, R.L. (1990). Diffusivity of ultrasound in polycrystals. *Journal of the Mechanics and Physics of Solids*, **38**, 55–86.

Weaver, R.L. and Lobkis, O.I. (2001). Ultrasonics without a source: Thermal fluctuation correlations at MHz frequencies. *Physical Review Letters*, **87**, 134301.

Weil, M.H., DeJong, J.T., Martinez, B.C. and Mortensen, B.M. (2011). Seismic and resistivity measurements for real-time monitoring of microbially induced calcite precipitation in sand. *Geotechnical Testing Journal*, **35**, 330–341.

Wiegmann, A. and Zemitis, A. (2006). EJ-HEAT: A fast explicit jump harmonic averaging solver for the effective heat conductivity of composite materials.

Wildenschild, D. and Sheppard, A.P. (2013). X-ray imaging and analysis techniques for quantifying pore-scale structure and processes in subsurface porous medium systems. *Advances in Water Resources*, **51**, 217–246.

Wood, A. (1941). A textbook of sound. *Bell, London*.

Wu, Y., Lai, Y. and Zhang, Z.Q. (2007). Effective medium theory for elastic metamaterials in two dimensions. *Physical Review B*, **76**, 205313.

Zhan, X., Schwartz, L.M., Toksöz, M.N., Smith, W.C. and Morgan, F.D. (2010). Pore-scale modeling of electrical and fluid transport in Berea sandstone. *Geophysics*, **75**, F135–F142.

Zhao, Y. and Curtis, A. (2019). Relative source location using coda wave interferometry: method, code package, and application to mining induced earthquakes. *Geophysics*, **84**, 1–58.

Zhao, Y., Curtis, A. and Baptie, B. (2017). Locating microseismic sources with a single seismometer channel using coda wave interferometry. *Geophysics*, **82**, A19–A24.

Zimmer, M.A. (2004). *Seismic velocities in unconsolidated sands: Measurements of pressure, sorting, and compaction effects*. Ph.D. thesis, Stanford University.

Zoback, M.L. and Zoback, M. (1980). State of stress in the conterminous United States. *Journal of Geophysical Research: Solid Earth*, **85**, 6113–6156.